



HAL
open science

Interdigitated ITO sensor for ECIS monitoring of breast cancer cells

Jaime Andres Martinez Santamaria

► **To cite this version:**

Jaime Andres Martinez Santamaria. Interdigitated ITO sensor for ECIS monitoring of breast cancer cells. Biotechnology. Université de Lyon, 2019. English. NNT : 2019LYSE1005 . tel-02125936

HAL Id: tel-02125936

<https://theses.hal.science/tel-02125936>

Submitted on 10 May 2019

HAL is a multi-disciplinary open access archive for the deposit and dissemination of scientific research documents, whether they are published or not. The documents may come from teaching and research institutions in France or abroad, or from public or private research centers.

L'archive ouverte pluridisciplinaire **HAL**, est destinée au dépôt et à la diffusion de documents scientifiques de niveau recherche, publiés ou non, émanant des établissements d'enseignement et de recherche français ou étrangers, des laboratoires publics ou privés.



N° d'ordre NNT : 2019LYSE1005

THÈSE DE DOCTORAT DE L'UNIVERSITÉ DE LYON
opérée au sein de
l'Université Claude Bernard Lyon 1

École Doctorale ED 160
Electronique, Electrotechnique, Automatique de Lyon (EEA)

Spécialité de doctorat : Ingénierie du vivant

Soutenue publiquement à huis clos le 05/02/2019, par :
Jaime Andres Martinez Santamaria

Interdigitated ITO sensor for ECIS monitoring of breast cancer cells

Devant le jury composé de :

Nom Prénom, grade/qualité, établissement/entreprise	Président(e)
M. DUNLOP Patrick, Professeur, Université de Ulster	Rapporteur
M. NADI Mustapha, Professeur des Universités, Université de Lorraine	Rapporteur
Mme. FAIVRE Magalie, Chargée de Recherche, CNRS	Examinatrice
M. MAILLEY Pascal, Directeur de recherche, CEA Grenoble	Examinateur
Mme. PAYEN Lea, Professeure des Universités, Université Lyon 1	Examinatrice
Mme. PHAM Pascale, Ingénieure-Chercheuse, CEA Grenoble	Examinatrice
Mme. FERRIGNO Rosaria, Professeure des Universités, Université Lyon 1	Directrice de thèse
M. MCADAMS Eric, Professeur des Universités, INSA Lyon	Co-directeur de thèse

UNIVERSITÉ CLAUDE BERNARD-LYON 1

Président de l'Université

Président du Conseil Académique

Vice-président du Conseil d'Administration

Vice-président du Conseil Formation et Vie Universitaire

Vice-président de la Commission Recherche

Directrice Générale des Services

M. le Professeur Frédéric FLEURY

M. le Professeur Hamda BEN HADID

M. le Professeur Didier REVEL

M. le Professeur Philippe CHEVALIER

M. Fabrice VALLÉE

Mme Dominique MARCHAND

COMPOSANTES SANTE

Faculté de Médecine Lyon Est-Claude Bernard

Directeur: M. le Professeur G.RODE

Faculté de Médecine et de Maïeutique Lyon Sud-Charles

Mérieux

Directeur: Mme la Professeure C.BURILLON

Faculté d'Odontologie

Directeur: M. le Professeur D.BOURGEOIS

Institut des Sciences Pharmaceutiques et Biologiques

Directeur: Mme la Professeure C.VINCIGUERRA

Institut des Sciences et Techniques de la Réadaptation

Directeur: M.X.PERROT

Département de la formation et Centre de Recherche
en Biologie Humaine

Directeur: Mme la Professeure A-M.SCHOTT

COMPOSANTES ET DEPARTEMENTS DE SCIENCES ET TECHNOLOGIE

Faculté des Sciences et technologies

Directeur: M. F.DE MARCHI

Département Biologie

Directeur: M. le Professeur F.THEVENARD

Département Chimie Biochimie

Directeur: Mme C.FELIX

Département GEP

Directeur: M. Hassan HAMMOURI

Département Informatique

Directeur: M. le Professeur S.AKKOUCHE

Département Mathématiques

Directeur: M. le Professeur G.TOMANOV

Département Mécanique

Directeur: M. le Professeur H.BEN HADID

Département Physique

Directeur: M. le Professeur J-C PLENET

UFR Sciences et Techniques des Activités Physiques et Sportives

Directeur: M. Y.VANPOULLE

Observatoire des Sciences de l'Univers de Lyon

Directeur: M. B.GUIDERDONI

Polytech Lyon

Directeur: M.le Professeur E.PERRIN

Ecole Supérieure de Chimie Physique Electronique

Directeur: M.G.PIGNAULT

Institut Universitaire de Technologie de Lyon 1

Directeur: M.le Professeur C.VITON

Ecole Supérieure du Professorat et de l'Education

Directeur: M.le Professeur A.MOUGNIOTTE

Institut de Science Financière et d'Assurances

Directeur: M.N.LEBOISNE

Contents

	Page
Nomenclature	13
Acknowledgements	17
Résumé	18
Abstract	19
Introduction	20
Bibliography	22
1 Impedance sensing for personalized medicine in cancer treatment	25
1.1 Personalized medicine and Cancer	25
1.1.1 Molecular profiling of healthy and cancer patients	27
1.1.2 Cell based assays for drug testing	28
1.2 Strategies implemented in cell-based assays for drug screening	29
1.2.1 <i>Ex-vivo</i> tumor culture models for drug testing	30
1.2.2 Detection methods	31
1.3 Electrical Cell-substrate Impedance Sensing (ECIS)	41
1.3.1 Electrodes' geometries	41
1.3.2 Electrode material	43
1.3.3 Cell-substrate impedance sensing experiment	43
1.4 Drug screening applications based on ECIS sensing	50
1.4.1 Barrier function activities	53
1.4.2 Ion channel activities	53
1.4.3 Cell signaling	54
1.4.4 Cell metabolism	54
1.4.5 Cytotoxicity and drug resistance	55
1.4.6 Photodamaging and Photoprotective effects	56
1.5 Conclusions	57
Bibliography	58

2	Materials and Methods	77
2.1	Cell lines	77
2.2	Preparation of solutions	79
2.2.1	Potassium chloride solutions	79
2.2.2	PBS 1X solution	79
2.2.3	Iridium bath	79
2.2.4	Cell culture medium	81
2.2.5	CN/BSA coating solution	81
2.2.6	5-FU solution	81
2.3	Cell culture procedure	82
2.3.1	Cell culture conditions	82
2.3.2	Sub-culturing cells	82
2.3.3	Cell preparation for ECIS experiments	83
2.4	ECIS device fabrication	83
2.4.1	Gold electrodes	85
2.4.2	ITO electrodes	86
2.4.3	Electrodeposition of IrO _x	87
2.5	Experimental set-up	87
2.5.1	Device preparation for ECIS experiments	87
2.5.2	Impedance measurement set-up	87
	Bibliography	92
3	Characterization of Au and ITO IDEs for ECIS experiments	96
3.1	Interdigitated electrodes in contact with an electrolyte	96
3.1.1	Theoretical aspects	96
3.1.2	Impedance response of gold and ITO IDEs in KCl solutions	101
3.1.3	Impedance response of Au and ITO IDEs in culture medium	118
3.2	Conclusion	121
	Bibliography	123
4	Au and ITO behaviors during ECIS and cytotoxicity experiments	127
4.1	IDEs in contact with biological cells	127
4.1.1	MCF-7 and MDA-MB-231 morphology comparison on different materials	127
4.1.2	Monitoring cell proliferation with impedance	131
4.1.3	Normalized impedance Z_{norm}	140
4.1.4	Normalized impedance at low frequency (f_{LF}), high frequency (f_{HF}) and peak frequency (f_{peak})	142
4.1.5	Evolution of f_{peak} as a function of time	145
4.1.6	Equivalent circuit model of cells adhered on Au and ITO IDEs	147
4.2	Real-time monitoring of cellular response to 5-FU exposure	154
4.2.1	Impedance response of cancer cells to 5-FU	154
4.2.2	Concentration effect of 5-FU	160
4.3	Equivalent circuit modeling of breast cancer cells exposed to 5-FU	164
4.3.1	Cytotoxicity effects on MDA-MB-231 cell line	164
4.3.2	Cytotoxicity effects on MCF-7 cell line	166
4.4	Conclusion	170
	Bibliography	172

5	Strategy to enhance sensitivity of ITO IDEs	180
5.1	Surface modification of electrodes used in ECIS	181
5.2	Surface-modified electrodes with IrO _x	187
5.2.1	Electrodeposition of IrO _x on Au and ITO IDEs	187
5.2.2	Modified electrodes in cell culture medium	193
5.2.3	Electrical parameters in cell culture medium	198
5.3	Monitoring cell growth with IrO _x modified ITO IDEs	202
5.3.1	Impedance response of IrO _x /ITO in contact with cells	202
5.3.2	Normalized impedance	204
5.3.3	Equivalent circuit model of MCF-7 cells adhered on IrO _x /ITO IDEs	205
5.4	Conclusion	207
	Bibliography	208
6	Conclusion	217

List of Tables

1.1	Advantages and limitations of different label-based methods.	33
1.2	Advantages and limitations of different label-free based assays.	40
1.3	Commercialized impedance based biosensors.	51
2.1	Conductivities of the various KCl solutions at room temperature.	79
2.2	Composition of the supplemented cell culture medium used for MDA-MB-231 and MCF-7 cells. (DMEM was supplemented with FBS and PS).	81
2.3	Impedance of standard circuit components.	89
3.1	Impedance fitting results of Au IDEs in contact with KCl solutions using fitting model 2 (Mean \pm SD).	109
3.2	Values of K_{IDE} calculated and measured of IDEs with different w sizes.	109
3.3	Impedance fitting results of Au and ITO IDEs in contact with KCl solutions using fitting model 2 (Mean \pm SD).	112
3.4	Impedance fitting results of Au and ITO IDEs in contact with KCl solutions at low and high frequency interface parts (Mean \pm SD).	115
3.5	Values obtained from Bode plots of Au and ITO IDEs in contact with KCl (Mean \pm SD).	117
3.6	Impedance fitting results of the Au IDEs before/after CN/BSA in contact with the supplemented DMEM (Mean \pm SD) (*:statistically significant and **: not statistically significant).	120
3.7	Impedance fitting results of Au-CN/BSA and ITO-CN/BSA IDEs in contact with the supplemented DMEM and using fitting model 2 (Mean \pm SD with $n = 5$ for Au and $n = 8$ for ITO) (*:statistically significant and **: not statistically significant).	121
4.1	Parameters extracted with ImageJ for each cell line proliferating on Petri dish, ITO-CN/BSA and Glass-CN/BSA (Mean \pm SD) with $n = 14$ for each cell line.	130
4.2	$(Z_{norm})_{peak}$ and f_{peak} values when $\eta = 99\%$ for Au IDEs and $\eta = 96\%$ for ITO IDEs. (Mean \pm SD with $n=6$ for Au and $n=4$ for ITO).	142
5.1	Impedance fitting results of the ITO IDEs in contact with 100 mM KCl for different electrodeposition cycles.	192
5.2	Impedance fitting results of the Au and ITO IDEs in contact with the supplemented DMEM before and after IrO_x electrodeposition. $n=5$ for IrO_x/Au , $n=5$ for Au, $n=4$ for IrO_x/ITO and $n=8$ for ITO (Mean \pm SD).	198

List of Figures

1.1	Percentage (in blue) of the patient population for which a particular drug in a class is ineffective, on average	25
1.2	Impedance based microfluidic systems: (a) Wong’s chip and (b) Kim’s platform	29
1.3	Different culture methods: (a) 2D monolayer culture, (b) 3D organoid culture and (c) Patient-derived xenograft	30
1.4	Principle of different label-free techniques: (a) Resonant wave guide grating, (b) Surface acoustic wave, (c) Surface plasmon resonance, (d) Quartz crystal microbalance and (e) Electrical impedance	34
1.5	Impedance based microfluidic systems: (a) Zhang’s system, (b) Rothbauer’s system, (c) Nguyen’s device, (d) Henry’s system and (e) Luongo’s system	38
1.6	Monopolar and IDEs used in ECIS. (a) Arrangement of four small WEs (0.03 cm ²) and a common CE (0.6 cm ²), (b) Array of electrodes with different areas 0.00025 cm ² , 0.0004 cm ² , 0.0013 cm ² and 0.004 cm ² , (c) ECIS [®] array of 10 electrodes of 250 μm, (e) Interdigitated parallel line electrode array, (f) Electrode structures with disc electrodes added on the electrode lines and (g) Interdigitated finger configuration of ECIS [®] electrodes	42
1.7	ECIS measurement graph showing various cellular morphological changes of normal human dermal fibroblasts neonatal cells (HDFn) growth response for 20 hours	44
1.8	(a) Electrical model of cell in suspension, (b) Simplified electrical model of cell in suspension and (c) Circuit model neglecting R_m with $C_m^* = C_m/2$	45
1.9	Equivalent circuit model used by Wang et al. where R_s represents the resistance of the solution. R_{gap} corresponds to the gaps between the underside of the attached cells and the electrode surface, and its value is related to the closeness of cell adhesion to the substrate. C_m is associated with the capacitive behavior of the cell membrane	46
1.10	Equivalent circuit model used by Benson et al. where C_m is the membrane capacitance, R_s is the resistance of the cell culture medium and the electrode-electrolyte interfacial capacitance is C_{int}	46
1.11	Equivalent circuit model used by Xiaoliang et al. where $C_{parasitic}$ represents the parasitic effects in the chip and measuring system, CPE_{int} represents the interfacial impedance, R_s is the cell culture medium resistance, C_m is the cell membrane capacitance, R_{intra} is the intracellular resistance and R_{gap} is the resistance between the adhered cells and the electrode surface	47

LIST OF FIGURES

1.12	Equivalent circuit model used by Meissner et al. where $C_{parasitic}$ corresponds to parasitic effects in the system, CPE_{int} represents the interfacial impedance, R_{extra} is the extracellular resistance, R_{intra} is the intracellular resistance and CPE_{cells} corresponds to the cell membrane	47
1.13	Schematic of electrical impedance measurement on planar electrodes (Draw not to scale) . . .	48
1.14	Current pathways at (a) low frequencies and at (b) high frequencies in an ECIS system. . . .	48
1.15	Diagram of the cells in tissue culture and the model used to calculate the specific impedance of a cell-covered electrode	49
1.16	Different applications of ECIS. (a) Barrier function, (b) Cancer metastasis, (c) Ion channel activity, (d) Cell signaling analysis, (e) Cell metabolism analysis, (f) Cytotoxicity screening, (g) Drug resistance and (h) Photoprotectivity	52
2.1	Phase contrast microscopy images of the cell lines MCF-7 and MDA-MB-231 grown in Petri dish at (a,b) 20X and (c,d) 40X magnification (Leica D2000).	78
2.2	Steps in the Yamanaka protocol for the preparation of the iridium bath: (i,ii) water and Ir(IV) salt mixing; (iii) hydrogen peroxide addition; (iv) oxalic acid addition; (v) potassium carbonate addition	80
2.3	Color changes during aging process of iridium oxide solution at room temperature	80
2.4	Mechanism of action of 5-FU drug inside the cell	82
2.5	(a) Top view of the ECIS system with bonded PDMS reservoir (5 mm diameter). (b) Interdigitated electrode dimensions: $s = 20 \mu\text{m}$, $w = 20 \mu\text{m}$ and $l = 1 \text{ mm}$	84
2.6	(a) Fabrication process of Au IDEs: S1813 spin coating, UV exposure on mask, photoresist development, Au evaporation and lift-off. (The drawing is not to scale) (b) Microscopy image of Au IDEs on glass slides.	85
2.7	(a) Fabrication process of ITO IDEs: S1813 spin coating, UV exposure on mask, photoresist development, Cr evaporation, Cr Lift-off, RIE and Cr etching (the drawing is not to scale). (b) Microscopy image of ITO IDEs on glass slides.	86
2.8	IrO_x electrodeposition set-up. Working electrode (WE), Counter electrode (CE) and Reference electrode (RE)	87
2.9	Schematic view of the different electrode configurations. a) 2-electrode setup. b) 3-electrode setup and c) 4-electrode setup	90
2.10	Measurement set-up elements: (a) PC-data acquisition with Nova software (b) ECIS device connected to the Potentiostat.	91
3.1	Schematic of the different impedance contributions in a coplanar two electrode system in absence of cells during an ECIS assay (the drawing is not to scale).	97
3.2	Models of the double layer structure: (a) Helmholtz model (b) Gouy-Chapman model and (c) Gouy-Chapman-Stern model (ψ_s is the surface electrical potential and r is the diameter of solvated ions)	99
3.3	Equivalent circuits models of IDEs in contact with an electrolyte reported by (a) Timmer et al., (b) Hong et al., (c) Rana et al. and (d) Baccar et al	101
3.4	(a) Magnitude and (b) Phase of the impedance spectra of Au IDEs ($s = 20 \mu\text{m}$, $w = 20 \mu\text{m}$ and $L = 1 \text{ mm}$) in contact with KCl solutions of different concentrations in the frequency range from 1 MHz to 100 mHz.	102
3.5	Imaginary part $-Z''$ vs real part Z' of impedance spectra of Au IDEs ($s = 20 \mu\text{m}$, $w = 20 \mu\text{m}$ and $L = 1 \text{ mm}$) in contact with KCl solutions of different concentrations in the frequency range (a) from 1 MHz to 100 mHz, (b) from 1 MHz to 40.7 Hz, (c) from 1 MHz to 1.8 kHz and (d) from 1MHz to 16.6 kHz.	104
3.6	(a) Fitting model 1 of the electrodes in contact with DI water and KCl solutions. (b) Fitting model 2 of the electrodes in contact with DI water and KCl solutions.	105

LIST OF FIGURES

3.7	Comparing equivalent circuit models for Au electrodes in contact with 100 mM KCl solution. (a) Nyquist plot in the frequency range from 1 MHz to 100 mHz and (b) from 1 MHz to 16.6 kHz.	106
3.8	Impedance loci for different shapes of pore on the electrode surface	106
3.9	(a) R_2 (b) Q_2 and α_2 (c) versus KCl concentration for Au IDEs. (n = 7, Mean \pm SD).	107
3.10	Sketch of the Nyquist plot of Au IDEs depicting the effect of increased concentration on the semi circular arc due to $R_2 // CPE_2$	108
3.11	Impedance magnitudes of ITO IDEs normalized with $R_{t,Au}$ at different KCl concentrations: (a) DI water, (b) 1 mM and (c) 100 mM. (d) Phase of the impedance spectra of ITO IDEs in the frequency range from 1 MHz to 100 mHz.	110
3.12	Imaginary part $-Z''$ vs real part Z' of impedance spectra of ITO IDEs in contact with KCl solutions at different concentrations in the frequency range (a) from 1 MHz to 100 mHz, (b) from 1 MHz to 23.6 Hz, (c) from 1 MHz to 1 kHz and (d) from 1 MHz to 2.4 kHz.	111
3.13	Atomic force microscopy images of the surface of (a) Au IDEs and (b) ITO IDEs on $2\mu\text{m} \times 2\mu\text{m}$ areas.	113
3.14	High frequency impedance spectra for (a) flat metal electrode and (b) rough surfaced electrode. Figure adapted from figures 3 and 4 in [McAdams]. Copyright 1995 by Elsevier. Adapted with permission.	113
3.15	Diagram of the Nyquist plot showing the bending effect on the impedance spectrum at 100 mM for Au IDEs.	116
3.16	(a) Magnitude and (b) Phase of the impedance of Au and Au-CN/BSA IDEs in contact with the supplemented DMEM in the frequency range from 1 MHz to 100 mHz.	118
3.17	Nyquist plot of Au and Au-CN/BSA IDEs in contact with the supplemented DMEM : (a) from 1 MHz to 100 mHz, (b) from 1 MHz to 362 Hz and (c) from 1 MHz to 9.6 kHz.	119
3.18	(a) Magnitude and (b) Phase of the impedance of Au-CN/BSA and ITO-CN/BSA IDEs in contact with the supplemented DMEM over the frequency range 1 MHz to 100 mHz.	120
4.1	Phase contrast micrographs of MCF-7 and MDA-MB-231 cells after 46 h of cell culture on different substrates covered with CN/BSA at 40X magnification (Leica D2000).	128
4.2	Axes used in ImageJ for each cell line. L_a : big axis, L_b : small axis.	129
4.3	Phase contrast micrographs of MCF-7 cells on the surface of the Au IDEs at 10X magnification (Leica D2000).	133
4.4	Phase contrast micrographs of MCF-7 cells on the surface of the ITO IDEs at 10X magnification (Leica D2000).	134
4.5	Stages of the cell adhesion process: (I) Sedimentation, (II) Cell attachment and (III) Cell spreading and stable adhesion	135
4.6	Magnitude and Phase of the impedance spectra of MCF-7 cells on Au IDEs during cell growth in the frequency range (a, c) from 1 MHz to 100 mHz and (b, d) from 1 MHz to 100 Hz.	136
4.7	Magnitude and Phase of the impedance spectra of MCF-7 cells on ITO IDEs during cell growth in the frequency range (a, c) from 1 MHz to 100 mHz and (b, d) from 1 MHz to 100 Hz.	137
4.8	Imaginary part vs Real part of the impedance spectra of MCF-7 cells on Au IDEs in the frequency range from (a) 1 MHz to 100 mHz, (b) 476 Hz to 100 mHz, (c) 1 MHz to 12.6 kHz and (d) Diagram of the evolution of the Nyquist curves during cell growth on Au IDEs.	138
4.9	Imaginary part vs Real part of the impedance spectra of MCF-7 cells on ITO IDEs in the frequency range from (a) 1 MHz to 100 mHz, (b) from 1 MHz to 1 kHz, (c) from 1 MHz to 3.2 kHz and (d) Diagram of the evolution of the Nyquist curves during cell growth on ITO IDEs.	139

LIST OF FIGURES

4.10	Normalized impedance of MCF-7 cells grown on Au IDEs and measured over a frequency range from 1 MHz to 100 mHz.	140
4.11	Normalized impedance of MCF-7 cells grown on ITO IDEs and measured over a frequency range from 1 MHz to 100 mHz.	141
4.12	Z_{norm} versus frequency with f_{peak} , f_{LF} and f_{HF} indicated during cell proliferation on (a) Au IDEs and (b) ITO IDEs.	143
4.13	Z_{norm} at f_{peak} (21.8 kHz), f_{LF} (4.2 kHz) and f_{HF} (194 kHz) versus time during MCF-7 proliferation on Au IDEs.	144
4.14	Z_{norm} at f_{peak} (5.5 kHz), f_{LF} (1.8 kHz) and at f_{HF} (194 kHz) versus time during MCF-7 proliferation on ITO IDEs.	144
4.15	Simulation results of Z_{norm} versus frequency for MCF-7 cells proliferating on ITO IDEs, the resistance R_{extra} was varied as described in the text. $f_{peak} = 5.5$ kHz ($R_{extra} = 3.4$ k Ω), $f_{peak} = 4.2$ kHz ($R_{extra} = 8.4$ k Ω) and $f_{peak} = 2.4$ kHz ($R_{extra} = 28.4$ k Ω).	145
4.16	Temporal evolution of f_{peak} of MCF-7 cells on Au IDEs	146
4.17	Temporal evolution of f_{peak} of MCF-7 cells on ITO IDEs.	147
4.18	Model 3 with R_{extra} , R_{intra} and CPE_{cells}	147
4.19	Comparing equivalent circuit models for Au IDEs covered with MCF-7 cell monolayer. (a) Nyquist plot in the frequency range from 1 MHz to 100 mHz and (b) from 1 MHz to 16.6 kHz.	148
4.20	Temporal evolution of the extracted parameters of MCF-7 cells on top of Au IDEs: (a) Q_{int} , (b) α_{int} , (c) R_{extra} , (d) R_{intra} , (e) Q_{cells} , (f) α_{cells} and (g) R_t	149
4.21	Equivalent cylindrical shape of the cell	150
4.22	Temporal evolution of the extracted parameters of MCF-7 cells on top of ITO IDEs: (a) Q_{int} , (b) α_{int} , (c) R_{extra} , (d) R_{intra} , (e) Q_{cells} , (f) α_{cells} and (g) R_t . Monolayer reached at $\eta = 96$ %.	151
4.23	Schematics of the different contributions of model 3 to the impedance locus for IDEs in the presence of biological cells. Drawing not to scale.	152
4.24	Schematics of the dependency of the phase angle to the impedance locus for IDEs in the presence of biological cells. Drawing not to scale.	153
4.25	Phase contrast images of MCF-7 after 200 μ M 5-FU addition on the surface of the Au IDEs at 10 X magnification (Leica D2000). 19,800 cells were injected for this experiment.	156
4.26	Magnitude and Phase of the impedance spectra for MCF-7 cells on Au IDEs in the frequency range (a, c) from 1 MHz to 100 mHz and (b, d) from 1 MHz to 100 Hz during 200 μ M 5-FU exposure.	157
4.27	Imaginary part vs Real part of the impedance spectra for MCF-7 cells on Au IDEs over the frequency range (a) 1 MHz to 100 mHz, (b) 1 MHz to 1 kHz, (c) 1 MHz to 21.8 kHz and (d) Diagram of the evolution of the Nyquist curves during cytotoxicity experiments with 200 μ M 5-FU	158
4.28	Normalized Z_{norm} versus T for MCF-7 cells exposed to 200 μ M 5FU on the surface of Au IDEs. Measurements were carried out outside of the incubator.	160
4.29	Microscopy images of the cell monolayer before and after 24 h of exposure to (a) 10 μ M 5-FU and (b) 50 mM 5-FU on ITO IDEs. (c) The cell monolayer before and after 24 h of exposure to 200 μ M 5-FU on Au IDEs. Images were taken at 10 X magnification (Leica D2000).	161
4.30	Comparison of normalized Z_{norm} for 10 μ M and 50 mM 5-FU after 24 h drug exposure to MCF-7 cells.	162
4.31	Comparison of normalized Z_{norm} for 10 μ M and 50 mM 5-FU after 48 h drug exposure to MCF-7 cells.	163
4.32	Temporal evolution of the extracted parameters of 100 μ M 5-FU treated MDA-MB-231 cells on ITO IDEs: (a) Q_{int} , (b) α_{int} , (c) R_{extra} , (d) R_{intra} , (e) Q_{cells} , (f) α_{cells} and (g) R_t	165

LIST OF FIGURES

4.33	Temporal evolution of the extracted parameters of 10 μM 5-FU treated MCF-7 cells on ITO IDEs: (a) Q_{int} , (b) α_{int} , (c) R_{extra} , (d) R_{intra} , (e) Q_{cells} , (f) α_{cells} and (g) R_t	167
4.34	Phase contrast micrographs of 10 μM 5-FU treated MCF-7 cells on the surface of the ITO IDEs at 10X magnification (Leica D2000).	168
5.1	SEM images of (a) platinum black electrochemically synthesized on platinum substrate, (b) titanium nitride deposited by physical vapor deposition on titanium substrate, (c) CNTs grown by CVD on a Ti-barrier layer, (d) PEDOT electrodeposited on Au neural micro-electrode, (e) Gold nanoflakes on gold electrodes and (f) electrodeposited IrO_x by cyclic voltammetry on Pt electrodes	183
5.2	(a) Cyclic voltammogram of IrO_x growth at pH 10.5 with 20 mV/s scan rate and cycling potential between 0 and 0.7 V Ag-AgCl on (a) Au IDEs and (b) ITO IDEs.	188
5.3	(a) Magnitude of impedance versus frequency of ITO IDEs after different number of cycles in contact with 1 M KCl . (b) Microscopic images of ITO IDEs after electrodeposition. Magnification 10X.	189
5.4	Magnitude of impedance versus frequency of ITO IDEs in contact with Ir(IV) solution for different time intervals.	190
5.5	Phase impedance spectra of ITO IDEs (a) after IrO_x electrodeposition and (b) after being in contact with the Ir(IV) solution without cycling potential.	190
5.6	(a) Sketch of the Nyquist plot of ITO IDEs after different IrO_x coating cycles. Nyquist representation of the ITO IDEs after different IrO_x coating cycles and in contact with 100 mM KCl in the frequency range from (b) 1 MHz to 100 mHz, (c) from 1 MHz to 53 Hz and (d) from 1 MHz to 18 Hz.	191
5.7	AFM images of the ITO IDEs surface (a) before and (d) after IrO_x on $2\mu\text{m} \times 2\mu\text{m}$ areas.	192
5.8	Z_{int} at 10 Hz for the ITO IDEs before and after 5, 10 and 25 cycles of coating. Measurements carried out in 100 mM KCl solution.	193
5.9	(a) Magnitude and (b) Phase impedance spectra of Au IDEs before and after IrO_x electrodeposition in contact with the supplemented DMEM	194
5.10	(a) Sketch of the Nyquist plot of Au IDEs before and after 25 cycles of cyclic voltammetry. Nyquist representation of the Au IDEs before and after 25 cycles of IrO_x coating and in contact with the supplemented DMEM in the frequency range from (b) 1 MHz to 100 mHz, (c) from 1 MHz to 1 kHz and (d) from 1 MHz to 28.6 kHz.	195
5.11	(a) Magnitude and (b) Phase impedance spectra of ITO IDEs before and after IrO_x electrodeposition in contact with the supplemented DMEM	196
5.12	(a) Diagram of the Nyquist plot of ITO IDEs before and after 10 cycles of cyclic voltammetry. Nyquist representation of the ITO IDEs before and after 10 cycles of IrO_x coating and in contact with the supplemented DMEM in the frequency range from (b) 1 MHz to 100 mHz, (c) from 1 MHz to 31 Hz and (d) from 1 MHz to 823 Hz.	197
5.13	Comparison of the electrical parameters of the Au IDEs coated with CN/BSA and in contact with the supplemented DMEM before and after 25 cycles of IrO_x : (a) $C_{parasitic}$ (b) R_t (c) Q_{int} and (d) α_{int} . Error bars are the standard deviation with $n=5$ for IrO_x/Au and $n=5$ for Au . * : Significantly different and ** : Not significantly different.	199
5.14	Comparison of the electrical parameters of the ITO IDEs coated with CN/BSA and in contact with the supplemented DMEM before and after 10 cycles of IrO_x : (a) $C_{parasitic}$ (b) R_t (c) Q_{int} and (d) α_{int} . Error bars are the standard deviation with $n=4$ for IrO_x/ITO and $n=8$ for ITO . * : Significantly different and ** : Not significantly different.	200
5.15	Z_{int} at 10 Hz for (a) the Au IDEs before and after 25 cycles and (b) the ITO IDEs before and after 10 cycles. Both electrodes in contact with the supplemented DMEM . Error bars correspond to the standard deviations with $n = 5$ for IrO_x/Au and Au ; $n = 4$ for IrO_x/ITO and $n = 8$ for ITO . * : Significantly different and ** : Not significantly different.	201

5.16	Phase contrast micrographs of MCF-7 cells on the surface of IrO _x /ITO IDEs at 10X magnification (Leica D2000): (a) $t = 6$ h, $\eta = 65$ %; (b) $t = 21$ h, $\eta = 72$ %; (c) $t = 30$ h, $\eta = 80$ %; (d) $t = 52$ h, $\eta = 94$ % (20 600 cells were injected).	202
5.17	(a) Magnitude and (b) Phase of impedance of IrO _x /ITO IDEs in contact with MCF-7 cells.	203
5.18	(a) Sketch of the Nyquist plots for MCF-7 cells proliferating on IrO_x/ITO IDEs . Nyquist representation of the IrO_x/ITO IDEs covered with MCF-7 cells in the frequency range from (b) 1 MHz to 100 mHz, (c) from 1 MHz to 0.4 Hz and (d) from 1 MHz to 6 Hz.	204
5.19	Normalized impedance of MCF-7 cells grown on ITO IDEs, IrO _x /ITO IDEs and Au IDEs. ($\eta = 99$ % for Au, $\eta = 96$ % for ITO and $\eta = 94$ % for IrO _x /ITO).	205
5.20	Temporal evolution of the extracted parameters of MCF-7 cells on IrO_x/ITO IDEs : (a) Q_{int} , (b) α_{int} , (c) R_{extra} , (d) R_{intra} , (e) Q_{cells} , (f) α_{cells} and (g) R_t	206

Nomenclature

5-FU	5-Fluorouracil
5-FdUMP	5-fluorodeoxyuridine monophosphate
T_{abs}	Absolute temperature
BSA	Albumin bovine serum
AC	Alternative current
ω	Angular frequency
Ar	Argon
Q_{pore}	Average occupied surface
N_A	Avogadro constant
k_B	Boltzmann constant
c_0	Bulk concentration ions in solution
K_{IDE}	Cell constant of interdigitated electrodes
R_{ct}	Charge transfer resistance
Cr	Chromium
$\kappa(k)$	Complete elliptic integral of the first kind
CPE	Constant Phase Element
CE	Counter electrode
f_0	Critical frequency
dTMP	deoxythymidine monophosphate

dUMP	deoxyuridine monophosphate
r	Diameter of solvated ions
r_p	Diameter of the pores
C_{diff}	Diffuse layer capacitance
DMSO	Dimethyl Sulfoxide
DMEM	Dubelcco's Modified Eagle Medium
$\sigma_{solution}$	Electrical conductivity of the solution
$\bar{Z}_{CPE_{int}}$	Electrical impedance of CPE
L	Electrode bands' length
w	Electrode bands' width
e	Electron charge
J_0	Equilibrium exchange current density
F	Faraday's constant
FBS	Fetal bovine serum
R	Gas constant
Au	Gold
C_H	Helmholtz layer capacitance
d_H	Helmholtz layer thickness
f_{high}	High crossover frequency
H ₂ O ₂	Hydrogen peroxide
H ₂	Hydrogen
j	Imaginary unit
ITO	Indium-tin-oxide
s	Inter-electrode gap
IDE	Interdigitated electrodes
C_{int}	Interfacial capacitance
Q_{int}	Interfacial pseudocapacitance
IrO _x	Iridium oxide
IrCl ₄ .H ₂ O	Iridium(IV) chloride hydrate

L_a	Large axis
R_{lead}	Lead resistance
l	Length of the pores
f_{low}	Low crossover frequency
MDA-MB-231	M. D. Anderson cancer center Metastatic Breast adenocarcinoma cell line
f_{max}	Maximum frequency
CH ₄	Methane
MCF-7	Michigan Cancer Foundation-7 cell line
M_{KCl}	Molar mass of KCl
Z_{norm}	Normalized impedance
T	Normalized time
n	Number of electrons involved in the charge transfer reaction
C ₂ H ₂ O ₄	Oxalic acid
O ₂	Oxygen
α_{int}	Parameter of CPE
$C_{parasitic}$	Parasitic capacitance
λ	Penetration depth
PS	Penicilin and Streptomycin
ϵ_0	Permittivity of free space
ϕ	Phase angle
h	Planck constant
PDMS	PolyDiMethyl Siloxane
S1813	Positive photoresist
K ₂ CO ₃	Potassium carbonate
KCl	Potassium chloride
$Q_{CN/BSA}$	Pseudocapacitance inside of the CN/BSA coating
Q_{pore}	Pseudocapacitance inside of the pore
RE	Reference electrode
ϵ_r	Relative dielectric constant

Ag/Ag/Cl Silver to Silver Chloride

ρ_{low} Slope of zone I in the Bode plot

ρ_{high} Slope of zone III in the Bode plot

L_b Small axis

R_t Solution resistance

c Speed of light in a vacuum inertial frame

R_s Spreading resistance

ψ_s Surface electrical potential

N Total number of electrode bands

CN Type IV collagen

z Valence of the ion in solution

WE Working electrode

Acknowledgements

It has been three years since I started my PhD research at the "Institut des Nanotechnologies de Lyon" (INL), and now that I have to write the acknowledgements, I feel so excited to end this important chapter of my life because only people who got a PhD can understand how much of a roller-coaster this whole journey can be. Here, I would like to thank the people who have helped me going through the ups and downs of this adventure.

First of all, I would like to acknowledge my PhD grant provided by the French Ministry of research and the "Ecole doctorale" EEA. Without this funding, none of this work would have been possible. I sincerely thank my supervisors Rosaria Ferrigno and Eric McAdams for their valuable support, advice and encouragement during my PhD and the thesis-writing process. I am also grateful to each of the members of my thesis committee. I would like to especially thank Prof. Nadi and Prof. Dunlop for taking their time to evaluate this manuscript.

I would also like to of course acknowledge people of the LOCI team. Magalie for her help with the cell culture and keeping my "babies" (the cells) alive. Jerome and Nicolas for their technical support in the NanoLyon platform, Louis for his interesting travel stories, Pascal, Yasmina, Jean François, Anne Laure and Marie Charlotte for their helpful advice and feedback during the team meetings. I would also like to thank Patrick for his support in clean room and Laurent for his help on the lab sessions of analogue electronics.

Thanks to my lab colleagues, interns, PhD students and Post Doc researchers. My friend Amin with whom I started my PhD and had fun everyday at the lab, particularly with the arabic learning sessions. Sergkei with whom I also shared good moments. I am thankful with the japanese expert and talkative Pierrick for bringing good chocolate, Samir for making us laugh with his funny performances. The brazilian couple, Thais and Tulio, who became my latino family in Lyon and sponsors of good food and wine. I cannot express enough thanks to Michele, such an intelligent and funny buddy who helped me a lot in this journey. I would also like to thank Amalric from the biomedical devices team for his helpful impedance advice during the meetings.

Nobody has been more important to me in this adventure abroad than the members of my family. Although trying to explain to them my research project was like talking in a alien language, they were always there for me. I would like to thank my parents and sister for their unconditional love and support. Thank you!

Résumé

Dans la lutte contre le cancer, la médecine personnalisée est une stratégie nécessaire et très prometteuse. En effet, il est primordial de pouvoir tester l'innocuité et l'efficacité de médicaments anticancéreux sur des échantillons provenant du patient lui-même, du fait de la diversité des réponses entre patients. Le but est d'améliorer la performance des soins et d'éviter des traitements inutiles et même parfois nocifs pour le patient. Ainsi, l'exemple de la chimiothérapie illustre parfaitement cette stratégie. Le coût élevé des molécules thérapeutiques, la nocivité de ces molécules et les réponses variées des patients face à une même molécule implique le recours aux tests de ces molécules sur un échantillon provenant du patient lui-même. Il en résulte un intérêt croissant dans le développement de tests simples, robustes et peu coûteux permettant l'évaluation de la chimio sensibilité de cellules biologiques issues d'une biopsie. Les problématiques liées à la mise en place de tels tests sont la quantité de cellules disponibles dans une biopsie, la diversité des molécules thérapeutiques à tester et également le choix d'une technique de détection permettant de suivre la cinétique d'action des molécules sur les cellules biologiques. L'une des réponses à la faible quantité de cellules est le développement de tests dans des environnements microfluidiques qui nécessitent donc l'intégration et la miniaturisation d'une technique de détection. La stratégie qui sera étudiée dans cette thèse est l'utilisation de l'impédancemétrie par le biais d'électrodes interdigitées d'Oxyde d'Etain et d'Indium (ITO) pour l'analyse quantitative de l'état de cellules de cancer du sein pour des applications de criblage de médicaments anticancéreux. Ce matériau présente l'avantage d'être transparent permettant ainsi des mesures d'impédance qui pourrait être couplées à des mesures optiques dans un environnement microfluidique.

Dans une première partie, nous avons caractérisé et étudié des électrodes interdigitées d'or et d'ITO pour des mesures d'impédance avec des cellules cancéreuses. Cette caractérisation par spectroscopie d'impédance réalisée dans des solutions de milieu de culture en présence et absence de cellules, ont permis de démontrer que la différence de sensibilité entre ces deux matériaux provenaient à la fois d'une différence de comportement résistif mais également d'une différence d'impédance interfaciale, dans les deux cas à la défaveur de l'ITO. Après ce constat, nous avons donc poursuivi l'étude afin d'évaluer les capacités de l'ITO pour des mesures de chimiosensibilité de la molécule 5-fluorouracil et également proposé une stratégie pour améliorer la sensibilité de l'ITO tout en conservant sa transparence. La stratégie développée consiste en la modification de la surface de d'électrodes d'ITO avec de l'oxyde d'iridium pour améliorer la sensibilité de l'ITO, tout en gardant sa transparence. Cette approche est intéressante pour pouvoir concevoir un dispositif transparent et facile à coupler avec un système d'observation microscopique dans un environnement microfluidique.

Mots clés : Médecine personnalisée, électrodes interdigitées, impédancemétrie, ITO, oxyde d'iridium, cellules de cancer du sein

Abstract

In the fight against cancer, personalized medicine is a necessary and very promising strategy. In fact, it is essential to be able to test the safety and effectiveness of anticancer drugs on samples from the patient, due to the diversity of responses between patients. The aim is to improve the performance of health care and avoid unnecessary and sometimes harmful treatments. Thus, chemotherapy perfectly illustrates this strategy. The high cost of therapeutic molecules, the harmfulness of these molecules and the varied responses of patients involve the use of tests with chemotherapeutic molecules on samples coming from cancer patients. This results in a growing interest in the development of simple, robust and inexpensive tests for assessing the chemo sensitivity of biological cells from a biopsy. The problems related to carrying out such tests are the quantity of cells available in a biopsy, the diversity of the therapeutic molecules to be tested and also the choice of a detection technique, able to monitor the kinetics of action of the molecules on the biological cells. One solution to the small amount of cells is to carry out the tests in microfluidic environments which therefore require the integration and miniaturization of a detection technique. The strategy that will be studied in this thesis is the use of electrical impedance with interdigitated electrodes of indium tin oxide (ITO) for the quantitative analysis of the state of breast cancer cells for screening applications of anticancer drugs. This material has the advantage of being transparent allowing impedance measurements that could be coupled to optical measurements in a microfluidic environment.

In the first part, we characterized and studied interdigitated electrodes of gold and ITO for impedance measurements with cancer cells. This impedance spectroscopy characterization carried out in culture medium solutions, in the presence and absence of cells, demonstrated that the difference in sensitivity between these two materials comes from a difference in resistive behavior and also from a difference in interfacial impedance, in both cases to the disadvantage of ITO. After this, we continued the study to evaluate the capabilities of ITO for chemosensitivity measurements using the molecule 5-fluorouracil and we suggested a strategy to improve the sensitivity of ITO while maintaining its transparency. The strategy developed consists of modifying the surface of ITO electrodes with iridium oxide to improve the sensitivity of the ITO, while keeping its transparency. This approach is interesting for developing a transparent device and easy to couple with a microscopic observation system in a microfluidic environment.

Keywords: Personalized medicine, interdigitated electrodes, impedance sensing, ITO, iridium oxide, breast cancer cells

Introduction

Generally, the health care system is based on "trial and error" model. This means that doctors prescribe drugs following the same standardized treatment process for each patient suffering the same condition. If the medication does not help the patient, then the doctor may change the drug or the dosage. However, there is variability between patients and not all drugs are as effective as they should be for every patient with the same illness[1]. Some of them, that work for some patients with a condition are completely useless on others and can cause unwanted side effects. Due to this heterogeneity of the patient population, the "one drug fits all" approach needs to be changed, leading to the application of the new approach known as Personalized Medicine. Within this approach, doctors can provide "the right drug, with the right dose at the right time to the right patient"[2]. This type of medicine aims at offering more effective treatments based on individual features of each patient by identifying particular biological markers. These markers will help to diagnose the disease before clinical signs and symptoms appear[1].

In this manuscript, we are focused on cancer, which ranks the second most common cause of death worldwide following cardiovascular diseases[3]. Cancer is considered a disease that starts by genetic mutation[4]. Due to this mutation, cancer cells cannot enter into the programmed cell death process and they start to accumulate mutations, becoming abnormal cells. One of their principal characteristics is that they can uncontrollably divide forming tumors in the body[5]. Moreover, cancer cells are able to invade new body parts through bloodstream and lymphatic system, leading to metastasis and invasion of neighboring tissues[6]. Additionally, in cancer, several tumors may share the same genetic information, but the gene expression pattern varies in different tumor types[7]. Hence, identifying a treatment based on the molecular and genetic information of patient's tumor is highly needed. This will avoid unnecessary toxicity and costs for patients who are not good candidates for a certain treatment. Personalized medicine could be extremely helpful in chemotherapy, the principal method for cancer therapy, where its effectiveness is limited by drug resistance[8]. It has been shown that tumors can contain high degree of molecular heterogeneity, leading to drug resistance through the therapy-induced selection of a resistant minor subpopulation of cells that was present in the original tumor[9]. However, before finding which medical treatments and procedures will work best for each patient, it is necessary that the patient's molecular and genetic information are available. This means that for each patient, proteins, different expression patterns and gene variants associated with the disease need to be identified. In addition, prediction of individual treatment responses by *in vitro* assays using cells extracted from patients is highly needed if more effective treatments want to be offered to patients. In order to achieve this, scientists need to take repeated biopsies of resistant tumors or biopsies of distant metastatic sites and then perform *in vitro* tests[10]. However, one of the major challenges in drug screening of cancer biopsies is the small amount of available cells. For instance, in mammary tumors, a sample may result in less than 1 million cells in total after dissociation of the tumor[11]. As for liquid biopsies, contain-

ing circulating tumor cells (CTCs), the number of available cells is extremely low, 1 to 10 CTCs in 7.5 mL of blood sample[12]. To circumvent this limitation, a possible solution could be to work in a microfluidic environment. The use of micro-volume channels not only could reduce sample size, but also could reduce costs as less reagents are consumed during tests.

Furthermore, in order to improve the success rate of cancer chemotherapy, it is necessary to have a rapid and sensitive assay to predict chemosensitivity of individual patients. Usually, in drug screening, an early part of the experimental process often involves screening a large number of compounds using defined biochemical assays in an ultrahigh-throughput format[13]. Nevertheless, the effect of a drug on an organism is complex and involves interactions at multiple levels that cannot be predicted using only biochemical assays. Therefore, in order to understand this complexity, cell-based screening assays have become biologically relevant candidates to predict the response of the organism. There is also the need to carry out multiplexing during the assays so that multiple compounds can be tested at the same time. Another important aspect that has to be taken into account is the method used to follow the cell response to the drugs without damaging cells during assays. In the literature, there are two types of assays to study cell activity for drug discovery and screening. First, label-based methods, such as colorimetry[14] based on color changes, luminescence[15] and fluorescence[16] based on fluorophores and emission of light after a chemical reaction. Label-based methods offer rapid and selective detection. Nevertheless, one of the limitations of these end-point label-based methods is the labeling step. It has been demonstrated that chemical labels interferes with the natural functions of proteins[17]. Therefore, the second type of assays, real-time label-free detection methods have become an attractive approach over traditional end-point assays for screening and profiling drugs in native cells[18]. In the literature there are several techniques, such as resonant waveguide grating[19], surface plasmon resonance[20] based on evanescent wave and refractive index, surface acoustic wave[21] and quartz crystal microbalance[22] based on piezoelectric effect, and finally electrical impedance sensing based on impedance changes[23]. As we mentioned earlier, in the personalized medicine approach, we would need a technique compatible with microfluidics and multiplexing but also inoffensive to cells. Among the label-free methods, we have chosen electrical impedance sensing as the method for following cell activity in drug screening and cytotoxicity assays. However, reducing the dimensions of an impedimetric sensing system in order to work in a microfluidic environment, brings some challenges, such as the small sized electrodes inducing high impedance which affects the sensitivity of the measurements.

This thesis aims at studying Indium-Tin-Oxide (ITO) as electrode material for Electrical Cell-substrate Impedance Sensing (ECIS) experiments in the context of personalized medicine. This transparent material provides the advantage of combining electrical impedance with microscopy. We therefore focus on evaluating the ability and compatibility of ITO with the integration in microfluidic systems. In the following manuscript, we introduce the context of personalized medicine in cancer treatment and the technique used for monitoring cell activity in real-time, ECIS, in Chapter 1. Chapter 2 presents the different materials and methods that were used in this thesis for studying cancer cell activity using electrical impedance sensing. Following this, in Chapter 3 we discuss the results about the characterization of gold and ITO interdigitated electrodes for ECIS experiments. We studied the impedance response of both electrode materials in absence of biological cells. Here, we tried to understand why ITO is not widely used for ECIS experiments despite its transparency. As for Chapter 4, we present the results obtained for both electrode materials in the presence of biological cells and an example of cytotoxicity assay using the chemotherapeutic agent 5-FU on breast cancer cells. We investigated the response to 5-FU exposure using electrical equivalent circuit to describe the cytotoxic effects of this chemotherapeutic drug on the cell lines, MCF-7 and MDA-MB-231. Later, in Chapter 5 we evaluated a possible strategy to enhance the sensitivity of ITO IDEs (Interdigitated Electrodes). We focused on how to obtain transparent ITO electrodes that offer both transparency and sensitivity close to that of gold electrodes. Finally, Chapter 6 resumes the conclusions of this PhD thesis and give some perspectives for future works using impedance sensing.

Bibliography

- [1] Personalized Medicine Coalition. *The Personalized Medicine Report: Opportunity, Challenges, and the Future*. URL: http://www.personalizedmedicinecoalition.org/Resources/The_Personalized_Medicine_Report_An_Annual_Overview_of_the_Field.
- [2] Sunil Mathur and Joseph Sutton. “Personalized medicine could transform healthcare (Review)”. In: *BIOMEDICAL REPORTS* 7.1 (2017), pp. 3–5. DOI: <https://doi.org/10.3892/br.2017.922>.
- [3] Ma Xiaomei and Yu Herbert. “Global Burden of Cancer”. In: *The yale journal of biology and medicine* 79.3-4 (2006), pp. 85–94.
- [4] American Society of Clinical Oncology (ASCO). *The Genetics of Cancer*. URL: <https://www.cancer.net/navigating-cancer-care/cancer-basics/genetics/genetics-cancer>.
- [5] Geoffrey M. Cooper. *The Cell: A Molecular Approach*. Sunderland MA: ASM Press, 2000.
- [6] Geoffrey M. Cooper. *Elements of Human Cancer*. Sudbury, MA: Jones and Bartlett Publishers, 1992.
- [7] Mukesh Verma. “Personalized Medicine and Cancer”. In: *Journal of Personalized Medicine* 2.1 (2010), pp. 1–14. DOI: <https://doi.org/10.3390/jpm2010001>.
- [8] Helen M. Coley. “Mechanisms and consequences of chemotherapy resistance in breast cancer”. In: *European Journal of Cancer Supplements* 7.1 (2009), pp. 3–7. DOI: [https://doi.org/10.1016/S1359-6349\(09\)70003-5](https://doi.org/10.1016/S1359-6349(09)70003-5).
- [9] Caitriona Holohan, Sandra Van Schaeybroeck, Daniel B. Longley, and Patrick G/ Johnston. “Cancer drug resistance: an evolving paradigm”. In: 13.10 (2013), pp. 714–726. DOI: <https://doi.org/10.1038/nrc3599>.
- [10] Arran K. Turnbull. “Personalized medicine in cancer: where are we today?” In: *Future Oncology* 11.20 (2015), pp. 2795–2798. DOI: <https://doi.org/10.2217/fon.15.204>.

- [11] Ada Hang-Heng Wong, Haoran Li, Yanwei Jia, Pui-In Mak, Rui Paulo da Silva Martins, Yan Liu, Chi Man Vong, Hang Cheong Wong, Pak Kin Wong, Haitao Wang, Heng Sun, and Chu-Xia Deng. “Drug screening of cancer cell lines and human primary tumors using droplet microfluidics”. In: *Scientific Reports* 7.9109 (2017), pp. 1–15. DOI: <https://doi.org/10.1038/s41598-017-08831-z>.
- [12] Meghaan M. Ferreira, Vishnu C. Ramani, and Stefanie S. Jeffrey. “Circulating tumor cell technologies”. In: *Molecular Oncology* 10.3 (2016), pp. 374–394. DOI: <https://doi.org/10.1016/j.molonc.2016.01.007>.
- [13] Terry Riss. *SELECTING CELL-BASED ASSAYS FOR DRUG DISCOVERY SCREENING*. URL: https://beta-static.fishersci.com/content/dam/fishersci/en_US/documents/programs/scientific/brochures-and-catalogs/publications/promega-selecting-cell-based-assays-drug-screening-publication.pdf.
- [14] M. Wodnicka, R. D. Guarino, J. J. Hemperly, M. R. Timmins, D. Stitt, and J. B. Pitner. “Novel fluorescent technology platform for high throughput cytotoxicity and proliferation assays”. In: *Journal of biomolecular screening* 5.3 (2000), pp. 141–152. DOI: <https://doi.org/10.1177/108705710000500306>.
- [15] Kyle Durick and Paul Negulescu. “Cellular biosensors for drug discovery”. In: *Biosensors and Bioelectronics* 16.7-8 (2001), pp. 587–592. DOI: [https://doi.org/10.1016/S0956-5663\(01\)00173-7](https://doi.org/10.1016/S0956-5663(01)00173-7).
- [16] Paul A. Clemons, Nicola J. Tolliday, and Bridget K. Wagner. *Cell-Based Assays for High-Throughput Screening: Methods and Protocols*. Totowa, NJ: Humana Press, 2009.
- [17] Frank A. Alexander, Dorielle Tucker Price, and Shekhar Bhansali. “From Cellular Cultures to Cellular Spheroids: Is Impedance Spectroscopy a Viable Tool for Monitoring Multicellular Spheroid (MCS) Drug Models?” In: *IEEE Reviews in Biomedical Engineering* 6 (2012), pp. 63–76. DOI: <https://doi.org/10.1109/RBME.2012.2222023>.
- [18] Brian T Cunningham and Lance G Laing. “Advantages and application of label-free detection assays in drug screening”. In: *Expert Opinion on Drug Discovery* 3.8 (2008), pp. 891–901. DOI: <https://doi.org/10.1517/17460441.3.8.891>.
- [19] J.Vörös, R.Graf, G.L.Kenausis, A.Bruinink, J.Mayer, M.Textor, E.Wintermantel, and N.D.Spencer. “Feasibility study of an online toxicological sensor based on the optical waveguide technique”. In: *Biosensors and Bioelectronics* 15.9-10 (2000), pp. 423–429. DOI: [https://doi.org/10.1016/S0956-5663\(00\)00102-0](https://doi.org/10.1016/S0956-5663(00)00102-0).
- [20] Hoang Hiep Nguyen, Jeho Park, Sebyung Kang, and Moonil Kim. “Surface Plasmon Resonance: A Versatile Technique for Biosensor Applications”. In: *Sensors* 15.5 (2015), pp. 10481–10510. DOI: <https://doi.org/10.3390/s150510481>.
- [21] Li Fang, Qin Lifeng, Wu Huiyan, and Wang Qing-Ming. “Love mode surface acoustic wave sensors for cellular toxicity sensing”. In: *2014 IEEE International Ultrasonics Symposium*. IEEE, Oct. 2014, pp. 2548–2551.

- [22] Julien Fattison, Fereshteh Azari, and Nathalie Tufenkji. “Real-time QCM-D monitoring of cellular responses to different cytomorphic agents”. In: *Biosensors and Bioelectronics* 26.7 (2011), pp. 3207–3212. DOI: <https://doi.org/10.1016/j.bios.2010.12.027>.
- [23] Ivar Giaever and C. R. Keese. “Monitoring fibroblast behavior in tissue culture with an applied electric field”. In: *PNAS* 81.12 (1984), pp. 3761–3764. DOI: <https://doi.org/10.1073/pnas.81.12.3761>.

Impedance sensing for personalized medicine in cancer treatment

In this chapter, we would like to describe the concept of personalized medicine and the benefit of implementing this approach for cancer patients. Then, we present the interests of developing cell based assays in this context and the challenges linked to this work. Finally, based on the investigation of the literature, we explain the choices taken for this PhD thesis.

1.1 Personalized medicine and Cancer

Typically, patients and clinicians are involved in a medicine that is oriented towards "trial and error" model. In this approach, doctors take decisions about what drugs to prescribe following the same standardized treatment process for each patient suffering the same condition. For instance, for a person coming to see the doctor due to an infection, the doctor will prescribe some antibiotics. If the medication does not work after a few weeks, the doctor may change the drug or the dosage. However, it has been found that not all drugs are as effective as they should be for all the patient population[1] as shown in Fig.1.1. Some of them, that help some patients with a condition, are ineffective on others, causing sometimes severe or even life-threatening side effects that are worse than the condition itself.

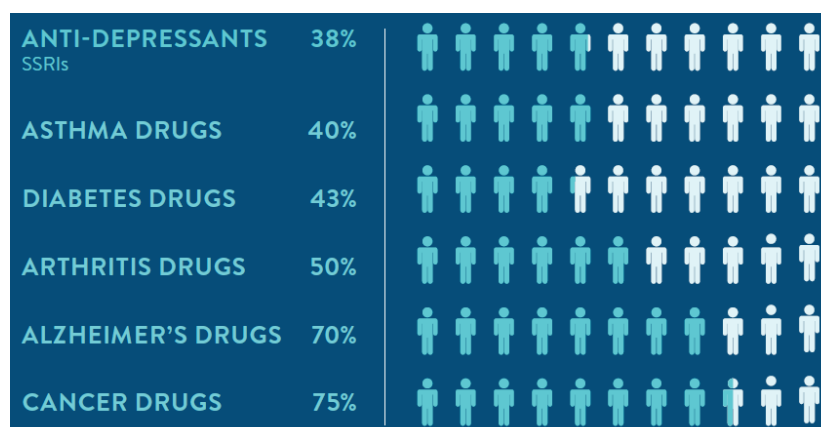


Figure 1.1 – Percentage (in blue) of the patient population for which a particular drug in a class is ineffective, on average. Figure adapted from figure 1 in[1].

1.1. Personalized medicine and Cancer

Based on this heterogeneity of the patient population, it is obvious that the "one drug fits all" approach is no longer valid, leading to the implementation of a new approach called: Personalized Medicine. The 21st century vision of this type of medicine is to provide "the right drug, with the right dose at the right time to the right patient"[2]. Personalized medicine seeks to offer more effective treatments based on individual characteristics of each patient by detecting specific biological markers. These markers may help to detect the disease before clinical signs and symptoms appear, offering an opportunity to focus on prevention and early intervention rather than on reaction at advanced stages of the disease[1]. In this work, we are focused on cancer, which is among the leading causes of death worldwide.

In many countries, cancer ranks the second most common cause of death following cardiovascular diseases[3]. For example in 2012, there were 14.1 million new cases and 8.2 million cancer-related deaths worldwide and the number of new cancer cases per year is expected to increase to 23.6 million by 2030[4]. Cancer is considered a disease of the genome, in which the process is initiated by mutation[5]. Cancer cells can start growing almost anywhere in the human body, which is made up of trillions of cells. Normally, human cells grow and divide to form new cells as the body needs them. When cells grow old or changes have occurred in their DNA sequence, they enter apoptosis, and new cells are created. Nonetheless, when cancer develops, this programmed cell death process, known as apoptosis, gets disrupted. Then cells become abnormal and start accumulating mutations because they do not die even though they become old. These damaged cells can divide without stopping and may form tumors. These tumors can be either benign tumors, which cannot spread to other parts of the body or malignant tumors which are able to invade new body parts through bloodstream and lymphatic system, leading to metastasis and invasion of neighboring tissues[6].

Nowadays, there are three primary modes of cancer treatment: surgery, radiation, and pharmacological therapy. Some patients receive all three modalities of treatment, while others receive only one or two. The choice of therapy depends on the type and stage of cancer, past response rates, legal and clinical infrastructure, patient's health conditions, *etc*[7]. Moreover, costs to the patient vary depending on the type and extent of the treatment.

- **Surgical resection or surgery:** It is often used to remove tumors, diagnose cancer, and/or to determine how far a cancer has disseminated. Many cancer patients have surgery at least once as part of their treatment in order to cut out primary tumors and surrounding tissues to prevent cancer spreading. When used as a single treatment, surgery cures more patients than any other cancer therapy method because with surgery 100 % of excised cells are killed[8]. However, this method is only effective when it is done on localized tumors, which are easy to get to without compromising vital organs, blood vessels or nerves. In addition, this method can result in several charges to patients and health insurers due to multiple medical bills from medical providers and hospitals or specialized facilities[9].
- **Radiation therapy:** It uses high doses of radiation to destroy or damage the DNA of cancer cells. Usually, cells whose DNA is damaged beyond repair stop dividing and then die. Radiation therapy using either external or internal beam is used as a curative option in a variety of tumor types such as early stage brain and neck tumors, nasopharyngeal cancers, prostate cancer and early stage Hodgkin's disease[7, 8]. Most of the time, this treatment method requires complex equipment and a team of health care providers. Moreover, treatment protocols might vary from one patient to the other. For instance, some cancer patients receive radiation daily or several times a week for many weeks, which contributes to relatively high patient costs[9]. The downside of this therapy is that radiation not only kills or slows the growth of cancer cells, but it can also affect surrounding healthy cells, leading to some side effects such as fatigue, nausea and skin problems[10].

1.1. Personalized medicine and Cancer

- **Chemotherapy:** It involves medication during cancer treatment as well as supportive care like pain or anti-nausea medication[9]. Chemotherapy has become one of the principal modes of treatment or as auxiliary therapy for surgically resected tumors. Nevertheless, its effectiveness is limited by drug resistance[11]. The drug resistance can be either intrinsic or acquired. Intrinsic resistance means that before receiving chemotherapy, the patient already has resistance mediating factors in the tumor cells that make the therapy ineffective. As for the acquired resistance, it can be developed during cancer treatment due to some DNA mutations and adaptive responses that promote drug inhibition and degradation over time [11, 12]. For instance, tumors are highly adaptable and the activation of survival signaling pathways and the inactivation of downstream death signalling pathways can lead to drug resistance.

As it was mentioned before, the main objective of personalized medicine is to prescribe the right drug at the right dose, with minimal or no toxicity, for the right patient at the right time[13]. With this approach, the scientific community wants to move away from the "one treatment fits all" mindset[14], particularly in cancer therapy. In cancer, various tumors may share the same DNA, but the gene expression pattern varies in different tumor types. Therefore finding a treatment based on the molecular and genetic information of patient's tumor is highly needed. This will avoid unnecessary toxicity and costs for patients who are unlikely to benefit from a treatment. Especially in chemotherapy, the principal method for cancer therapy, where its effectiveness is limited by drug resistance. It is increasingly recognized that tumors can contain high degree of molecular heterogeneity, leading to drug resistance through the therapy-induced selection of a resistant minor subpopulation of cells that was present in the original tumor[11]. Thus, in order to determine which medical treatments and procedures will work best for each patient, it is essential that the information about the patient's unique physiology and the components leading to cancer are available. In personalized medicine, for each patient it is crucial to identify proteins, different expression patterns and gene variants associated with the disease or the disease predisposition. For example, this approach allows to determine in advance who is at risk of developing cancer by getting information about a patient's proteinaceous, genetic and metabolic profile. In addition, prediction of individual treatment responses by *in vitro* assays using cells coming from patient biopsies is highly needed if more effective treatments want to be offered to patients.

1.1.1 Molecular profiling of healthy and cancer patients

Nowadays, different disciplines, known as "-omics" sciences, are used to characterize and better understand the heterogeneity of the tumors so that a physician can have enough information to select a treatment that may minimize negative side effects and guarantee a more successful result. The word "-omics" refers to a field of study in biological sciences that ends with -omics, such as genomics, transcriptomics, proteomics, or metabolomics. The ending -ome is used to address the objects of study of such fields, such as the genome, proteome, transcriptome, or metabolome, respectively.

- **Genomics:** It focuses on DNA sequencing and the analysis of the genomes of tumors and non-malignant cells from patients. It can reveal individual targetable alterations, mutational load, complex mutation signatures, and tumor-specific antigens, which might inform the utilization of targeted therapies, immune-checkpoint inhibitor, and personalized anticancer vaccines[15]. Understanding the genetic changes and gene expression profiles that are in cancer cells leads to develop more effective treatment strategies based on the genetic profile of each individual patient's cancer. Moreover, sequencing of tumor-derived RNA enables the identification of differentially expressed genes, gene fusions, small RNAs, aberrantly spliced isoforms and allele-specific expression patterns[15].
- **Pharmacogenomics:** It identifies patients who, based on their genotypes, will respond to a specific therapy. In fact, genetic variations influence the response of an individual to drug treatments. Thus, understanding this heterogeneity is essential for making cancer therapy safer and more effective by determining selection and dosing of drugs for an individual patient[16]. This is critical in

cancer therapy, particularly in chemotherapy where most of the anti-cancer drugs affect malignant and healthy cells. Pharmacogenomics aims at optimizing a therapy based on the unique genotype of patients, by ensuring maximum efficiency with minimal adverse effects. For instance, more than 100 pharmacogenomic biomarkers can be used to identify responders and non-responders to medications avoiding unfavorable events and optimizing the dosage for drugs[17].

- **Proteomics:** It is the large scale study of proteins, understanding protein profiles and their expression in normal and cancer states. Although the capability of functions is coded in genes, the actual function is accomplished by proteins. Therefore, being able to compare the profile of all the peptides and proteins present in a clinically healthy person and the proteomic profile of a cancer patient is crucial. As a matter of fact, most of the pathways in cancer development and their signal transduction are based on protein interactions[13].
- **Metabolomics:** It is the study of low molecular weight molecules, known as metabolites, found within cells and biological systems. Metabolomics is considered to be more representative of the functional state of a cell than other "omics" sciences such as genomics or proteomics[13]. In oncology, cancer cells are known to have a highly unique metabolic phenotype, thus it is possible to isolate specific biomarkers, which might be used in identifying fingerprints, profiles, or signatures to detect the presence of cancer by characterizing the tumor metabolome¹[19]. For example, tumors, in general, display high phospholipid levels, increased glycolytic capacity, high glutaminolytic function and overexpression of the isoenzyme pyruvate kinase type M2[20].

1.1.2 Cell based assays for drug testing

In personalized medicine, selection of the right therapy requires extensive molecular characterization of individual tumors. Particularly, due to the complexity and heterogeneity of cancer, research has been focused on finding more targeted anticancer drugs. The aim is to predict how the tumors might respond to certain chemotherapeutic drugs. In other words, for optimal personalized medicine clinicians need to take repeated biopsies of resistant tumors or biopsies of distant metastatic sites and then perform *in vitro* tests[14]. Carrying out those tests means that *ex vivo* tumor culture systems are also needed. In the literature, various culture methods can be used to preserve the tumor samples intact before testing. One of the greatest challenge in drug screening of cancer biopsies is the small amount of available cells. For example, in mammary tumors of 2 cm x 2 cm, a sample may result in less than 1 million cells in total after dissociation of the tumor[7]. In the case of fine needle aspiration biopsies, 1 to 4 million cells can be collected depending on the tumor structure and expertise of the clinician[21]. As for liquid biopsies, containing circulating tumor cells (CTCs), the number of available cells is extremely low. Usually, there are only 1 to 10 CTCs in 7.5 mL of blood sample[22]. Besides the small amount of available cells, sample quality also depends on the shipment time and storage method depending on the laboratory intended analyses[7].

Microfluidics is known as the science and technology on the processing and manipulation of small amounts of fluids (10^{-9} to 10^{-18} L) in channels with dimensions of tens of micrometers[23]. The micrometer dimension conveniently matches with the size of typical biological cells, making microfluidics an ideal platform for cell studies. Based on the advantageous features of microfluidic technologies, microfluidics has been used for characterizing the biochemical and/or biophysical properties of cells at the single-cell level[24, 25]. Moreover, many efforts have been made to miniaturize "high-end" systems. In fact, microfluidic chips can incorporate on-chip cell preparation, cell culture, lysis and different modules for optical, electrophoretic or genomic analysis[26]. For example, drug screening platforms based on nano- and micro- volume fluidic channels have been vastly explored[7, 27, 28]. Wong et al.[7] demonstrated that their centimeter-sized

¹The metabolome is the global collection of all low molecular weight metabolites that are produced by cells during metabolism, and provides a direct functional readout of cellular activity and physiological status[18]

1.2. Strategies implemented in cell-based assays for drug screening

PDMS-based droplet microfluidic chip, depicted in Fig. 1.2a, could be used to screen as few as 16,000 cells obtained from primary cancer for each treatment condition within 24 h after tumor resection from cancer patients. Rapid screening for effective therapy is extremely crucial, particularly for fast-growing cancers from the pancreas, lung, brain and oesophagus, which kill patients within one year after diagnosis[29]. As for Kim et al.[27], they developed a microfluidic high-throughput single-cell screening platform, shown in Fig. 1.2b, with the capability of capturing, culturing, and analyzing *C. reinhardtii* cells with single-cell resolution, followed by selectively extracting particular cells of interest off-chip for further study[27]. The use of micro-volume channels not only reduces sample size, but also reduces time of analysis and costs as less reagents are consumed during tests. Thus, in personalized medicine, miniaturization of the *in vitro* tests platforms and working in a microfluidic environment seems to be a highly needed strategy to circumvent the low sample "input" issue. In addition, some authors have incorporated microfluidics into impedance measurements as an interesting analytical approach for cell-based assays in personalized medicine.

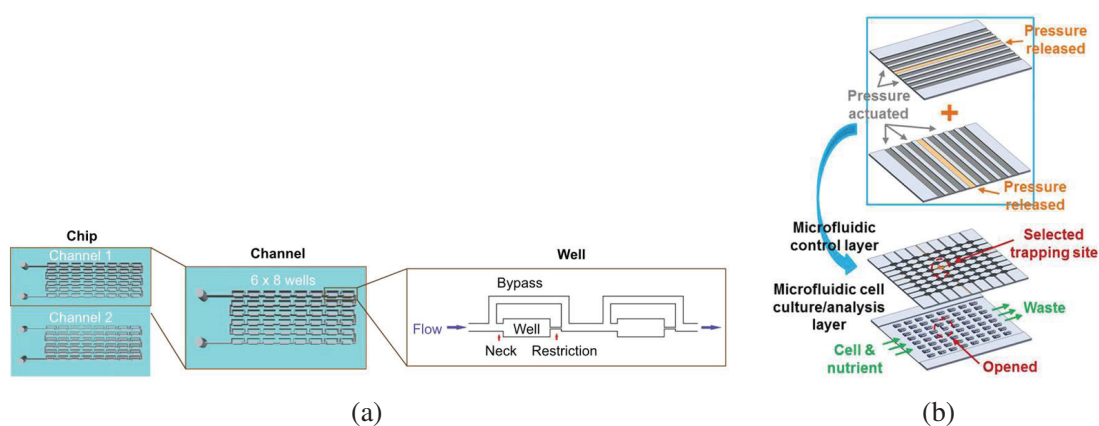


Figure 1.2 – Impedance based microfluidic systems: (a) Wong's chip. Figure adapted from figure 1 in[7] and (b) Kim's platform. Figure adapted from figure 1 in[27]. Copyright 2001 by Royal Society of Chemistry. Adapted with permission.

In the next section, we will present both aspects of cell based assays: (i) *ex-vivo* tumor culture models and (ii) detection methods.

1.2 Strategies implemented in cell-based assays for drug screening

Currently, chemotherapy is one of the most commonly used methods to treat cancer[11], but the success of treating cancer using chemotherapy remains limited[11]. The major reasons for limited success with cancer chemotherapy are drug resistance and the lack of rational approaches to select optimal therapy for individual patients[11]. Therefore, to improve the success rate of cancer chemotherapy, it is necessary to have a rapid and sensitive assay to predict chemosensitivity of individual patients.

Nowadays, pharmaceutical companies approach drug discovery in a variety of ways. An early part of the experimental process often involves screening a large number of compounds using defined biochemical assays in an ultrahigh-throughput format[30]. However, the effect of a drug on an organism is complex and involves interactions at multiple levels that cannot be predicted using only biochemical assays. Therefore, in order to understand this complexity, cell-based screening assays have become biologically relevant candidates to predict the response of the organism. For example, *in vitro* cultured cells exist as a heterogeneous

1.2. Strategies implemented in cell-based assays for drug screening

population even when cultured under controlled conditions. When populations of cells are exposed to test compounds, they do not all respond simultaneously. Cells exposed to toxin may respond over the course of several hours or days, depending on many factors including the mechanism of cell death, the concentration of the toxin and the duration of exposure. As a result of culture heterogeneity, the data from most plate-based assay formats represent an average of the signal from the population[30]. Furthermore, in drug discovery there is also the need to carry out multiplexing during the assays. Some general requirements for multiplexing include that the detection signals of the different assays are distinguishable from each other and that the assay chemistry must be compatible or separable in time and/or location.

1.2.1 *Ex-vivo* tumor culture models for drug testing

Since *in vitro* tests are limited by the low sample "input", various culture methods shown in Fig.1.3 for tumor cells "amplification", such as two-dimensional (2D) monolayer cell culture, three-dimensional (3D) organoid culture and patient-derived xenografts (PDX) models have been explored and coupled to detection methods in order to quantify drug effects on cells.

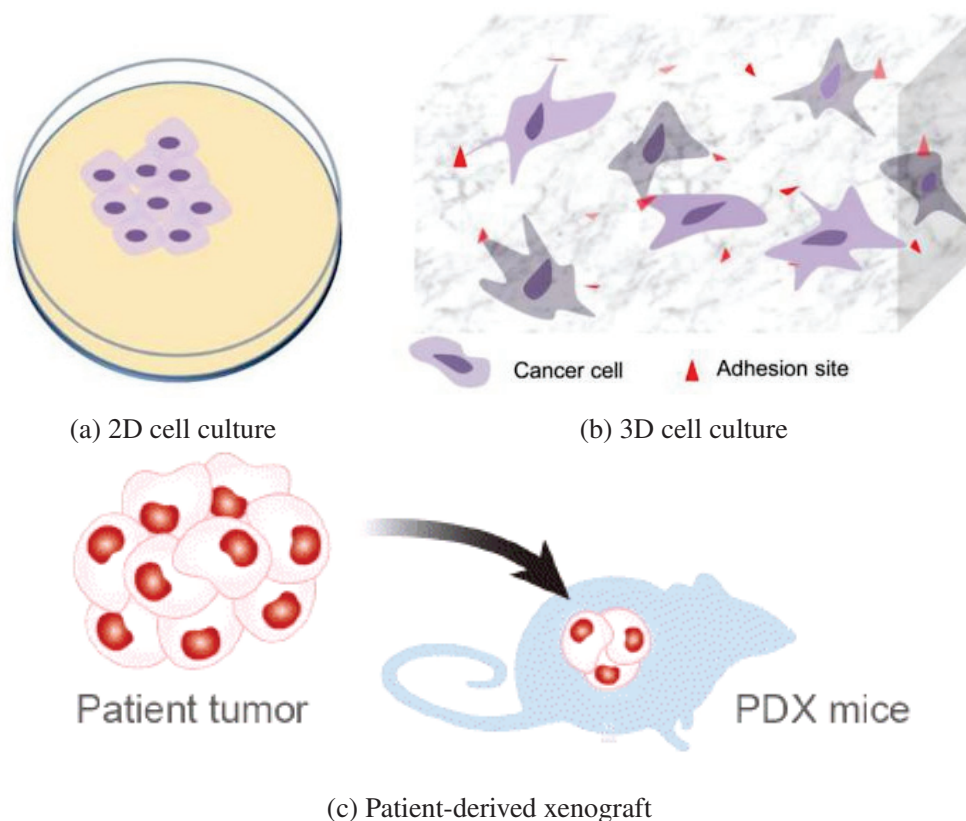


Figure 1.3 – Different culture methods: (a) 2D monolayer culture, (b) 3D organoid culture. Figures adapted from figure 1 in[31] and (c) Patient-derived xenograft. Figure adapted from figure 1 in[32].

- **2D monolayer cell culture:** This is the simplest culture method and it is the one we used in this work. First, in order to obtain the cancer cells, the tumor has to be dissociated by specific proteolytic enzymes such as collagenase, dispase and/or trypsin. Enzymatic digestion can be also combined with mechanical dissociation for better dispersal of the tumor mass if needed. However, not all tumors can be cultured *ex vivo* in monolayers. This culture method is only possible with adherent cells that

1.2. Strategies implemented in cell-based assays for drug screening

attach to the bottom of the culture dish. There are two types of 2D monolayer cultures: (i) primary or tumor cell cultures and (ii) immortalized cancer cell lines, which we used in this work. The first type keeps the heterogeneity of the original tumor but it does not have the limitless proliferative capacity of immortalized cell lines. The second type are considered as clonal outgrowths from a primary tumor cell culture and are useful tools for high-throughput screening[33]. However, although monolayer cultures may proliferate well, cells might become increasingly different from the tumor they were originally extracted from, showing many genetic, epigenetic and gene expression differences[34]. In addition, monolayers lack the 3-D structure of tissue *in vivo*, crucial for the formation of oxygen gradients and developing tumor resistance to hypoxia. This resistance, which is not developed in 2D monolayer cultures, is necessary for studies about tumor resistance to different radiotherapy and chemotherapy[35].

- **3D organoid culture:** As planar cultures are often insufficient for more complex studies, including drug interaction and cellular differentiation, 3D organoid models are chosen due to their proximity to the actual phenotype expressed *in vivo*[34]. The limited cell-cell and cell-extracellular matrix communication in 2D monolayer cultures, lead to changes in cellular physiology. The introduction of organoid cultures has created new opportunities for high-throughput drug screens helping personalized cancer treatment, biomarker discovery and studies on drug resistance mechanisms. Nevertheless, the requirement of a collagen gel for 3D culturing seems to complicate potential drug screening and it increases the complexity of the culturing[33].
- **Patient-derived xenografts (PDX):** This is another method to "amplify" tumor cells and preserve individual tumors from patients by implantation of fresh pieces of the tumor in immunodeficient mice, subcutaneously or in a place that more closely resembles the original tumor location[36]. PDX models maintain various characteristics of the *in vivo* tumor such as histopathological features, gene expression profiles, copy number variation and metastatic behavior. Thus, PDX are preferred models for drug screening, biomarker discovery, identification of resistance mechanisms and preclinical evaluation of treatment strategies[37]. However, there are still some drawbacks about the use of PDX in personalized medicine. One of them is the variability of the success rate of tumor engraftment[38]. For instance, compared to other tumors, clinically aggressive tumors with many proliferative cancer cells have the highest engraftment² rate[39]. A second major downside of PDX is the long generation time, between implantation and progressive growth of the PDX, ranging from 2 to 12 months[33]. This means that some patients might not survive this generation time. Furthermore, since animals are used as hosts, the heterogeneity in the human tumor micro environment is lost due to substitution of the tumor stroma by mouse stroma upon passaging[33].

1.2.2 Detection methods

a) Label based methods:

In order to fully understand the mechanisms underlying drug response variation in individuals, functional characterization on a physiologically relevant molecular and cellular level is essential. In the literature, several label-based assays are available to measure a variety of different markers that indicate the number of dead cells (cytotoxicity assay), the number of live cells (viability assay), the total number of cells, or the mechanism of cell death (e.g., apoptosis)[30] for drug screening.

- **Colorimetric assays:** This type of methods are based on color change of the growth medium after cell metabolites react with chemical agents such as ruthenium dye[40] and Alamar Blue[41]. For example, the CellTiter-Blue[®] cell viability assay commercialized by PROMEGA uses an optimized

²Engraftment is when the blood-forming cells present in the transplant, start to grow and make healthy blood cells

1.2. Strategies implemented in cell-based assays for drug screening

reagent containing resazurin, which is blue and non fluorescent. Then living cells reduce it to pink and highly fluorescent resorufin. This reagent is added directly to cells in culture, incubated, and the signal is read using a multiwell fluorometer[30]. In addition, there are also several methods based on the cleavage of a tetrazolium salts by a mitochondrial enzyme, succinate dehydrogenase, leading to the formation of a colored product, formazan that can be quantified by spectrophotometry[42]. Tetrazolium salts mostly used in drug screening are MTT [43], MTS[44] and XTT[45].

These assays have been associated with some drawbacks. For instance, the low sensitivity of ruthenium dye and the poor reliability of Alamar Blue for the measurement of kinetics limit their applications in the development of high-throughput screening. In addition, colorimetric methods are time consuming because they require multiple additions of chemicals at certain time points, which interfere or disrupt cellular events. Furthermore, they usually can only provide end-point data, an intrinsic drawback for *in vitro* cytotoxicity tests[46].

- **Luminescent methods:** Another type of methods commonly used in drug screening are the ones based on luminescence. In luminescent assays, the oxidation of luciferin catalyzed by luciferase in the presence of ATP, magnesium and molecular oxygen produces light that can be detected by a light sensitive apparatus such as an illuminometer or optical microscope, allowing observation of biological processes[47]. For example, Sykes et al.[48] reported the successful development and optimisation of a luciferase based cell viability assay in 384-well format for use in high throughput screening of the bloodstream parasite *T.b.brucei* BS427 based on ATP estimation. Regarding commercialized assays, we can find the CellTiter-Glo[®] reagent that works in three steps upon addition to cells. First, it lyses cell membranes to release ATP then it inhibits endogenous ATPases and it provides luciferin and luciferase necessary to measure ATP using a bio-luminescent reaction. The “glow-type” signal of the luciferase can be recorded with a luminometer, CCD camera or modified fluorometer and generally has a half-life of five hours, providing a consistent signal across large batches of plates[30]. There are two types of luciferase assays: “flash” vs. “glow”. As their names imply, a “flash” luciferase assay is one where the signal is strong but short-lived. “Glow” type assays prolong the signal, so their half-lives are on the order of hours, not minutes. The trade-off is that “Glow”-type assays have lower signal intensities[49]. Therefore, for most applications, the trade-off is a good deal.

Although firefly luciferase is widely used in cell based assays, its application is usually limited to end-point assays because the requirements of cell lysis and addition of luciferase substrates. Moreover, besides of the amount of luciferase, the bioluminescence intensity can also be affected by many other factors such as luciferin absorption, availability of co-factors, pH, and transparency of culture media or buffer, causing differences between the detected bioluminescence signals and actual changes in cellular activity[50].

- **Fluorescent assays:** This type of methods are widely used in high-throughput screening due to their high sensitivity, diverse selection of fluorophores, ease of operation and various readout modes[51]. Usually, the fluorophores used for labeling can be divided into intrinsic probes, which occur naturally in the system, and extrinsic probes, which need to be introduced into the system during assays. Intrinsic probes can be part of a protein’s covalent structure, a co-factor or a ligand such as the aromatic amino acids tryptophan and tyrosine and some fatty acids and lipids[52]. However, their typically short excitation wavelengths in the UV or mid-UV make them less suitable for assays used in high throughput screening. Therefore, extrinsic probes seem to be a better option for fluorescence sensing. For example, fluorogenic substrates are one type of tool that can be used to measure caspase activity. Fluorogenic substrates contain a peptide sequence that is based on the preferred cleavage site of each caspase and a fluorophore. When an active caspase cleaves the substrate, a detectable shift in the fluorescent properties of the fluorophore occurs and then it can be detected[53]. The activation of

1.2. Strategies implemented in cell-based assays for drug screening

caspases is a marker for cellular damage during the initiation and progression of apoptosis for drug research[54].

On the other hand, necrosis, which is another form of cell death, can be studied by the release of lactate dehydrogenase (LDH) activity. A key characteristic of necrotic cells is the permeabilization of plasma membrane. Cells that have lost membrane integrity release LDH into the surrounding medium[55]. For instance, the CytoTox-ONE™ homogeneous membrane integrity assay is a fluorescent method that uses coupled enzymatic reactions to drive the LDH conversion of lactate to pyruvate and NADH. This NADH, in the presence of diaphorase and resazurin, is used to drive the diaphorase-catalyzed production of the fluorescent resorufin product[30]. Although, fluorescent methods have high selectivity and sensitivity, there is still a critical issue concerning the photostability of the fluorophores, particularly for organic labels[56].

As shown in Table 1.1, each method has advantages and limitations that will determine the choice of the most appropriate assay depending on the application. All the aforementioned methods only provide endpoint data. Thus, it could be interesting to complement label-based assays with real-time measurements, leading to cell-based assays that are able to provide a continuous record of cellular activity.

Method	Advantages	Limitations	Information obtained	References
Colorimetry	<ul style="list-style-type: none"> • Designed for multiplexing • Rapid detection time 	<ul style="list-style-type: none"> • Low sensitivity • High background noise 	<ul style="list-style-type: none"> • Cell viability 	<p>[46]</p> <p>[56][57]</p>
Luminescence	<ul style="list-style-type: none"> • Rapid and simple assays • Long-lived signals • No Photobleaching 	<ul style="list-style-type: none"> • Interference by external factors • Cofactors/Substrates are required 	<ul style="list-style-type: none"> • Cell viability • Apoptosis 	<p>[58][46]</p>
Fluorescence	<ul style="list-style-type: none"> • High sensitivity • High selectivity • High specificity 	<ul style="list-style-type: none"> • Sensitive to the environment • Photostability of the fluorophores 	<ul style="list-style-type: none"> • Cytotoxicity • Apoptosis 	<p>[56]</p> <p>[59][60]</p>

Table 1.1 – Advantages and limitations of different label-based methods.

b) Label-free methods

Label-free detection methods not only overcome the problem of potential negative impact of labels on the cellular processes[34] but they also enable real-time kinetic measurements. This type of methods has been

1.2. Strategies implemented in cell-based assays for drug screening

emerging as an attractive approach over traditional endpoint assays for screening and profiling drugs in native cells, owing to their ability to provide rich information content, real-time kinetics, flexible assays and high throughput[61]. Label-free technologies generally consist of three components: a biological element such as living cells, a detector system and a transducer between them. In the literature, we find several label-free cell based assays used for drug discovery as shown in Fig.1.4:

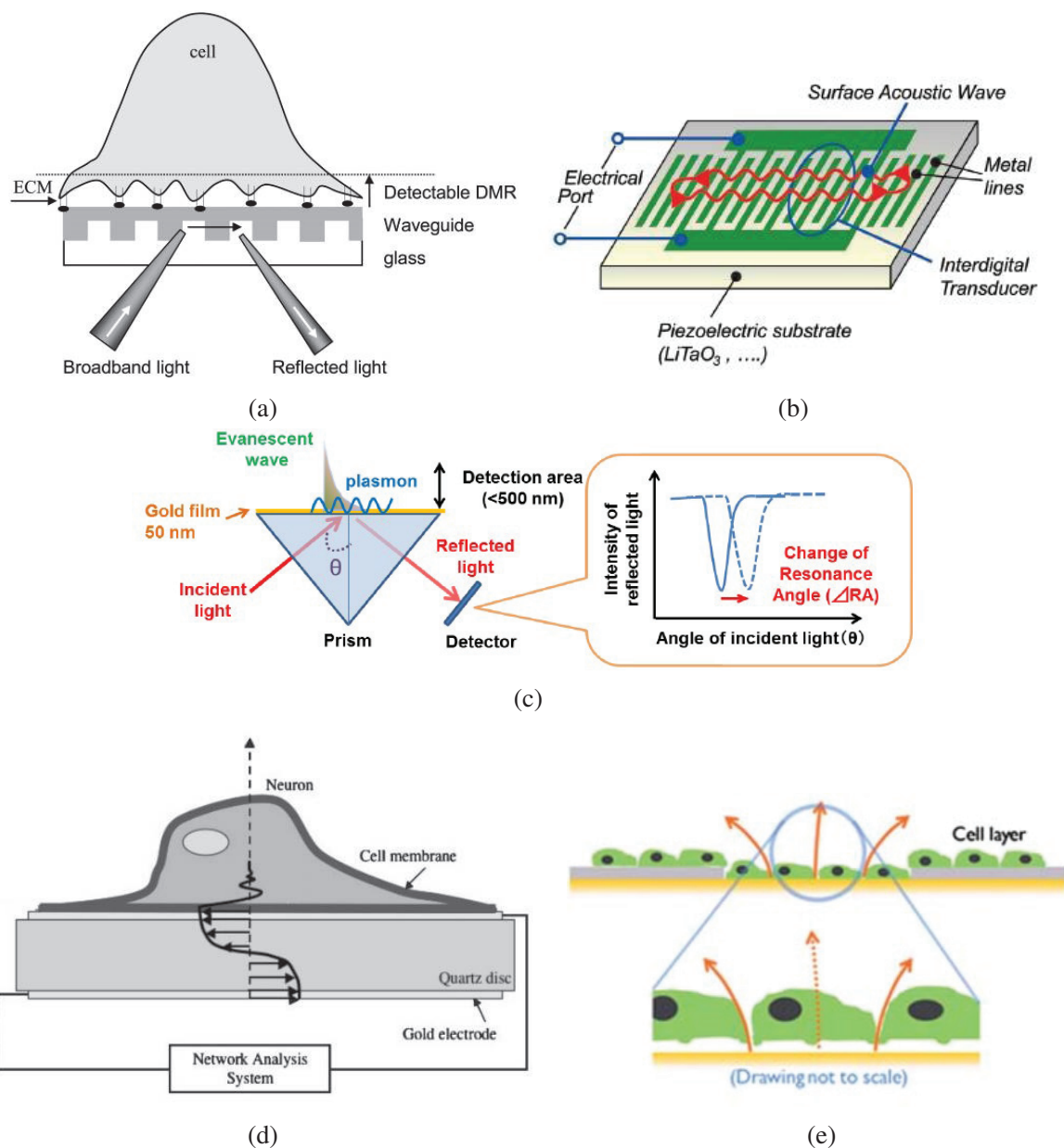


Figure 1.4 – Principle of different label-free techniques: (a) Resonant wave guide grating. Figure adapted from figure 2 in[62], (b) Surface acoustic wave. Figure adapted from[63], (c) Surface plasmon resonance. Figure adapted from figure 2 in[64], (d) Quartz crystal microbalance. Figure adapted with permission from figure 1 in[65](Copyright 1876 by Royal Society of Chemistry) and (e) Electrical impedance. Figure adapted with permission from figure 1 in[66]. Copyright 1876 by Royal Society of Chemistry.

- **Resonant Waveguide Grating (RWG):** In this technique there is a waveguide, which consists of a thin film of niobium pentoxide (Nb_2O_5) on a glass substrate having a nanograting structure. The Nb_2O_5 thin film act as a waveguide, since it has higher refractive index (~ 2.36) than either the glass substrate (~ 1.5) or live cells (~ 1.37)[67]. The diffraction grating allows the resonant coupling of light into the waveguide thin film, thus creating an evanescent wave at a solution-surface interface. With respect to cells, this evanescent wave is sensitive to perturbations in local refractive index at a short distance (100-200 nm) from the sensor surface into the cells. Local changes in the refractive index can give information about mass redistribution of proteins and organelles due to different treatments such as stimulation with toxic compounds. For example Voros et al.[68] demonstrated that is possible to carry out online toxicological evaluation by using optical waveguide light-mode spectroscopy, based on an RWG biosensor. As for Cunningham et al.[69], they have applied an RWG biosensor to study the potency of vinblastine, an antiproliferation agent, on the inhibition of cell proliferation. Zaytseva et al.[70] developed a microfluidic RWG biosensor system for studying the heterologous desensitization of $\beta 2$ -adrenergic receptor ($\beta 2\text{AR}$) by forskolin in native human epidermal carcinoma A431 cells. Their system enables medium throughput measurements of cellular responses under microfluidics in a 32-well format[70]. Similar to Zaytseva, Goral et al.[71] combined RWG and microfluidics for sensing ligand-directed functional selectivity on trafficking of PAR_1 thrombin receptor. The human lung adenocarcinoma epithelial cell line A549 was used as a model to describe a microfluidic RWG biosensor system which enables label-free cellular assays under the control of the duration of agonist exposure and of the functional recovery of activated receptors[71].
- **Surface Acoustic Wave (SAW):** SAW devices are made of piezoelectric materials on which a periodic comb-shaped interdigital transducer (IDT) is patterned. These electrodes are generally made of inert metals or alloys, for example Au or Cr/Au/Cr[72]. When an AC voltage is applied to the electrodes, an acoustic wave is generated which travels across the crystal surface, perpendicular to the IDT having penetration depths of a few wavelengths[72]. Fang et al.[73] demonstrated that wave-guided shear-horizontal surface acoustic wave, known as "Love mode" devices were capable of monitoring the dynamic procedure of Huh7 liver cells attachment and spreading, as well as detachment induced by toxicants such sodium calcium edetate (EDTA). Moreover, Mitsakakis et al.[74] developed a SAW device integrated with a multi-channel microfluidic module for the rapid and efficient analysis of cardiac markers. In their study four biomarkers were successfully detected, kinetics and affinity studies on their interactions with the surface immobilized antibodies were also presented. This device appears to be a potential diagnostic tool for cardiovascular risk assessment, where simultaneous analysis of various protein markers is required[74].
- **Surface Plasmon Resonance (SPR):** Surface plasmon resonance occurs when a photon of incident light hits a metallic surface (typically a gold surface). At a certain angle of incidence, a portion of the light energy couples through the metal coating with the electrons in the metal surface layer, which then move due to excitation. The electron movements are now called surface plasmons (SPs), and they propagate parallel to the metal surface. The plasmon oscillation in turn generates an electric field whose range is around 300 nm from the boundary between the metal surface and sample solution[75]. The angle at which the resonance occurs, the resonance angle, depends on the refractive index of the material near the metallic surface. Therefore, when there is a local change in the refractive index at the metallic surface due to target analyte recognition and capturing on the surface, SPs cannot be formed. Detection is thus accomplished by measuring the changes in the reflected light obtained on a detector. SPR-based technology has been explored in the discovery of drugs. For instance, Kosaihira et al.[76] verified apoptosis by cancer drugs (Herceptin, Quercetin and trans-Resveratrol) in living pancreatic cells cultured on a sensor chip with a surface plasmon resonance (SPR) sensor. Similarly, Maltais et al.[77] reported that SPR signal of apoptosis can be analyzed to quantify the duration of the latency period, the rate of the execution phase and the maximum extent of the apoptotic reaction. According to them, these parameters could be used to establish a SPR signature of apoptosis, which

1.2. Strategies implemented in cell-based assays for drug screening

is distinct from the responses produced by other molecules that also produce rounding, blebbing, detachment or disruption of the cellular membrane. Lei et al.[78] presented an automated polymer based microfluidic analysis system integrated with a SPR biosensor for detecting the specific binding of biomolecules and qualitatively monitoring of cell adhesion on the sensor surface. Tokel et al.[79] developed a portable, multiplex, inexpensive microfluidic-integrated SPR platform that detects and quantifies bacteria, such as *Escherichia coli* and *Staphylococcus aureus* rapidly. According to Tokel, plasmonic-based microchip sensitive pathogen detection could potentially be used for point of care applications[79]

- **Quartz Crystal Microbalance with dissipation (QCM-D):** This acoustic based biosensor is based on measuring the resonant frequency of piezoelectric quartz crystals. It consists of thin AT-cut³ quartz discs that are placed between two gold electrodes. Due to the piezoelectric nature of the quartz crystal, when an AC signal is applied across the electrodes, this leads to oscillating in-plane shear of the quartz crystal, which acts as a sensitive oscillator circuit[80]. The resonant frequency of this oscillating crystal is sensitive to nanogram-scale changes in mass coupled to the surface frequency. Therefore, by measuring this frequency as well as the decaying or dissipative frequency of cells associated with the crystals, it is possible to obtain relevant biological information such as cell adhesion, cell proliferation and cytotoxicity[80]. For instance, Wang et al.[81] reported the ability of a quartz crystal microbalance biosensor to distinguish benign from toxic exposures and reveal unique kinetic information about cellular responses of macrophages to varying doses of single-walled carbon nanotubes (SWCNTs). They found that high SWCNT treatment doses, 100-150 $\mu\text{g/ml}$, lead to a significant decrease in crystal oscillation frequency revealing toxicity in the form of apoptosis and cell loss compared to cell responses to Zymosan A and polystyrene beads. QCM-D can potentially be used in biodetection for applications in drug screening tests and diagnosis. For example, Fatisson et al.[82] showed that the cell response to different cytomorphic agents can generate different QCM-D signals. They found that these signatures are characteristic of cell morphology changes such as cell shrinkage, lysis and cell rounding, resulting from different mechanical and/or biochemical pathways. Moreover, they suggested that cell toxicity can be predicted since cytotoxic agents induced a decrease in dissipation, while non-cytotoxic agents lead to a normal increase in dissipation[82]. This technique has also been explored in microfluidics. For instance, Thies et al.[83] developed a particle-based microfluidic QCM biosensor combined with mass amplification and magnetic bead convection. According to them, this device could implement all of the sample preparation steps and target analyte quantification into one microfluidic chip while providing measurement results in a shorter time frame than commercial enzyme-linked immunosorbent assay tests[83]. Tao et al.[84] integrated QCM with a microfluidic chip for amyloid Beta-A β 42 quantitation, which is a biomarker of Alzheimer disease. They showed that this microfluidic device is reusable, has fast-response and small-sample consumption, and is applicable for early Alzheimer disease diagnosis in the clinic[84].

³One of the most widely used cut is the AT cut. This is at 35° 25' to the Z axis of the crystal.

- **Electrical Impedance Spectroscopy:** Impedance based assays have also emerged as an alternative technique to conventional label based methods. A small AC signal is applied to the system and then the resultant current is measured in order to compute the total impedance of the system. The applied AC signal is harmless to the cells and it does not adversely affect the physiology of the cells under study[80, 85, 86, 87]. Impedance has been measured in single cells[88], cells in suspension[89] and cells adhered to substrates[90]. Impedance based 2D culture devices have been developed for monitoring a multitude of cellular parameters. For instance, Park et al.[91] studied chitosan cytotoxicity to MCF-7 breast cancer cells using a multidisc ITO microelectrode array. They observed that chitosan treatment caused cell viability deterioration and detachment from the electrode surface, thus decreasing impedance in a concentration dependent manner in terms of applied chitosan. Chen et al.[92] investigated the direct biological function of endogenous placenta growth factor (PIGF), which is a key molecule in angiogenesis and vasculogenesis, in human lung cancer cell line A549. They used impedance measurements to determine that the migration of A549 cells and the activation of the PIGF resulted in remarkably reduced migrating capacity. Moreover, Ren et al.[93] conducted invasion assays of ovarian cancer cells (SKOV3 and HEY) using impedance sensing. They assessed the ability of SKOV3 cells to invade into a confluent monolayer of peritoneal mesothelial cells producing lysophosphatidic acid (LPA) which is a potential diagnostic marker and a therapeutic target for ovarian cancer. They observed that cell invasion through the mesothelial cell layer resulted in a significant decrease in resistance[93].

In the literature, some authors have presented impedance-based 3D culture monitoring studies. For example, Thielecke et al.[94] investigated the detection of the effect of active substances on spheroids positioned on planar electrode arrays. In their study as a 3D tissue model, multicellular aggregates (spheroids) of T47D clone 11 tumor cells was used. They demonstrated that the effect of cytotoxins, such as DMSO and Triton X-100 on spheroids can be detected by recording the effective impedance of planar electrodes covered by spheroids. Other researchers have employed planar microelectrodes fabricated onto microcavities to measure the impedance response of cellular spheroids to different stimuli. For instance, Kloss et al.[95] trapped human melanoma spheroids between four gold electrodes in 100 μm deep square microcavities and the cells were exposed to the drug Camptothecin (CTT) for various time intervals to induce apoptosis. They demonstrated that drug (CTT) induced apoptosis will not directly result in a disintegration and damage of a complex aggressive 3D *in vitro* melanoma tumor[95]. Similarly, Krinke et al.[96] optimized and redesigned a microcavity array for a feasible and sensitive detection of cellular alterations in neuroblastoma tumor spheroids. They observed that neuroblastoma spheroids exposed to okadaic acid formed hyperphosphorylated tau protein similar to the processes believed to cause Alzheimer's disease associated neurodegeneration[96]. Regarding impedance-based PDX systems, in the literature no studies were found on combining animal model with impedance sensing.

Zhang et al.[97] used microfluidic perfusion barriers inside cell culture chambers to minimize disruption of the cell monolayer, as shown in Fig. 1.5a. According to them, the perfusion barriers minimize fluid shear stress and are able to maintain the integrity of the cell monolayer. In their study, they showed that bovine aortic endothelial cells (BAECs) are suitable for impedance measurements using ECIS[®] gold interdigitated electrodes and toxicity testing because this cell line generated higher impedance values and formed cell monolayers at a faster rate compared to rat fat pad endothelial cells (RFPECs). In addition, they demonstrated that combining the advantages of label-free ECIS multiparametric cellular sensing with microfluidic technology can enhance long-term cell maintenance and cytotoxicity sensing capabilities for field use[97]. Similarly, Rothbauer et al.[98] presented a microfluidic cell culture system containing embedded gold IDEs microsensors to continuously and non-invasively monitor the effects of silica nanoparticles on human H441 lung adenocarcinoma cells under varying flow conditions, as shown in Fig.1.5b. They concluded that in addition to the physical,

1.2. Strategies implemented in cell-based assays for drug screening

chemical and biological characteristics of the nanoparticle, cellular nanoparticle uptake and toxicity is also governed by applied fluidic exposure scenarios[98].

Some authors have combined microfluidics with impedance sensing to study cells in a 3D environment. For instance, Nguyen et al.[88] have presented a microfluidic device integrated with multidisc ITO electrode array for investigating single cancer cell migration in 3D matrices, as shown in Fig.1.5c. They demonstrated that migration of single metastatic MDA-MB-231 cells in their initial stage can be monitored in real time. They observed a rapid change in impedance magnitude of approximately 10 Ω/s , whereas no prominent impedance change was observed for less metastatic MCF-7 cells. Henry et al.[99] described a microfluidic Organ Chip design that contains semi-transparent, platinum black sensing electrodes to measure both Trans-Epithelial Electrical Resistance (TEER) and cell layer capacitance using 4-points impedance measurements, as depicted in Fig.1.5d. They demonstrated the utility of this device for assessing formation and disruption of barrier function both within a human lung airway Chip lined by a fully differentiated mucociliary human airway epithelium and in a human Gut Chip lined by intestinal epithelial cells. Moreover, Luongo et al.[100] reported the design, fabrication, and testing of a lab-on-a-chip based microfluidic device, presented in Fig.1.5e, for application of trapping and measuring the dielectric properties of MCF-7 microtumor spheroids using gold electrodes. They observed that multicell spheroids induced changes in impedance magnitude consistent with diameter increase[100].

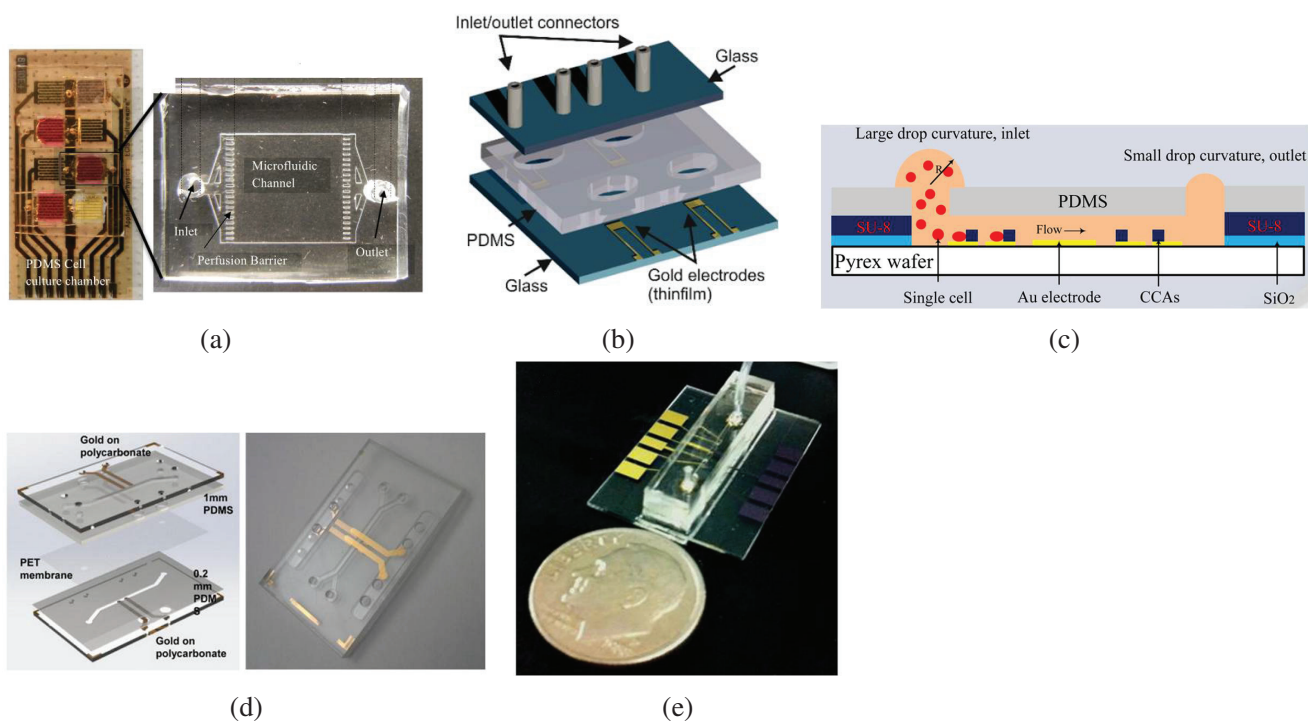


Figure 1.5 – Impedance based microfluidic systems: (a) Zhang’s system. Figure adapted with permission from figure 2 in[97] (Copyright 2015 by Elsevier), (b) Rothbauer’s system . Figure adapted from figure 1 in[98], (c) Nguyen’s device. Figure adapted with permission from figure 1 in[88] (Copyright 2013 by American Chemical Society), (d) Henry’s system. Figure adapted from figure 1 in[99] (Copyright 2001 by Royal Society of Chemistry) and (e) Luongo’s system. Figure adapted with permission from figure 4 in[100]. Copyright 2013 by AIP Publishing.

1.2. Strategies implemented in cell-based assays for drug screening

In this PhD thesis we focused on impedance measurements on adherent cell layers using ECIS. This method offers the possibility of recording a variety of cellular parameters such as proliferation[101], adhesion[102], and cellular morphology[103] in one combined read-out in real time. In addition, we worked with 2D monolayer culture because it is the simplest cell culture method to start with. However, in the future one could consider to extend this work to 3D organoid models which would increase the complexity of the system, particularly the design of the electrodes which need to be adapted to a 3D structure under study. Furthermore, we chose electrical impedance sensing as the method for monitoring cell activity because it is harmless to living cells, enables multiplexity and compared to the other methods, we consider that ECIS system can be easily miniaturized and integrated in a microfluidic environment. Thus, it appears to be interesting to explore ECIS experiments carried out with transparent electrodes so that in the future a transparent microfluidic impedance based chip can be developed. In addition, this could allow the combination of ECIS with microscopy observation which could be a promising approach in cancer treatment where the mechanism of action of chemotherapeutic agents need a thorough understanding.

1.2. Strategies implemented in cell-based assays for drug screening

Method	Advantages	Limitations	Information obtained	Ref.
RWG	<ul style="list-style-type: none"> • Ability for multiparameter measurements 	<ul style="list-style-type: none"> • Limited penetration depth of the evanescent wave (~ 100 nm) 	<ul style="list-style-type: none"> • Receptor mediated signaling 	[104]
			<ul style="list-style-type: none"> • Cell adhesion • Cell proliferation 	[105]
SAW	<ul style="list-style-type: none"> • Simple handling • Low consumption of chemicals 	<ul style="list-style-type: none"> • Damping problems in the liquid phase • Sensitive to perturbations 	<ul style="list-style-type: none"> • Cell adhesion 	[106]
			<ul style="list-style-type: none"> • Cell proliferation • Cytotoxicity 	[72]
SPR	<ul style="list-style-type: none"> • Easy multiplexing • High specificity 	<ul style="list-style-type: none"> • Poor sensitivity of the apical regions of cells • Low discrimination between specific and non-specific interactions 	<ul style="list-style-type: none"> • Cell adhesion 	[107]
			<ul style="list-style-type: none"> Cell proliferation Receptor mediated signaling 	[108]
QCM	<ul style="list-style-type: none"> • Well operated in optically opaque media • Ease of use 	<ul style="list-style-type: none"> • Poor sensitivity of the apical regions of cells • Multiplexing is complex 	<ul style="list-style-type: none"> • Cell proliferation 	[109]
			<ul style="list-style-type: none"> • Cytotoxicity • Cell adhesion 	[108]
ECIS	<ul style="list-style-type: none"> • It integrates many assays into one • Easy miniaturization • Sensitive to changes over the entire cell body 	<ul style="list-style-type: none"> • Low specificity • Only works with adherent cells • Poor image resolution (due to gold electrodes) 	<ul style="list-style-type: none"> • Cytotoxicity 	[110]
			<ul style="list-style-type: none"> • Cell adhesion • Cell proliferation • Barrier function • Receptor mediated signaling 	[111]

Table 1.2 – Advantages and limitations of different label-free based assays.

1.3 Electrical Cell-substrate Impedance Sensing (ECIS)

Electrical bioimpedance has been a subject of research for a long time, covering the electric currents and the biopotentials associated with the life processes. Bioimpedance measurements can be carried out on different types of tissue ranging from dead biological material to living plant, fruit, egg, animal or human[112]. These measurements give information about the electrical processes in the cells and tissue, becoming useful for monitoring physiological changes that are hidden inside the cells[112]. Many investigations have been carried out to exploit this potential technology in areas such as electrical impedance tomography[113], body composition[114], cell micromotion[115], organ viability[116], skin hydration and skin pathology[117]. In fact, bioimpedance can be used at different levels, such as tissues[118], organs[116] and cells[86].

In 1984, Electric cell-substrate impedance sensing (ECIS) was pioneered by Giaever and Keese[86], who were the first to grow mammalian cells directly on the surface of electrodes and to record and analyze the corresponding changes in the electrode electrical impedances. Since then, ECIS has become a well known technique capable of real-time and label-free impedance measurements for several biomedical applications[28].

1.3.1 Electrodes' geometries

In the literature, the planar electrodes used in ECIS experiments can be classified in two major categories, monopolar and interdigitated electrodes (IDEs), as shown in Fig. 1.6:

- **Monopolar electrodes:** This type of electrodes consists on an array of small sensing electrodes and a large counter electrode. Making an almost 1000 times larger counter electrode ensures that the impedance of the sensing electrode dominates the read out of the entire circuit[86]. The observed changes in the electrical impedance can be clearly assigned to changes that occur at the small sensing electrode with negligible contributions due to the presence of cells on the counter electrode or the electrical wiring of the setup[119]. Giaever and Keese first introduced ECIS measurements with small gold electrodes with a diameter of 250 μm and a much larger counter electrode, both located at the bottom of a cell culture well. Nevertheless, with monopolar electrodes only a few cells contribute to impedance measurement, which results in large fluctuations among experiments and becomes problematic for high throughput cell-based bioassays[120, 121]. Furthermore, fabricating a large counter electrode results in space waste, which hinders the miniaturization and integration of ECIS sensors, which is essential in a high-throughput screening system[120, 122]. Moreover, a large number of cells are required to be initially seeded on the electrode to obtain sufficient number on the working electrode. Hence, in order to address these problems and improve the utilization efficiency of electrodes, interdigitated electrodes were explored for bioimpedance measurements.

1.3. Electrical Cell-substrate Impedance Sensing (ECIS)

- **Interdigitated electrodes:** They are a series of parallel microband electrodes, in which alternating microbands are connected together, forming a set of interdigitated electrode fingers[123]. The branches of the counter electrode and the working electrode weigh equally during the measurement because they have identical dimensions in geometry. As the cells cover either one of the two branches, impedance changes in the same manner. Moreover, the typical dimensions of an individual microband finger are 0.1-0.2 μm in height; 1-20 μm in width and 2-10 mm in length with a gap of 1-20 μm between the fingers[123]. Among microelectrodes, IDEs have become an attractive option. IDEs offer ease of fabrication, ready integration in electronic devices, the potential for multi-analyte sensing through the fabrication of arrays and higher sensitivities compared to conventional electrodes[124]. In addition, the IDEs commonly cover up to about 50% of the area of each well, lowering the well-to-well differences in the high-throughput screening system[122]. Based on this, we decided to use interdigitated electrodes over conventional monopolar electrodes for our ECIS experiments with cell monolayers.

Several methods for fabricating planar electrodes have been developed depending on the type of array required such as mechanical methods[125], template approaches[126] and lithographic techniques[127]. However, lithographic methods have the advantage of being highly controllable and reproducible over mechanical and template approaches[128].

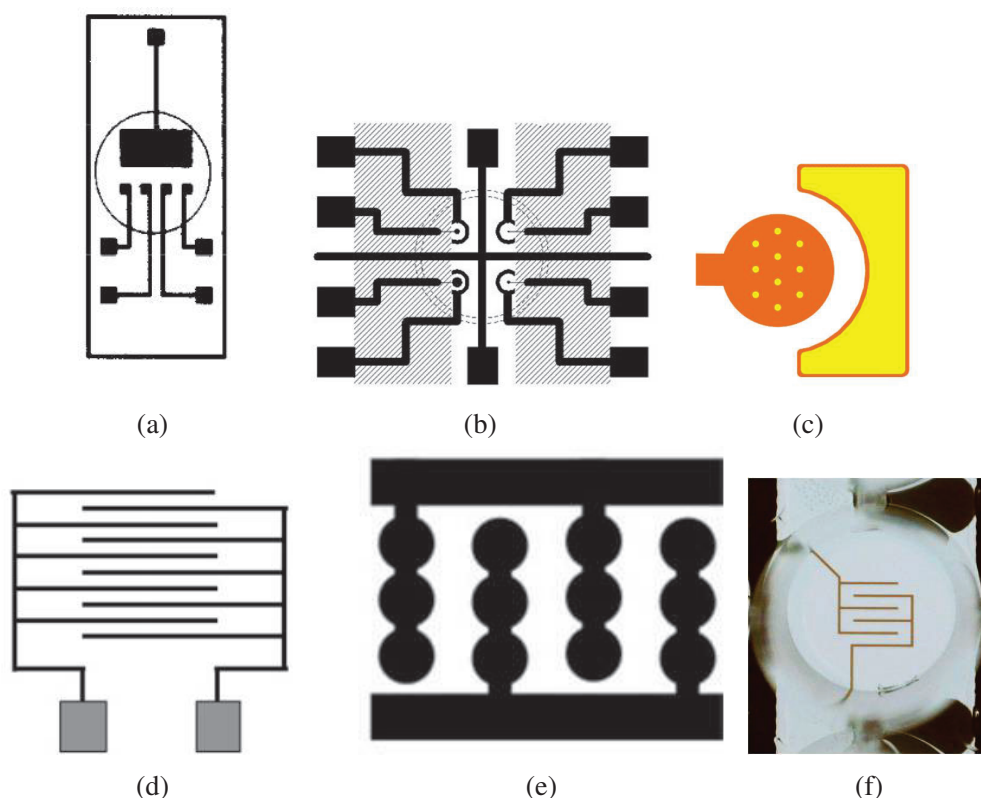


Figure 1.6 – Monopolar and IDEs used in ECIS. (a) Arrangement of four small WEs (0.03 cm^2) and a common CE (0.6 cm^2)[129]. Copyright 1996 by Elsevier. Adapted with permission. (b) Array of electrodes with different areas 0.00025 cm^2 , 0.0004 cm^2 , 0.0013 cm^2 and 0.004 cm^2 [130]. Copyright 2004 by John Wiley and Sons. Adapted with permission. (c) ECIS[®] array of 10 electrodes of $250 \mu\text{m}$ [131]. (e) Interdigitated parallel line electrode array[132]. (f) Electrode structures with disc electrodes added on the electrode lines[133]. (g) Interdigitated finger configuration of ECIS[®] electrodes[134].

1.3.2 Electrode material

ECIS technique is fully dependent on the use of patterned microelectrode arrays, in which cells can adhere and spread during the bioimpedance experiment. Hence, the electrode is an essential component for the sensitivity of the ECIS system. Usually, the electrodes are fabricated on two major substrate materials, glass and silicon. The glass substrate is transparent and thus compatible with diverse microscopy systems[135, 121]. Conversely, silicon substrates are not transparent, therefore observation it is only possible with reflected light microscopy[136, 137]. Nevertheless, silicon is more compatible with electronic circuits if supplementary structures need to be incorporated in the ECIS system. Despite their difference in transparency, both substrate materials seem suitable platforms for ECIS sensing. For instance, Srinivasaraghavan et al.[138] in their studies with MCF-10A cells proliferating on silicon and Pyrex/glass substrates, found similar electrode coverage and high cell viability for both materials[138].

Regarding the electrode material, in the literature we can find electrodes fabricated on a variety of materials such as gold (Au)[124, 139, 140, 86, 141], platinum (Pt)[123, 142, 143, 144] or indium tin oxide (ITO)[91, 145]. For instance, Pt has been used for impedance detection due to its attractive physical properties, such as biocompatibility, high melting point, high density, high electrical resistivity and slightly low electronegativity[123]. As for Au, it is the most used material in ECIS due to its high electrical conductivity, resistance to corrosion and non-toxicity[132]. This later property is very important when it comes to culturing cells on Au surfaces. In fact, Au electrodes are used in the aforementioned commercialized cell impedance analyzers xCELLigence[®] and ECIS[®]. In the case of ITO, although it offers an electrical conductivity (10^4 S/cm) three orders of magnitude less than that of gold, it has transparency over the visible domain, which allows morphological observation of cells and cell growth monitoring[132]. Despite of this advantage over Au and Pt, ITO is less used as electrode material for ECIS applications.

In this PhD thesis we believe that working with interdigitated electrodes can facilitate the miniaturization and integration of the electrodes in a microfluidic environment, compared to monopolar electrodes which are limited by the need of a large counter electrode. We focused on studying ITO, which is transparent, as an electrode material used in ECIS experiments and that can be combined with optical measurements. In this study, Au was considered as the reference electrode material for characterization in terms of sensitivity to cancer cell proliferation.

1.3.3 Cell-substrate impedance sensing experiment

A classic ECIS experiment consists on monitoring the adherence of cells in culture medium with planar electrodes. When cells are exposed to certain stimulants either environmental or chemical, they may respond in different ways such as: morphological changes, increased or decreased adhesion, as well as increased or decreased metabolic output[34]. Variation in cell behavior during cell culture can result in changes in impedance that can be monitored in real time, as shown in Fig. 1.7. Monitoring these impedance changes over a wide range of different frequencies can provide relevant information about the cells under study in culture medium. The basic principle of this technique consists on depositing two coplanar metallic film electrodes on a substrate and the cells are allowed to settle, adhere and spread on their surface under ordinary cell culture conditions[119]. The electrical connection between the two electrodes is provided by the culture medium, which contains all nutrients and growth factors that cells require. A schematic of an ECIS experiment is depicted in Fig. 1.13. Cells adhere to both the surface of the substrate and the electrodes influencing the current exchange through the culture medium. Many kinds of mammalian cells adhere to the substrate to grow and propagate, particularly cancer cells, which can also survive in suspension status and spread rapidly[133].

1.3. Electrical Cell-substrate Impedance Sensing (ECIS)

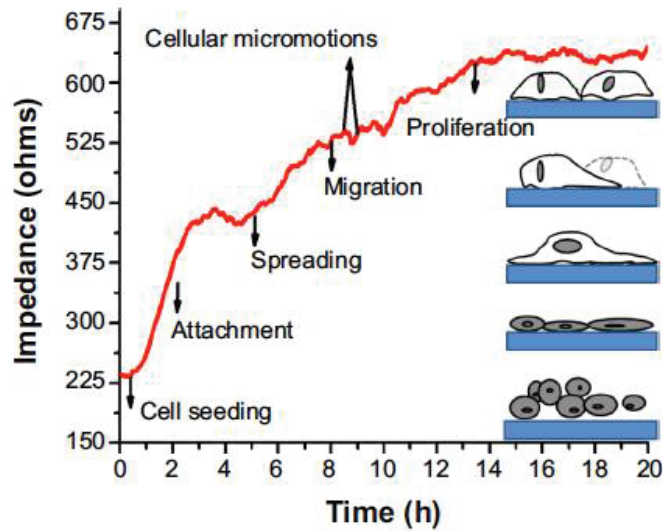


Figure 1.7 – ECIS measurement graph showing various cellular morphological changes of normal human dermal fibroblasts neonatal cells (HDFn) growth response for 20 hours. Figure adapted from figure 2 in [146]. Copyright 2006 by Dove Medical Press Ltd. Adapted with permission.

The impedance measured during each experiment can depend on different parameters related to the electrode and medium interface, the medium itself and the adherent cells. Ideally, contributions from cell behavior should be dominant over other contributions. However, this is not always the case, since contributions different from those of cells cannot be always neglected and they play an important role in the overall impedance of the system under study. In Chapter 3 these contributions and their electrical models are presented and discussed in more detail.

Here, we focused on the contributions from cells. Understanding the structure of biological cells helps to have a better insight about cell impedance in an ECIS system. Typically, mammalian cells have a phospholipid bilayer that separates the extracellular fluids from intracellular cytoplasm and organelles such as the nucleus. In addition, there are proteins of the membrane that either act as ion carriers or undergo conformational changes to form pores and channels through which ions can pass. Therefore, the cell membrane has both resistive and capacitive properties due to lipids acting as insulators and proteins serving as conducting channels [147]. Electrically, this means that the capacitive behavior of the membrane can be modeled with a capacitance C_m and the resistive behavior with a resistance R_m both being in parallel. In the literature, C_m is about $1 \mu\text{F}/\text{cm}^2$ [132] and as mentioned before it is related to the cell membrane structure, which is similar to a capacitor because the hydrophobic portions of the lipids forming the core of the membrane are insulators that separate conducting intracellular and extracellular fluids [132]. Moreover, the ion channels and proteins across the membrane, are responsible for the resistive behavior corresponding to R_m , which is about $10 \text{ k}\Omega$ - $200 \text{ k}\Omega$ [148]. Fig. 1.8 shows equivalent electrical circuit models proposed to represent a cell in suspension, which include four elements: C_m , R_m , R_s and R_i where R_s and R_i correspond to the extracellular medium resistance and the intracellular resistance of around 50Ω - 400Ω [149], respectively.

1.3. Electrical Cell-substrate Impedance Sensing (ECIS)

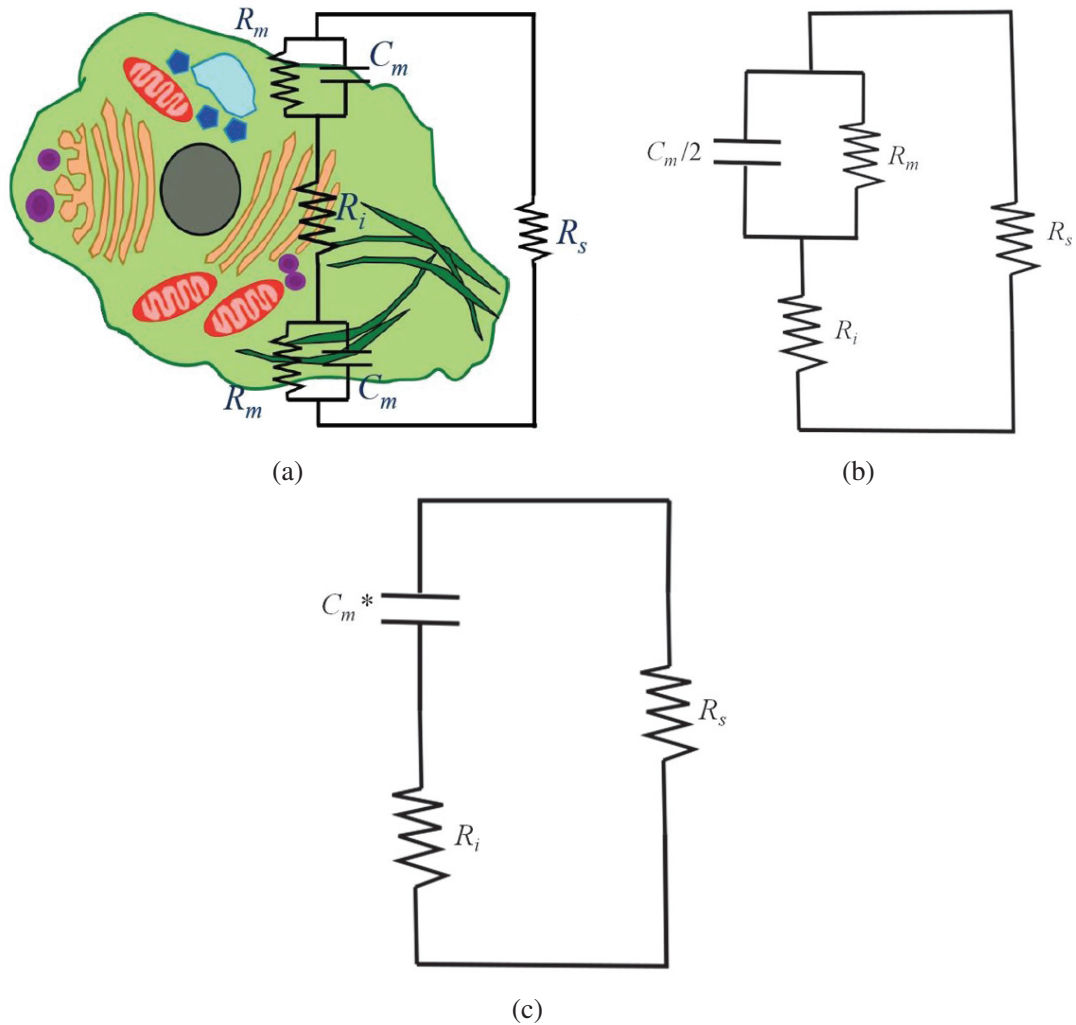


Figure 1.8 – (a) Electrical model of cell in suspension. Figure adapted from figure 1 in [132], (b) Simplified electrical model of cell in suspension. Figure adapted from figure 4 in [150] and (c) Circuit model neglecting R_m with $C_m^* = C_m/2$. Figure adapted from figure 8 in [151]

The aforementioned models were for cells in suspension, here we focused on cells adhered to the electrode surface. Few groups have studied the formation of a confluent cell layer using electric equivalent circuit models. Most of the studies found in the literature present the experimental data of cell proliferation in terms of normalized impedance [152, 153, 154] (detailed later) as a function of frequency (or time) but few [155] go further and use equivalent circuit modeling. This method consists of ascribing passive circuit elements to different components of the system in such a way as to have physical significance, hopefully isolating observed changes in the overall impedance to isolated components of the equivalent circuit. For instance, Wang et al. [156] proposed the model in Fig. 1.9 to study the cell cycle of Human cervical carcinoma (HeLa) cells with a cellular impedance-sensing chip. In the model, the authors take into account the solution resistance, the formation of a resistive gap, the cell membrane and the impedance of the electrode-electrolyte interface. The latter was divided into two components represented by constant phase elements (described later): CPE_{int1} and CPE_{int2} , which are thought to represent the impedance of the uncovered areas and of the cell-covered areas of the electrode surface, respectively. A large number of works usually do not distinguish between these two aspects of the impedance and hence the impedance value of the electrode-electrolyte interface is in effect an average involving covered and uncovered components. In these cases

1.3. Electrical Cell-substrate Impedance Sensing (ECIS)

only one CPE is used to represent the electrode-electrolyte interface.

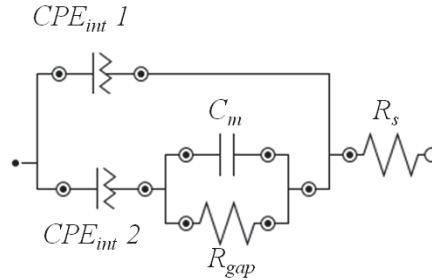


Figure 1.9 – Equivalent circuit model used by Wang et al.[156] where R_s represents the resistance of the solution. R_{gap} corresponds to the gaps between the underside of the attached cells and the electrode surface, and its value is related to the closeness of cell adhesion to the substrate. C_m is associated with the capacitive behavior of the cell membrane.

In contrast, Benson et al.[157] reported a model to analyze barrier function, where they included the influence of tight junctions between neighboring cells and denoted it as R_{TEER} , as shown in Fig. 1.10. This is a common name for the Transepithelial/Transendothelial Electrical Resistance (TEER), which measures the integrity of tight junction dynamics in cell culture models of endothelial and epithelial monolayers. R_{TEER} values are strong indicators of the integrity of the cellular barriers before they are evaluated for transport of drugs or chemicals[158]. For example, tight barriers should be expected to exhibit TEER values of $1,000 \Omega \cdot \text{cm}^2$ or more, which corresponds to absolute resistance values of $200,000 \Omega$ or more in an ECIS system[157].

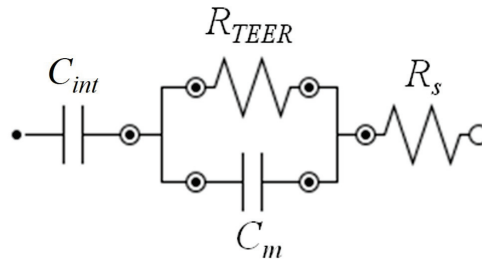


Figure 1.10 – Equivalent circuit model used by Benson et al.[157] where C_m is the membrane capacitance, R_s is the resistance of the cell culture medium and the electrode-electrolyte interfacial capacitance is C_{int} .

A more complex model in Fig. 1.11 was proposed by Xiaoliang et al.[155] to monitor the adhering behavior of HeLa cells. This included the intracellular resistance R_{intra} in series with C_m and in parallel with R_{gap} . In contrast to the other models, they represented the interfacial impedance by a CPE_{int} in series with the solution resistance R_s . Moreover, they included a parasitic capacitance $C_{parasitic}$, to represent the parasitic effects existing in the microchip and the measuring system due to the sensor substrate and electrical cables.

1.3. Electrical Cell-substrate Impedance Sensing (ECIS)

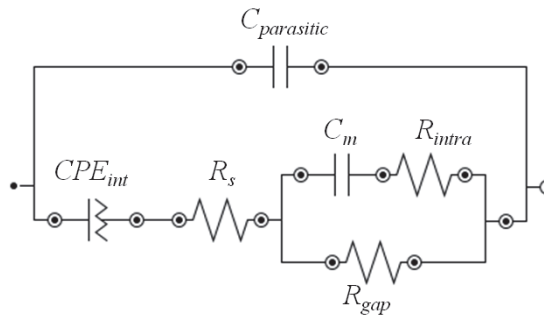


Figure 1.11 – Equivalent circuit model used by Xiaoliang et al.[155] where $C_{parasitic}$ represents the parasitic effects in the chip and measuring system, CPE_{int} represents the interfacial impedance, R_s is the cell culture medium resistance, C_m is the cell membrane capacitance, R_{intra} is the intracellular resistance and R_{gap} is the resistance between the adhered cells and the electrode surface.

So far, we have seen that the electrical properties of a cell can be described by means of an equivalent circuit made of C_m , R_{intra} , R_{gap} and R_{TEER} . Nevertheless, a cell population under study, comprises many cells with different microenvironments and variation of properties implying a multitude of such equivalent circuits with different time constants. Therefore, Meissner et al.[143] replaced C_m by a CPE_{cells} to take into account heterogeneity in the cell population. Usually, CPE behavior is attributed to interfacial heterogeneity and/or surface roughness. In Fig.1.12 we can assume that R_{extra} takes into account R_{TEER} , R_{gap} and R_s .

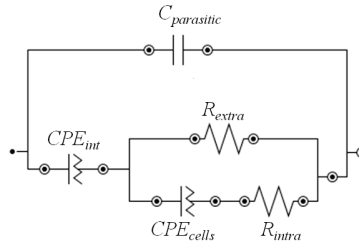


Figure 1.12 – Equivalent circuit model used by Meissner et al.[143] where $C_{parasitic}$ corresponds to parasitic effects in the system, CPE_{int} represents the interfacial impedance, R_{extra} is the extracellular resistance, R_{intra} is the intracellular resistance and CPE_{cells} corresponds to the cell membrane.

1.3. Electrical Cell-substrate Impedance Sensing (ECIS)

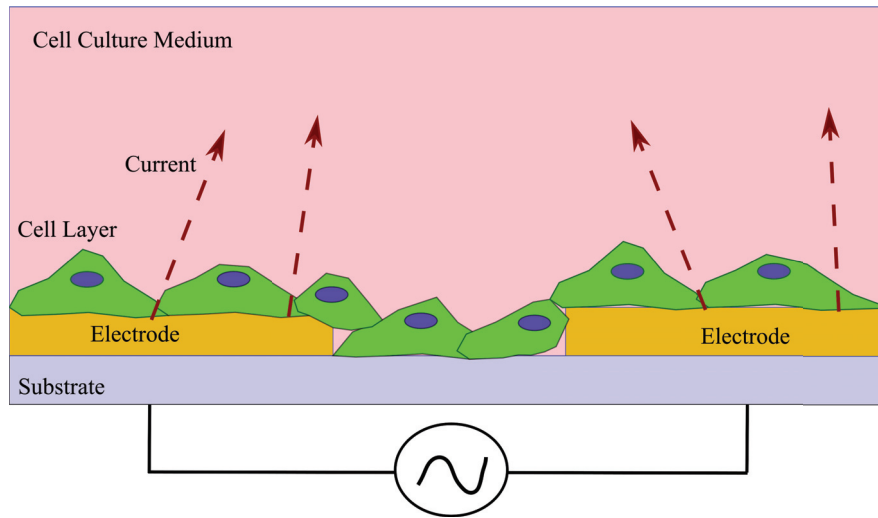


Figure 1.13 – Schematic of electrical impedance measurement on planar electrodes (Draw not to scale). Figure adapted from figure 7.1 in[133]

Furthermore, depending on the frequency of the applied AC signal, the current will follow different pathways when cells adhere on the electrode surface. At low frequencies ($f < 4$ kHz)[152], the cell membrane due to its bilayer structure becomes electrically insulating, so that current cannot easily go through the cells. Hence, most of the current will be forced to flow through the confined and narrow channels between the ventral plasma membrane⁴ and the electrode surface before it can escape through the tight junctions between adjacent cells into the medium, as shown in Fig. 1.14a. Since the current has to go around the cells, impedance contributions from the cell-substrate adhesion zones as well as from tight-junctions between neighboring cells can be investigated[119]. While at high frequencies ($f > 40$ kHz)[152], the current goes through the cell membrane and cytoplasm, as depicted in Fig. 1.14b. The current does not have to go around the cells anymore but can flow transcellularly through cells passing the ventral and dorsal membranes⁵[119].

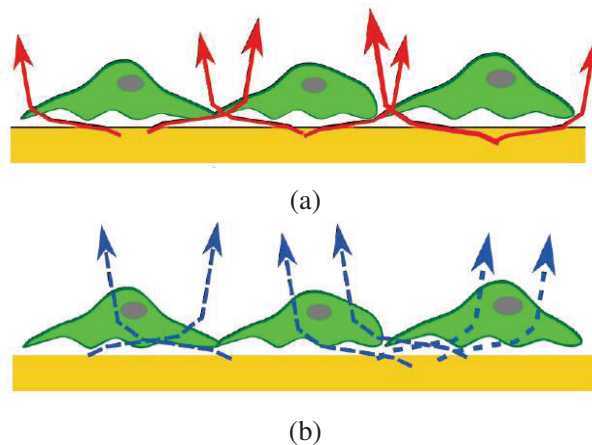


Figure 1.14 – Current pathways at (a) low frequencies and at (b) high frequencies in an ECIS system.

⁴Ventral plasma membrane: the portion of the cell membrane in contact with the electrode surface

⁵Dorsal plasma membrane: the portion of the cell membrane that is not in contact with the electrode surface (apical region)

1.3. Electrical Cell-substrate Impedance Sensing (ECIS)

Additionally, in an ECIS assay in order to extract the necessary information about the electrical parameters contributing to the impedance change, one must use a modeling method to explain the behavior of the system and there are two ways of doing it[34]:

- One is to use an analytical expression derived from a physical model. For instance, Giaever and Keese[115] used the model shown in Fig. 1.15 in order to calculate the impedance of cell-covered electrode Z_C as a function of the frequency and they found the following expressions:

$$\frac{1}{Z_C} = \frac{1}{Z_n} \left(\frac{Z_n}{Z_n + Z_m} + \frac{\frac{Z_m}{Z_n + Z_m}}{\frac{i\gamma r_c I_0(\gamma r_c)}{2I_1(\gamma r_c)} + R_b \left(\frac{1}{Z_n} + \frac{1}{Z_m} \right)} \right) \quad (1.1)$$

$$\gamma r_c = r_c \sqrt{\frac{\rho}{h} \left(\frac{1}{Z_n} + \frac{1}{Z_m} \right)} = \alpha \sqrt{\frac{1}{Z_n} + \frac{1}{Z_m}} \quad (1.2)$$

where $Z_m = -i/2\pi f(C_m/2)$ corresponds to the specific membrane impedance of the cells, Z_n is the impedance of a cell free electrode, R_b corresponds to the resistance between the cells for a unit area, I_0 and I_1 are modified Bessel functions of the first kind of order 0 and 1, r_c is the cell radius, h is the height of the space between the ventral surface of the cell and the electrode and ρ is the resistivity of the cell culture medium. Over the years, there have been a number of modifications in the electrical models of ECIS, resulting in two cell electrode models used for impedance analysis. One is appropriate for cells with dislike shape, such as transformed fibroblasts, endothelial cells and epithelial cells[159], whereas the other one is used for rectangular cells with semicircular ends, such as normal fibroblasts[160].

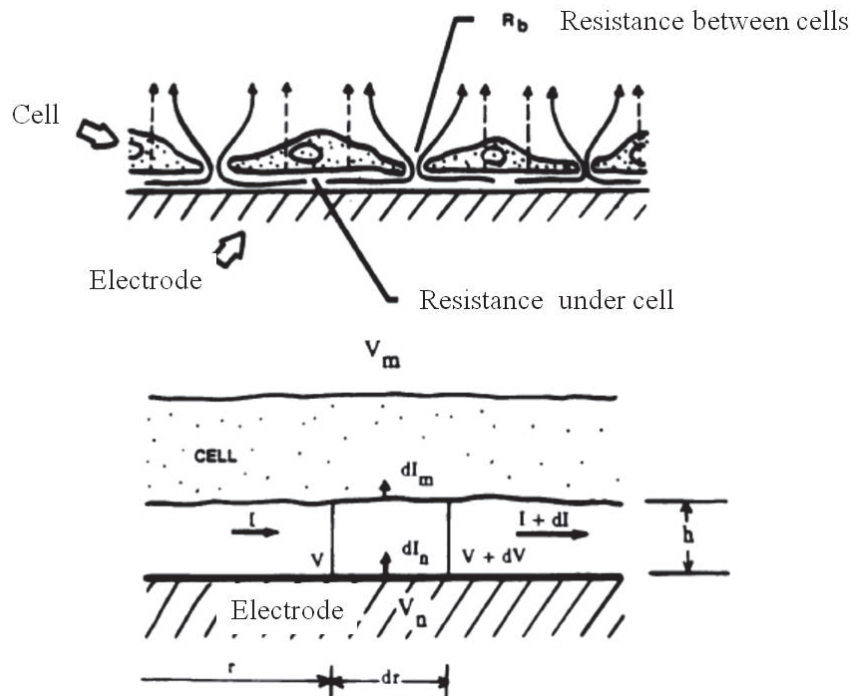


Figure 1.15 – Diagram of the cells in tissue culture and the model used to calculate the specific impedance of a cell-covered electrode. Figure adapted from figure 2 in[115].

- The second and most often used method to study ECIS experimental data consists on using an equivalent circuit model that ascribes passive circuit elements to different components of the system. This is the method that we used in this PhD thesis for impedance data analysis.

1.4 Drug screening applications based on ECIS sensing

ECIS has been used as a label-free method to study and monitor biological changes in different cellular assays. There are some companies that developed and now commercialize products based on ECIS sensing for *in vitro* monitoring of cells. These products developed by different companies are listed in Table 1.3. The first commercialized product is known as ECIS[®] by Applied BioPhysics, which was started by the pioneers Giaever and Keese. This system measures the impedance of mammalian cells cultured on small electrodes[161]. Another impedance-based biosensor is the Real-Time Cell Electronic Sensing (RT-CES) now called XCELLigence[®] supplied by ACEA Biosciences. In this technology, the cells are seeded in standard microplates that contain arrays of interdigitated electrodes (IDEs) located in the bottom of each well of a 16 or 96-well plate[162]. Likewise, MDS Sciex introduced the CellKey[®] system that enables the measurement of endogenous receptor targets in whole live cells seeded on a 96 or 384-well plate[163]. We can also find the Bionas 2500[®] analyzing system. This product is able to measure online and label-free many parameters of cell activity, such as metabolism (potentiometric sensor), respiration (Clark-type electrodes), cell adhesion and cell confluence (interdigitated electrodes)[164]. However, all of the aforementioned commercial cell analyzers are based on gold electrodes which is an opaque material. Although the gold film on the electrodes is only 500 nanometers thick[165], none of the commercial systems offers impedance assays with transparent electrodes. In the perspective of combining impedance with optical quantification, it is relevant to explore this type of electrodes in which cell morphology changes, due to cell adhesion, spreading, proliferation and chemosensitivity effects, can be monitored as if cells were proliferating on glass slides and complement the impedance data. In addition, most of the commercial cell analyzers are not designed for microfluidic environment[166]. They do not monitor the cell activity in microfluidic channels but in wells of electronic microtiter plates filled with cell culture medium and the electrodes at the bottom. In addition, in the approach of integrating ECIS into microfluidics and into a more biomimetic environment, electrode geometries need to be adapted. This brings some challenges, such as reducing the dimensions of the electrodes which induces high impedance that can affect the sensitivity of the measurements.

1.4. Drug screening applications based on ECIS sensing

Company	Product	Cell-based assays	Selected References
Bionas	Bionas 2500	Cell adhesion, proliferation, metabolism, and cytotoxicity	[167][168]
Applied Biophysics	ECIS	Cell adhesion, proliferation, barrier function, receptor-mediated signaling, and wound healing	[169][101]
ACEA Biosciences and Roche	xCELLigence (RT-CES)	Cell adhesion, proliferation, cytotoxicity, receptor-mediated signaling, barrier function, immune-cell signaling, cell migration, and invasion	[170][171][140]
MDS Sciex	Cellkey	Cell adhesion, proliferation, receptor-mediated signaling	[172][173]

Table 1.3 – Commercialized impedance based biosensors.

In Fig.1.16, we present several applications of ECIS in drug screening studies, which are critical in the context of personalized medicine. For example, it is important to understand the mechanism of action of a drug before the development of effective treatment for various health problems such as cancer. Hence, ECIS appears to be a helpful tool to analyze treatment responses in *in vitro* assays using cells extracted from patients so that more effective treatments can be offered to patients.

1.4. Drug screening applications based on ECIS sensing

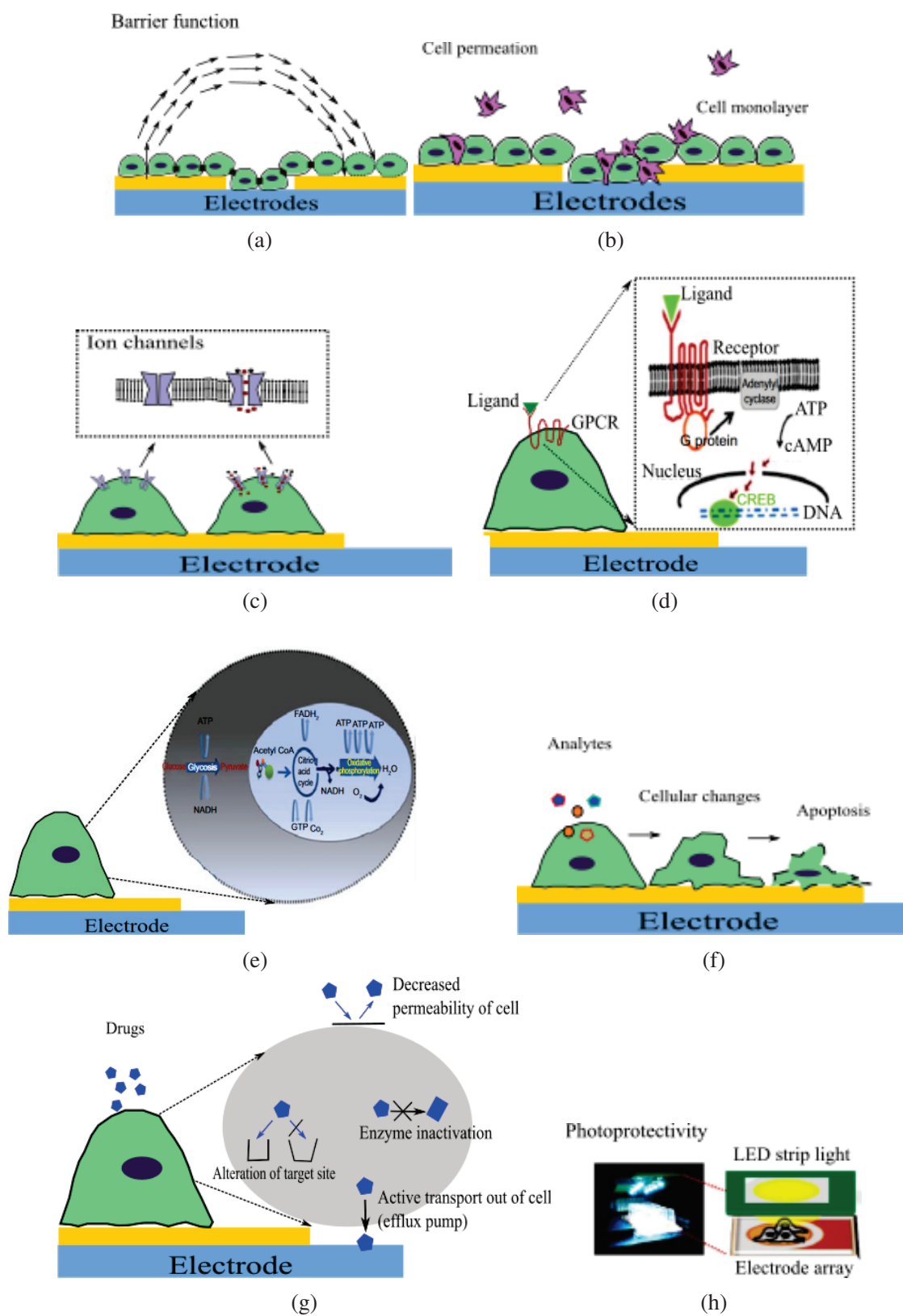


Figure 1.16 – Different applications of ECIS. (a) Barrier function, (b) Cancer metastasis, (c) Ion channel activity, (d) Cell signaling analysis, (e) Cell metabolism analysis, (f) Cytotoxicity screening, (g) Drug resistance and (h) Photoprotectivity. Figure adapted from figure 4 in [146]. Copyright 2006 by Dove Medical Press Ltd. Adapted with permission.

1.4.1 Barrier function activities

In vivo, barriers are formed by monolayers of epithelial cells, separating organs from their environment or endothelial cells, separating the blood stream from underlying tissues[174]. These cell layers play an important role regulating the free movement of molecules between different tissues and/or interstitial compartments. In many diseases as well as in inflammation, these barriers become compromised, and hence, measuring their permeability is of considerable interest to biologists. For example, Mei et al[175] examined the affinity modulation and homophilic⁶ adhesive properties of the Platelet Endothelial Cell Adhesion Molecule (PECAM-1) as well as endothelial monolayer resistance by ECIS. PECAM-1 is a cellular adhesion and signaling receptor, which mediate homophilic adhesion molecule interactions. These interactions are directly responsible for enhancing intercellular junctions, which provide steady-state barrier stability to endothelial cells and have the capability to recover vascular endothelium[146]. This study demonstrated that the homophilic binding affinity of PECAM-1 can be enhanced by IgD6-specific antibodies, which could be a novel therapeutic strategy for treating vascular endothelial injury-related disorders[175]. Similarly, Heijink et al.[176] investigated the junctional integrity of human bronchial epithelial cells using ECIS sensing and immunofluorescent staining. They observed that the addition of house dust mite (HDM) induced a rapid and substantial decrease in electrical resistance whereas the capacitance was not affected, indicating selective disruption of cell-to-cell adhesion.

Some authors have used ECIS to study barrier function in cancer metastasis. Metastasis occurs when cancer cells gain the ability to attack neighboring cells and tissues. Thus, it is important to understand the migratory, adhesive, and invasive capabilities of malignant tumors[146]. For instance, Ren et al.[93] used three different cell lines NIH3T3, MCF-7 and SKOV3 (two with low or no metastatic potential) versus metastatic ovarian cancer SKOV3 cells to carry out invasion assays on confluent monolayer of peritoneal mesothelial cells⁷ using the ECIS system. When metastatic cells invade the endothelial monolayer, they break down the barrier function of the endothelial cell layer, resulting in large drops in impedance, which is not visible with non-metastatic cells. Their work demonstrated that the measured resistance changes reflect the ability of cells to affect cell junctions and penetrate monolayer peritoneal mesothelial cells, which reflects the metastatic potential of the cells[93]. Likewise, Kuo et al.[177] studied the invasive behavior of human breast carcinoma cell lines by electrical impedance measurements. They monitored the real-time invasion of human breast carcinoma cell lines (MDA-MB-435 cells) to human umbilical vein endothelial cells (HUVECs). In their work, MDA-MB-435 cells pretreated with transforming growth factor TGF- β reduced the intact HUVEC monolayer resistance. They observed a change in impedance at 4 h when the tumor cells first attached to the HUVECs. As they then invaded through the HUVEC monolayer, there was a breakdown in the cell-cell contact of the monolayer leading to a fast decrease of impedance. Moreover, they elucidated that TGF- β would induce CD44⁸ cleavage on the cell surface and this enhanced the migration and invasiveness of the MDA-MB-435 cells[177].

1.4.2 Ion channel activities

From a drug discovery point of view, ion channels are very interesting and challenging targets. They play a central role in human physiology by helping regulate cellular ion homeostasis, shaping the electrical activity of nerve and muscle cells, and controlling the release of transmitters and hormones[178]. Electrical impedance has been utilized as tool for monitoring ion channel activities in the cell membrane. For example, Marimuthu et al.[179] found several possible mechanisms by which fibroblast cells (L929) oscillate during their culture period using ECIS sensing. The possible mechanisms involved in L929 oscillation were the

⁶That reacts only with a specific antigen

⁷Cells that line the body's serous cavities and internal organs

⁸Cell surface glycoprotein associated with various adhesion-dependent cellular processes including cell migration, tumor cell metastasis and invasion[66]

1.4. Drug screening applications based on ECIS sensing

periodic extension and contraction of lamellipodia followed by blebbing⁹, which is produced by signals from the actomyosin complex initiated by connexin hemichannel opening and adenosine triphosphate (ATP) release. They applied the connexin hemichannel inhibitor, flufenamic acid, then the hindrance of ATP release and calcium transients were analyzed to elucidate their hypothesis. As for Han et al.[180], they developed a micro electrical impedance spectroscopy system to differentiate ion channel activities of bovine chromaffin cells. They found differences in the magnitude and the phase impedances between cells with K⁺ and Ca²⁺ channels blocked and unblocked chromaffin cells. This demonstrated that positive/negative information of ion channel blockage can be distinguished using impedance sensing.

1.4.3 Cell signaling

Cell-signaling mechanisms correspond to molecular events activated within cells to mediate growth, proliferation, differentiation, and survival. Usually, regulatory pathways are activated by extracellular factors such as hormones, growth factors or cytokines[181]. These extracellular factors activate intracellular cascades of protein networks within the cell to transmit the signal. Most diseases present aberrations of cell-signaling processes and the compounds that target disease-specific alterations of cell-signaling mechanisms are considered interesting compounds for future therapies[181]. For example, Huang et al.[182] investigated the hypothesis that the signals of Lysophosphatidylcholine (LPC), which is a bioactive proinflammatory lipid that can be generated by pathological activities, increase endothelial permeability. In this study, when human dermal microvascular cells and bovine pulmonary microvascular cells were treated with LPC, the transendothelial electrical resistance decreased whereas the endothelial permeability increased. They found that LPC stimulation directly impairs the endothelial barrier function that is sensitive to albumin concentration. This LPC-induced barrier dysfunction was dependent, at least in part, on cross talk of the phosphotransferase PKC α and RhoA¹⁰ signals. Furthermore, Sawhney et al.[183] studied multiple cell signaling mechanisms regulating cell adhesion functions in human colon cancer cells (HCT116) by cell motility measurements using ECIS. Attachment and movement of the cells on the electrode changed the flow of the current, resulting in fluctuations in the electrode resistance and capacitance. These cellular movements were called micromotion and were a measure of the motile ability of the cell being examined. Moreover, by inhibition of different phosphorylation sites of S6K¹¹ with MEK¹² inhibitors, bisindolylmaleimide¹³ and rapamycin¹⁴, they showed for the first time that autocrine TGF α ¹⁵ regulates cell adhesion function by multiple signaling pathways via specific phosphorylation sites of S6K in cancer cells.

1.4.4 Cell metabolism

With the help of bioimpedance measurements, metabolism studies are providing a more physiologically relevant model of several types of cellular metabolism, and such ECIS systems can help to identify drugs with high potential in preclinical novel drug development[146]. General characteristics of cell metabolic activities are the uptake of metabolites, pathways regulating metabolisms in cells, energy metabolism, and elimination of waste acid and byproducts. Park et al.[184] used impedance measurements to distinguish normal mouse fibroblasts cells (NIH3T3) from NIH3T3 transformed with a constitutively active chemokine receptor, CXCR2. This receptor is a member of the G-protein coupled receptor (GPCR) family, which is

⁹The formation of irregular bulge in the plasma membrane of a cell

¹⁰RhoA: Type of GTPases known as molecular switches that control a wide variety of signal transduction pathways

¹¹S6K : Ribosomal protein S6 kinase

¹²MEK : Mitogen-activated protein kinase kinase enzymes

¹³Protein kinase C (PKC) inhibitor

¹⁴Macrolide immunosuppressant

¹⁵TGF α : Transforming growth factor α

normally involved in cellular activation and migration. They found that ECIS is sensitive enough to distinguish between transformed and untransformed cells. Both the resistance and reactance of transformed cells increased more rapidly and peaked higher. Moreover, they observed that the increase in the impedance fluctuations was also consistent with increased micromotility associated with transformed cells. These microfluctuations were the result of cytoskeletal changes reflecting increased motility[184]. This demonstrates that ECIS could allow the assessment of potential anti-cancer or anti-transforming drugs that uniquely affect transformed cells with minimal effects on non-transformed cells. In another study with neonatal Sprague Dawley rat renal cells, Hu et al.[185] combined ECIS with a light addressable potentiometric sensor to simultaneously detect the change of cell electrical impedance and extracellular acidification, which could be used for monitoring and analyzing the correlation between cell growth status and cell energy metabolism status in a noninvasive and label-free way.

1.4.5 Cytotoxicity and drug resistance

In the literature, electrical impedance has been used to evaluate in real-time cell movement morphological changes and functional alterations when exposed to harmful substances. For example, we can find in the literature studies about detection of toxic compounds, such as the detergents Tween 20, benzalkonium chloride (BAK), Triton X100 and sodium lauryl sulfate on WI-38/VA13 fibroblastic and MDCK epithelial cells[186]. Keese et al.[186] demonstrated that analysis of these cytotoxicity measurements can correctly rank the different detergents according to their established *in vivo* toxicity. Other substances, such as cadmium chloride (CdCl_2), sodium arsenate (Na_2HAsO_4), mercury chloride (HgCl_2), 1,3,5-trinitrobenzene (TNB) have also been tested on fibroblastic V79 cells by Xiao et al.[187]. In their study, they showed that the exposure time to the different toxicants made the cells detach from the working electrode leading to a gradual decrease in capacitance. Moreover, their inhibition assays revealed that the half inhibition concentration in real time agreed with that of the standard neutral red uptake assay, which provides a quantitative estimation of the number of viable cells in a culture[187]. Arndt et al.[188] monitored porcine brain capillary endothelial cells (PBCECs) exposed to cycloheximide (CHX), which is an antibiotic produced by *S. griseus*. They observed that disassembly of barrier-forming tight junctions preceded changes in cell–substrate contacts and correlated strongly with the time course of protease activation. All the aforementioned works studied how cell attachment and spreading are affected by different toxin concentrations, varying inoculation and exposure time. In general, a pronounced resistance change corresponding to different toxin concentrations was observed with great reproducibility[189].

Opp et al.[190] examined dose-dependent responses for cytochalasin B, known to disrupt actin filaments, on human umbilical vein endothelial cells (HUVECS) and they studied how the cellular morphology was affected. They observed that the cytochalasin B caused a decrease of cell-to-cell junction resistance, reduction in micromotion and increase in membrane capacitance at concentrations lower than $0.1 \mu\text{M}$ [190]. Yeon et al.[191] demonstrated a microfabricated cell chip to monitor cell growth and cytotoxic effects of human hepatocellular carcinoma cells (HepG2) after treatments with the chemotherapeutic agents, tamoxifen and menadione. Tamoxifen induces apoptosis in human malignant cell lines, especially in hepatocytes[192]. Menadione produces superoxide radicals and induces apoptosis[193]. In their study, when the concentration of the two toxicants increased the impedance decreased, which was associated with damaged cells detaching from the gold electrode surface[191]. Similarly, Adcock et al.[194] used impedance sensing for screening effective anticancer drugs, such as Docetaxel, Carboplatin, Abiraterone acetate, Mitoxantrone and Sunitinib Malate to different types of prostate cancers (DU145, LNCaP and PC-3). Each drug works on the cancer cells via a different mechanism of action. Docetaxel prevents the de-polymerization of microtubules required for mitosis, which induces cell apoptosis. Carboplatin undergoes activation inside cells and forms reactive platinum complexes that cause cross-linkage of DNA molecules within the cell. Abiraterone acetate induces a significant loss of androgen production in the peripheral organs, particularly adrenal androgens. Mitoxantrone causes DNA fragmentation and inhibits the enzyme topoisomerase II, which is essential

for DNA replication, transcription, and repair. Sunitinib malate inhibits multiple receptor tyrosine kinases (RTKs)[194]. In this study, they noted that all the tested cell lines did not draw them to the same conclusion for the drug combination treatments. For instance, the reduction in impedance for the PC-3 cell line was greater in the presence of the combined drugs docetaxel with sunitinib malate whereas the signal for DU145 cells was not affected by the same combination. These results demonstrated that electrical impedance experiments can be used to identify drug combinations that can effectively be used to treat prostate cancer[194]. Furthermore, Xie et al.[195] investigated the cytotoxic effects of several anticancer drugs, such as carboplatin, (CDP), the antimetabolite 5-fluorouracil (5-FU) and the DNA alkylating agent cyclophosphamide (CTX) on human proximal tubular epithelial cells (HK2). They found that the impedance measurements with CTX displayed a different cytotoxic time-response pattern compared to those of CDP and 5-FU. They observed that the cellular impedance drastically decreased a few hours after exposure to all concentrations of CTX and then it slowly increased to a level which diminished with increasing concentrations. According to them, the drug specific observations illustrate the advantage of the continuous monitoring with ECIS assays, as the standard end-point measurements would not readily detect intermediate time events such as significant decrease induced by CTX or the subsequent recovery of the HK2 cells after the initial decrease[195].

Furthermore, ECIS has been utilized by Eker et al[196] to distinguish drug resistant breast cancer cells (MCF-7 DOX) from their parental cells (MCF-7 WT) by studying their inherent dielectric properties using electrical equivalent circuit modeling. They demonstrated that drug resistant breast cancer cells could be distinguished from their parental cell population based on the differences in the values of extracellular resistance. In addition, the effect of doxorubicin, an anti-tumor antibiotic, was investigated over a wide frequency range and revealed sharp differences in the temporal evolution of cellular changes between the two phenotypes. According to them, this is the first study that differentiates drug resistant breast cancer cells from their parental cells based on their dielectric properties and investigates their drug response at different stages of the disease using impedance screening at different frequencies[196].

1.4.6 Photodamaging and Photoprotective effects

Besides drugs and chemical compounds, scientists have been interested in studying the effect of light radiation, which is the primary cause of skin photo-oxidative damage, leading to chronic skin conditions such as premature aging of the skin, melanomas, and non-melanoma skin cancers[197, 198]. Due to the presence of chromophores in the skin, intense light from the sun can penetrate skin cells, causing cellular damage and mitochondrial oxidative stress, which is the principal responsible of cellular dysfunction and even cell death. Therefore, the oxidative stress pathways are interesting targets for the development of new therapeutic drugs for photooxidative diseases and for exploration of photooxidative and protective mechanisms[146]. For instance, Bennet et al.[199] used the ECIS system for the study of continuous light radiation toxicity and protective effects of enhanced nanoparticles containing Apple Peel Ethanolic Extract (nano-APETE) to inhibit the production of free radicals on human dermal fibroblast, neonatal cells (HDFn). In this study, the ECIS data of cellular activities in response to photooxidative stress correlated well with data from cell viability assay such as MTT assay. Moreover, they found that among three different preparations of nano-APETE, the preparation with the lowest concentration showed small, spherical, monodispersed and uniform particles[199] with enriched antioxidant properties. This shows that the ECIS has potential to screen the photoprotective agents in early stages of drug discovery. Furthermore, Bennet et al.[200] demonstrated the usefulness of ECIS for the continuous measurement of different color light-induced effects on the response of retinal ganglion cells (RGC-5) that were exposed to protective drugs such as β -carotene, quercetin, agmatine, and glutathione. These measurements showed that ECIS could be used to evaluate different RGC-5 cell behaviors due to different color light-induced damage.

1.5 Conclusions

We have seen that personalized medicine seeks the right drug at the right dose, with minimal or no toxicity, for the right patient at the right time[13]. This is particularly important in cancer therapy where clinicians want to avoid unnecessary toxicity and costs for patients who are unlikely to benefit from a treatment. This is why cell based assays using cells coming from patient biopsies are highly needed if more effective treatments want to be offered to patients. Electrical impedance measurements have emerged as an alternative technique to conventional label based methods to monitor cell activity. The applied AC signal is harmless to the cells and it does not adversely affect the physiology of the cells under study[80, 85, 86, 87] which makes it an attractive tool for label-free and real-time cell monitoring. However, one of the greatest challenges in drug screening of cancer biopsies is the small amount of available cells. A possible solution would be to work in a microfluidic environment in order to reduce sample volumes. The micrometer dimension conveniently matches with the size of typical biological cells, making microfluidics an ideal platform for cell studies. The miniaturization of an impedimetric platform brings some challenges, such as reducing the dimensions of the electrodes which induces high impedance that can affect the sensitivity of the measurements. Furthermore, if one wants to couple the impedance measurements with optical quantification, it is relevant to explore transparent electrodes, such as ITO IDEs in which cell morphology changes, due to cell adhesion, spreading, proliferation and chemosensitivity effects, can be monitored as if cells were proliferating on glass slides and complement the impedance data. Despite of this advantage over Au and other materials, ITO is less used as electrode material for ECIS applications. Probably due to the fact that it offers an electrical conductivity (10^4 S/cm) three orders of magnitude less than that of gold, which represents a significant limitation in a miniaturized impedance system. The objective of this thesis is to evaluate ITO as electrode material for ECIS experiments in the context of personalized medicine. First, we focus on understanding the relationship between the electrical components in the ECIS system and the sensitivity of the measurement. Then, we evaluate this material used in chemosensitivity assays with a chemotherapeutic agent on breast cancer cells. Finally, we study a possible strategy to enhance the sensitivity of ITO electrodes for ECIS experiments that can be coupled with optical quantification.

Bibliography

- [1] Personalized Medicine Coalition. *The Personalized Medicine Report: Opportunity, Challenges, and the Future*. URL: http://www.personalizedmedicinecoalition.org/Resources/The_Personalized_Medicine_Report_An_Annual_Overview_of_the_Field.
- [2] Sunil Mathur and Joseph Sutton. “Personalized medicine could transform healthcare (Review)”. In: *BIOMEDICAL REPORTS* 7.1 (2017), pp. 3–5. DOI: <https://doi.org/10.3892/br.2017.922>.
- [3] Ma Xiaomei and Yu Herbert. “Global Burden of Cancer”. In: *The yale journal of biology and medicine* 79.3-4 (2006), pp. 85–94.
- [4] The National Cancer Institute. *Cancer Statistics*. URL: <https://www.cancer.gov/about-cancer/understanding/statistics>.
- [5] American Society of Clinical Oncology (ASCO). *The Genetics of Cancer*. URL: <https://www.cancer.net/navigating-cancer-care/cancer-basics/genetics/genetics-cancer>.
- [6] Kriti Lew. *THE TRUTH ABOUT CANCER: Understanding and Fighting a Deadly Disease*. Berkeley Heights: Enslow Publishers, 2009.
- [7] Ada Hang-Heng Wong, Haoran Li, Yanwei Jia, Pui-In Mak, Rui Paulo da Silva Martins, Yan Liu, Chi Man Vong, Hang Cheong Wong, Pak Kin Wong, Haitao Wang, Heng Sun, and Chu-Xia Deng. “Drug screening of cancer cell lines and human primary tumors using droplet microfluidics”. In: *Scientific Reports* 7.9109 (2017), pp. 1–15. DOI: <https://doi.org/10.1038/s41598-017-08831-z>.
- [8] A. Urruticoechea, R. Alemany, J. Balart, A. Villanueva, F. Viñals, and G. Capellá. “Recent Advances in Cancer Therapy: An Overview”. In: *Current Pharmaceutical Design* 16.1 (2016), pp. 3–10. DOI: <https://doi.org/10.2174/138161210789941847>.
- [9] American Cancer Society. *The Costs of Cancer*. URL: <https://www.acscan.org/sites/default/files/Costs%20of%20Cancer%20-%20Final%20Web.pdf>.

BIBLIOGRAPHY

- [10] National Cancer Institute NIH. *Radiation Therapy Side Effects*. URL: <https://www.cancer.gov/about-cancer/treatment/types/radiation-therapy/side-effects>.
- [11] Caitriona Holohan, Sandra Van Schaeybroeck, Daniel B. Longley, and Patrick G/ Johnston. “Cancer drug resistance: an evolving paradigm”. In: 13.10 (2013), pp. 714–726. DOI: <https://doi.org/10.1038/nrc3599>.
- [12] Genevieve Housman, Shannon Byler, Sarah Heerboth, Karolina Lapinska, Mckenna Longacre, Nicole Snyder, and Sibaji Sarkar. “Drug Resistance in Cancer: An Overview”. In: *Cancers (Basels)* 6.3 (2014), pp. 1769–1792. DOI: <https://doi.org/10.3390/cancers6031769>.
- [13] Mukesh Verma. “Personalized Medicine and Cancer”. In: *Journal of Personalized Medicine* 2.1 (2010), pp. 1–14. DOI: <https://doi.org/10.3390/jpm2010001>.
- [14] Arran K. Turnbull. “Personalized medicine in cancer: where are we today?” In: *Future Oncology* 11.20 (2015), pp. 2795–2798. DOI: <https://doi.org/10.2217/fon.15.204>.
- [15] Michael F. Berger and Elaine R. Mardis. “The emerging clinical relevance of genomics in cancer medicine”. In: *Nature Reviews Clinical Oncology* 15 (2018), pp. 353–365. DOI: <https://doi.org/10.1038/s41571-018-0002-6>.
- [16] Heather E. Wheeler, Michael L. Maitland, M. Eileen Dolan, Nancy J. Cox, and Mark J. Ratain. “Cancer pharmacogenomics: strategies and challenges”. In: *Nature Reviews Genetics* 14.1 (2013), pp. 23–34. DOI: <https://doi.org/10.1038/nrg3352>.
- [17] U.S. Food and Drug Administration. *Table of Pharmacogenomic Biomarkers in Drug Labeling*. URL: <https://www.fda.gov/Drugs/ScienceResearch/ucm572698.htm>.
- [18] Yan V.Sun and Yi-Juan Hu. “Chapter Three - Integrative Analysis of Multi-omics Data for Discovery and Functional Studies of Complex Human Diseases”. In: *Advances in Genetics* 93 (2016), pp. 147–190. DOI: <https://doi.org/10.1016/bs.adgen.2015.11.004>.
- [19] Jennifer L. Spratlin, Natalie J. Serkova, and S. Gail Eckhardt. “Clinical Applications of Metabolomics in Oncology: A Review”. In: *Clinical Cancer Research* 15.2 (2009), pp. 431–440. DOI: <https://doi.org/10.1158/1078-0432.CCR-08-1059>.
- [20] Sybille Mazurek and Erich Eigenbrodt. “The tumor metabolome”. In: *Anticancer Research* 23.2A (2003), pp. 1149–1154.
- [21] Mirjana Rajer and Marko Kmet. “Quantitative analysis of fine needle aspiration biopsy samples”. In: *Radiology and Oncology* 39.4 (2005), pp. 269–272.
- [22] Meghaan M. Ferreira, Vishnu C. Ramani, and Stefanie S. Jeffrey. “Circulating tumor cell technologies”. In: *Molecular Oncology* 10.3 (2016), pp. 374–394. DOI: <https://doi.org/10.1016/j.molonc.2016.01.007>.

BIBLIOGRAPHY

- [23] Jian Chen, Chengcheng Xue, Yang Zhao, Deyong Chen, Min-Hsien Wu, and Junbo Wang. “Microfluidic Impedance Flow Cytometry Enabling High-Throughput Single-Cell Electrical Property Characterization”. In: *International Journal of Molecular Sciences* 16.5 (2015), pp. 9804–9830. DOI: <https://doi.org/10.3390/ijms16059804>.
- [24] Christopher E. Simsa and Nancy L. Allbritton. “Analysis of single mammalian cells on-chip”. In: *Lab on a Chip* 7.4 (2007), pp. 423–740. DOI: <https://doi.org/10.1039/b615235j>.
- [25] Dino Di Carlo and Luke P. Lee. “Dynamic Single-Cell Analysis for Quantitative Biology”. In: *Analytical Chemistry* 78.23 (2006), pp. 7918–7925. DOI: <https://doi.org/10.1021/ac069490p>.
- [26] Karen C. Cheung, Marco di Berardino, Grit Schade-Kampmann, Monika Hebeisen, Arkadiusz Pierzchalski, Jozsef Bocsi, Anja Mitag, and Attila Tarnok. “Microfluidic Impedance-Based Flow Cytometry”. In: *Cytometry PART A: Journal of the International Society for Advancement of Cytometry* 77.7 (2010), pp. 648–666. DOI: <https://doi.org/10.1002/cyto.a.20910>.
- [27] Hyun Soo Kim, Timothy P. Devarenne, and Arum Han. “A high-throughput microfluidic single-cell screening platform capable of selective cell extraction”. In: *Lab on Chip* 15.11 (2015), pp. 2467–2475. DOI: <https://doi.org/10.1039/c4lc01316f>.
- [28] Z. Xu, Y. Gao, Y. Hao, E. Li, Y. Wang, J. Zhang, W. Wang, Z. Gao, and Q. Wang. “Application of a microfluidic chip-based 3D co-culture to test drug sensitivity for individualized treatment of lung cancer”. In: *Biomaterials* 34.16 (2013), pp. 4109–4117. DOI: <https://doi.org/10.1016/j.biomaterials.2013.02.045>.
- [29] Cancer Resaerch UK. *Cancer Statistics for the UK*. URL: <https://www.cancerresearchuk.org/health-professional/cancer-statistics-for-the-uk#heading-One>.
- [30] Terry Riss. *SELECTING CELL-BASED ASSAYS FOR DRUG DISCOVERY SCREENING*. URL: https://beta-static.fishersci.com/content/dam/fishersci/en_US/documents/programs/scientific/brochures-and-catalogs/publications/promega-selecting-cell-based-assays-drug-screening-publication.pdf.
- [31] Isaac M. Adjei and Sharma Blanka. “Modulation of the Tumor Microenvironment for Cancer Treatment: A Biomaterials Approach”. In: *Journal of functional biomaterials* 6.1 (2015), pp. 81–103. DOI: <https://doi.org/10.3390/jfb6010081>.
- [32] Sung-Yup Cho, Wonyoung Kang, Jee Yun Han, Seoyeon Min, Jinjoo Kang, Ahra Lee, Jee Young Kwon, Charles Lee1, and Hansoo Park. “An Integrative Approach to Precision Cancer Medicine Using Patient-Derived Xenografts”. In: *Molecules and Cells* 39.2 (2016), pp. 77–86. DOI: <https://doi.org/10.14348/molcells.2016.2350>.
- [33] Titia G. Meijer, Kishan AT. Naipal, Agnes Jager, and Dik C. van Gent. “Ex vivo tumor culture systems for functional drug testing and therapy response prediction”. In: *Future Science OA* 3.2 (2017), pp. 1–13. DOI: <https://doi.org/10.4155/fsoa-2017-0003>.

BIBLIOGRAPHY

- [34] Frank A. Alexander, Dorielle Tucker Price, and Shekhar Bhansali. “From Cellular Cultures to Cellular Spheroids: Is Impedance Spectroscopy a Viable Tool for Monitoring Multicellular Spheroid (MCS) Drug Models?” In: *IEEE Reviews in Biomedical Engineering* 6 (2012), pp. 63–76. DOI: <https://doi.org/10.1109/RBME.2012.2222023>.
- [35] Douglas Hanahan and Robert A Weinberg. “The Hallmarks of Cancer”. In: *Cell* 100.1 (2000), pp. 57–70. DOI: [https://doi.org/10.1016/S0092-8674\(00\)81683-9](https://doi.org/10.1016/S0092-8674(00)81683-9).
- [36] M. Hidalgo, F. Amant, A. V. Biankin, E. Budinská, A. T. Byrne, C. Caldas, R. B. Clarke, S. de Jong, J. Jonkers, G. M. Maeldansmo S. Roman-Roman, J. Seoane, L. Trusolino, and A. Villanueva. “Patient-derived xenograft models: an emerging platform for translational cancer research”. In: *Cancer Discovery* 4.9 (2014), pp. 998–1013. DOI: <https://doi.org/10.1158/2159-8290.CD-14-0001>.
- [37] Y. S. DeRose, G. Wang, Y. C. Lin, P. S. Bernard, S. S. Buys, M. T. Ebbert, R. Factor, C. Matsen, B. A. Milash, E. Nelson, L. Neumayer, R. L. Randall, I. J. Stijleman, B. E. Welm, and A. L. Welm. “Tumor grafts derived from women with breast cancer authentically reflect tumor pathology, growth, metastasis and disease outcomes”. In: *Nature medicine* 17.11 (2011), pp. 1514–1520. DOI: <https://doi.org/10.1038/nm.2454>.
- [38] M. Hidalgo, E. Bruckheimer, N. V. Rajeshkumar, I. Garrido-Laguna, E. De Oliveira, B. Rubio-Viqueira, S. Strawn, M. J. Wick, J. Martell, and D. Sidransky. “A pilot clinical study of treatment guided by personalized tumorgrafts in patients with advanced cancer”. In: *Molecular cancer therapeutics* 10.8 (2011), pp. 1311–1316. DOI: <https://doi.org/10.1158/1535-7163.MCT-11-0233>.
- [39] M. G. Lawrence, D. W. Pook, H. Wang, L. H. Porter, M. Frydenberg, J. Kourambas, S. Appu qnd C. Poole, E. K. Beardsley, A. Ryan, S. Norden, M. M. Papargiris, G. P. Risbridger, and R. A. Taylor. “Establishment of primary patient-derived xenografts of palliative TURP specimens to study castrate-resistant prostate cancer”. In: 75.13 (2015), pp. 1475–1483. DOI: <https://doi.org/10.1002/pros.23039>.
- [40] M. Wodnicka, R. D. Guarino, J. J. Hemperly, M. R. Timmins, D. Stitt, and J. B. Pitner. “Novel fluorescent technology platform for high throughput cytotoxicity and proliferation assays”. In: *Journal of biomolecular screening* 5.3 (2000), pp. 141–152. DOI: <https://doi.org/10.1177/108705710000500306>.
- [41] John O’Brien, Ian Wilson, Terry Orton, and François Pognan. “Investigation of the Alamar Blue (resazurin) fluorescent dye for the assessment of mammalian cell cytotoxicity”. In: *European Journal of Biochemistry* 267.17 (2000), pp. 5421–5426. DOI: <https://doi.org/10.1046/j.1432-1327.2000.01606.x>.
- [42] Marine Ginouves, Bernard Carme, Pierre Couppie, and Ghislaine Prevot. “Comparison of Tetrazolium Salt Assays for Evaluation of Drug Activity against *Leishmania* spp”. In: *Journal of Clinical Microbiology* 52.6 (2014), pp. 131–2138. DOI: <https://doi.org/10.1128/JCM.00201-14/>.
- [43] Austin M. Derfus, Warren C. W. Chan, and Sangeeta N. Bhatia. “Probing the Cytotoxicity of Semiconductor Quantum Dots”. In: *NanoLetters* 4.1 (2004), pp. 11–18. DOI: <https://doi.org/10.1021/nl0347334>.

BIBLIOGRAPHY

- [44] Gregor Malich, Boban Markovic, and Chris Winder. “The sensitivity and specificity of the MTS tetrazolium assay for detecting the in vitro cytotoxicity of 20 chemicals using human cell lines”. In: *Toxicology* 124.3 (1997), pp. 179–192. DOI: [https://doi.org/10.1016/S0300-483X\(97\)00151-0](https://doi.org/10.1016/S0300-483X(97)00151-0).
- [45] François-Xavier Mahon, Francis Belloc, Valérie Lagarde, Claudine Chollet, François Moreau-Gaudry, Josy Reiffers, John M. Goldman, and Junia V. Melo. “MDR1 gene over-expression confers resistance to imatinib mesylate in leukemia cell line models”. In: *Blood* 101.6 (2003), pp. 2368–2373. DOI: <https://doi.org/10.1182/blood.V101.6.2368>.
- [46] Ru Zang, Ding Li, I-Ching Tang, Jufang Wang, and Shang-Tian Yang. “Cell-Based Assays in High-Throughput Screening for Drug Discovery”. In: *International Journal of Biotechnology for Wellness Industries* 1 (2012), pp. 31–51.
- [47] Kyle Durick and Paul Negulescu. “Cellular biosensors for drug discovery”. In: *Biosensors and Bioelectronics* 16.7-8 (2001), pp. 587–592. DOI: [https://doi.org/10.1016/S0956-5663\(01\)00173-7](https://doi.org/10.1016/S0956-5663(01)00173-7).
- [48] Melissa L. Sykes and Vicky M. Avery. “A luciferase based viability assay for ATP detection in 384-well format for high throughput whole cell screening of *Trypanosoma brucei brucei* bloodstream form strain 427”. In: *Parasit Vectors* 2.54 (2009), pp. 1–12. DOI: <https://doi.org/10.1186/1756-3305-2-54>.
- [49] Promega. *Designing a Bioluminescent Reporter Assay - Choosing Your Experimental Reporter*. URL: https://france.promega.com/en/resources/pubhub/tpub_176-designing-a-bioluminescent-reporter-assay-choosing-your-experimental-reporter/.
- [50] Yusuke Inoue, Arinobu Tojo, Rieko Sekine, Yasushi Soda, Seiichiro Kobayashi, Akiko Nomura, Kiyoko Izawa, Toshio Kitamura, Toshiyuki Okubo, and Kuni Ohtomo. “In vitro validation of bioluminescent monitoring of disease progression and therapeutic response in leukaemia model animals”. In: *European Journal of Nuclear Medicine and Molecular Imaging* 33.5 (2006), pp. 557–565. DOI: <https://doi.org/10.1007/s00259-005-0048-4>.
- [51] Paul A. Clemons, Nicola J. Tolliday, and Bridget K. Wagner. *Cell-Based Assays for High-Throughput Screening: Methods and Protocols*. Totowa, NJ: Humana Press, 2009.
- [52] John F. Eccleston, Jonathan P. Hutchinson, and David M. Jameson. “Fluorescence-Based Assays”. In: *Progress in Medicinal Chemistry* 43 (2005), pp. 19–48. DOI: [https://doi.org/10.1016/S0079-6468\(05\)43002-7](https://doi.org/10.1016/S0079-6468(05)43002-7).
- [53] Laura E. Edgington-Mitchell and Matthew Bogyo. “Detection of Active Caspases During Apoptosis Using Fluorescent Activity-Based Probes”. In: *Methods in Molecular Biology* 1419 (2016), pp. 27–39. DOI: https://doi.org/10.1007/978-1-4939-3581-9_3.
- [54] BD Biosciences. *Caspase-3 Activation: An Indicator of Apoptosis in Image-Based Assays*. URL: https://www.bdbiosciences.com/documents/Bioimaging_AppNote_Apoptosis.pdf.

BIBLIOGRAPHY

- [55] Francis Ka-Ming Chan, Kenta Moriwaki, and Maria Jose De Rosa. "Detection of Necrosis by Release of Lactate Dehydrogenase (LDH) Activity". In: *Methods in Molecular Biology* 979 (2013), pp. 65–70. DOI: https://doi.org/10.1007/978-1-62703-290-2_7.
- [56] Binghe Wang and Eric V. Anslyn. *Chemosensors: Principles, Strategies, and Applications*. Hoboken, New Jersey: Wiley, 2011.
- [57] Xiaonan Lu. *Food Chemistry, Function and Analysis. Sensing Techniques for Food Safety and Quality Control*. United Kingdom: Royal society of Chemistry, 2017.
- [58] Jason Niehaus. *Plasmids 101: Luciferase*. URL: <https://blog.addgene.org/plasmids-101-luciferase>.
- [59] Richard B. Thompson. *Fluorescence Sensors and Biosensors*. Boca raton, Florida: Taylor and Francis, 2005.
- [60] Simone Kunzelmann, Claudia Solscheid, and Martin R. Webb. *Fluorescent Biosensors: Design and Application to Motor Proteins*. Basel: Springer, 2014.
- [61] Brian T Cunningham and Lance G Laing. "Advantages and application of label-free detection assays in drug screening". In: *Expert Opinion on Drug Discovery* 3.8 (2008), pp. 891–901. DOI: <https://doi.org/10.1517/17460441.3.8.891>.
- [62] Ye Fang. "Non-Invasive Optical Biosensor for Probing Cell Signaling". In: *Sensors (basel)* 7.10 (2007), pp. 2316–2329. DOI: <https://doi.org/10.3390/s7102316>.
- [63] TMR - Research Reports. *Surface Acoustic Wave Sensors Market Gaining Importance due to Increase its Applications in Safety Monitoring and Communication Fields*. URL: <https://www.openpr.com/news/369699/Surface-Acoustic-Wave-Sensors-Market-Gaining-Importance-due-to-Increase-its-Applications-in-Safety-Monitoring-and-Communication-Fields.html>.
- [64] Yuhki Yanase, Takaaki Hiragun, Kaori Ishii, Tomoko Kawaguchi, Tetsuji Yanase, Mikio Kawai, Kenji Sakamoto, and Michihiro Hide. "Surface Plasmon Resonance for Cell-Based Clinical Diagnosis". In: *Sensors* 14.3 (2014), pp. 4948–4959. DOI: <https://doi.org/10.3390/s140304948>.
- [65] Larisa-Emilia Cheran, Shilin Cheung, Arij Al Chawaf, Jonathan S. Ellis, Denise D. Belsham, William A. MacKay, David Lovejoy, and Michael Thompson. "Label-free detection of neuron–drug interactions using acoustic and Kelvin vibrational fields". In: *The Analyst* 132.3 (2007), pp. 242–255. DOI: <https://doi.org/10.1039/b615476j>.
- [66] Jongin Hong, Karthikeyan Kandasamy, Mohana Marimuthu, Cheol Soo Choi, and Sanghyo Kim. "Electrical cell-substrate impedance sensing as a non-invasive tool for cancer cell study". In: *The Analyst* 136.2 (2011), pp. 237–245. DOI: <https://doi.org/10.1039/c0an00560f>.
- [67] Keith E. Herold and Avraham Rasooly. *Biosensors and Molecular Technologies for Cancer Diagnostics*. Boca Raton, FL: CRC Press, 2012.

BIBLIOGRAPHY

- [68] J.Vörös, R.Graf, G.L.Kenausis, A.Bruinink, J.Mayer, M.Textor, E.Wintermantel, and N.D.Spencer. “Feasibility study of an online toxicological sensor based on the optical waveguide technique”. In: *Biosensors and Bioelectronics* 15.9-10 (2000), pp. 423–429. DOI: [https://doi.org/10.1016/S0956-5663\(00\)00102-0](https://doi.org/10.1016/S0956-5663(00)00102-0).
- [69] P. Li B. T. Cunningham, S. Schulz, B. Lin, C. Baird, J. Gerstenmaier, C. Genick, F. Wang, E. Fine, and L. Laing. “Label-free assays on the BIND system”. In: *Journal of biomolecular screening* 9.6 (2004), pp. 481–490. DOI: <https://doi.org/10.1177/1087057104267604>.
- [70] Natalya Zaytseva, William Miller, Vasily Goral, Jerry Hepburn, and Ye Fang. “Microfluidic resonant waveguide grating biosensor system for whole cell sensing”. In: *Applied Physics Letters* 98.1 (2011), pp. 1–3. DOI: <https://doi.org/10.1063/1.3582611>.
- [71] Vasily Goral, Qi Wu, Haiyan Sun, and Ye Fang. “Label-free optical biosensor with microfluidics for sensing ligand-directed functional selectivity on trafficking of thrombin receptor”. In: *FEBS Letters* 585.7 (2011), pp. 1054–1060. DOI: <https://doi.org/10.1016/j.febslet.2011.03.003>.
- [72] Adnan Mujahid and Franz L. Dickert. “Surface Acoustic Wave (SAW) for Chemical Sensing Applications of Recognition Layers”. In: *Sensors(basel)* 17.12 (2017), pp. 1–26. DOI: <https://doi.org/10.3390/s17122716>.
- [73] Li Fang, Qin Lifeng, Wu Huiyan, and Wang Qing-Ming. “Love mode surface acoustic wave sensors for cellular toxicity sensing”. In: *2014 IEEE International Ultrasonics Symposium*. IEEE, Oct. 2014, pp. 2548–2551.
- [74] Konstantinos Mitsakakis and Electra Gizeli. “Detection of multiple cardiac markers with an integrated acoustic platform for cardiovascular risk assessment”. In: *Analytica Chimica Acta* 699.1 (2011), pp. 1–5. DOI: <https://doi.org/10.1016/j.aca.2011.05.016>.
- [75] Hoang Hiep Nguyen, Jeho Park, Sebyung Kang, and Moonil Kim. “Surface Plasmon Resonance: A Versatile Technique for Biosensor Applications”. In: *Sensors* 15.5 (2015), pp. 10481–10510. DOI: <https://doi.org/10.3390/s150510481>.
- [76] Atsushi Kosaihiro and Toshihiro Ona. “Rapid and quantitative method for evaluating the personal therapeutic potential of cancer drugs”. In: *Analytical and bioanalytical chemistry* 391.5 (2008), pp. 1889–1897. DOI: <https://doi.org/10.1007/s00216-008-2152-3>.
- [77] Jean-Sebastien Maltais, Jean-Bernard Denault, Louis Gendron, and Michel Grandbois. “Label-free monitoring of apoptosis by surface plasmon resonance detection of morphological changes”. In: *Apoptosis* 17.8 (2012), pp. 916–925. DOI: <https://doi.org/10.1007/s10495-012-0737-y>.
- [78] Kin Fong Lei, Wing Cheung Law, Yick-Keung Suen, Wen J. Li, Ho Pui Ho, Chinlon Lin, and Siu-Kai Kong. “Bio-molecular and cellular detection using SPR sensor and all-transparent microfluidic platform”. In: *5th IEEE Conference on Nanotechnology*. IEEE, July 2005, pp. 490–496.

BIBLIOGRAPHY

- [79] Onur Tokel, Umit Hakan Yildiz, Fatih Inci, Naside Gozde Durmus, Okan Oner Ekiz, Burak Turker, Can Cetin, Shruthi Rao, Kaushik Sridhar, Nalini Natarajan, Hadi Shafiee, Aykutlu Dana, and Utkan Demirci. “Portable Microfluidic Integrated Plasmonic Platform for Pathogen Detection”. In: *Scientific Reports* 5.9152 (2015), pp. 1–9. DOI: <https://doi.org/10.1038/srep09152>.
- [80] Biao Xi, Naichen Yu, Xiaobo Wang, Xiao Xu, and Yama A. Abassi. “The application of cell-based label-free technology in drug discovery”. In: *Biotechnology Journal* 3.4 (2008), pp. 484–495. DOI: <https://doi.org/10.1002/biot.200800020>.
- [81] Gang Wang, Abiche H Dewilde, Jianping Zhang, Anoop Pal, Malavika Vashist, Dhimiter Bello, Kenneth A Marx, Susan J Braunhut, and Joel M Therrien. “A living cell quartz crystal microbalance biosensor for continuous monitoring of cytotoxic responses of macrophages to single-walled carbon nanotubes”. In: *Particle and Fibre Toxicology* 8.4 (2011), pp. 1–17. DOI: <https://doi.org/10.1186/1743-8977-8-4>.
- [82] Julien Fatisson, Fereshteh Azari, and Nathalie Tufenkji. “Real-time QCM-D monitoring of cellular responses to different cytomorphic agents”. In: *Biosensors and Bioelectronics* 26.7 (2011), pp. 3207–3212. DOI: <https://doi.org/10.1016/j.bios.2010.12.027>.
- [83] Jan-W. Thies, Bettina Thürmann, Anke Vierheller, and Andreas Dietzel. “Particle-Based Microfluidic Quartz Crystal Microbalance (QCM) Biosensing Utilizing Mass Amplification and Magnetic Bead Convection”. In: *Micromachines* 9.4 (2018), pp. 1–15. DOI: <https://doi.org/10.3390/mi9040194>.
- [84] Wenyan Tao Qingji Xie, Hairui Wang, Shanming Ke, Peng Lin, and Xierong Zeng. “Integration of a Miniature Quartz Crystal Microbalance with a Microfluidic Chip for Amyloid Beta-A β 42 Quantitation”. In: *Sensors (Basel)* 15.10 (2015), pp. 25746–25760. DOI: <https://doi.org/10.3390/s151025746>.
- [85] Weng G. Jiang. *Electric Cell-Substrate Impedance Sensing and Cancer Metastasis*. Dordrecht Heidelberg New York London: Springer, 1997.
- [86] Ivar Giaever and C. R. Keese. “Monitoring fibroblast behavior in tissue culture with an applied electric field”. In: *PNAS* 81.12 (1984), pp. 3761–3764. DOI: <https://doi.org/10.1073/pnas.81.12.3761>.
- [87] Leena Jaatinen, Eleanore Young, Jari Hyttinen, János Voros, Tomaso Zambelli, and László Demkó. “Quantifying the effect of electric current on cell adhesion studied by single-cell force spectroscopy”. In: *Biointerphases* 11.1 (2016), p. 011004. DOI: <https://doi.org/10.1116/1.4940214>.
- [88] Tien Anh Nguyen, Tsung-I Yin, Diego Reyes, and Gerald A. Urban. “Microfluidic Chip with Integrated Electrical Cell-Impedance Sensing for Monitoring Single Cancer Cell Migration in Three-Dimensional Matrixes”. In: *Analytical chemistry* 85.22 (2013), pp. 11068–11076. DOI: <https://doi.org/10.1021/ac402761s>.
- [89] M. Evander, A. J. Ricco, J. Morser, G. T. Kovacs, L. L. Leung, and L. Giovannardi. “Microfluidic impedance cytometer for platelet analysis”. In: *Lab on a Chip* 13.4 (2013), pp. 722–729. DOI: <https://doi.org/10.1039/c2lc40896a>.

BIBLIOGRAPHY

- [90] S. Reitingner, J. Wissenwasser, W. Kapferer, R. Heer, and G. Lepperdinger. “Electric impedance sensing in cell-substrates for rapid and selective multipotential differentiation capacity monitoring of human mesenchymal stem cells”. In: *Biosensors & Bioelectronics* 34.1 (2012), pp. 63–69. DOI: <https://doi.org/10.1016/j.bios.2012.01.013>.
- [91] Ilhwan Park, Tra Nguyen, Jinsoo Park, Ah Young Yoo, Jae Kweon Park, and Sungbo Cho. “Impedance Characterization of Chitosan Cytotoxicity to MCF-7 Breast Cancer Cells Using a Multidisc Indium Tin Oxide Microelectrode Array”. In: *Journal of The Electrochemical Society* 165.2 (2018), pp. 55–59. DOI: <https://doi.org/10.1149/2.1201802jes>.
- [92] Jinfeng Chen Lin Ye Lijian Zhang Wen G. Jiang. “Placenta growth factor, PLGF, influences the motility of lung cancer cells, the role of Rho associated kinase, Rock1”. In: *Journal of Cellular Biochemistry* 105.1 (2008), pp. 313–320. DOI: <https://doi.org/10.1002/jcb.21831>.
- [93] Juan Ren, Yi-jin Xiao, Lisam Shanjukumar Singh, Xiaoxian Zhao, Zhenwen Zhao, Li Feng, Tyler M. Rose, Glenn D. Prestwich, and Yan Xu. “Lysophosphatidic Acid Is Constitutively Produced by Human Peritoneal Mesothelial Cells and Enhances Adhesion, Migration, and Invasion of Ovarian Cancer Cells”. In: *Cancer Research* 66.6 (2006), pp. 3006–3014. DOI: <https://doi.org/10.1158/0008-5472>.
- [94] Hagen Thielecke, Alexandra Mack, and Andrea Robitzki. “Biohybrid microarrays—impedimetric biosensors with 3D in vitro tissues for toxicological and biomedical screening”. In: *Fresenius Journal of Analytical Chemistry* 369.1 (2001), pp. 23–29.
- [95] Daniel Kloss, Randy Kurz, Heinz-Georg Jahnke, Michael Fischer, Andrée Rothermel, Ulf Anderegg, Jan C. Simon, and Andrea A. Robitzki. “Microcavity array (MCA)-based biosensor chip for functional drug screening of 3D tissue models”. In: *Biosensors and Bioelectronics* 23.10 (2008), pp. 1473–1480. DOI: <https://doi.org/10.1016/j.bios.2008.01.003>.
- [96] Dana Krinke, Heinz-Georg Jahnke, Till G. A. Mack, Anika Hirche, Frank Striggow, and Andrea A. Robitzki. “A novel organotypic tauopathy model on a new microcavity chip for bioelectronic label-free and real time monitoring”. In: *Biosensors and Bioelectronics* 26.1 (2010), pp. 162–168. DOI: <https://doi.org/10.1016/j.bios.2010.06.002>.
- [97] Xudong Zhang, Fang Li, Anis Nurashikin Nordin, John Tarbell, and Ioana Voiculescu. “Toxicity studies using mammalian cells and impedance spectroscopy method”. In: *Sensing and Bio-Sensing Research* 3 (2015), pp. 112–121. DOI: <https://doi.org/10.1016/j.sbsr.2015.01.002>.
- [98] Mario Rothbauer, Irene Praisler, Dominic Docter, Roland H. Stauber, and Peter Ertl. “Microfluidic Impedimetric Cell Regeneration Assay to Monitor the Enhanced Cytotoxic Effect of Nanomaterial Perfusion”. In: *Biosensors (Basel)* 5.4 (2015), pp. 736–749. DOI: <https://doi.org/10.3390/bios5040736>.

BIBLIOGRAPHY

- [99] Olivier Y. F. Henry, Remi Villenave, M. Crouce, W. Leineweber, M. Benz, and Donald E. Ingber. “Organs-on-Chips with integrated electrodes for Trans-Epithelial Electrical Resistance (TEER) measurements of human epithelial barrier function”. In: *Lab Chip* 17.13 (2017), pp. 2264–2271. DOI: <https://doi.org/10.1039/c7lc00155j>.
- [100] Kevin Luongo, Angela Holton, Ajeet Kaushik, Paige Spence, Beng Ng, Robert Deschenes, Shankar Sundaram, and Shekhar Bhansali. “Microfluidic device for trapping and monitoring three dimensional multicell spheroids using electrical impedance spectroscopy”. In: *Biomicrofluidics* 7.3 (2013), pp. 1–12. DOI: <https://doi.org/10.1063/1.4809590>.
- [101] J. Wegener, C. R. Keese, and I. Giaever. “Electric cell-substrate impedance sensing (ECIS) as a noninvasive means to monitor the kinetics of cell spreading to artificial surfaces”. In: *Experimental cell research* 259.1 (200), pp. 158–166. DOI: <https://doi.org/10.1006/excr.2000.4919>.
- [102] Adrienne Spencer and Aaron B. Baker. “High Throughput Label Free Measurement of Cancer Cell Adhesion Kinetics Under Hemodynamic Flow”. In: *Scientific Reports* 6.19854 (2016), pp. 1–10. DOI: <https://doi.org/10.1038/srep19854>.
- [103] Matthew R. Pennington and Gerlinde R. Van de Walle. “Electric Cell-Substrate Impedance Sensing To Monitor Viral Growth and Study Cellular Responses to Infection with Alpha-herpesviruses in Real Time”. In: *mSphere* 2.2 (2017), pp. 1–12. DOI: <https://doi.org/10.1128/mSphere.00039-17>.
- [104] Hikmat N. Daghestani and Billy W. Day. “Theory and Applications of Surface Plasmon Resonance, Resonant Mirror, Resonant Waveguide Grating, and Dual Polarization Interferometry Biosensors”. In: *Sensors* 10.11 (2010), pp. 9630–9646. DOI: <https://doi.org/10.3390/s101109630>.
- [105] Ye Fang, Ann M. Ferrie, Norman H. Fontaine, John Mauro, and Jitendra Balakrishnan. “Resonant Waveguide Grating Biosensor for Living Cell Sensing”. In: *Biophysical* 91.5 (2006), pp. 1925–1940. DOI: <https://doi.org/10.1529/biophysj.105.077818>.
- [106] Michael J. Tullier. *Acoustic Sensors*. URL: <http://www.eng.auburn.edu/files/file1007.pdf>.
- [107] Farid E. Ahmed, John E. Wiley, Douglas A. Weidner, Chris Bonnerup, and Helvecio Mota. “Surface Plasmon Resonance (SPR) Spectrometry as a Tool to Analyze Nucleic Acid–Protein Interactions in Crude Cellular Extracts”. In: *Cancer, Genomics and Proteomics* 7.6 (2010), pp. 303–309.
- [108] Biosensing Instrument. *TECHNICAL NOTE 103: SURFACE PLASMON RESONANCE V. QUARTZ CRYSTAL MICROBALANCE*. URL: <http://biosensingusa.com/technical-notes/technical-note-103-surface-plasmon-resonance-v-quartz-crystal-microbalance/>.
- [109] Jun Xi, Jennifer Y. Chen, Marcela P. Garcia, and Lynn S. Penn. “Quartz Crystal Microbalance in Cell Biology Studies”. In: *Biochips & Tissue Chips* 5 (2013), pp. 1–9. DOI: <https://doi.org/10.4172/2153-0777.S5-001>.

BIBLIOGRAPHY

- [110] Julia M. Hillger, Wai-Ling Lieuw, Laura H. Heitman, and Adriaan P. IJzerman. “Label-free technology and patient cells: from early drug development to precision medicine”. In: *Drug Discovery Today* 22.12 (2017), pp. 1808–1815. DOI: <https://doi.org/10.1016/j.drudis.2017.07.015>.
- [111] Jonathan S. Daniels and Nader Pourmanda. “Label-Free Impedance Biosensors: Opportunities and Challenges”. In: *Electroanalysis* 19.12 (2007), pp. 1239–1257. DOI: <https://doi.org/10.1002/elan.200603855>.
- [112] Sverre Grimnes. *Bioimpedance and Bioelectricity Basics*. London, UK: ACADEMIC PRESS, 2000.
- [113] Beatriz Lobo, Cecilia Hermosa, Ana Abella, and Federico Gordo. “Electrical impedance tomography”. In: *Annals of Translational Medicine* 6.2 (2018), pp. 1–9. DOI: <https://doi.org/10.21037/atm.2017.12.06>.
- [114] L. C. Ward and B. L. Heitmann. “Assessment of body composition by bioelectrical impedance analysis without the need for measurement of height”. In: *Annals of Translational Medicine* 20.1 (2001), pp. 21–26. DOI: <https://doi.org/10.1054/clnu.2000.0362>.
- [115] Ivar Giaever and C. R. Keese. “Micromotion of mammalian cells measured electrically”. In: *PNAS* 88.17 (1991), pp. 7896–7900.
- [116] Meritxell Genesca, Antoni Ivorra, Anna Sola, Luis Palacios, Jean-Michel Goujon, Thierry Hauet, Rosa Villa, Jordi Aguilo, and Georgina Hotter. “Electrical bioimpedance measurement during hypothermic rat kidney preservation for assessing ischemic injury”. In: *Biosensors and Bioelectronics* 20.9 (2005), pp. 1866–1871. DOI: <http://dx.doi.org/10.1016/j.bios.2004.06.038>.
- [117] Yaël A. Glickman, Orna Filo, Magda David, Avner Yayon, Moris Topaz, Bosmat Zamir, Alexander Ginzburg, Dganit Rozenman, and Gad Kenan. “Electrical impedance scanning: a new approach to skin cancer diagnosis”. In: *Skin Research and Technology* 9.3 (2003), pp. 262–268. DOI: <https://doi.org/10.1034/j.1600-0846.2003.00022.x>.
- [118] Atte Kekonen, Mikael Bergelin, Jan-Erik Eriksson, Annikki Vaalasti, Heimo Ylänen, and Jari Viik. “Bioimpedance measurement based evaluation of wound healing”. In: *Physiological Measurement* 38.7 (2017), pp. 1373–1383. DOI: <http://dx.doi.org/10.1088/1361-6579/aa63d6>.
- [119] Andreas Janshoff, Angelika Kunze, Stefanie Michaelis, Vanessa Heitmann, Bjoern Reiss, and Joachim Wegener. “Cell Adhesion Monitoring Using Substrate-Integrated Sensors”. In: *Journal of Adhesion Science and Technology* 24.13-14 (2010), pp. 2079–2104. DOI: <https://doi.org/10.1163/016942410X507939>.
- [120] Qingjun Liu, Chunsheng Wu, Hua Cai, Ning Hu, Jun Zhou, and Ping Wang. “Cell-Based Biosensors and Their Application in Biomedicine”. In: *Chemical Reviews* 114.12 (2014), pp. 6423–6461. DOI: <http://dx.doi.org/10.1021/cr2003129>.

BIBLIOGRAPHY

- [121] Jun Wang, Chengxiong Wu, Ning Hu, Jie Zhou, Liping Du, and Ping Wang. “Micro-fabricated Electrochemical Cell-Based Biosensors for Analysis of Living Cells *In Vitro*”. In: *Biosensors* 2.2 (2012), pp. 127–170. DOI: <https://doi.org/10.3390/bios2020127>.
- [122] Ping Wang, Chunsheng Wu, Ning Hu, and K. Jimmy Hsia. *Micro/Nano Cell and Molecular Sensors*. Singapore: Springer, 2016.
- [123] Madhukar Varshney and Yanbin Li. “Interdigitated array microelectrodes based impedance biosensors for detection of bacterial cells”. In: *Biosensors and Bioelectronics* 24.10 (2009), pp. 2951–2960. DOI: <https://doi.org/10.1016/j.bios.2008.10.001>.
- [124] Jaouad Mamouni and Liju Yang. “Interdigitated microelectrode-based microchip for electrical impedance spectroscopic study of oral cancer cells”. In: *Biomedical Microdevices* 13.6 (2011), pp. 1075–1088. DOI: <https://doi.org/10.1007/s10544-011-9577-8>.
- [125] Andrew C. Barton, Stuart D. Collyer, Frank Davis, Davinia D. Gornall, Karen A. Law, Emma C. D. Lawrence, Daniel W. Mills, Suzy Myler, Jeanette A. Pritchard, Mark Thompson, and Seamus P. J. Higson. “Sonochemically fabricated microelectrode arrays for biosensors offering widespread applicability: Part I”. In: *Biosensors and Bioelectronics* 20.2 (2004), pp. 328–337. DOI: <https://doi.org/10.1016/j.bios.2004.02.002>.
- [126] Charles R. Martin. “Nanomaterials: A Membrane-Based Synthetic Approach”. In: *Science* 266.5193 (1994), pp. 1961–1966. DOI: <https://doi.org/10.1126/science.266.5193.1961>.
- [127] Younan Xia, John A. Rogers, Kateri E. Paul, and George M. Whitesides. “Unconventional Methods for Fabricating and Patterning Nanostructures”. In: *Chemical Reviews* 99.7 (1999), pp. 1823–1848. DOI: <https://doi.org/10.1021/cr980002q>.
- [128] Cynthia G. Zoski. *Handbook of Electrochemistry*. Amsterdam, the Netherlands: Elsevier, 2007.
- [129] Joachim Wegener, Manfred Sieber, and Hans-Joachim Galla. “Impedance analysis of epithelial and endothelial cell monolayers cultured on gold surfaces”. In: *Journal of Biochemical and Biophysical methods* 32.3 (1996), pp. 151–170. DOI: [https://doi.org/10.1016/0165-022X\(96\)00005-X](https://doi.org/10.1016/0165-022X(96)00005-X).
- [130] Duc D. Nguyen, Xiaoqiu Huang, David W. Greve, and Michael M. Domach. “Fibroblast Growth and H-7 Protein Kinase Inhibitor Response Monitored in Microimpedance Sensor Arrays”. In: *Biotechnology and bioengineering* 87.2 (2004), pp. 138–144. DOI: <https://doi.org/10.1002/bit.20070>.
- [131] AppliedBiophysics. *Choosing The Proper ECIS[®] Array*. URL: <http://www.biophysics.com/downloads/TN01%5C%20Array%5C%20Choices.pdf>.
- [132] Eric Moore, Orla Rawley, Terri Wood, and Paul Galvin. “Monitoring of cell growth *in vitro* using biochips packaged with indium tin oxide sensors”. In: *Sensors and Actuators B: Chemical* 139.1 (2009), pp. 187–193. DOI: <https://doi.org/10.1016/j.snb.2008.11.025>.

BIBLIOGRAPHY

- [133] Ping Wang and Qingjun Liu. *Cell-Based Biosensors Principles and Applications*. Norwood, MA: ArtechHouse, 2010.
- [134] AppliedBiophysics. *ECIS Cultureware™ Disposable Electrode Arrays*. URL: <http://www.biophysics.com/cultureware.php#link2>.
- [135] S. Gawad, L. Schild, and Ph. Renaud. “Micromachined impedance spectroscopy flow cytometer for cell analysis and particle sizing”. In: *Royal Society of Chemistry* 1.1 (2001), pp. 76–82. DOI: <https://doi.org/10.1039/B103933B>.
- [136] S. Schafer, S. Eick, B. Hofmann, T. Dufaux, R. Stockmann, G. Wrobel, A. Offenhäusser, and S. Ingebrandt. “Time-dependent observation of individual cellular binding events to field-effect transistors”. In: *Biosensors and Bioelectronics* 24.5 (2009), pp. 1201–1208. DOI: <https://doi.org/10.1016/j.bios.2008.07.003>.
- [137] A. Susloparova, D. Koppenhofer, X. T. Vu, M. Weil, and S. Ingebrandt. “Impedance spectroscopy with field-effect transistor arrays for the analysis of anti-cancer drug action on individual cells”. In: *Biosensors and Bioelectronics* 40.1 (2013), pp. 50–56. DOI: <https://doi.org/10.1016/j.bios.2012.06.006>.
- [138] Vaishnavi Srinivasaraghavan. “Bioimpedance spectroscopy of breast cancer cells: A microsystems approach”. PhD thesis. Virginia Polytechnic Institute and State University, 2015.
- [139] Dan Kho, Christa MacDonald, Rebecca Johnson, Charles P. Unsworth, Simon J. O’Carroll, Elyce du Mez, Catherine E. Angel, and E. Scott Graham. “Application of xCELLigence RTCA Biosensor Technology for Revealing the Profile and Window of Drug”. In: *Biosensors* 5.2 (2015), pp. 199–222. DOI: <https://doi.org/10.3390/bios5020199>.
- [140] C. Xiao, B. Lachance, G. Sunahara, and JH. Luong. “An in-depth analysis of electric cell-substrate impedance sensing to study the attachment and spreading of mammalian cells”. In: *Analytical Chemistry* 74.6 (2002), pp. 1333–1339.
- [141] V. Srinivasaraghavan, J. Strobl, D. Wang, J. R. Heflin, and M. Agah. “A comparative study of nano-scale coatings on gold electrodes for bioimpedance studies of breast cancer cells”. In: *Biomedical microdevices* 16.5 (2014), pp. 689–696. DOI: <https://doi.org/10.1007/s10544-014-9873-1>.
- [142] Chin Fhong Soon, Mee Kei Foong, Mohd Khairul Ahmad, Rosliza MD Zin, Kok Tung Thong, and Kian Sek Tee. “Characterization of Platinum Electrodes and In-situ Cell Confluency Measurement Based on Current Changes of Cell-Electrodes”. In: *Sensors & Transducers* 187.4 (2015), pp. 113–119.
- [143] Robert Meissner, Bilge Eker, Harsha Kasi, Arnaud Bertsch, and Philippe Renaud. “Distinguishing drug-induced minor morphological changes from major cellular damage via label-free impedimetric toxicity screening”. In: *Lab Chip* 11.14 (2011), pp. 2352–2361. DOI: <https://doi.org/10.1039/c1lc20212j>.
- [144] W. Franks, I. Schenker, P. Schmutz, and A. Hierlemann. “Impedance characterization and modeling of electrodes for biomedical applications”. In: *IEEE Transactions on Biomedical Engineering* 52.7 (2005), pp. 1295–1302. DOI: <https://doi.org/10.1109/TBME.2005.847523>.

BIBLIOGRAPHY

- [145] Chang K. Choi, Chuck H. Margraves, Seung I. Jun, Anthony E. English, Philip D. Rack, and Kenneth D. Kihm. “Opto-Electric Cellular Biosensor Using Optically Transparent Indium Tin Oxide (ITO) Electrodes”. In: *Sensors (Basel)* 8.5 (2008), pp. 3257–3270. DOI: <https://doi.org/10.3390/s8053257>.
- [146] Sakthivel Ramasamy, Devasier Bennet, and Sanghyo Kim. “Drug and bioactive molecule screening based on a bioelectrical impedance cell culture platform”. In: *International Journal of Nanomedicine* 9 (2014), pp. 5789–5809. DOI: <https://doi.org/10.2147/IJN.S71128>.
- [147] Tetsuya Watanabe. *Biophysical Basis of Physiology and Calcium Signaling Mechanism in Cardiac and Smooth Muscle*. Oxford, UK: Academic Press, 2018.
- [148] Meyer B. Jackson. *Molecular and Cellular Biophysics*. Cambridge, UK: Cambridge University Press, 2006.
- [149] Gang Bao and Subra Suresh. “Cell and molecular mechanics of biological materials”. In: *Nature Materials* 2.11 (2003), pp. 715–725. DOI: <https://doi.org/10.1038/nmat1001>.
- [150] Hugo Fricke. “The Electric Impedance of Suspensions of Biological Cells”. In: *Cold Spring Harbor Symposia on Quantitative Biology* 8.1 (1924), pp. 117–124. DOI: <https://doi.org/10.1101/SQB.1933.001.01.015>.
- [151] Ronald Pethig and Douglas B. Kell. “The passive electrical properties of biological systems: their significance in physiology, biophysics and biotechnology”. In: *Physics in Medicine & Biology* 32.8 (1987), pp. 933–970. DOI: <https://doi.org/10.1088/0031-9155/32/8/001>.
- [152] Weng G. Jiang. *Electric Cell-Substrate Impedance Sensing and Cancer Metastasis*. Dordrecht: Springer, 2012.
- [153] Joachim Wegener. *Measuring Biological Impacts of Nanomaterials*. Switzerland: Springer, 2016.
- [154] Paolo Armando Gagliardi, Alberto Puliafito, Laura di Blasio, Federica Chianale, Desiana Somale, Giorgio Seano, Federico Bussolino, and Luca Primo. “Real-time monitoring of cell protrusion dynamics by impedance responses”. In: *Scientific Reports* 5.10206 (2015), pp. 1–12. DOI: <https://doi.org/10.1038/srep10206>.
- [155] Guo Xiaoliang, Zhu Rong, and Zong Xianli. “A microchip integrating cell array positioning with *in situ* single-cell impedance measurement”. In: *Analyst* 140.19 (2015), pp. 1–16. DOI: <https://doi.org/10.1039/c5an01193k>.
- [156] L Wang, H. Yin, W. Xing, Z Yu, M Guo, and J Cheng. “Real-time, label-free monitoring of the cell cycle with a cellular impedance sensing chip”. In: *Biosensors and Bioelectronics* 25.5 (2009), pp. 990–995. DOI: <https://doi.org/10.1016/j.bios.2009.09.012>.
- [157] Kathrin Benson, Sand Cramer, and Hans-Joachim Galla. “Impedance-based cell monitoring: barrier properties and beyond”. In: *Fluids Barriers CNS* 10.5 (2013), pp. 1–11. DOI: <https://doi.org/10.1186/2045-8118-10-5>.

BIBLIOGRAPHY

- [158] Balaji Srinivasan, Aditya Reddy Kolli, Mandy Brigitte Esch, Hasan Erbil Abaci, Michael L. Shuler, and James J. Hickman. “TEER Measurement Techniques for *in vitro* Model Systems”. In: *J. Lab. Autom.* 20.2 (2015), pp. 107–126. DOI: <https://doi.org/10.1177/2211068214561025>.
- [159] Lavanya Balasubramanian, Kay-Pong Yip, Tai-Hsin Hsu, and Chun-Min Lo. “Impedance analysis of renal vascular smooth muscle cells”. In: *Methods in Cell Physiology* 295.4 (2008), pp. C954–C965. DOI: <https://doi.org/10.1152/ajpcell.00009.2008>.
- [160] Chun-Min Lo and Jack Ferrier. “Impedance analysis of fibroblastic cell layers measured by electric cell-substrate impedance sensing”. In: *Physical Review E, Statistical physics, plasmas, fluids, and related interdisciplinary topics* 57.6 (1998), pp. 6982–6987. DOI: <https://doi.org/10.1103/PhysRevE.57.6982>.
- [161] AppliedBiophysics. *ECIS Time Course Measurements*. URL: <http://www.biophysics.com/Product%5C%20Sheets/ABP%5C%202014%5C%20Catalog%5C%200514.pdf>.
- [162] ACEA Biosciences. *Real-Time and Dynamic Monitoring of Cell Proliferation and Viability for Adherent Cells*. URL: <https://www.aceabio.com/wp-content/uploads/Monitoring-Cell-Proliferation-and-Viability-for-Adherent-Cells.pdf>.
- [163] Molecular Devices. *MDS Sciex introduces the CellKey System*. URL: <https://www.moleculardevices.com/news/mds-sciex-introduces-cellkey-system>.
- [164] Pedro Mestres and Andrea Morguet. “The Bionas technology for anticancer drug screening”. In: *Expert Opinion on Drug Discovery* 4.7 (2009), pp. 785–797. DOI: <https://doi.org/10.1517/17460440903018840>.
- [165] Applied BioPhysics. *Choosing The Proper ECIS[®] Array*. URL: <https://http://www.biophysics.com/downloads/TN01%5C%20Array%5C%20Choices.pdf>.
- [166] Fan-Gang Tseng and Tuhin Subhra Santra. *Micro/Nanofluidic Devices for Single Cell Analysis*. Basel, Switzerland: MDPI, 2015.
- [167] Elke Thedinga, Axel Kob, Heiko Holst, Andreas Keuer, Sabine Drechsler, Ricarda Nien-dorf, Werner Baumann, Ingo Freund, Mirko Lehmann, and Ralf Ehret. “Online monitoring of cell metabolism for studying pharmacodynamic effects”. In: *Toxicology and Applied Pharmacology* 220.1 (2007), pp. 33–44. DOI: <https://doi.org/10.1016/j.taap.2006.12.027>.
- [168] Tobias Henning, Martin Brischwein, Werner Baumann, Ralf Ehret, Ingo Freund, Robert Kammerer, Mirko Lehmann, Anne Schwinde, and Bernhard Wolf. “Approach to a multi-parametric sensor-chip-based tumor chemosensitivity assay”. In: *Anti-Cancer Drugs* 12.1 (2011), pp. 21–32.

BIBLIOGRAPHY

- [169] Chun-Min Lo, Charles R. Keese, and Ivar Giaever. “Impedance Analysis of MDCK Cells Measured by Electric Cell-Substrate Impedance Sensing”. In: *Biophysical journal* 69.6 (1995), pp. 2800–2807. DOI: [https://doi.org/10.1016/S0006-3495\(95\)80153-0](https://doi.org/10.1016/S0006-3495(95)80153-0).
- [170] Kelli Solly, Xiaobo Wang, Xiao Xu, Berta Strulovici, and Wei Zheng. “Application of Real-Time Cell Electronic Sensing (RT-CES) Technology to Cell-Based Assays”. In: *ASSAY and Drug Development Technologies* 2.4 (2004), pp. 363–374. DOI: <https://doi.org/10.1089/adt.2004.2.363>.
- [171] Wen G Jiang, Tracey A Martin, Jonathan M Lewis-Russell, Anthony Douglas-Jones, Lin Ye, and Robert E Mansel. “Eplln-alpha expression in human breast cancer, the impact on cellular migration and clinical outcome”. In: *Molecular Cancer* 7.71 (2008), pp. 1–10. DOI: <https://doi.org/10.1186/1476-4598-7-71>.
- [172] Vivian F. Liu Gary J. Ciambrone, Ryan P. M C. Guinness Deborah C. Lin, Gordon K. Leung, and Simon Pitchford. “Cellular Dielectric Spectroscopy: A Powerful New Approach to Label-Free Cellular Analysis”. In: *Journal of Biomolecular Screening* 9.6 (2004), pp. 467–480. DOI: <https://doi.org/10.1177/1087057104267788>.
- [173] Zhiyuan Zhang, Laura Hernandez-Lagunas, William C. Horne, and Roland Baron. “Cytoskeleton-dependent Tyrosine Phosphorylation of the p130^{Cas} Family Member HEF1 Downstream of the G Protein-coupled Calcitonin Receptor CALCITONIN INDUCES THE ASSOCIATION OF HEF1, PAXILLIN, AND FOCAL ADHESION KINASE”. In: *Journal of Biological Chemistry* 274.35 (1999), pp. 25093–25098. DOI: <https://doi.org/10.1074/jbc.274.35.25093>.
- [174] Alexander Garcia-Ponce, Sandra Chanez Paredes, Karla Fabiola Castro Ochoa, and Michael Schnoor. “Regulation of endothelial and epithelial barrier functions by peptide hormones of the adrenomedullin family”. In: *Tissue Barriers* 4.4 (2016), pp. 1–19. DOI: <https://doi.org/10.1080/21688370.2016.1228439>.
- [175] Heng Mei, Cathy Paddock, Jay Campbell, Ralph Albrecht, and Peter J. Newman. “Enhancement Of Endothelial Cell Barrier Function By Antibody-Driven Affinity Modulation Of PECAM-1”. In: *Blood* 122.21 (2013).
- [176] I. H. Heijink, A. van Oosterhout, and A. Kapus. “Epidermal growth factor receptor signalling contributes to house dust mite-induced epithelial barrier dysfunction”. In: *European Respiratory journal* 36.5 (2010), pp. 1016–1026. DOI: <https://doi.org/10.1183/09031936.00125809>.
- [177] “Transforming growth factor- β induces CD44 cleavage that promotes migration of MDA-MB-435s cells through the up-regulation of membrane type 1-matrix metalloproteinase”. In: *International Journal of Cancer* 124.11 (2009), pp. 2568–2576. DOI: <https://doi.org/10.1002/ijc.24263>.
- [178] Ramakrishna Seethala and Prabhavathi Fernandes. *Handbook of Drug Screening*. Boca Raton: CRC Press, 2001.

BIBLIOGRAPHY

- [179] Mohana Marimuthu, Cheolsoo Park, Sanghyo Kim, and Cheo Soo Choi^{3*}. “Real-time electrical measurement of L929 cellular spontaneous and synchronous oscillation.” In: *International Journal of Nanomedicine* 7 (2012), pp. 83–92. DOI: <https://doi.org/10.2147/IJN.S28465>.
- [180] Arum Hana and A. Bruno Frazier. “Ion channel characterization using single cell impedance spectroscopy”. In: *Lab on A Chip* 6.11 (2006), pp. 1412–1414. DOI: <https://doi.org/10.1039/b608930e>.
- [181] M. H. Teiten, R. Blasius, F. Morceau, M. Diederich, and M. Dicato. “Signaling Chains”. In: *Comprehensive Medicinal Chemistry II* 3 (2007), pp. 189–214. DOI: <https://doi.org/10.1016/B0-08-045044-X/00083-3>.
- [182] Fei Huang, Papasani V. Subbaiah, Oksana Holian, Jihang Zhang, Arnold Johnson, Nancy Gertzberg, and Hazel Lum. “Lysophosphatidylcholine increases endothelial permeability: role of PKC α and RhoA cross talk”. In: *American Journal of Physiology. Lung cellular and molecular physiology* 289.2 (2005), pp. L176–L185. DOI: <https://doi.org/10.1152/ajplung.00003.2005>.
- [183] Rajinder S. Sawhney, Michelle M. Cookson, Bhavya Sharma, Jennie Hauser, and Michael G. Brattain. “Autocrine Transforming Growth Factor α Regulates Cell Adhesion by Multiple Signaling via Specific Phosphorylation Sites of p70S6 Kinase in Colon Cancer Cells”. In: *Journal of Biological Chemistry* 279.45 (2004), pp. 47379–47390. DOI: <https://doi.org/10.1074/jbc.M402031200>.
- [184] Giljun Park, Chang K. Choi, Anthony E. English, and Tim E. Sparer. “Electrical impedance measurements predict cellular transformation”. In: *Cell Biology International* 3.3 (2009), pp. 429–433. DOI: <https://doi.org/10.1016/j.cellbi.2009.01.013>.
- [185] Ning Hu, Jie Zhou, Kaiqi Su, Diming Zhang, Lidan Xiao, Tianxing Wang, and Ping Wang. “An integrated label-free cell-based biosensor for simultaneously monitoring of cellular physiology multiparameter *in vitro*”. In: *Biomedical Microdevices* 15.3 (2013), pp. 473–480. DOI: <https://doi.org/10.1007/s10544-013-9747-y>.
- [186] C. R. Keese, N. Karra, B. Dillon, A. M. Goldberg, and I. Giaever. “Cell-substratum interactions as a predictor of cytotoxicity”. In: *In Vitro and Molecular Toxicology: Journal of Basic and Applied Research* 11.2 (1998), pp. 183–192.
- [187] Caide Xiao and John H.T. Luong. “Assessment of cytotoxicity by emerging impedance spectroscopy”. In: *Toxicology and Applied Pharmacology* 206.2 (2005), pp. 102–112. DOI: <http://dx.doi.org/10.1016/j.taap.2004.10.025>.
- [188] Silke Arndt, Jochen Seebach, Katherina Psathaki, Hans-Joachim Galla, and Joachim Wegener. “Bioelectrical impedance assay to monitor changes in cell shape during apoptosis”. In: *Biosensors and Bioelectronics* 19.6 (2004), pp. 583–594. DOI: [http://dx.doi.org/10.1016/S0956-5663\(03\)00269-0](http://dx.doi.org/10.1016/S0956-5663(03)00269-0).
- [189] Fareid Asphahani and Miqin Zhang. “Cellular impedance biosensors for drug screening and toxin detection”. In: *The Analyst* 132.9 (2007), pp. 835–841. DOI: <https://doi.org/10.1039/b704513a>.

BIBLIOGRAPHY

- [190] Daniel Opp, Brian Wafula, Jennifer Lim, Eric Huang, Jun-Chih Lo, and Chun-Min Lo. “Use of electric cell–substrate impedance sensing to assess *in vitro* cytotoxicity”. In: *Biosensors and Bioelectronics* 24.8 (2009), pp. 2625–2629. DOI: <https://doi.org/10.1016/j.bios.2009.01.015>.
- [191] Ju Hun Yeon and Je-Kyun Park. “Cytotoxicity test based on electrochemical impedance measurement of HepG2 cultured in microfabricated cell chip”. In: *Analytical Biochemistry* 341.2 (2005), pp. 308–315. DOI: <https://doi.org/10.1016/j.ab.2005.03.047>.
- [192] Albert P. Li, Chuang Lu, Julie A. Brent, Chuong Pham, Andrew Fackett, Charles E. Ruegg, and Paul M. Silber. “Cryopreserved human hepatocytes: characterization of drug-metabolizing activities and applications in higher throughput screening assays for hepatotoxicity, metabolic stability, and drug–drug interaction potential”. In: *Chemico-Biological Interactions* 121.1 (1999), pp. 17–35. DOI: [https://doi.org/10.1016/S0009-2797\(99\)00088-5](https://doi.org/10.1016/S0009-2797(99)00088-5).
- [193] “Immortalized hepatocytes as *in vitro* model systems for toxicity testing: the comparative toxicity of menadione in immortalized cells, primary cultures of hepatocytes and HTC hepatoma cells”. In: *Toxicology in Vitro* 10.6 (1996), pp. 721–727. DOI: [https://doi.org/10.1016/S0887-2333\(96\)00059-8](https://doi.org/10.1016/S0887-2333(96)00059-8).
- [194] Audrey F. Adcock, Chiagozie O. Agbai, and Liju Yang. “Application of electric cell-substrate impedance sensing toward personalized anti-cancer therapeutic selection”. In: *Journal of Analytical Science and Technology* 9.17 (2018), pp. 1–11. DOI: <https://doi.org/10.1186/s40543-018-0149-x>.
- [195] Fengbo Xie, Youchun Xu, Lei Wang, Keith Mitchelson, Wanli Xing, and Jing Cheng. “Use of cellular electrical impedance sensing to assess *in vitro* cytotoxicity of anticancer drugs in a human kidney cell nephrotoxicity model”. In: *Analyst* 137.6 (2012), pp. 1343–1350. DOI: <https://doi.org/10.1039/C2AN16141A>.
- [196] Bilge Eker, Robert Meissner, Arnaud Bertsch, Kapil Mehta, and Philippe Renaud. “Label-Free Recognition of Drug Resistance via Impedimetric Screening of Breast Cancer Cells”. In: *PLoS One* 8.3 (2013), pp. 1–12. DOI: <https://doi.org/10.1371/journal.pone.0057423>.
- [197] Svetomir N. Markovic, Lori A. Erickson, Ravi D. Rao, Roger H. Weenig, Barbara A. Pockaj, Aditya Bardia, Celine M. Vachon, Steven E. Schild, Robert R. McWilliams, Jennifer L. Hand, Susan D. Laman, Lisa A. Kittschade, William J. Maples, Mark R. Pittelkow, Jose S. Pulido, J. Douglas Cameron, Edward T Creagan, and Melanoma Study Group of the Mayo Clinic Cancer Center. “Malignant melanoma in the 21st century, part 1: epidemiology, risk factors, screening, prevention, and diagnosis”. In: *Symposium on solid tumors*. Mayo Clinic, Mar. 2007, pp. 364–380.
- [198] G. Tim Bowden. “Prevention of non-melano,a skin cancer by trageting ultraviolet-B-light signaling”. In: *Nature Reviews Cancer* 4.1 (2004), pp. 23–35. DOI: <https://doi.org/10.1038/nrc1253>.

BIBLIOGRAPHY

- [199] Devasier Bennet, Se Chan Kang, Jongback Gang, and Sanghyo Kim. “Photoprotective effects of apple peel nanoparticles”. In: *International Journal of Nanomedicine* 9.1 (2014), pp. 93–108. DOI: <https://doi.org/10.2147/IJN.S54048>.
- [200] Devasier Bennet and Sanghyo Kim. “Impedance-based cell culture platform to assess light-induced stress changes with antagonist drugs using retinal cells”. In: *Analytical Chemistry* 85.10 (2014), pp. 4902–4911. DOI: <https://doi.org/10.1021/ac303068t>.

Materials and Methods

In this chapter we describe all of the experimental procedures used in this work. It includes the preparation protocols for the different solutions; the cell culture procedures; the electrode fabrication protocols and the experimental set-up for the electrical impedance measurements.

2.1 Cell lines

Dr. Hichem Mertani from the Centre de Recherche en Cancérologie de Lyon (CRCL) supplied both of the human breast adenocarcinoma cell lines, MCF-7 and MDA-MB-231. These two cell lines are widely used for breast cancer studies due to their different invasive and metastatic abilities[1]. For instance, MCF-7 breast cancer cells are non metastatic and poorly invasive, containing receptor proteins specific for androgen, glucocorticoids and progesterone[2]. These cells are classified into luminal subtype and tend to form tight cell-cell junctions[1]. On the other hand, MDA-MB-231 is known as a "triple-negative" breast cancer (TNBC) cell line because it lacks expression of estrogen receptor, progesterone receptor and human epidermal growth factor receptor 2[3]. MDA-MB-231 cells are classified into claudin-low subtype and they are highly invasive and metastatic[4]. As can be observed in Fig.2.1, MCF-7 cells grown *in vitro* exhibit the classical "cobblestone" morphology[2] whereas MDA-MB-231 cells form loosely cohesive stellate structures consistent with a more invasive phenotype[5].

2.1. Cell lines

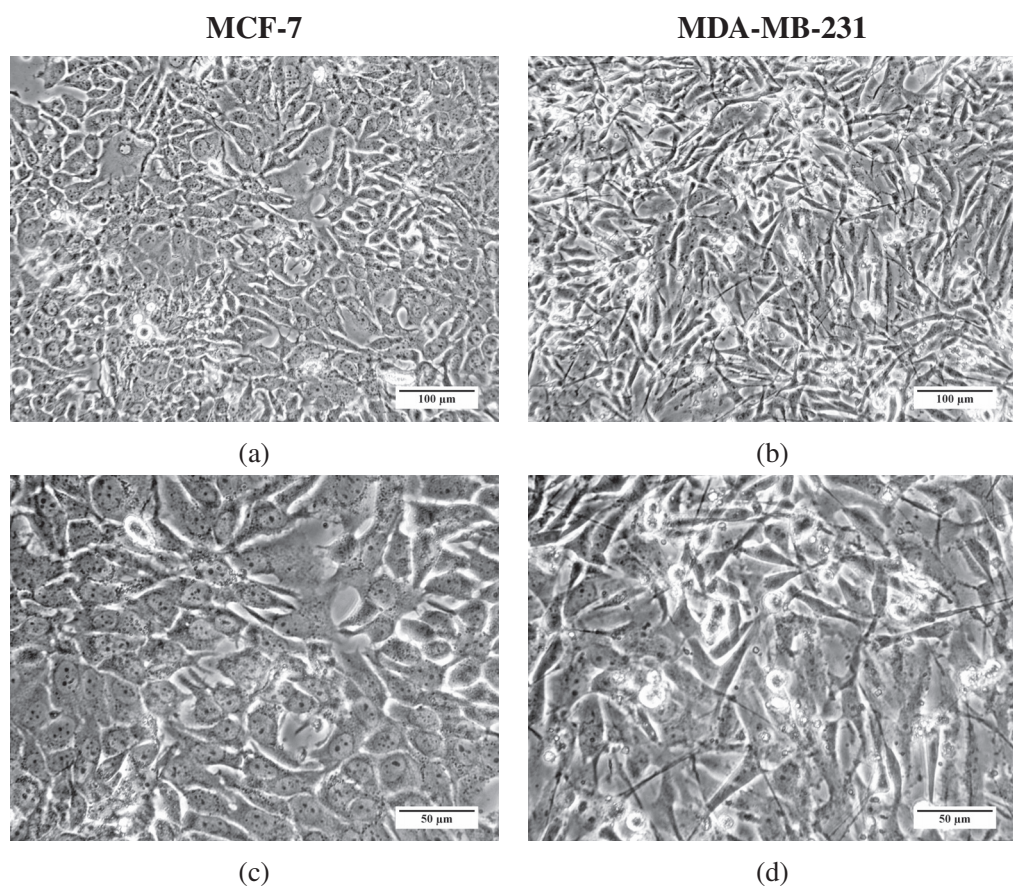


Figure 2.1 – Phase contrast microscopy images of the cell lines MCF-7 and MDA-MB-231 grown in Petri dish at (a,b) 20X and (c,d) 40X magnification (Leica D2000).

2.2 Preparation of solutions

All the described solutions were filtered using a sterile filter (pore size: 0.20 μm) before any experiment involving living cells.

2.2.1 Potassium chloride solutions

Potassium chloride (KCl, Sigma-Aldrich) $M_{\text{KCl}} = 74.5 \text{ g/mol}$) was dissolved in deionized water to prepare the KCl solutions at the desired concentrations shown in Table 2.1. During the experiments, these solutions were used at room temperature and then stored at 4°C.

KCl Concentration	Conductivity σ
0 mM (D.I water)	2.0 $\mu\text{S/cm}$
1 mM	183 $\mu\text{S/cm}$
100 mM	15.7 mS/cm

Table 2.1 – Conductivities of the various KCl solutions at room temperature.

2.2.2 PBS 1X solution

Phosphate buffered saline (PBS, Bisolve Chemicals BV) was used as a washing solution during cell sub-culture and electrode preparation for bioimpedance measurements. The solution of PBS 1X ($\sigma = 16 \text{ mS/cm}$) was prepared by diluting 50 mL of PBS 10X concentrated solution in 450 mL of sterilized deionized water and stored at 4°C.

2.2.3 Iridium bath

The solution used to electrodeposit iridium oxide (IrO_x) was prepared following the steps reported by K. Yamanaka[6]. First, 4.5 mM of $\text{IrCl}_4 \cdot \text{H}_2\text{O}$ (Alfa Aesar) was dissolved in deionized water. Then, 400 μL of H_2O_2 (35%) was added and the solution gently mixed for 10 min. At this point, the solution turned yellow due to oxidation of iridium (Fig.2.2). Afterwards, 55.5 mM of oxalic acid $\text{C}_2\text{H}_2\text{O}_4$ (Alfa Aesar) was added and mixed for a further 10 min in order to form the complex Ir(IV)-oxalate, which stabilizes the (IrO_x) nanoparticles[7] during the aging process. Then, the pH of the solution was adjusted to a value of 10.5 by slowly adding K_2CO_3 (Sigma-Aldrich). Finally, the solution was kept at room temperature for 5 days to age, until it turned violet as shown in Fig.2.3, and then stored at 4°C.

2.2. Preparation of solutions

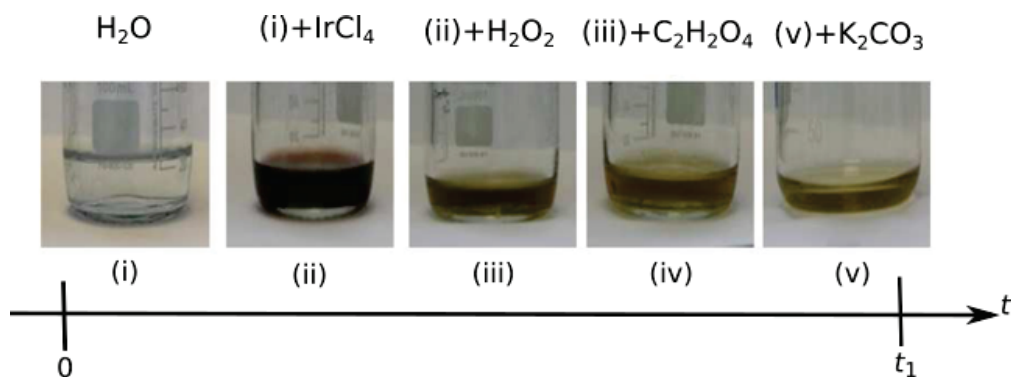


Figure 2.2 – Steps in the Yamanaka protocol for the preparation of the iridium bath: (i,ii) water and Ir(IV) salt mixing; (iii) hydrogen peroxide addition; (iv) oxalic acid addition; (v) potassium carbonate addition. Figure adapted from Fig.III-8 in [7].

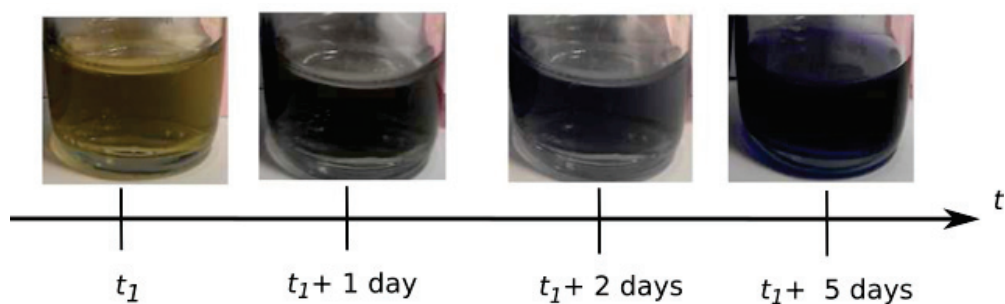


Figure 2.3 – Color changes during aging process of iridium oxide solution at room temperature. Figure adapted from Fig.III-9 in [7].

2.2. Preparation of solutions

2.2.4 Cell culture medium

Cells were grown in Dubelcco's Modified Eagle Medium (DMEM, ThermoFisher), which is a widely used basal culture medium for supporting the growth of many different mammalian cells. This medium contains no proteins, lipids or growth factors[8]. We therefore added fetal bovine serum (FBS, ThermoFisher) and antibiotics, penicillin and streptomycin (PS, ThermoFisher). FBS provides most of the growth factors required for cell attachment, growth and proliferation[9] whereas antibiotics PS are added to prevent bacterial contamination of cell cultures. This supplemented DMEM medium ($\sigma = 15.37$ mS/cm) was stored at 4°C. The composition of the DMEM medium and the additives that we used are listed in Table 2.2

Supplemented DMEM		Concentration
DMEM	L-Glutamine	4 mM
	D-Glucose (Dextrose)	25 mM
	Phenol Red	15 mg/L
	Sodium Pyruvate	1 mM
+ Fetal Bovine Serum		10% (v/v)
+ Penicilin-streptomycin		1% (v/v)

Table 2.2 – Composition of the supplemented cell culture medium used for MDA-MB-231 and MCF-7 cells. (DMEM was supplemented with FBS and PS).

2.2.5 CN/BSA coating solution

In order to enhance cell adhesion, we used a coating solution containing a mixture of type IV collagen (CN, Sigma-Aldrich) and bovine serum albumin (BSA, Sigma-Aldrich) where the ratio of $n_{CN}/n_{BSA} = 99$ [10]. Type IV collagen is essential for the formation of stable and functional basement membranes, which play fundamental roles in differentiation, proliferation, survival and migration of cells[11]. Moreover, combined with non-adhesive proteins such as BSA, CN/BSA coating promotes cell attachment[12]. First, we mixed 10 μ L of CN solution (Sigma-Aldrich, 1 mg/mL) and 490 μ L of acetic acid (0.25 % (v/v)) in order to prepare a CN solution (20 μ g/mL). Then, we prepared a BSA solution (Sigma-Aldrich, 0.02 % (w/v)) in PBS 1X. Finally, the CN/BSA coating solution was obtained by mixing 298.8 μ L of CN solution (20 μ g/mL) and 1.2 μ L of BSA solution (0.02 % (w/v)).

2.2.6 5-FU solution

The cytotoxicity experiments were carried out by adding 5-fluorouracil (5-FU) to the cell culture medium. 5-FU is a chemotherapy drug commonly used for colorectal and metastatic breast cancers, which are resistant to first line chemotherapy drugs[13]. 5-FU's mechanism of action is depicted in Fig.2.4. This chemotherapy drug enters the cells through a carrier-mediated transport system. Once, inside the cell, 5-FU is converted to 5-fluorodeoxyuridine monophosphate (5-FdUMP) and , this product binds to the nucleotide-binding site of the enzyme thymidylate synthase, thereby blocking binding of the normal substrate deoxyuridine monophosphate (dUMP)[14]. This enzyme, converts dUMP to deoxythymidine monophosphate (dTMP) during DNA replication and repair. As a result, 5-FU drug inhibits DNA synthesis and eventually blocks cell division.

2.3. Cell culture procedure

A 7 mM solution of 5-FU (Sigma-Aldrich) was prepared by dissolving 5-FU ($M_{5-FU} = 130.08$ g/mol) in dimethyl sulfoxide (DMSO). DMSO is a frequently used organic solvent for drugs in cell culture[15]. For the cytotoxicity assays, 5-FU (7 mM) was diluted in the supplemented DMEM at the desired concentrations $10\ \mu\text{M}$ and $100\ \mu\text{M}$ for the cytotoxicity experiments.

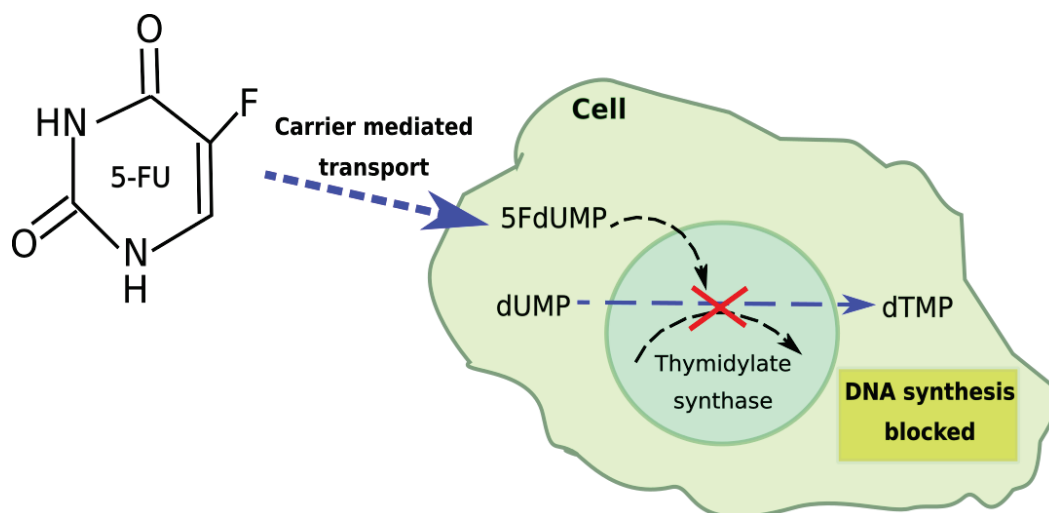


Figure 2.4 – Mechanism of action of 5-FU drug inside the cell. Figure adapted from Fig.1 in [16]. Copyright 2016 by Elsevier. Adapted with permission.

2.3 Cell culture procedure

2.3.1 Cell culture conditions

The cells were cultured in a humidified incubator at 37°C and under a 5% CO_2 environment to maintain physiological pH. Moreover, cell culture work was carried out under sterile conditions in a laminar flow Cytosafe 2004 (Faster) with autoclaved cell culture equipment.

2.3.2 Sub-culturing cells

MCF-7 and MDA-MB-231 cells were cultured in Petri dishes (5 mL), where they freely proliferated. However, in cell culture, when the cells reach a confluent state occupying all the available surface, contact inhibition within the cell layer occurs[17]. This means that cell proliferation is significantly slowed down. Therefore, in order to maintain an active cell cycle and cell proliferation, the cells were sub-cultured before reaching confluency by seeding a fraction of the cells in new Petri dishes filled with fresh growth medium. First, cell medium was gently removed using a Pasteur pipette and the cell monolayer was washed twice with PBS 1X. Afterwards, 1 mL of Trypsin (ThermoFisher), which is a proteolytic enzyme frequently used to detach cells from the adherent substrate, was added. Then, the Petri dish was incubated at 37°C for 3 min to ensure optimum activity of the enzyme[18]. After that, detached cells were transferred to 4 mL of cell culture medium and centrifuged at $1000\ g$ for 5 min. Right after, the supernatant was removed and the spun down cell pellet was re-suspended in 1 mL of fresh culture medium. Finally, cells were transferred into new Petri dishes. The seeding densities were adjusted for a sub-cultivation of cells twice a week for both MCF-7 and MDA-MB-231 cells.

2.3.3 Cell preparation for ECIS experiments

Cells for ECIS experiments were collected following the sub-culturing steps described in the previous section. In addition, before electrode inoculation, cells were counted to determine a cell density ~ 1000 cells/mm² and then seeded.

2.4 ECIS device fabrication

In electrical impedance experiments, another important aspect that has been explored is the electrode design optimization of the microelectrodes used for the cell-based assays. A geometrically optimized sensor for bioimpedance measurements can result in enhancement of the electrode sensitivity. Therefore, several design parameters have been evaluated to understand their effects on the sensitivity and overall working of the IDEs, such as the number, width, height and length of bands as well as the inter-band spacing[19]. For example, IDE optimization was performed by Radke et al.[20] for enhanced detection of bacteria. Their simulations revealed that the optimal IDE electrode band width and spacing were 3 and 4 μm , respectively for their application. They demonstrated that careful design of the electrode spacing influenced the penetration depth of the electric captured bacteria instead of the bulk solution[20]. Similarly, Alexander Jr et al.[21] examined the effect of electrode width and spacing of IDEs for impedance-based breast tumor cells (Hs 578T) detection and characterization. Their results were in agreement with Radke[20], IDEs with smaller electrode spacing (on the order of cell size), in their case 15 μm , were more sensitive to the presence of cells due to the concentrated penetration depth. By decreasing the electrode gap the effective electrode area was increased causing an increase in the sensitivity of the device[21].

Another group interested on optimization of IDEs for bioimpedance experiments was Ibrahim et al.[22], who investigated the optimal ratio between the width of the electrodes and the gap between the electrodes to expand the useful frequency range and the optimal number of electrode bands. According to them, the optimized geometry of an interdigitated sensor is to choose a ratio between the gap and the width of the electrodes equal to 0.66 in order to expand the useful frequency range. This design rule contrasts with the results of Radke and Alexander with ratios of 0.75 and 0.33, respectively. It is important to bear in mind that if the electrode width and length are reduced to increase the sensitivity, the number of effective cells covering the electrodes would be reduced, which is not desirable. Therefore, a trade-off of the sensitivity and the effective cell number has to be made in sensor design[23]. Additionally, as the electrode width reduces, the impedance of each electrode branch will increase, which would cause a large electrical potential difference along the electrode[23]. Moreover, reducing the width and the gap of the electrode bands might increase the complexity of the fabrication process described in this chapter, particularly during the lift-off process where adjacent electrode bands could easily be removed. Thus, we decided to work with a ratio between the gap and the width of the electrodes equal to 1, a value near the one proposed by Ibrahim[22] and easy to fabricate.

2.4. ECIS device fabrication

In this work, the ECIS system was made using interdigitated electrodes (IDEs) located at the bottom of a reservoir (diameter of 5 mm) of PolyDiMethyl Siloxane (PDMS). The IDEs were patterned on glass slides following the protocols described in the next sections. PDMS is a chemically inert and hydrophobic silicone elastomer frequently used in soft lithography and microfabrication for biomedical applications[24]. It was bonded to the glass slides by surface activation with oxygen plasma treatment for 3 min at 1100 mTorr with 40 sccm O_2 and 29.6 W. The interdigitated electrode configuration comprised 39 electrode fingers of $20\ \mu\text{m}$ width, 1 mm length and with inter-electrode gaps of $20\ \mu\text{m}$ as depicted in Fig.2.5. The following sections describe the fabrication processes for Au, ITO, Au coated with IrO_x and ITO coated with IrO_x IDEs.



Figure 2.5 – (a) Top view of the ECIS system with bonded PDMS reservoir (5 mm diameter). (b) Interdigitated electrode dimensions: $s = 20\ \mu\text{m}$, $w = 20\ \mu\text{m}$ and $l = 1\ \text{mm}$.

2.4.1 Gold electrodes

Au IDEs were fabricated following the process depicted in Fig. 2.6:

- A 1.5 μm layer of positive photoresist (S1813, ROHM Haas) was spun coated at 3000 rpm for 30 s onto glass slides (76 x 26 mm, Knittel glass).
- After softbaking on a hotplate at 120°C, for 3 min, the glass slides were exposed to UV light (7.5 mW/cm^2) using a photomask.
- The photoresist was then developed in an alkaline solution (Developer 351, dilution 1:10) for 1 min.
- The slides were cleaned using oxygen plasma treatment (29,6 W, 1100 mTorr and 40 sccm O_2 for 3 min).
- A layer of titanium (15 nm) and a layer of gold (50 nm) were deposited by electron beam physical vapor deposition (EVA300, Alliance Concept).
- The photoresist was removed by lift-off with acetone leaving only the Au electrode pattern on the glass slide.

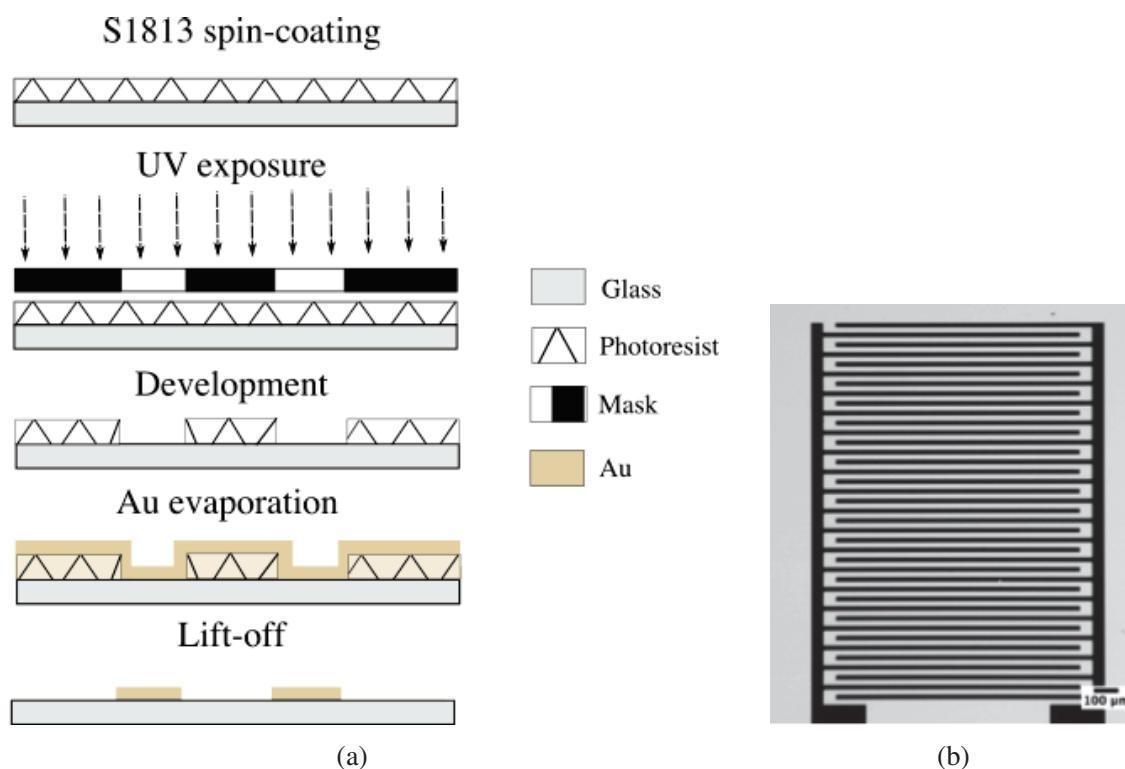


Figure 2.6 – (a) Fabrication process of Au IDEs: S1813 spin coating, UV exposure on mask, photoresist development, Au evaporation and lift-off. (The drawing is not to scale) (b) Microscopy image of Au IDEs on glass slides.

2.4.2 ITO electrodes

The ITO IDEs were fabricated using the same photolithography steps (spin coating, exposure and development) as Au IDEs. However, there were a few differences. As substrates we used glass slides coated with a 370 nm layer of ITO (76 x 26 mm, Solems) as depicted in Fig. 2.7a:

- Following the photolithography steps, we deposited a 200 nm layer of chromium (Cr) instead of Au by electron beam vapor deposition. The Cr layer was used as a mask to locally protect ITO during the subsequent Reactive Ion Etching (RIE, Oxford Instruments) steps.
- A lift-off step with acetone was then used to reveal the Cr pattern on the slides.
- The following RIE process was adapted from previous studies[25] and it consisted of the following two phases:
 - First, plasma etching with CH_4 and H_2 (5 sscm and 50 sscm respectively) 100 mTorr and 250 W for 50 min to etch the unprotected ITO surface.
 - Second, a treatment with Ar and O_2 (100 sscm and 100 sscm respectively) with 400 mTorr and 350 W for 20 min to remove the amorphous carbon layer produced during the first step.
- Finally, the Cr layer covering the ITO electrodes was removed with a Cr etch solution for 2 min (Chrome etch 18, OSC).

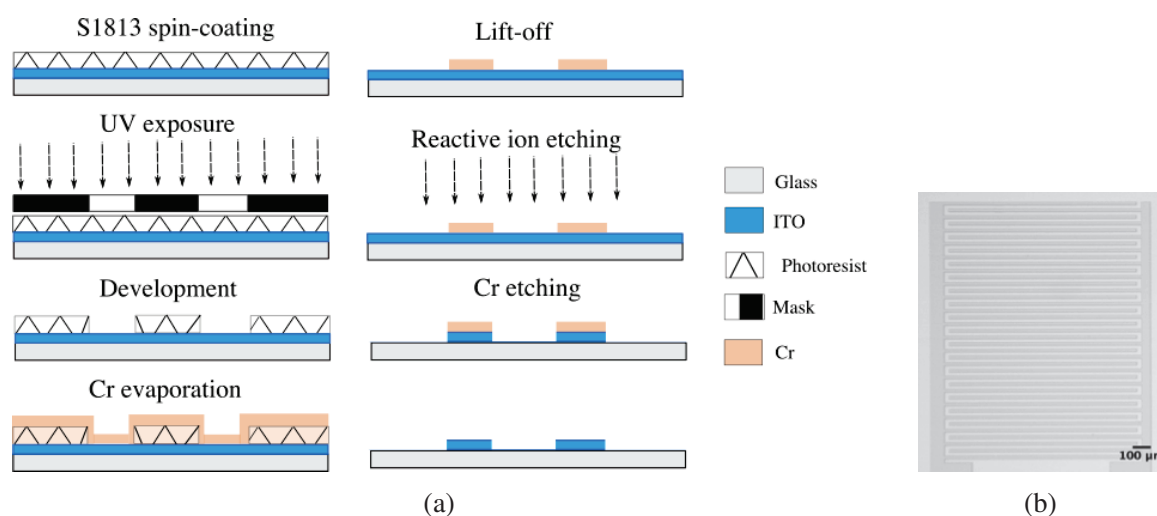


Figure 2.7 – (a) Fabrication process of ITO IDEs: S1813 spin coating, UV exposure on mask, photoresist development, Cr evaporation, Cr Lift-off, RIE and Cr etching (the drawing is not to scale). (b) Microscopy image of ITO IDEs on glass slides.

2.4.3 Electrodeposition of IrO_x

The electrodeposition step was carried out using filtered IrO_x solution at room temperature (pore, 0.20 μm). Fig.2.8 shows the three-electrode configuration used. The working electrode (WE) was the IDEs, the reference electrode was an Ag-AgCl electrode (RE) and finally we used a Pt electrode as the counter electrode (CE). IrO_x was deposited on the electrodes by cycling the WE potential between 0 and 0.7 V Ag-AgCl at a scan rate of 20 mV/s.

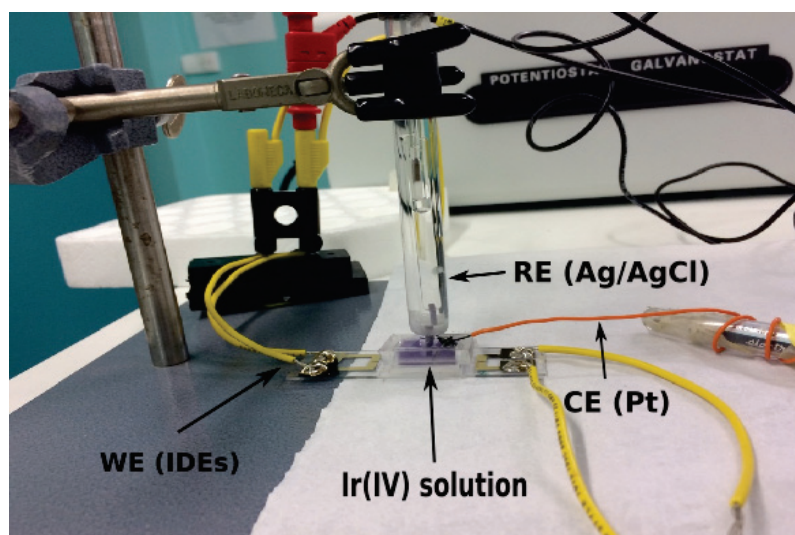


Figure 2.8 – IrO_x electrodeposition set-up. Working electrode (WE), Counter electrode (CE) and Reference electrode (RE)

2.5 Experimental set-up

2.5.1 Device preparation for ECIS experiments

Electrode connections for Au-IDEs were welded with soldering tin, whereas for ITO-IDEs connections were made with an electrically conductive, silver-filled epoxy paste (EPO-TEK[®] E4110). We then rinsed the electrodes with ethanol for 3 min. When electrodes were prepared for cell adhesion, we cleaned the electrodes 3 times with supplemented DMEM and with PBS 1X. Once cleaned, the electrode surfaces were incubated with the mixture CN/BSA at 37 °C for 30 min. After that, the electrodes were rinsed again with PBS 1X and the supplemented DMEM. This coating step was used to enhance cell adhesion[10].

2.5.2 Impedance measurement set-up

The standard Electrical Impedance Spectroscopy method (EIS) consists on using electrodes to apply a small amplitude sinusoidal voltage to the system under test, for a wide range of frequencies and measuring the resultant AC current. The excitation signal, expressed as a function of time is:

$$V(t) = V_0 \sin(\omega t) \quad (2.1)$$

where V_0 and ω represent the voltage amplitude and the angular frequency, respectively.

2.5. Experimental set-up

Due to the fact that a small voltage is used, the system remains in the linear response region and the resulting current can be described by the following expression:

$$I(t) = I_0 \sin(\omega t + \phi) \quad (2.2)$$

where I_0 is the current amplitude and ϕ is the phase shift. The current signal will have the same frequency as $V(t)$ but with a shift in phase[26]. The electrical impedance $Z(\omega)$ of the system can then be calculated using an expression similar to Ohm's law:

$$\underline{Z}(\omega) = \frac{V(t)}{I(t)} \quad (2.3)$$

For practical reasons, this impedance is represented as a complex number detailed as follows:

$$\underline{Z} = \frac{V}{I} = Z' + jZ'' = |\underline{Z}(\omega)|e^{j\phi} \quad (2.4)$$

where Z' and Z'' correspond to the real and imaginary component respectively; j is the imaginary unit number that satisfies $j^2 = -1$, and $|\underline{Z}(\omega)|$ is the magnitude of the impedance.

\underline{Z} is associated to a vector quantity that has a magnitude and a direction given by the angle $\phi = \tan^{-1}(\frac{Z''}{Z'})$ which depends on the frequency of the signal $f = \frac{\omega}{2\pi}$. Hence, by varying the frequency of the applied signal one can get the impedance of the system as a function of the frequency. This electrical impedance can be considered as the opposition encountered when an alternating current (AC) flows through the system. EIS measurements are typically visualized using two kinds of plots. One of them is the **Nyquist plot** in which $-Z'$ is plotted as a function of Z'' . In this plot, low frequency data are found on the right side and high frequency data on the left. However, they have one major drawback: frequency values are implicit rather than explicit[27]. Therefore, **Bode plot** format is also widely used to represent the data. In this case, both impedance magnitude and phase shift are represented as a function of frequency in a logarithmic scale. Both Nyquist and Bode plots complement each other in the analysis of impedance results.

EIS is a commonly used experimental technique that can deconvolute the contributions of multiple physical processes to the overall electrical impedance of a sample. Typically, researchers fit the experimental impedance spectrum with an appropriate physical model in order to quantify relevant properties of the system[28]. Nonetheless, the choice of the model is a fundamental step because it requires careful justification, as there is more than one model that may fit the EIS data equally well. That is why the choice of the model will depend on the system under investigation and on the physical intuition of the researcher, which can be reinforced by the use of numerical simulation[29]. A common way to model EIS data is to use an equivalent circuit, made of a network of resistors, capacitors and other circuit elements that can describe the system behavior. Depending on how the electronic components are configured, both the magnitude and the phase shift of the resulting current in a measurement can be determined. Hence, some knowledge of the impedance of the standard circuit components, shown in Table 2.3 is quite useful to start with electrical circuit modeling.

2.5. Experimental set-up

Element	Impedance Z	Phase angle	Frequency Dependence
Resistor (R)	R	0°	No
Capacitor (C)	$\frac{1}{j\omega C}$	-90°	Yes
Constant Phase Element (CPE)	$\frac{1}{Q(j\omega)^\alpha}$	$0-90^\circ$	Yes

Table 2.3 – Impedance of standard circuit components.

Furthermore, in impedance spectroscopy there are three main electrode configurations that can be used in measurement setup. In order to understand these setups, it is essential to know the common designations for the electrodes: Working, Reference and Counter or Auxiliary electrode. The working electrode (WE) is the sensing electrode on which cells adhere and relevant data are collected whereas the counter electrode (CE) is the one that closes the current circuit in the experiment. As for the reference electrode (RE), it is characterized by a stable and well defined electrochemical potential (at constant temperature), which does not change with the change of ions concentration in solution and are used as a reference for measuring potentials of other electrodes[30].

2.5. Experimental set-up

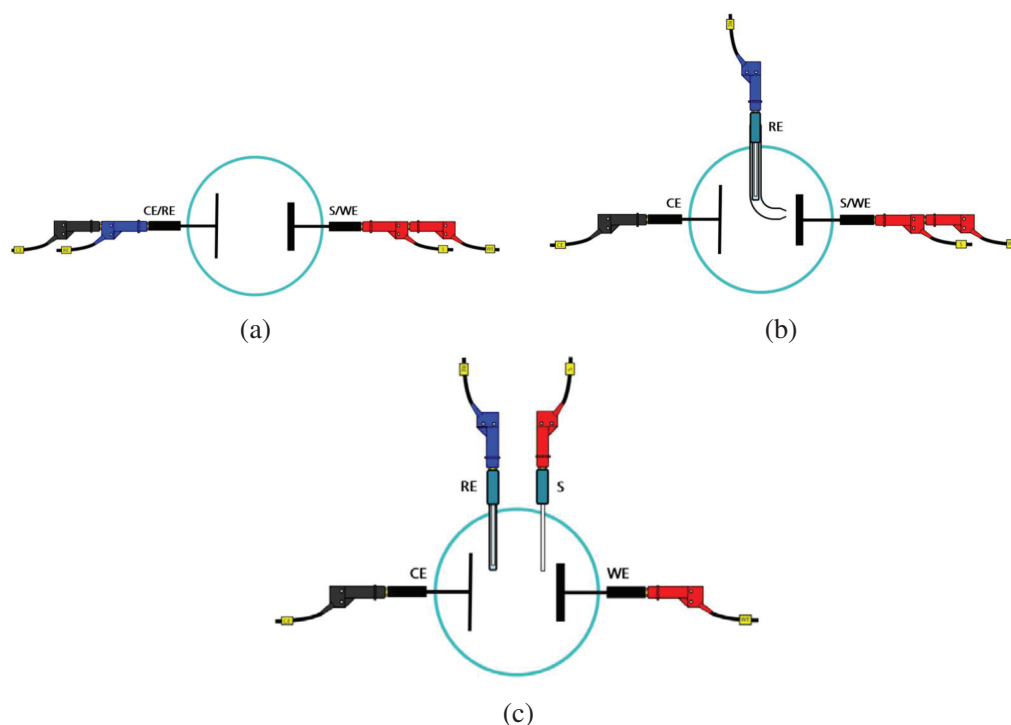


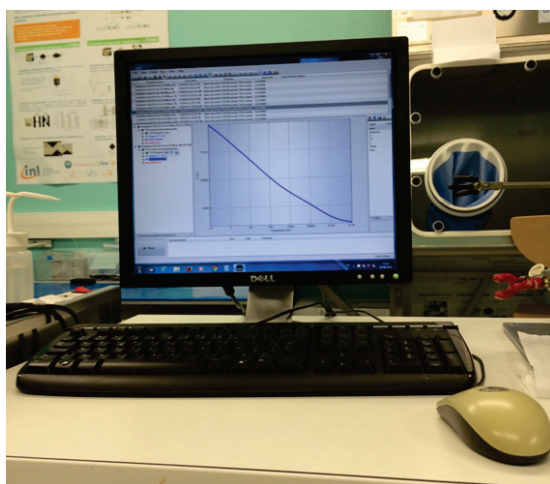
Figure 2.9 – Schematic view of the different electrode configurations. a) 2-electrode setup. b) 3-electrode setup and c) 4-electrode setup. Figure adapted from figures 4-6 in[31].

- **Two electrode configuration:** It is the simplest set up in which voltage is being applied through the WE and measured through CE and RE connected together, as shown in Fig. 2.9a. Hence, total impedance corresponds to contributions from connections, electrodes, electrode-electrolyte interfaces at both electrodes and impedance between the two of them[32].
- **Three electrode configuration:** In this mode, the potential difference is controlled between the WE and CE while the RE is kept at close proximity of the WE, as depicted in Fig. 2.9b. This kind of setup is often used to measure the voltage drop depending on the position of RE and WE. Therefore, it is useful for studying changes on the WE surface without the influence of electrode polarization effects (discussed later) coming from the CE. Thus undesirable drifting of electrode potential can be avoided by using three electrode configuration[32].
- **Four electrode configuration:** In this configuration, the sensing electrode is decoupled from working electrode and potential drop is measured between inner two electrodes (sensing and RE) while current is passed through outer two electrodes (WE and CE), as shown in Fig. 2.9c. Basically, this method provides information of the medium between the inner electrodes[32].

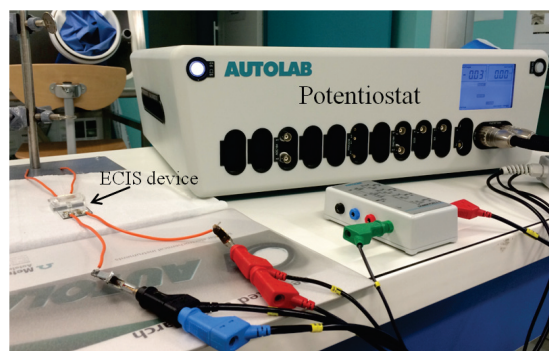
In our case, we chose a two electrode configuration which is well suited for an IDE geometry. We carried out the impedance measurements using a potentiostat (PGSTAT, Metrohm). Results were analyzed using the Nova 2.1 (Metrohm) software (Fig.2.10). The two classical impedance representations of the measured data, Bode and Nyquist, are available. Measurements were performed from 1 MHz to 100 mHz, using a sinusoidal signal amplitude of 10 mV_{RMS} (0 V off-set). The small AC signal applied should be harmless to the cell and does not adversely affect the physiology of the cells during the experiment[33]. With a signal of 10 mV_{RMS}, the average applied electric field between the interdigitated electrodes separated by 20 μm would be approximately 500 V/m, which is a low value. Nevertheless, we have to take into account that

2.5. Experimental set-up

the electric field will not be the same along the electrode surfaces due to both the ohmic loss along the electrode itself (ITO for example) and the hemispherical symmetry of the electrodes' geometry. The electric field applied to the cells on the border of the electrodes will be higher (> 500 V/m) than that applied to the cells on the center. Therefore, we would need to use a finite element simulation in order to determine the electric field at each point on the electrode surfaces. According to the literature, in addition to Joule heating, the application of an external electric field may cause the formation of pores in the cell membrane, termed electroporation[34]. This formation requires high-intensity electric fields (tenths of kV/m)[35] that increase the membrane potential from its resting value of around 100 mV up to the breakdown membrane potential, which, depending on the cell membrane, ranges from 200 mV to 1 V[36]. Finally, in order to isolate the system from external interferences, measurements were carried out inside a home-made Faraday cage.



(a)



(b)

Figure 2.10 – Measurement set-up elements: (a) PC-data acquisition with Nova software (b) ECIS device connected to the Potentiostat.

Bibliography

- [1] Xiaofeng Dai, Hongye Cheng, Zhonghu Bai, and Jia Li. “Breast Cancer Cell Line Classification and Its Relevance with Breast Tumor Subtyping”. In: *Journal of Cancer* 8.16 (2017), pp. 3131–3141. DOI: <https://doi.org/10.7150/jca.18457>.
- [2] Jose Russo and Irma H. Russo. *Molecular Basis of Breast Cancer: Prevention and Treatment*. Verlag Berlin Heidelberg: Springer, 2004.
- [3] Kathryn J. Chavez, Sireesha V. Garimella, and Stanley Lipkowitz. “Triple Negative Breast Cancer Cell Lines: One Tool in the Search for Better Treatment of Triple Negative Breast Cancer”. In: *Breast Disease* 32.1-2 (2010), pp. 35–48. DOI: <https://doi.org/10.3233/BD-2010-0307>.
- [4] Aleix Prat and Charles M. Perou. “Deconstructing the molecular portraits of breast cancer”. In: *Molecular Oncology* 5.1 (2011), pp. 5–23. DOI: <https://doi.org/10.1016/j.molonc.2010.11.003>.
- [5] Deborah L Holliday and Valerie Speirs. “Choosing the right cell line for breast cancer research”. In: *Breast Cancer Research* 13.4 (2011), pp. 1–7. DOI: <https://doi.org/10.1016/j.molonc.2010.11.003>.
- [6] Kazusuke Yamanaka. “Anodically Electrodeposited Iridium Oxide Films (AEIROF) from Alkaline Solutions for Electrochromic Display Devices”. In: *Japanese Journal of Applied Physics* 28.4 (1989), pp. 1–9. DOI: <https://doi.org/10.1143/jjap.28.632>.
- [7] Imene Feriel AIT-ALI. “Développement et intégration de microcapteurs de pH et de température dans des dispositifs microfluidiques polymères”. PhD thesis. Université Claude Bernard Lyon 1, 2014.
- [8] ThermoFisher SCIENTIFIC. *Dulbecco’s Modified Eagle Medium description*. URL: <https://www.thermofisher.com/fr/fr/home/life-science/cell-culture/mammalian-cell-culture/classical-media/dmem.html>.
- [9] Chih-Yeuh Fang, Chung-Chun Wu, Chia-Lang Fang, Wei-Yu Chen, and Chi-Long Chen. “Long-term growth comparison studies of FBS and FBS alternatives in six head and neck cell lines”. In: *PLoS ONE* 12.6 (2017), pp. 1–27. DOI: <http://dx.doi.org/10.1371/journal.pone.0178960>.

BIBLIOGRAPHY

- [10] Antoine Confavreux. “Optimisation des conditions de migration et de détachement de lignées cancéreuses du cancer du sein en vue de leur tri fonctionnel”. PhD thesis. Université Claude Bernard Lyon 1, 2014.
- [11] Ernst Pöschl, Ursula Schlötzer-Schrehardt, Bent Brachvogel, Kenji Saito, Yoshifumi Ni-nomiya, and Ulrike Mayer. “Collagen IV is essential for basement membrane stability but dispensable for initiation of its assembly during early development”. In: *Development* 131 (2004). DOI: <https://doi.org/10.1242/dev.01037>.
- [12] Jennifer E. Koblinski, Michael Wu, Borries Demeler, Karin Jacob, and Hynda K. Kleinman. “Matrix cell adhesion activation by non-adhesion proteins”. In: *Journal of Cell Science* 118 (2005). DOI: <https://doi.org/10.1242/jcs.02411>.
- [13] Reyhaneh Akbari and Hamid Akbari Javar. “Efficacy of Capecitabine and 5-Fluorouracil (5-FU) on the human breast cancer cell line (MCF7)-effect of concentration”. In: *American Journal of Research Communication* 1.6 (2013), pp. 75–91.
- [14] Daniel B. Longley, D. Paul Harkin, and Patrick G. Johnston. “5-FLUOROURACIL: MECHANISMS OF ACTION AND CLINICAL STRATEGIES”. In: *Nature Reviews* 3 (2003), pp. 330–338. DOI: <https://doi.org/10.1038/nrc1074>.
- [15] Edward J. Massaro. *handbook of HUMAN TOXICOLOGY*. Boca Raton, Florida: CRC Press LLC, 1997.
- [16] T.Gracia-Cazaña, S.González, and Y.Gilaberte. “Resistance of Nonmelanoma Skin Cancer to Nonsurgical Treatments. Part I: Topical Treatments”. In: *Actas Dermo-Sifiliográficas (English Edition)* 107.730-739 (2016), pp. 75–91. DOI: <https://doi.org/10.1016/j.adengl.2016.08.016>.
- [17] Alberto Puliafito, Lars Hufnagel, Pierre Neveu, Sebastian Streichan, Alex Sigal, Kuchnir Fygenon, and Boris I. Shraiman. “Collective and single cell behavior in epithelial contact inhibition”. In: *Proc Natl Acad Sci U S A* 109.3 (2012), pp. 739–744. DOI: <https://doi.org/10.1073/pnas.1007809109>.
- [18] Sigma-Aldrich. *Cell Dissociation with Trypsin*. URL: <https://www.sigmaaldrich.com/technical-documents/articles/biology/cell-dissociation-with-trypsin.html>.
- [19] Madhukar Varshney and Yanbin Li. “Interdigitated array microelectrodes based impedance biosensors for detection of bacterial cells”. In: *Biosensors and Bioelectronics* 24.10 (2009), pp. 2951–2960. DOI: <https://doi.org/10.1016/j.bios.2008.10.001>.
- [20] Stephen M. Radke and Evangelyn C. Alocilja. “Design and Fabrication of a Microimpedance Biosensor for Bacterial Detection”. In: *Journal of Physics: Conference Series* 4.4 (2004), pp. 434–440. DOI: <https://doi.org/10.1109/JSEN.2004.830300>.
- [21] Frank Alexander Jr, Dorielle T Price, and Shekhar Bhansali. “Optimization of interdigitated electrode (IDE) arrays for impedance based evaluation of Hs 578T cancer cells”. In: *Journal of Physics: Conference Series* 224.1 (2010), pp. 1–4. DOI: <https://doi.org/10.1088/1742-6596/224/1/012134>.

BIBLIOGRAPHY

- [22] Mouhamad Ibrahim, Julien Claudela, Djilali Kourtiche, and Mustapha Nadi. “Geometric parameters optimization of planar interdigitated electrodes for bioimpedance spectroscopy”. In: *Journal of Electrical Bioimpedance* 4.1 (2013), pp. 13–22. DOI: <https://doi.org/10.5617/jeb.304>.
- [23] Ping Wang and Qingjun Liu. *Cell-Based Biosensors Principles and Applications*. Norwood, MA: ArtechHouse, 2010.
- [24] Ali Khademhosseini, Jeffrey Borenstein, Mehmet Toner, and Suichi Takayama. *Micro and Nanoengineering of the Cell Microenvironment: Technologies and Applications*. BOSTON: ARTECH HOUSE, 2008.
- [25] Mikio Mohri, Hiroaki Kakinuma, Masaaki Sakamoto, and Hideo Sawai. “Plasma Etching of ITO Thin Films Using a CH_4/H_2 Gas Mixture”. In: *Japanese Journal of Applied Physics* 29.10 (1990). DOI: <https://doi.org/10.1143/JJAP.29.L1932>.
- [26] Frank A. Alexander, Dorielle Tucker Price, and Shekhar Bhansali. “From Cellular Cultures to Cellular Spheroids: Is Impedance Spectroscopy a Viable Tool for Monitoring Multicellular Spheroid (MCS) Drug Models?” In: *IEEE Reviews in Biomedical Engineering* 6 (2012), pp. 63–76. DOI: <https://doi.org/10.1109/RBME.2012.2222023>.
- [27] Metrohm. *Electrochemical Impedance Spectroscopy (EIS) Part 1 – Basic Principles*. URL: <https://www.metrohm.com/en-gb/applications/AN-EIS-001>.
- [28] Benjamin E. McNealy, Jun Jiang, and Joshua L. Hertz. “A Precise, Reduced-Parameter Model of Thin Film Electrolyte Impedance”. In: *Journal of The Electrochemical Society* 162.6 (2015), F537–F546. DOI: <https://doi.org/10.1149/2.0281506jes>.
- [29] Pascale Pham, Sébastien Roux, Frédéric Matonti, Florent Dupont, Vincent Agache, and Frédéric Chavane. “Post-implantation impedance spectroscopy of subretinal microelectrode arrays, OCT imaging and numerical simulation: towards a more precise neuroprosthesis monitoring tool”. In: *Journal of Neural Engineering* 10.4 (2013), pp. 1–13. DOI: <https://doi.org/10.1088/1741-2560/10/4/046002>.
- [30] Metrohm Autolab B. V. *Reference electrodes and their usage*. URL: <http://www.autolabj.com/appl.files/appl%5C%20note/App1038.pdf>.
- [31] Metrohm Autolab B. V. *Basic overview of the working principle of a potentiostat/galvanostat (PGSTAT)– Electrochemical cell setup*. URL: http://www.ecochemie.nl/download/Applicationnotes/Autolab_Application_Note_EC08.pdf.
- [32] Rangadhar Pradhan, Analava Mitra, and Soumen Das. “Characterization of Electrode/Electrolyte Interface of ECIS Devices”. In: *Electroanalysis* 24.12 (2012), pp. 2405–2414. DOI: <https://doi.org/10.1002/elan.201200455>.
- [33] Biao Xi, Naichen Yu, Xiaobo Wang, Xiao Xu, and Yama A. Abassi. “The application of cell-based label-free technology in drug discovery”. In: *Biotechnology Journal* 3.4 (2008), pp. 484–495. DOI: <https://doi.org/10.1002/biot.200800020>.
- [34] Eugène Vorobiev and Nikolai Lebovka. *Electrotechnologies for Extraction from Food Plants and Biomaterials*. Springer Science+Business Media, LLC: Springer, 2008.

BIBLIOGRAPHY

- [35] Gorazd Pucihar, Jasna Krmelj, Matej Rebersek, Tina Batista Napotnik, and Damijan Miklavcic. “Equivalent Pulse Parameters for Electroporation”. In: *IEEE Transactions on Biomedical Engineering* 58.11 (2011), pp. 3279–3288. DOI: <https://doi.org/10.1109/TBME.2011.2167232>.
- [36] T Y Tsong. “Electroporation of cell membranes”. In: *Biophysical Journal* 60.2 (1991), pp. 297–306. DOI: [https://doi.org/10.1016/S0006-3495\(91\)82054-9](https://doi.org/10.1016/S0006-3495(91)82054-9).

Characterization of Au and ITO IDEs for ECIS experiments

The objective of this chapter is to compare Au and ITO as electrode materials in ECIS experiments. As explained previously, Au material is largely exploited for the development of ECIS assays in both academic and commercial systems. Conversely, ITO is scarcely reported in literature. Therefore, we decided to start our study with a comparison of Au and ITO IDEs responses from an impedance viewpoint. These electrode materials were characterized by impedance spectroscopy. This chapter includes the measurements carried out in KCl solutions at different concentrations and in the supplemented cell culture medium before and after functionalization of the electrodes with the CN/BSA coating. In addition, we characterized these materials in terms of ECIS sensitivity by introducing a normalized impedance. Finally, we compared different strategies including equivalent circuit modeling, to compare and extract the electrical parameters of our Au and ITO IDEs without the presence of biological cells.

3.1 Interdigitated electrodes in contact with an electrolyte

3.1.1 Theoretical aspects

3.1.1.1 Impedance contributions in an ECIS system without cells

The experimental setup for ECIS studies is a complex system in which the electrical impedance of every component contributes to the total impedance measured during an experiment. An example of an equivalent electrical impedance model representing a coplanar two-electrode configuration in the absence of biological cells, is presented in Fig. 3.1. The total impedance of the system is affected by several contributions: Z_{lead} represents the impedance of the connecting cables and bonding wires of the system; $Z_{electrode}$ includes the ohmic resistance of the electrodes; $Z_{interface}$ results from the formation of an electrical double layer at the electrode/electrolyte interface when the electrode is immersed in an electrolyte; $Z_{parasitic}$ is associated with direct coupling between the two electrodes and $Z_{solution}$ corresponds to the resistive behavior of the cell culture solution in between the two electrodes. Among these contributions, depending on the experimental conditions, Z_{lead} can generally be neglected. We will next present in detail the different contributions that can affect the value of the total impedance and therefore, electrode sensitivity and response.

3.1. Interdigitated electrodes in contact with an electrolyte

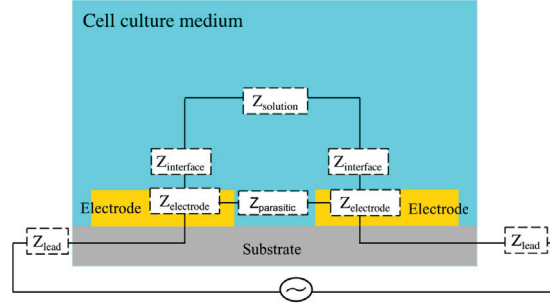


Figure 3.1 – Schematic of the different impedance contributions in a coplanar two electrode system in absence of cells during an ECIS assay (the drawing is not to scale).

1. **Contribution of the cell culture medium:** As mentioned earlier, during an ECIS experiment, cells need to be immersed in culture medium. Generally, cell culture media and physiological buffers contain a high concentration of ions such as Na^+ , Cl^- , K^+ , Ca^{2+} , Mg^{2+} and SO_4^{2-} in order to provide osmotic balance for the cells and also contain necessary inorganic chemicals[1]. In Fig. 3.1, Z_{solution} corresponds to the resistance of the culture medium. Its value can be determined from the "spreading resistance", which is the resistance encountered by the current as it spreads in through the electrolyte from one electrode to the other. For microelectrodes fabricated using planar fabrication techniques, there is only one side of the electrodes that is exposed to the electrolyte solution. In the case of planar interdigitated electrodes, the spreading resistance R_s can be expressed by the following equation[2]:

$$R_s = \frac{K_{IDE}}{\sigma} \quad (3.1)$$

where σ is the medium conductivity and K_{IDE} is the IDE cell constant which is expressed by[2]:

$$K_{IDE} = \frac{2}{(N-1)L} \cdot \frac{\kappa(k)}{\kappa(\sqrt{1-k^2})} \quad (3.2)$$

where N is the total number of electrode bands in IDE configuration, L is the electrode band length. $\kappa(k)$ is the complete elliptic integral of the first kind calculated using relation 3.3 and k is expressed by equation 3.4 in the case of more than two bands.

$$\kappa(k) = \int_0^1 \frac{1}{\sqrt{(1-t^2)(1-k^2t^2)}} dt \quad (3.3)$$

$$k = \cos\left(\frac{\pi}{2} \cdot \frac{w}{s+w}\right) \quad (3.4)$$

where s and w are respectively, the inter-electrode gap and the electrode band width.

3.1. Interdigitated electrodes in contact with an electrolyte

Additionally, $Z_{parasitic}$ which represents the direct capacitive coupling between electrodes, also depends on the cell culture medium and the geometry of the electrodes. The value of its parasitic capacitance $C_{parasitic}$ for IDE can be expressed as[2]:

$$C_{parasitic} = \frac{\varepsilon_r \varepsilon_0}{K_{IDE}} \quad (3.5)$$

where ε_0 is the permittivity of free space ($8.854 \cdot 10^{-12}$ F/m) and ε_r is the relative dielectric constant of the medium between the two electrodes.

- 2. Contribution of the electrode-electrolyte interface:** When metallic electrodes are immersed in an electrolyte, there are two processes that can occur: non-faradaic and faradaic processes[3]. In faradaic processes electrons are transferred between the metallic electrode and a chemical species, resulting in either reduction or oxidation of this species present in the electrolyte solution. The electron transfer phenomenon can be modeled for example as a linear resistive component, called the charge transfer resistance R_{ct} [4]:

$$R_{ct} = \frac{RT}{J_0 z F} \quad (3.6)$$

where J_0 is the equilibrium exchange current density, R is the gas constant, T is the temperature, n is the number of electrons involved in the charge transfer reaction and F is the Faraday's constant.

In non-faradaic reactions, no charges are transferred between the metallic electrode and species in solution. The flow of current is induced by ion organization after metal polarization. Indeed, if the metal electrode surface is polarized, a layer of ions of opposite charge on the electrolyte side of the interface is formed in order to restore charge balance. This results in the formation of a thin layer of solution where electrical neutrality is not kept, in the solution side and in close proximity to the electrode surface. This layer is referred to as an electrical double layer as shown in Fig.3.2. Since charges cannot cross the electrode-electrolyte interface, this latter phenomenon is modeled by an interfacial capacitance, also known as the double layer capacitance. Various models are presented in the literature to describe this capacitance. For example, in the early Helmholtz model, all the counterions were assumed to be adsorbed at the electrode surface. This structure is associated with a conventional dielectric capacitor with two planar electrodes separated by a distance d_H . Later, Gouy and Chapman developed an electric double layer model accounting for the fact that the ions are mobile in electrolyte solutions and are driven by the coupled influences of diffusion and electrostatic forces. In this model, the ions are treated as point charges in the so called diffuse layer[5]. There is also the Gouy-Chapman-Stern model combining the two models previously described. According to this model, the double layer is formed by two layers: (i) a first layer known as the Stern (or Helmholtz) layer consisting of the compact layer of immobile ions adsorbed to the electrode surface and (ii) the diffuse layer where the ions are mobile and the Gouy-Chapman model applies[5].

3.1. Interdigitated electrodes in contact with an electrolyte

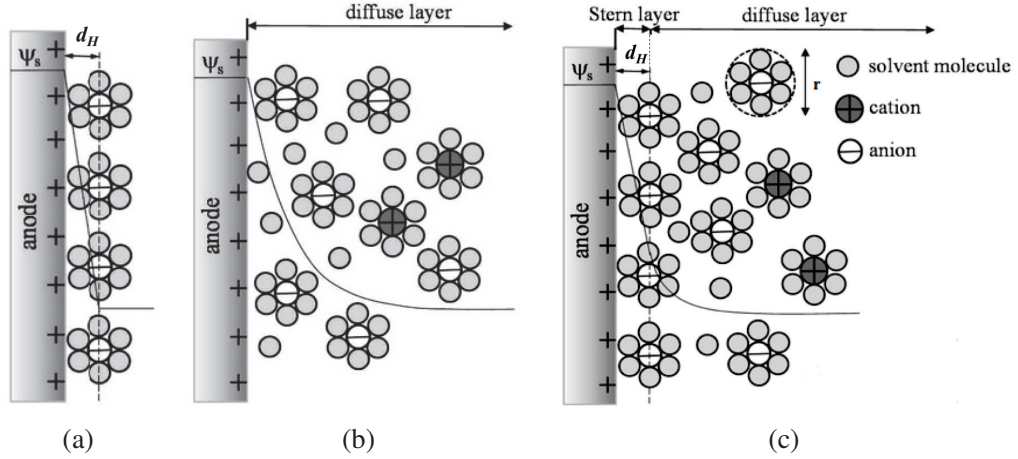


Figure 3.2 – Models of the double layer structure: (a) Helmholtz model (b) Gouy-Chapman model and (c) Gouy-Chapman-Stern model (ψ_s is the surface electrical potential and r is the diameter of solvated ions). Figure adapted from Fig.1 in [5]. Copyright 2011 by American Chemical Society.

According to the Gouy-Chapman-Stern model, the interfacial capacitance C_{int} is the series connection of the Helmholtz layer capacitance C_H and the diffuse layer capacitance (Gouy-Chapman capacitance) C_{diff} [4]. The interfacial capacitance is given by the following expression[4, 6]:

$$\frac{1}{C_{int}} = \frac{1}{C_H} + \frac{1}{C_{diff}} = \frac{d_H}{\epsilon'_r \epsilon_0} + \sqrt{\frac{k_B T_{abs}}{2.10^{-3} z^2 e^2 \epsilon_r \epsilon_0 c_0 N_A}} \quad (3.7)$$

where d_H is the thickness of the Helmholtz layer (approximated as the radius of solvated ions), ϵ'_r is the permittivity of the double layer, z is the valence of the ion in solution, c_0 is the bulk concentration of ions in the solution, N_A is the Avogadro constant, e is the electron charge, k_B is the Boltzmann constant and T is the absolute temperature.

If the electrolyte is very dilute, $C_H \gg C_{diff}$ leading to $C_{int} \approx C_{diff}$ whereas for highly concentrated solutions, $C_H \ll C_{diff}$ leading to $C_{int} \approx C_H$. The double layer capacitance for our electrodes is mainly determined by the relatively small diffusive capacitance for ionic concentrations below 1 M.

Nevertheless, due to the fact that in real systems, capacitance is almost never ideal, the double layer capacitance in equivalent circuit models is often replaced by an empirical frequency-dependent pseudo capacitive Constant Phase angle Element (CPE) that fits better experimental results. This CPE behavior has been attributed to different phenomena, such as non-uniformity, electrode roughness and surface reactivity[7] [8]. The electrical impedance of this element is given empirically by the expression:

$$\bar{Z}_{CPE_{int}} = \frac{1}{Q_{int}(j\omega)^{\alpha_{int}}} \quad (3.8)$$

where Q_{int} is a measure of the magnitude of the pseudo capacitance, which is equal to the ideal capacitance when $\alpha_{int} = 1$ [9], α_{int} being a factor between 0 and 1.

- 3. Contribution of the connecting cables:** The connections contribute to the total impedance of the system. For instance, the cables and bonding wires can give rise to parasitic resistance and inductance[10]. Based on the experimental conditions of the present studies, these contributions can be neglected.

3.1.1.2 Equivalent circuit modeling

In the literature, several studies have been published on the characterization of interdigitated electrodes using impedance spectroscopy. Various equivalent circuit models representing the experimental impedance data of these electrodes in contact with an electrolyte have been suggested[11] [12][6][13]. For instance, in Fig.3.3a, Timmer et al.[6] used an equivalent circuit comprising a double layer capacitance C_{int} , a parasitic capacitance $C_{parasitic}$, a solution resistance R_t and a lead resistance R_{lead} to study the frequency response of a conductivity platinum detector in contact with NaCl solutions at low ion concentrations. In another study, Hong et al.[13] used Pt electrodes in contact with 1X Tris-EDTA buffer solution to determine AC frequency characteristics as design parameters for coplanar impedance sensors (Fig.3.3b). In fact, they suggested two equivalent circuits: one model with C_{int} and a second model with CPE_{int} . They showed that using CPE_{int} ($WSS^1 < 0.1$), the fitting was much better than using C_{int} ($WSS < 5$). They therefore chose the model with C_{int} in order to simplify the complexity of real systems for developing impedance equations whereas the model with CPE_{int} was used for phenomenological interpretation. Similarly, Rana et al.[10] reported the equivalent circuit model in Fig.3.3c for Au IDEs in contact with KCl solutions. They focused on the quantification of R_t and $C_{parasitic}$ in the equivalent circuit, comprising R_t in series with C_{int} , both of which are in parallel with $C_{parasitic}$. Conversely, Baccar et al.[14] introduced the circuit model in Fig.3.3d for gold interdigitated electrodes in PBS solution for *E. Coli* detection using T4 phages. Here, in their model they did not take into account $C_{parasitic}$ and the double layer is represented by CPE_{int} instead of C_{int} . R_{ct} corresponds to the resistance of charge transfer at the chip/electrolyte.

¹Within Sum of Squares (WSS) estimates the population variance based on the variance within each of the samples

3.1. Interdigitated electrodes in contact with an electrolyte

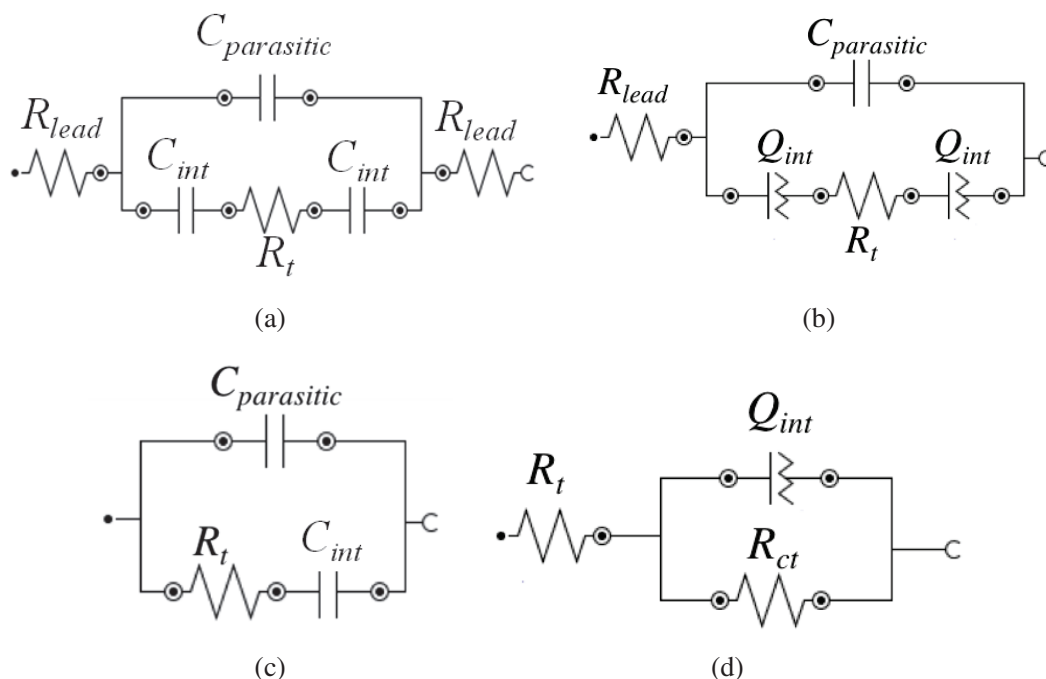


Figure 3.3 – Equivalent circuits models of IDEs in contact with an electrolyte reported by (a) Timmer et al.[6] (Copyright 2001 by Royal Society of Chemistry. Adapted with permission), (b) Hong et al.[13] (Copyright 2001 by Royal Society of Chemistry. Adapted with permission), (c) Rana et al.[10] (Copyright 2011 by Elsevier. Adapted with permission) and (d) Baccar et al.[14].

3.1.2 Impedance response of gold and ITO IDEs in KCl solutions

In this section, we studied at room temperature the behavior of Au and ITO electrodes in contact with solutions containing KCl at different concentrations over the frequency range $f = 1$ MHz to $f = 100$ mHz.

3.1.2.1 Gold IDEs

Gold IDEs were used here as the model electrode since it is the material that has been mainly used in reported ECIS assays. The impedance magnitudes and phases of Au IDEs using Bode representation are shown in Fig.3.4.

3.1. Interdigitated electrodes in contact with an electrolyte

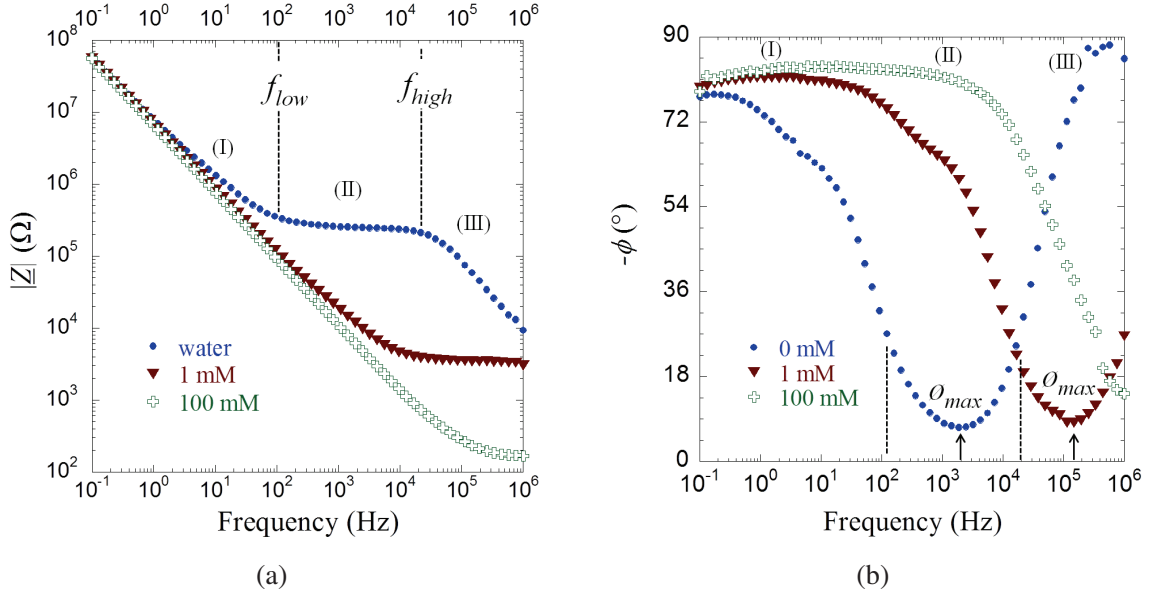


Figure 3.4 – (a) Magnitude and (b) Phase of the impedance spectra of Au IDEs ($s = 20 \mu\text{m}$, $w = 20 \mu\text{m}$ and $L = 1 \text{ mm}$) in contact with KCl solutions of different concentrations in the frequency range from 1 MHz to 100 mHz.

Both magnitude and phase plots depend on the presence or absence of KCl in solution and its concentration. For the solution of deionized water, we can observe three regions in the impedance spectrum:

1. In zone (I), at low frequencies from 100 mHz to $\sim 100 \text{ Hz}$, $\log|Z|$ decreases linearly with a slope of $p_{low} = -0.76$ with $\log(f)$. This corresponds to CPE behavior associated with the electrical double layer formed at the interface Au/solution. The slope measured here demonstrated clearly that a CPE component ($\bar{Z}_{CPE_{int}}$) is more suited than an ideal capacitor. However, in order to simplify the approach, several authors still use a capacitor C_{int} . In this region, the overall phase angle, ϕ , varies from -28° at 100 Hz to -80° at 100 mHz.
2. In zone (II), at mid-frequencies from $\sim 100 \text{ Hz}$ to $\sim 85 \text{ kHz}$, $|Z|$ is approximately constant and is associated with a resistive behavior due to the resistance of the system R_t , which can have different resistive contributions: from the solution conductivity giving R_s , the electrode material resistivity R_e and the connector resistance R_{lead} . In this region, the overall phase angle ϕ reaches a maximum value of -7° at a frequency $f_{max} = 1.8 \text{ kHz}$
3. In zone (III), at high frequencies from $\sim 85 \text{ kHz}$ to 1 MHz, $\log|Z|$ once again decreases linearly with a slope $p_{high} = -0.92$. In this region, the slope is closer to one, indicating characteristic of pure capacitive behavior and is attributed to the parasitic capacitance $C_{parasitic}$. In addition, the overall phase angle ϕ varies from -7° at 1.8 kHz to -90° at 1 MHz.

As the KCl concentration was increased, we noticed that the low "crossover" frequency f_{low} , the frequency at which the system changes from a CPE to a resistive behavior (from zone I to zone II), shifted towards higher frequencies. More precisely, it shifts from 100 Hz to 10 kHz and to 100 kHz for 1 mM and 100 mM, respectively. For DI water, we can define a high crossover frequency, f_{high} , i. e. the frequency at which the system changes from a resistive to a capacitive behavior. For DI water, $f_{high} = 16 \text{ kHz}$. At concentrations above 1 mM, this frequency has a value above 1 MHz and therefore cannot be observed with our spectra. Another visible effect of the increase in the concentration was that the resistive plateau in the spectrum associated with R_t decreased. Indeed, increasing KCl concentration leads to a higher amount of

3.1. Interdigitated electrodes in contact with an electrolyte

ions dissociated in the solution, which increases the conductivity of the solution $\sigma_{solution}$ [7]. As shown in equation 3.1, R_s for IDEs depends on $1/\sigma_{solution}$ and on the cell constant K_{IDE} , i. e. on electrode geometry. Therefore, by increasing $\sigma_{solution}$, we expect that R_s will diminish, leading to a decrease in R_t .

At lower frequencies, in zone I, we observed that increasing KCl concentration appears to have little effect on the curves. However, we found a slight difference between the values of ρ_{low} for the three concentrations. After increasing the concentration, ρ_{low} slightly increased from -0.76 to -0.90. The behavior in this frequency range goes from a CPE characteristic with $\alpha_{int} = 0.76$ to a behavior closer to that of a pure capacitor. Although this difference is not readily visible in the Bode plot due to the log scale, we know that the diffusive capacitance is affected by ion concentration. Thus, differences are expected in zone I which are associated with the double layer. Similarly to the plot of the magnitude of impedance, the frequency at which ϕ reaches its maximum value shifted towards higher frequencies when KCl concentration was increased.

The experimental data were also presented using Nyquist representations in Fig.3.5. For a concentration of DI water, we observed an impedance locus with a semi-circular arc at high frequency, corresponding to the contribution of $C_{parasitic}$ and R_t in parallel. As the concentration is incremented, this semi-circle shrinks (due to the reduction of R_t) and eventually disappears due to the shift of f_{high} out of the experimental frequency "window" used in this study. Hence, the value of the parasitic capacitance $C_{parasitic}$ can only be measured at low electrolyte concentration. At lower frequencies, we identified a non vertical straight line, which seems to be identical for all three concentrations. Nevertheless, we found a slight increment in the slopes, as concentration was increased, in the frequency range from 3 kHz to 100 mHz. This non vertical line can be attributed to the dominant CPE pseudo-capacitive behavior of the double layer formed at the electrode-electrolyte interface, which is affected by the ion concentration and surface roughness (discussed later).

3.1. Interdigitated electrodes in contact with an electrolyte

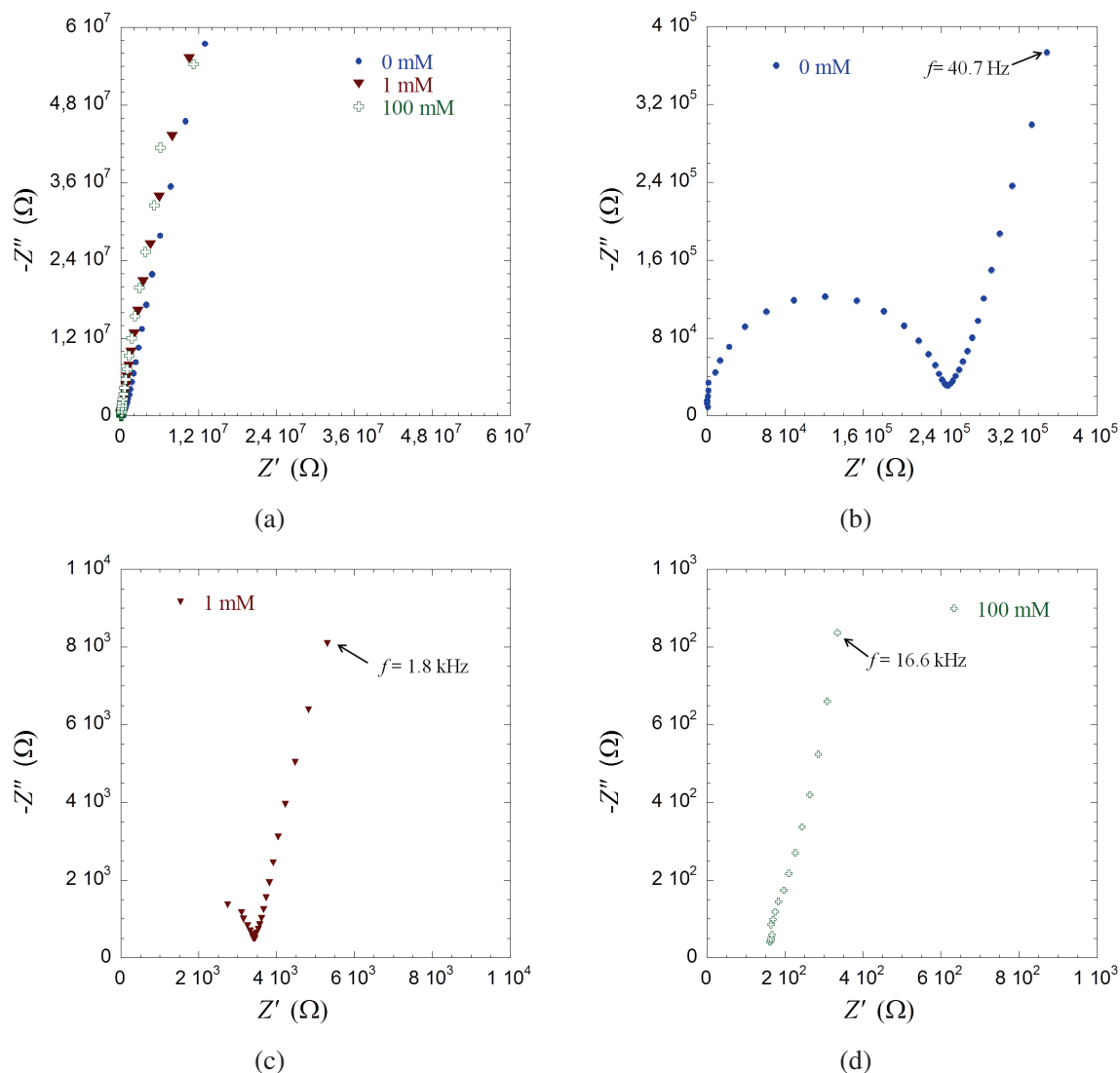


Figure 3.5 – Imaginary part $-Z''$ vs real part Z' of impedance spectra of Au IDEs ($s = 20 \mu\text{m}$, $w = 20 \mu\text{m}$ and $L = 1 \text{ mm}$) in contact with KCl solutions of different concentrations in the frequency range (a) from 1 MHz to 100 mHz, (b) from 1 MHz to 40.7 Hz, (c) from 1 MHz to 1.8 kHz and (d) from 1 MHz to 16.6 kHz.

3.1. Interdigitated electrodes in contact with an electrolyte

In parallel, we did equivalent circuit modeling of the Au IDEs in contact with KCl solutions to analyze the impedance spectra. Based on the models reported in the literature, the simplest circuit model describing the impedance of the IDEs in contact with an electrolyte would comprise a capacitance ($C_{parasitic}$) attached in parallel to a resistance (R_t) and a constant phase element (CPE_{int}) (Model 1) in Fig.3.6a. Due to our polarization conditions, we consider that there is no electrochemical reaction taking place at the electrode surface. We can therefore assume a value for R_{ct} sufficiently high that we do not need to include it in the model.

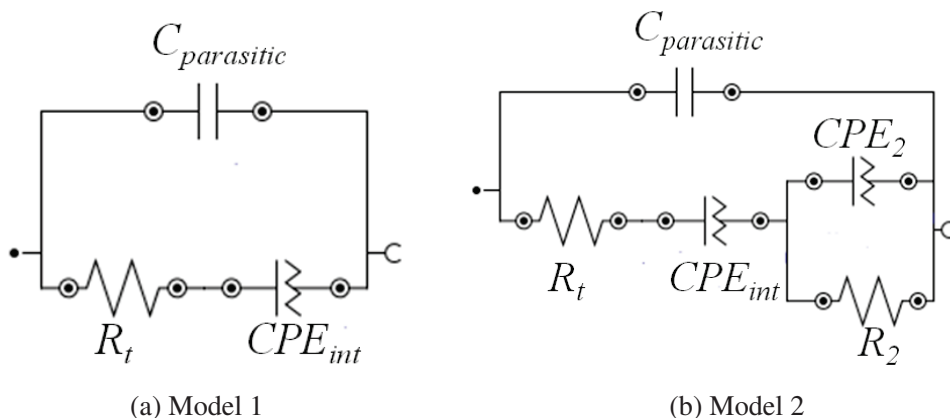


Figure 3.6 – (a) Fitting model 1 of the electrodes in contact with **DI water** and **KCl** solutions. (b) Fitting model 2 of the electrodes in contact with **DI water** and **KCl** solutions.

Ideally, this electrical model would have been used to fit our data. However, we found that this circuit did not fit very well at low frequencies with our experimental data of IDEs in contact with KCl solutions. The quality of the fit was characterized visually but also by using χ^2 values², as shown in Fig. 3.7. In the case of Au IDEs in contact with a 100 mM KCl solution, we obtained a χ^2 value of 0.172 when using Model 1. Several times, when we tried to fit the experimental data of Au IDEs using Model 1, we observed that it did not provide a good visual fit, particularly at the high frequency part of the impedance spectrum. Initially, we thought that the fitting process with Model 1 did not work because of a missing "time constant". We therefore developed a second circuit model (Model 2) to better fit our data. This new equivalent circuit model shown in Fig.3.6b is the same circuit as in Fig.3.6a except that a combination of ($CPE_2 // R_2$) was added in series with R_t and CPE_{int} . We believed that $CPE_2 // R_2$ could be associated with adsorption of ions on the metallic surface. However, the results with DI water did not show a good visual fit either, suggesting that the second time constant does not appear to be associated with adsorption of ions but with the surface of the electrodes. We hypothesized then that Model 2 with $CPE_2 // R_2$ may include the contribution from surface defects, such as "pore like irregularities" on the electrode surface. Keiser et al[15] showed that the pore shape has an important impact on the impedance locus. As shown in Fig. 3.8, the impedance loci varies depending on the shape of the pores. According to Lei et al.[16], a model of porous electrodes can include the ionic resistance, which is the electrolyte ionic resistance inside the pores of the electrodes. This resistance depends on the electrolyte conductivity and the porous texture of the electrode[16]. Nevertheless, it appears that modeling the effect of the surface by an arrangement of electrical components is more complicated than what it seems[17]. An alternative approach could be to use fractal geometry, which is a mathematical concept that describes objects of irregular shape, in order to describe the expected physics of the system under study. For instance, Ball et al.[18] presented a fractal model for a rough interface between an electrode and an electrolyte. Despite this, the data of Au IDEs in contact with 100 mM KCl solution was fitted using

²A quantity commonly used to test whether any given data are well described by some hypothesized function. Such a determination is called a χ^2 test to determine the goodness of the fit.

3.1. Interdigitated electrodes in contact with an electrolyte

Model 2, which provides a better visual fit and a χ^2 value of 0.025, lower than with Model 1, as depicted in Fig. 3.7. In fact, for every KCl concentration that we measured, we obtained lower χ^2 values using the Model 2. We then decided to continue our analysis of the IDEs in contact with an electrolyte using the fitting model 2.

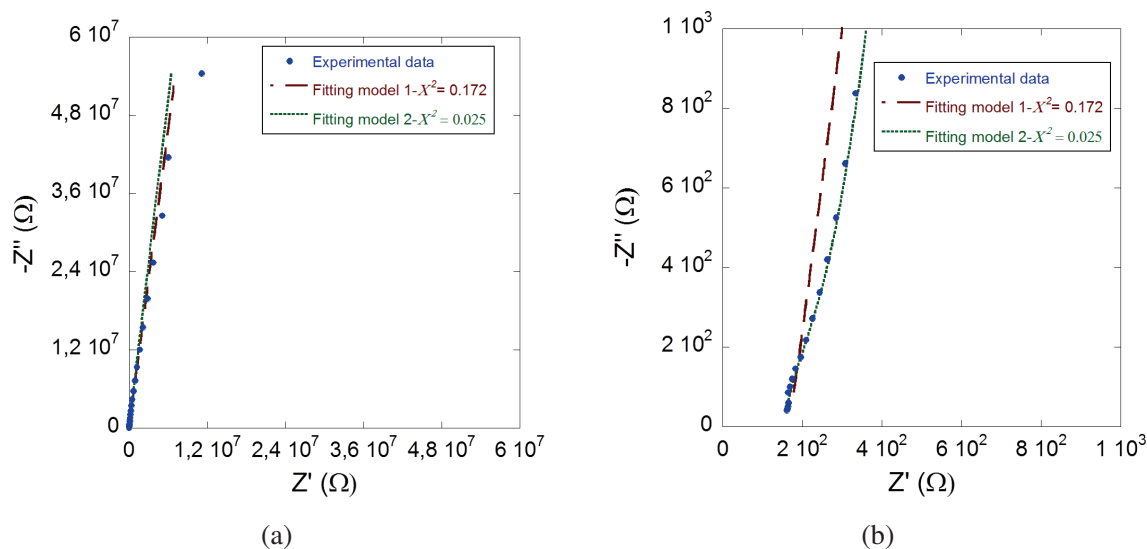


Figure 3.7 – Comparing equivalent circuit models for **Au** electrodes in contact with 100 mM **KCl** solution. (a) Nyquist plot in the frequency range from 1 MHz to 100 mHz and (b) from 1 MHz to 16.6 kHz.

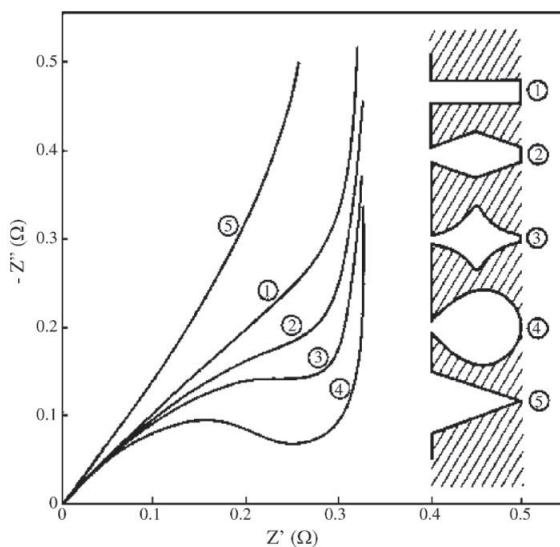


Figure 3.8 – Impedance loci for different shapes of pore on the electrode surface. Figure adapted from figure 5 in [19]. Copyright 2006 by Elsevier. Adapted with permission.

3.1. Interdigitated electrodes in contact with an electrolyte

Fig. 3.9 shows the electrical parameters Q_2 , α_2 and R_2 of model 2 as a function of the concentration. We observed that when the KCl concentration was increased, R_2 decreased from 716 k Ω to 226 Ω while Q_2 increased from $6.1 \times 10^{-8} \text{ s}^\alpha \cdot \Omega^{-1}$ to $1.9 \times 10^{-7} \text{ s}^\alpha \cdot \Omega^{-1}$ and α_2 remained relatively constant. These behaviors could be explained by the fact that ionic resistance depends on the electrolyte conductivity and as mentioned earlier, the double layer capacitance of the IDEs is mainly dependent on the ionic concentration. As shown in Fig. 3.10, the semi circular arc due to $R_2 // CPE_2$ shrinks when the concentration increases. We observed the same behavior for the ITO IDEs in contact with KCl solutions, presented later. We therefore decided to neglect $R_2 // CPE_2$ in the model for cells proliferating on the IDEs with cell culture medium, as described later.

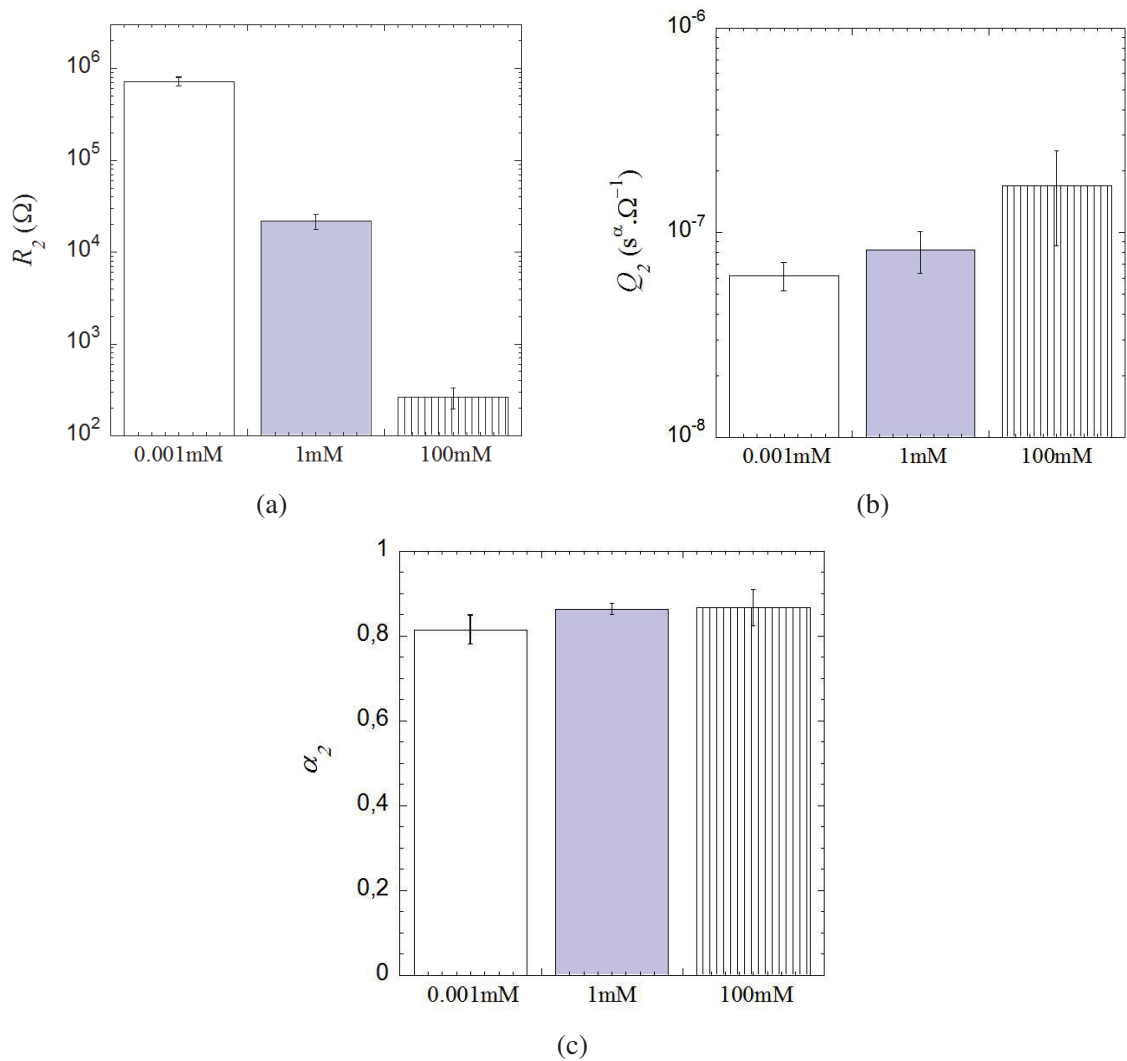


Figure 3.9 – (a) R_2 (b) Q_2 and α_2 (c) versus KCl concentration for Au IDEs. (n = 7, Mean \pm SD).

3.1. Interdigitated electrodes in contact with an electrolyte

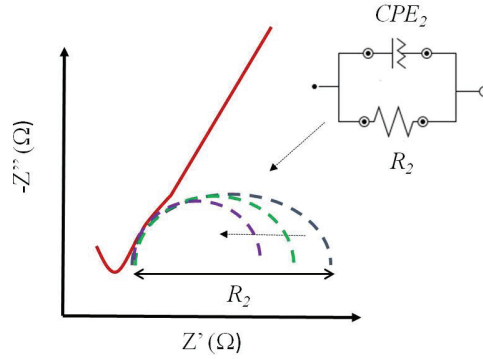


Figure 3.10 – Sketch of the Nyquist plot of Au IDEs depicting the effect of increased concentration on the semi circular arc due to $R_2 \parallel CPE_2$.

The rest of the electrical parameters obtained with Model 2 are shown in Table 3.1. Here, we observed that as the KCl concentration increased, $C_{parasitic}$ increased. As shown in equation 3.5, this parameter depends on the electrode geometry and the relative permittivity of the solution in contact with IDEs. As K_{IDE} is kept constant, $C_{parasitic}$ can evolve due to the variation of the solution relative permittivity caused by the addition of KCl. Chen et al.[20] and Mollerup et al.[21] showed that ϵ_r decreases as KCl concentration increases. This trend is in opposition to what is observed from our measurements. We have to bare in mind that estimating $C_{parasitic}$ using high electrolyte concentrations might not be precise because we have shown that the capacitive behavior due to $C_{parasitic}$ is not visible in the frequency range used in this work at high KCl solution. Therefore, the fitting can only be done with few points, leading to unprecise values. As for the parameter R_t , it decreased due to the fact that the resistance of the solution depends on the concentration of dissolved ions. As shown in equation 3.1, R_s varies linearly with $1/\sigma_{solution}$ with a slope corresponding to K_{IDE} . We measured R_t for different KCl concentrations and for different values for the electrode band width w (20 μm , 10 μm and 5 μm). For these IDE geometries, Table 3.2 shows the value of K_{IDE} calculated from equation 3.2 and obtained from our measurements. We can note that as the inter-electrode gap decreases, both theoretical and experimental values of K_{IDE} increase.

Theoretical and experimental values were close but not identical. For $w = 20 \mu\text{m}$ we calculated a value for K_{IDE} of 51 m^{-1} , whereas we obtained from our measurements a value of 34 m^{-1} . The difference found between these two values could be explained by the fact that equation 3.4 only takes into account the number of electrode bands in contact with the solution. However, in the PDMS reservoir of 5 mm, part of the track connections are also in contact with the electrolyte, affecting the experimental K_{IDE} value. In order to minimize the error between these two values, we would need to carry out the measurements with a reservoir where only the electrode bands are in contact with the solution. A possible strategy might be to use an insulating layer for the gold traces, leaving only the electrode bands exposed. Nevertheless, this requires additional photolithography steps that would make our electrode fabrication more complex. Moreover, the insulation layer must not be toxic for the cells, which will later on proliferate on top of the electrodes.

Concerning CPE_{int} , we can notice that Q_{int} increased at higher electrolyte concentrations whereas α_{int} remained relatively constant. This could be explained by the fact that, as shown before, higher KCl concentrations increase the double layer capacitance, which is associated with the pseudo-capacitance Q_{int} . α_{int} , which is associated with the state of the surface, was not affected.

3.1. Interdigitated electrodes in contact with an electrolyte

Concentration KCl	$C_{parasitic}$ (pF)	R_t (k Ω)	CPE_{int}	
			Q_{int} (ns $^\alpha \cdot \Omega^{-1}$)	α_{int}
0 mM (n = 5)	19.4 \pm 0.3	16.8 \pm 25.5	28.7 \pm 4.9	0.873 \pm 0.011
1 mM (n = 6)	29.8 \pm 0.4	3.250 \pm 0.052	128 \pm 25	0.899 \pm 0.014
100 mM (n = 7)	200 \pm 19	0.106 \pm 0.008	286 \pm 83	0.890 \pm 0.020

Table 3.1 – Impedance fitting results of **Au** IDEs in contact with **KCl** solutions using fitting model 2 (Mean \pm SD).

w (μm)	$K_{IDE_{theoretical}}$ (m^{-1})	$K_{IDE_{experimental}}$ (m^{-1})
20	51	34
10	65	37
5	83	49

Table 3.2 – Values of K_{IDE} calculated and measured of IDEs with different w sizes.

3.1.2.2 Indium Tin Oxide IDEs

We also characterized ITO IDEs in contact with the same KCl solutions. In order to compare the ITO impedance spectra with those of Au in Bode graph, we normalized $|Z|$ with the value of $R_{t,Au}$ obtained with the fitting model 2. In Fig.3.11, we observed that for the 3 concentrations, at lower frequencies there is a difference between the spectra. This could be associated with differences in the interfacial impedance for each material. Moreover, results with 1 mM KCl showed that the resistive plateau for ITO IDEs has a higher value compared to Au IDEs and at 100 mM KCl, this difference is noticeably marked. This could be explained by the fact that there is a difference in resistivity between Au ($10^{-8} \Omega \cdot \text{m}$)[22] and ITO ($10^{-2} \Omega \cdot \text{m}$)[23], which leads to a higher resistive behavior for ITO electrodes. This is particularly observable at high concentrations of KCl where the resistive contribution of the solution is minimal, leaving only a resistive contribution from the electrode material. Regarding the phase response, we found a similar behavior to the case of Au IDE where the frequency f_{max} at which ϕ reaches its maximum value was shifted towards higher frequencies after increasing the concentration. However, contrary to Au IDEs at 100 mM, the frequency of the maximal phase angle is still visible within the measurement range. As for the Nyquist representations in Fig.3.12, we also observed a reduction of the semi-circular arc due to the decrease in R_t as the concentration incremented.

3.1. Interdigitated electrodes in contact with an electrolyte

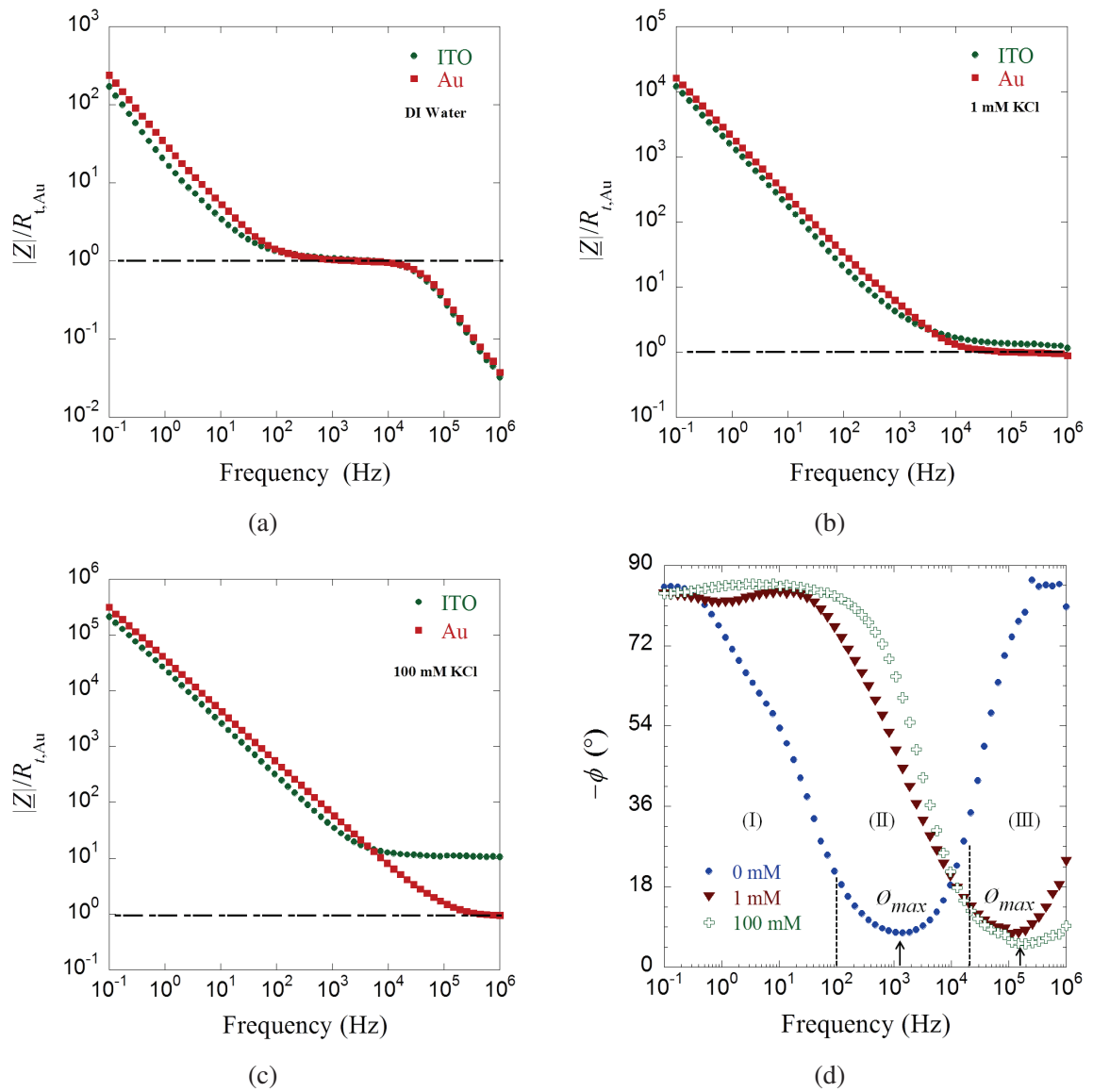


Figure 3.11 – Impedance magnitudes of **ITO** IDEs normalized with $R_{t,Au}$ at different **KCl** concentrations: (a) DI water, (b) 1 mM and (c) 100 mM. (d) Phase of the impedance spectra of **ITO** IDEs in the frequency range from 1 MHz to 100 mHz.

3.1. Interdigitated electrodes in contact with an electrolyte

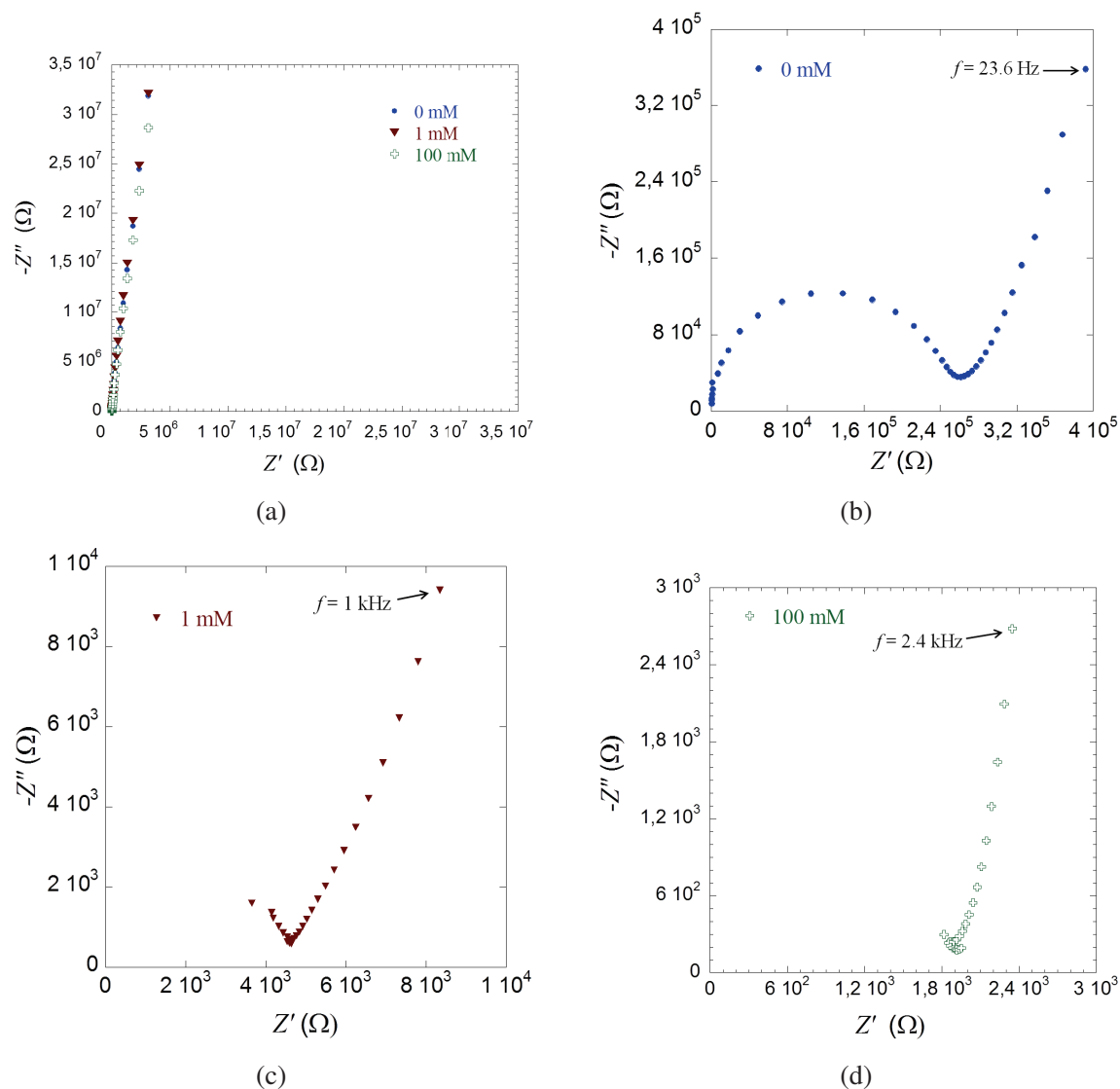


Figure 3.12 – Imaginary part $-Z''$ vs real part Z' of impedance spectra of **ITO** IDEs in contact with **KCl** solutions at different concentrations in the frequency range (a) from 1 MHz to 100 mHz, (b) from 1 MHz to 23.6 Hz, (c) from 1 MHz to 1 kHz and (d) from 1 MHz to 2.4 kHz.

3.1. Interdigitated electrodes in contact with an electrolyte

We present the electrical parameters extracted by fitting the equivalent circuit model 2 to the impedance spectra of both materials in Table 3.3.

Concentration KCl	Material	$C_{parasitic}$ (pF)	R_t (k Ω)	CPE_{int}	
				Q_{int} (ns $^{\alpha}$ · Ω^{-1})	α_{int}
0 mM	Au (n = 5)	19.4 ± 0.3	168 ± 25	29 ± 5	0.87 ± 0.01
	ITO (n = 5)	20.2 ± 0.1	228 ± 28	38.7 ± 0.3	0.991 ± 0.004
1 mM	Au (n = 6)	29.8 ± 0.4	3.25 ± 0.05	128 ± 25	0.90 ± 0.2
	ITO (n = 4)	15.8 ± 0.5	4.2 ± 0.3	47 ± 8	0.93 ± 0.05
100 mM	Au (n = 7)	200 ± 19	0.106 ± 0.008	286 ± 83	0.89 ± 0.02
	ITO (n = 6)	13.6 ± 0.6	1.920 ± 0.144	70 ± 14	0.939 ± 0.005

Table 3.3 – Impedance fitting results of **Au** and **ITO** IDEs in contact with **KCl** solutions using fitting model 2 (Mean ± SD).

We observed, as described earlier for Au electrodes that as we increased the KCl concentration, $C_{parasitic}$ increased whereas the same parameter decreased for ITO IDEs. As the solution permittivity decreases with the increase in KCl concentration[20, 21], we see that the behavior of ITO electrodes is in agreement with the evolution of the permittivity. However, as we mentioned earlier, values at high electrolyte concentrations such as 1 mM and 100 mM are not precise due to the lack of sufficient data points for the fitting of higher frequencies phenomena. Regarding R_t , we notice a difference of 1800 Ω between the two materials, corresponding to a difference in internal electrode resistance. Conversely, for both materials, the parameter Q_{int} increased while α_{int} remained relatively constant. Although, the behaviors of these electrical parameters appeared to be the same, we noticed that ITO IDEs, for the same KCl concentration, have lower values of Q_{int} suggesting higher values of interfacial impedance associated to the $Z_{CPE_{int}}$ in equation 3.9. Furthermore, for each concentration, Au IDEs show lower values of α_{int} . As this parameter is associated with the electrode roughness, we evaluated electrode roughness using atomic force microscopy (AFM) (Fig.3.13). The AFM results revealed that ITO IDEs, with a square root mean (RMS) roughness of 6.6 nm on 2 μ m x 2 μ m area, appears to have a rougher surface than Au IDEs, with a RMS roughness of 2.2 nm on 2 μ m x 2 μ m area. These measurements would imply a term α_{int} for ITO which should be smaller than that of Au, however, experimentally we found the opposite.

3.1. Interdigitated electrodes in contact with an electrolyte

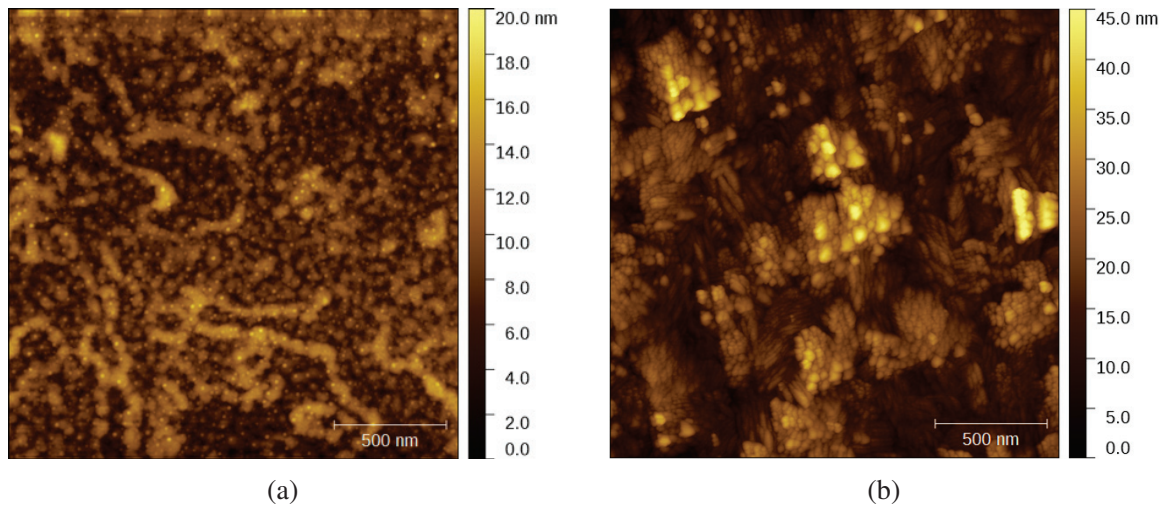


Figure 3.13 – Atomic force microscopy images of the surface of (a) **Au** IDEs and (b) **ITO** IDEs on $2\mu\text{m} \times 2\mu\text{m}$ areas.

This could be explained by the fact that for a rough surfaced electrode, the frequency range used for the fitting process is extremely important. As shown in Fig.3.14a, the Nyquist plot of a "flat" electrode with a CPE_{int} pseudo-capacitive behavior is a straight line at an angle θ to the real axis. Fricke[24] found that this angle is related to α_{int} such that:

$$\theta = \alpha_{int} \cdot 90^\circ \quad (3.9)$$

For a rough surfaced electrode, when viewed over a very wide frequency range, the value of θ (therefore α_{int}) has been observed to gradually vary, leading to a concave impedance spectrum at higher frequencies especially in the presence of pronounced surface roughness effects[25], as depicted in Fig.3.14b.

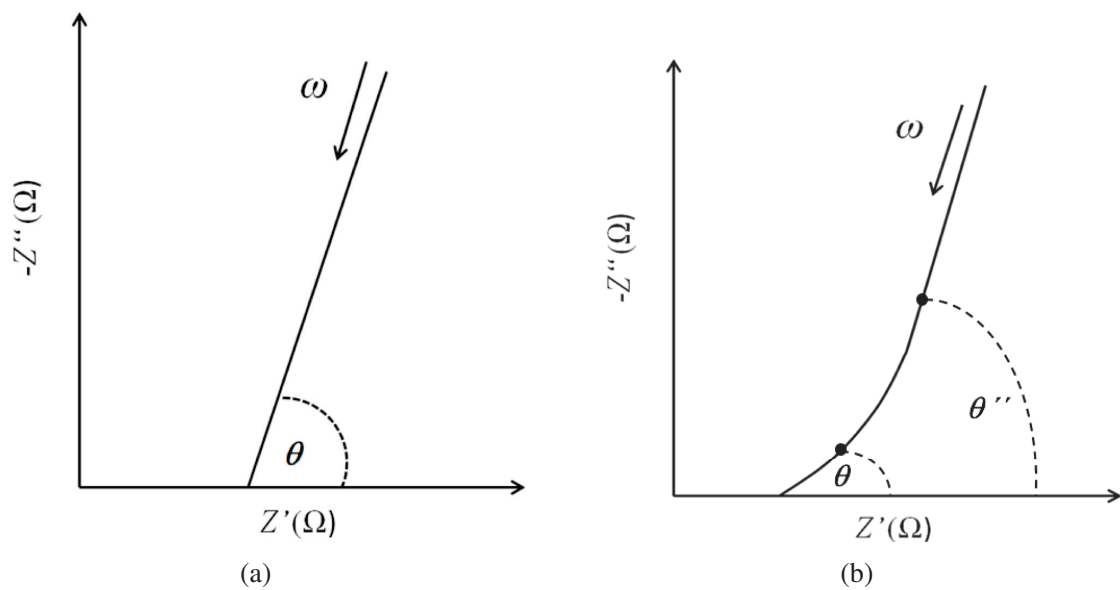


Figure 3.14 – High frequency impedance spectra for (a) **flat** metal electrode and (b) **rough** surfaced electrode. Figure adapted from figures 3 and 4 in [25]. Copyright 1995 by Elsevier. Adapted with permission.

3.1. Interdigitated electrodes in contact with an electrolyte

In order to better understand how surface roughness affects the impedance response, we focused on the simple and qualitative model of De Levie[26]. This model seeks to explain the influence of surface roughness of solid electrodes on electrochemical measurements. De Levie postulated that the impedance response of a porous electrode on which no Faradaic process takes place can be thought to consist of two parts:

(i) a low frequency interface part consisting of a capacitive response associated with a "smooth surface" and an angle θ that tends to 90° .

(ii) a high frequency interface part where the interfacial impedance is proportional to the square root of the "smooth surface" impedance, leading to $\theta = 45^\circ$. The De Levie model is based on the assumption that the pores are cylindrical, of uniform diameter r_p and semi-infinite length l , not interconnected and homogeneously filled with electrolyte[26]. Moreover, the behavior of the porous electrodes depends on their geometry, which is represented by the penetration depth λ of the AC signal in the pore given by the expression[27]:

$$\lambda = \frac{1}{2} \sqrt{\frac{\sigma_{solution} r_p}{\omega C_{int}}} \quad (3.10)$$

The low frequency end of the interface part corresponds to frequencies at which λ is large enough to penetrate the entire pore depth so that porosity of the electrode is no longer reflected in the electrode impedance and a "smooth" electrode impedance is seen in the Nyquist plot[28]. As for the high frequency interface part, this corresponds to the frequencies at which the AC signal penetrates the pores only partially since λ is not large. According to Musiani et al.[29], the transition between "capacitive behavior" (low frequency) and "porous behaviour" (high frequency) occurs around a critical frequency f_0 , given by[29]:

$$f_0 = \frac{3r\sigma_{solution}}{4\pi l^2 C_{int}} \quad (3.11)$$

We therefore decided to fit manually our data with an equivalent circuit comprising CPE_{int} in series with a resistance in order to extract the electrical parameters Q_{int} and α_{int} at high and low frequency portions of the impedance responses for each KCl concentration, as shown in Table 3.4.

3.1. Interdigitated electrodes in contact with an electrolyte

Concentration KCl	Material	High frequency interface		Low frequency interface	
		Q_{int} ($\text{ns}^\alpha \cdot \Omega^{-1}$)	α_{int}	Q_{int} ($\text{ns}^\alpha \cdot \Omega^{-1}$)	α_{int}
0 mM	Au (n = 5)	32 ± 7	0.81 ± 0.01	29 ± 5	0.85 ± 0.05
	ITO (n = 5)	58.1 ± 0.2	0.762 ± 0.003	38 ± 2	0.962 ± 0.004
1 mM	Au (n = 6)	84 ± 21	0.83 ± 0.02	119 ± 24	0.86 ± 0.02
	ITO (n = 4)	136 ± 75	0.76 ± 0.06	46 ± 8	0.91 ± 0.01
100 mM	Au (n = 7)	400 ± 151	0.85 ± 0.03	302 ± 83	0.88 ± 0.04
	ITO (n = 6)	127 ± 47	0.88 ± 0.01	80 ± 22	0.93 ± 0.01

Table 3.4 – Impedance fitting results of **Au** and **ITO** IDEs in contact with **KCl** solutions at low and high frequency interface parts (Mean \pm SD).

At high frequency end of the interface impedance, we observed that Q_{int} and α_{int} for Au IDEs increased as the concentration incremented. As for ITO IDEs we found the same tendency with higher concentrations, except for the 100 mM where Q_{int} decreased. At this part of the impedance response, low values of α_{int} and high values of Q_{int} compared to those of Au IDEs are in good agreement with the roughness of each material found by AFM measurements. Musiani et al.'s calculations demonstrated that the value of $\sigma_{solution}$ affects the impedance response through the critical frequency f_0 . For larger $\sigma_{solution}$ values, f_0 shifts towards higher frequencies and the phase angle of 45° is not attained within the explored frequency range. This could explain why at the high frequency interface part ($f > 16.7$ kHz), for 100 mM KCl concentration, ITO appears "smoother" exhibiting lower Q_{int} and higher α_{int} compared to those of Au. Perhaps, at this concentration the critical frequency shifts out of the frequency range where we can see the roughness effect of ITO, leading to unexpected values.

At the low frequency interface part ($f < 2$ Hz), we found that ITO behaves as a very "smooth" material with α_{int} closer to the unity, which is coherent with De Levie's model that postulates that in the low frequency domain the roughness effect wears off, leading to a "smooth surface" impedance. Surprisingly, however Au IDEs still show rough electrode surface behavior with low α_{int} and high Q_{int} compared to ITO IDEs. Furthermore, if we compare Q_{int} values of Au at high and low frequency interface parts of the spectrum, we expected lower values at low frequencies indicating a smoother surface. However, at 1 mM KCl, Au IDEs show higher Q_{int} . This could be explained by the fact that in some of the measurements at 1 mM KCl, we observed that the spectrum bends towards the real part of the impedance axis, as shown in Fig. 3.15.

3.1. Interdigitated electrodes in contact with an electrolyte

We think that this could be due to a switching of scales of the measuring instrument, which increases the apparent value of Q_{int} , giving a rough surfaced electrode behavior to Au IDEs at the low frequency interface part.

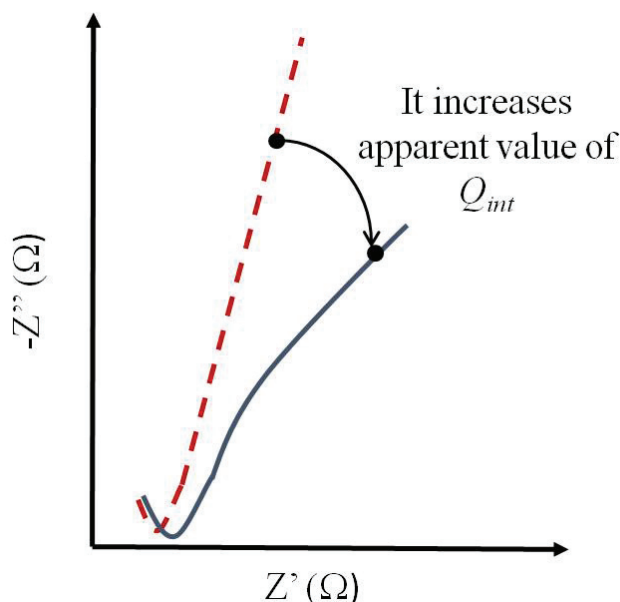


Figure 3.15 – Diagram of the Nyquist plot showing the bending effect on the impedance spectrum at 100 mM for Au IDEs.

As we have seen, De Levie's model explains qualitatively many aspects of the interface impedance we observed. Nevertheless, the effect of the surface roughness on the impedance response appears to be more complex than what De Levie's model can explain. For instance, in contrast to what we presented earlier, some authors have proposed that high values of Q_{int} or low values of α_{int} do not necessarily correspond to "rougher" electrode surface. For example, Torres et al.[30] found no direct relationship between α_{int} behavior and surface topography. In contrast to what is widely accepted, it has been shown in some works[31, 32, 33] that α_{int} may in some cases be observed to increase with the surface roughness. For example, Kerner and Pajkossy[34] suggested that the CPE behavior seemed to be more associated with surface disorder, i.e. heterogeneities on the atomic scale such as crystallographic orientations rather than to "roughness", which corresponds to geometric irregularities much larger than the atomic scale. Atomic scale irregularities can not be monitored with microscopy techniques, such as AFM, leading to the apparent erroneous results concerning an electrode's actual degree of surface "roughness" and its effects on the measured interface impedance. We have demonstrated that in electrode characterization by electrical impedance, the term "roughness" goes beyond the concept of the electrode texture which is due to some irregularities on the surface.

Finally, the values of f_{low} , f_{high} , f_{max} , ϕ_{max} , p_{low} , p_{high} and R_t derived from the Bode representations for Au and ITO IDEs in contact with KCl are listed in Table 3.5.

3.1. Interdigitated electrodes in contact with an electrolyte

Concentration	Material	f_{low} (kHz)	f_{high} (kHz)	p_{low}	p_{high}
0 mM	Au (n = 5)	~ 0.121	~ 38	-0.776 ± 0.024	-0.860 ± 0.029
	ITO (n = 5)	0.043 ± 0.006	43 ± 12	-0.775 ± 0.003	-0.941 ± 0.005
1 mM	Au (n = 8)	7 ± 2	n/a	-0.747 ± 0.063	n/a
	ITO (n = 4)	2.6 ± 1.1	n/a	-0.855 ± 0.019	n/a
100 mM	Au (n = 9)	153 ± 16	n/a	-0.774 ± 0.076	n/a
	ITO (n = 6)	3.1 ± 0.6	n/a	-0.916 ± 0.014	n/a

Table 3.5 – Values obtained from Bode plots of **Au** and **ITO** IDEs in contact with **KCl** (Mean \pm SD).

We noticed that for both materials, the value of f_{low} increased at higher electrolyte concentrations and that Au IDEs showed higher f_{low} values than ITO IDEs. Ibrahim et al.[35] found that in order to improve the sensitivity of the impedance measurement, the influence of the interfacial double layer on the total impedance needs to be removed by shifting f_{low} towards lower frequencies. Based on this, one could conclude that ITO IDEs show better sensitivity than Au IDEs. However, we found the opposite in the experiments with IDEs in the presence of biological cells, which are detailed later. This difference may be attributed to the fact that ITO shows higher internal resistance. Thus, it would be better to compare both materials using solely the values of their interfacial impedances Z_{int} . On the other hand, at 0 mM (DI water), f_{high} of ITO IDEs is higher than that of Au IDEs. We also saw that for Au IDEs at 100 mM it was not possible to extract this parameter from the Bode plots. Furthermore, the value of p_{low} slightly increased with higher concentrations for both materials. As for p_{high} at 0 mM we found values between -0.86 for Au and -0.941 for ITO. For both, p_{low} and p_{high} we did not find the expected values of $p_{low} = -\alpha_{int}$ (associated with CPE_{int}) and $p_{high} = -1$ (associated with the pure capacitance $C_{parasitic}$). This makes us think that extracting the values manually from the Bode plots is less precise than using the equivalent circuit model 2 to fit our data. In fact, when using the Bode plots, one is manually extracting the slopes values and frequencies from specific regions of the impedance curves whereas the equivalent circuit model takes into account the overall impedance contributions of the system and each circuit component comes from a physical process occurring in the system.

Overall we have seen that although Au and ITO IDEs in contact with KCl solutions seem to show similar impedance responses, we observed two major differences between these two electrode materials. First, ITO IDEs have higher resistive behavior, which is particularly visible for high concentrations. In addition, we could obtain the values of the parameters of CPE_{int} from the fit and we found that ITO showed higher interfacial impedances compared to those of gold.

3.1.3 Impedance response of Au and ITO IDEs in culture medium

3.1.3.1 Influence of CN/BSA coating

In this section we studied the impedance response of the Au and ITO IDEs in contact with the supplemented DMEM. We first focused on the effect of the CN/BSA coating on the IDEs. For instance, the Bode plots for the Au IDEs before and after the CN/BSA coating in contact with the supplemented DMEM ($\sigma = 15.37$ mS/cm) are shown in Fig.3.16. Qualitatively, there is no significant difference in the magnitude impedance plot between Au and Au-CN/BSA IDEs. As for the phase angle plot, from 100 mHz to 14 Hz there was a slight decrease and then from 14 Hz to 1 kHz an increase. Moreover, in fig. 3.17, we present the Nyquist plot where we observed that at low frequency the slope of the impedance spectrum increased from 2.9 (Au) to 4.1 (Au-CN/BSA) whereas at higher frequencies both spectra overlapped.

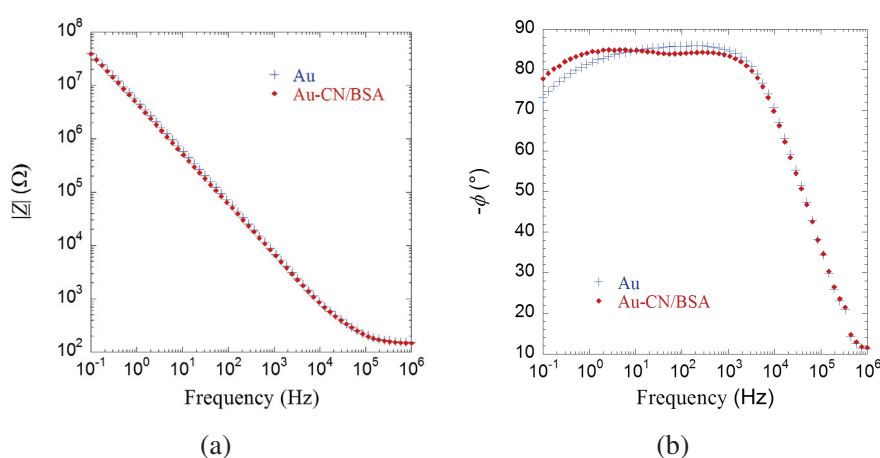


Figure 3.16 – (a) Magnitude and (b) Phase of the impedance of **Au** and **Au-CN/BSA** IDEs in contact with **the supplemented DMEM** in the frequency range from 1 MHz to 100 mHz.

3.1. Interdigitated electrodes in contact with an electrolyte

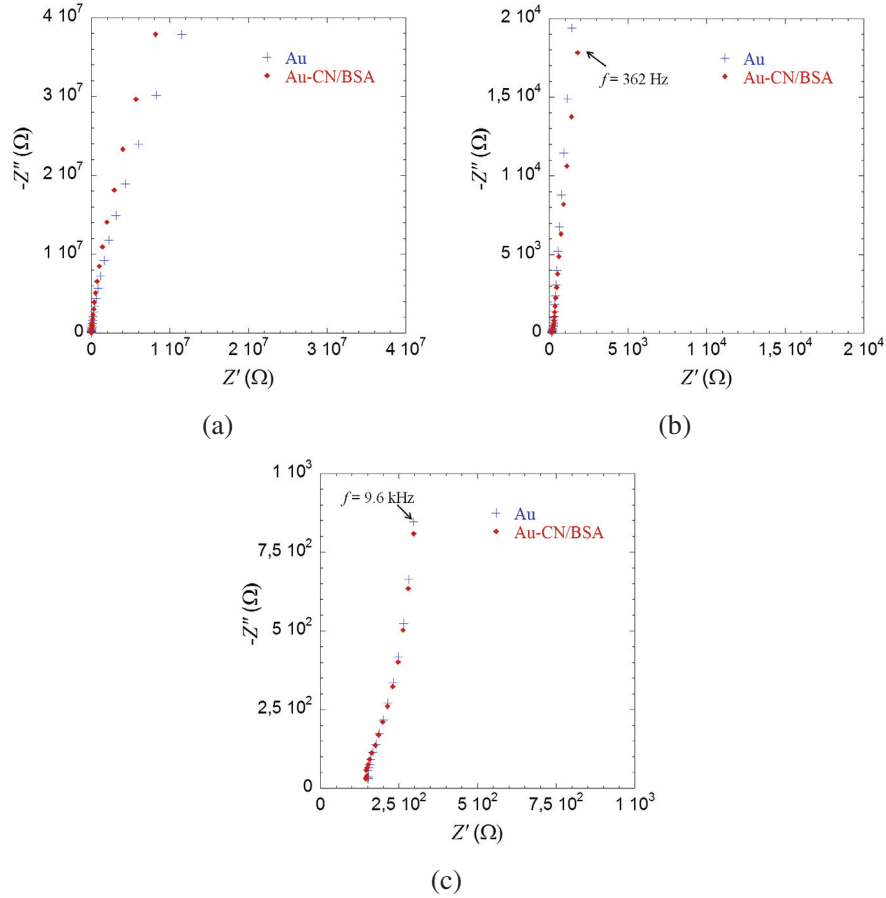


Figure 3.17 – Nyquist plot of **Au** and **Au-CN/BSA** IDEs in contact with **the supplemented DMEM**: (a) from 1 MHz to 100 mHz, (b) from 1 MHz to 362 Hz and (c) from 1 MHz to 9.6 kHz.

In addition, we extracted the electrical equivalent circuit parameters for the Au IDEs before and after CN/BSA coating by fitting the impedance spectra with model 2. Results of the fit are listed in Table 3.6. We conducted a t -test³ to determine if the differences found in Table 3.6 were statistically significant. The parameter $C_{parasitic}$ does not seem to be affected by the coating since both values are not statistically different. R_t decreased after the CN/BSA coating whereas Q_{int} and α_{int} increased. This is coherent with the results of Nguyen et al.[36] who observed the same effect on Q_{int} and α_{int} after covering Au electrodes with a fibronectin layer to provide better surface properties for cell adhesion. The effect on the parameters of Q_{int} and α_{int} could be explained by the fact that the CN/BSA coating does not completely cover the electrode surface. In fact, Freire et al.[37] demonstrated that there are pores among proteins of macromolecules such as collagen type IV. Therefore, following Qiu et al.[38], we can assume that electrical current can follow two different paths: (i) via protein molecules in the coating and (ii) via the solution in the pores in the CN/BSA coating. In other words, we can imagine a Q_{pore} accounting for the interface in the pore that is not covered by CN/BSA and a $Q_{CN/BSA}$ associated with the coating layer. Since both Q values are in parallel, the equivalent Q_{int} would be higher, leading to an increase in Q_{int} after CN/BSA coating.

³A statistical test that uses the t Student distribution to compare the means of two independent samples on a given variable.

3.1. Interdigitated electrodes in contact with an electrolyte

Au IDEs	$C_{parasitic}$ (pF)	R_t (Ω)	CPE_{int}	
			Q_{int} ($ns^\alpha \cdot \Omega^{-1}$)	α_{int}
Au (n = 4)	165 ± 48	159 ± 10	35.2 ± 5.5	0.918 ± 0.023
Au-CN/BSA (n = 5)	185 ± 18	126 ± 4	133 ± 23	0.960 ± 0.003
<i>t</i> -test	** 0.5	* 0.004	* 0.0004	* < 0.03

Table 3.6 – Impedance fitting results of the Au IDEs before/after CN/BSA in contact with the supplemented DMEM (Mean \pm SD) (*:statistically significant and **: not statistically significant).

In Fig.3.18 we compared the impedance response of Au and ITO IDEs covered with CN/BSA. As expected, due to the conductivity of the medium, the impedance spectra of Au-CN/BSA and ITO-CN/BSA IDEs are similar to the ones of IDEs in contact with the 100 mM KCl solution ($\sigma_{solution} = 15.7$ mS/cm) in Fig.3.11.

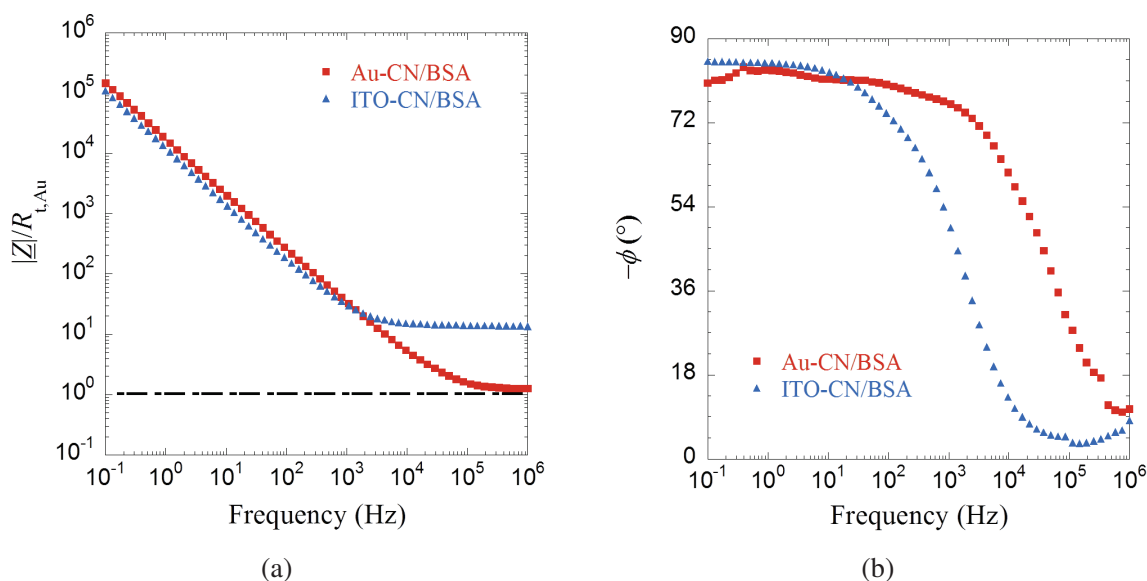


Figure 3.18 – (a) Magnitude and (b) Phase of the impedance of Au-CN/BSA and ITO-CN/BSA IDEs in contact with the supplemented DMEM over the frequency range 1 MHz to 100 mHz.

As we did for the data of the IDEs in contact with KCl solution, we fitted our data with model 2. The fitting parameters presented in Table 3.7 revealed differences between Au-CN/BSA and ITO-CN/BSA electrodes in contact with the supplemented medium. The first difference concerns the parameter $C_{parasitic}$. We observed that $C_{parasitic}$ for Au is higher than the $C_{parasitic}$ for ITO. Nevertheless, as we mentioned before, determining $C_{parasitic}$ for a high concentration solution, such as the supplemented DMEM is not precise as the region corresponding to this electrical parameter is not clearly visible on the impedance spectra. As for R_t , we found that despite measuring with the same solution of supplemented DMEM, there is again a difference of 1,700 Ω between Au IDEs and ITO IDEs, similar to what was observed with KCl 100 mM

3.2. Conclusion

and corresponding to ITO lower electrode resistance. Two additional differences concern the electrical parameters Q_{int} and α_{int} . We observed that Au IDEs have a higher value of Q_{int} , which could reflect a lower interfacial impedance. The parameter α_{int} for Au was slightly higher than α_{int} for ITO. A lower interfacial impedance could explain why in most of the studies, Au is chosen as the electrode material. In ECIS, the global impedance corresponds to different impedance contributions of the elements of the system, therefore one would prefer that the measured impedance is not governed by the interfacial impedance. If this impedance due to the electrical double layer at the interface between the solution and the electrodes is high enough, it can mask the impedance contribution coming from the cells in the measurement data, leading to loss of information about cell proliferation. Hence, ECIS requires low electrode-solution interface impedance, especially for biomedical and biophysical applications[39].

Material	$C_{parasitic}$ (pF)	R_t (Ω)	CPE_{int}	
			Q_{int} ($ns^\alpha \cdot \Omega^{-1}$)	α_{int}
Au-CN/BSA	185 ± 18	126 ± 4	133 ± 23	0.960 ± 0.003
ITO-CN/BSA	14 ± 1	1840 ± 71	84 ± 8	0.936 ± 0.009
<i>t</i> -test	* < 0.001	* < 0.001	* 0.0077	* < 0.001

Table 3.7 – Impedance fitting results of **Au-CN/BSA** and **ITO-CN/BSA** IDEs in contact with **the supplemented DMEM** and using fitting model 2 (Mean \pm SD with $n = 5$ for Au and $n = 8$ for ITO) (*:statistically significant and **: not statistically significant).

3.2 Conclusion

In this chapter, we first presented the characterization of Au and ITO interdigitated electrodes in contact with KCl solutions at different concentrations. As it has been previously reported in studies using IDEs[10][6], we identified for both materials 3 regions in the impedance spectrum. We observed a capacitive response in the high frequency region, a CPE behavior in the low frequency region, whereas in the mid-frequency region we saw a resistive response. This means that depending on the measuring frequency, we can study different behaviors of the interdigitated electrodes. In addition, we observed that the high frequency capacitive zone is not visible when the KCl concentration increases due to the fact that as the solution conductivity increased, the resistive region shifted towards high frequencies. Nevertheless, despite of having similar behaviors, we noticed that for high conductivity solution, ITO electrodes show higher resistive plateau than that of Au IDEs.

Additionally, we did equivalent circuit modeling in order to obtain the electrical parameters describing the Au and ITO electrodes covered with the CN/BSA coating and in contact with the supplemented DMEM. The fitting parameters revealed two differences between Au and ITO electrodes. The first one was that the value of R_t , $126 \pm 4 \Omega$ for Au and $1,860 \pm 72 \Omega$ for ITO, which might be due to differences in resistivity between the materials, leading to higher values of the resistive plateau for ITO. The second difference concerns the value of the interfacial impedance given by the parameters of CPE_{int} . We observed that in the frequency range from 1 MHz to 100 mHz, Au IDEs showed lower interfacial impedance than ITO IDEs. This is important in ECIS, where low impedance contribution from the electrical double layer that

3.2. Conclusion

forms at the electrode-solution interface is required, especially when measuring the impedance of live cells and biological molecules[40]. The differences in resistive behavior and interfacial impedance between Au and ITO, obtained by equivalent circuit modeling, might explain why most of the studies prefer using Au as electrode material over ITO despite of its transparency. Furthermore, using the De Levie's model for "rough" electrodes and AFM measurements, we have demonstrated that when one characterizes electrodes by electrical impedance, the term "roughness" goes beyond the concept of the electrode texture which is due to some irregularities on the surface. For example, roughness could also depend on heterogeneities on the atomic scale such as, crystallographic orientations[34]. This type of irregularities can not be monitored with microscopy techniques, such as AFM, leading to the apparent erroneous results concerning an electrode's actual degree of surface "roughness" and its effects on the measured interface impedance. Here, we found that Au IDEs are not completely flat electrodes and their impedance results can be analyzed using porous electrode theory.

Bibliography

- [1] Aaron Takami Ohta. “Optofluidic Devices for Cell, Microparticle, and Nanoparticle Manipulation”. PhD thesis. University of California, Berkeley, 2008.
- [2] W. Olthuis, W. Streekstra, and P. Bergveld. “Theoretical and experimental determination of cell constants of planar-interdigitated electrolyte conductivity sensors”. In: *Sensors and Actuators B: Chemical* 24.1-3 (1995), pp. 252–256. DOI: [https://doi.org/10.1016/0925-4005\(95\)85053-8](https://doi.org/10.1016/0925-4005(95)85053-8).
- [3] David D. Zhou and Elias Greenbaum. *Implantable Neural Prostheses 2: Techniques and Engineering Approaches*. Dordrecht Heidelberg New York London: Springer, 2010.
- [4] W. Franks, I. Schenker, P. Schmutz, and A. Hierlemann. “Impedance characterization and modeling of electrodes for biomedical applications”. In: *IEEE Transactions on Biomedical Engineering* 52.7 (2005), pp. 1295–1302. DOI: <https://doi.org/10.1109/TBME.2005.847523>.
- [5] Hainan Wang and Laurent Pilon. “Accurate Simulations of Electric Double Layer Capacitance of Ultramicroelectrodes”. In: *The Journal of Physical Chemistry C* 115.33 (2011), pp. 16711–16719. DOI: <https://doi.org/10.1021/jp204498e>.
- [6] Björn Timmer, Wouter Sparreboom, Wouter Olthuis, Piet Bergveld, and Albert van den Berg. “Optimization of an electrolyte conductivity detector for measuring low ion concentrations”. In: *Lab Chip* 2.2 (2002), pp. 121–124. DOI: <https://doi.org/10.1039/b201225a>.
- [7] Lisandra F. Lima, Admilson L. Vieira, Hatsumi Mukai, Cid M.G. Andrade, and Paulo R.G. Fernandes. “Electric impedance of aqueous KCl and NaCl solutions: Salt concentration dependence on components of the equivalent electric circuit”. In: *Journal of Molecular Liquids* 241 (2017), pp. 530–539. DOI: <https://doi.org/10.1016/j.molliq.2017.06.069>.
- [8] Thomas Jansch, Jens Wallauer, and Bernhard Roling. “Influence of Electrode Roughness on Double Layer Formation in Ionic Liquids”. In: *THE JOURNAL OF PHYSICAL CHEMISTRY* 119 (2015), pp. 4620–4626. DOI: <https://doi.org/10.1021/jp512617j>.

BIBLIOGRAPHY

- [9] Frank A. Alexander, Dorielle Tucker Price, and Shekhar Bhansali. “From Cellular Cultures to Cellular Spheroids: Is Impedance Spectroscopy a Viable Tool for Monitoring Multicellular Spheroid (MCS) Drug Models?” In: *IEEE Reviews in Biomedical Engineering* 6 (2012), pp. 63–76. DOI: <https://doi.org/10.1109/RBME.2012.2222023>.
- [10] Sunil Rana, Robin H Page, and Calum J McNeil. “Impedance spectra analysis to characterize interdigitated electrodes as electrochemical sensors”. In: *Electrochimica Acta* 56.24 (2011), pp. 8559–8563. DOI: <https://doi.org/10.1016/j.electacta.2011.07.055>.
- [11] L.A Geddes. “Historical evolution of circuit models for the electrode-electrolyte interface”. In: *Annals of Biomedical Engineering* 25.1 (1997), pp. 1–14. DOI: <https://doi.org/10.1007/BF02738534>.
- [12] Aliaksandr S. Bandarenka. “Exploring the interfaces between metal electrodes and aqueous electrolytes with electrochemical impedance spectroscopy”. In: *Analyst* 138.19 (2013), pp. 5540–5554. DOI: <https://doi.org/10.1039/c3an00791j>.
- [13] Jongin Hong, Dae Sung Yoon, Sung Kwan Kim, Tae Song Kim, Sanghyo Kim, Eugene Y. Pak, and Kwangsoo Noa. “AC frequency characteristics of coplanar impedance sensors as design parameters”. In: *Lab On Chip* 5.3 (2004), pp. 270–279. DOI: <https://doi.org/10.1039/b410325d>.
- [14] H. Baccar, MB. Mejri, R. Prehn, FJ. del Campo, E. Baldrich, M. Rosemonde, and A. Abdelghani. “Interdigitated Microelectrode Arrays Integrated in Microfluidic Cell for Biosensor Applications”. In: *Nanomedicine and Nanotechnology* 5.6 (2014), pp. 1–4. DOI: <https://doi.org/10.4172/2157-7439.1000243>.
- [15] H. Keiser, K. D. Beccu, and M. A. Gutjahr. “Abschätzung der porenstruktur poroser elektroden aus impedanzmessungen”. In: *Electrochimica Acta* 21.8 (1976), pp. 539–543. DOI: [https://doi.org/10.1016/0013-4686\(76\)85147-x](https://doi.org/10.1016/0013-4686(76)85147-x).
- [16] Chunhong Lei, Foivos Markoulidis, Zenya Ashitaka, and Constantina Lekakou. “Reduction of porous carbon/Al contact resistance for an electric double-layer capacitor (EDLC)”. In: *Electrochimica Acta* 92 (2013), pp. 183–187. DOI: <https://doi.org/10.1016/j.electacta.2012.12.092>.
- [17] Samuel J. Cooper, Antonio Bertei, Donal P. Finegan, and Nigel P. Brandon. “Simulated impedance of diffusion in porous media”. In: *Electrochimica Acta* 251 (2017), pp. 681–689. DOI: <https://doi.org/10.1016/j.electacta.2017.07.152>.
- [18] Robin Ball and Martin Blunt. “A fractal model for the impedance of a rough surface”. In: *Journal of Physics A: Mathematical and General* 21.1 (1988), pp. 197–204. DOI: <https://doi.org/10.1088/0305-4470/21/1/024>.
- [19] Digby D. Macdonald. “Reflections on the history of electrochemical impedance spectroscopy”. In: *Electrochimica Acta* 51.8-9 (2006), pp. 1376–1388. DOI: <https://doi.org/10.1016/j.electacta.2005.02.107>.
- [20] Ting Chen, Glenn Hefter, and Richard Buchner. “Dielectric Spectroscopy of Aqueous Solutions of KCl and CsCl”. In: *The Journal of Physical Chemistry A* 107.20 (2003), pp. 4025–4031. DOI: <https://doi.org/10.1021/jp026429p>.

BIBLIOGRAPHY

- [21] Jorgen M. Mollerup and Martin P. Breil. “Modeling the Permittivity of Electrolyte Solutions”. In: *AIChE Journal* 61.9 (2015), pp. 2854–2860. DOI: <https://doi.org/10.1002/aic.14799>.
- [22] Robert E. Newnham. *Properties of Materials: Anisotropy, Symmetry, Structure*. New York: OXFORD University Press, 2005.
- [23] Mansour S. Farhan, Erfan Zalnezhad, Abdul Razak Bushroa, and Ahmed Aly Diao Sarhan. “Electrical and Optical Properties of Indium-tin Oxide (ITO) Films by Ion-Assisted Deposition (IAD) at Room Temperature”. In: *INTERNATIONAL JOURNAL OF PRECISION ENGINEERING AND MANUFACTURING* 14.8 (2013), pp. 1465–1469. DOI: <https://doi.org/10.1007/s12541-013-0197-5>.
- [24] Hugo Fricke. “The theory of electrolytic polarization”. In: *Philosophical Magazine* 7.14 (1932), pp. 310–318. DOI: <https://doi.org/10.1080/14786443209462064>.
- [25] E. T. McAdmas, A. Lackermeier, J. A. McLaughlin, and D. Macken. “The linear and non-linear electrical properties of the electrode-electrolyte interface”. In: *Biosensors and Bioelectronics* 10.1-2 (1995), pp. 67–74. DOI: [https://doi.org/10.1016/0956-5663\(95\)96795-Z](https://doi.org/10.1016/0956-5663(95)96795-Z).
- [26] R. De Levie. “The influence of surface roughness of solid electrodes on electrochemical measurements”. In: *Electrochimica Acta* 10.2 (1965), pp. 113–130. DOI: [https://doi.org/10.1016/0013-4686\(65\)87012-8](https://doi.org/10.1016/0013-4686(65)87012-8).
- [27] Vadim F. Lvovich. *Impedance Spectroscopy: Applications to Electrochemical and Dielectric Phenomena*. New Jersey: John Wiley and Sons, 2012.
- [28] Jean-Pierre Candy, Pierre Fouillox, Michel Keddam, and Hisasi Takenouti. “The Characterization of Porous Electrodes by Impedance Measurements”. In: *Electrochimica Acta* 26.8 (1981), pp. 1029–1034. DOI: [https://doi.org/10.1016/0013-4686\(81\)85072-4](https://doi.org/10.1016/0013-4686(81)85072-4).
- [29] Marco Musiani, Mark Orazem, Bernard Tribollet, and Vincent Vivier. “Impedance of blocking electrodes having parallel cylindrical pores with distributed radii”. In: *Electrochimica Acta* 56.23 (2011), pp. 8014–8022. DOI: <https://doi.org/10.1016/j.electacta.2010.12.2004>.
- [30] Pedro Córdoba-Torres, Thiago J. Mesquita, and Ricardo P. Nogueira. “Relationship between the Origin of Constant-Phase Element Behavior in Electrochemical Impedance Spectroscopy and Electrode Surface Structure”. In: *Physical Chemistry C* 119.8 (2015), pp. 4136–4147. DOI: <https://doi.org/10.1021/jp512063f>.
- [31] Tamás Pajkossy. “Impedance of Rough Capacitive Electrodes”. In: 364.1-2 (1994), pp. 111–125. DOI: [https://doi.org/10.1016/0022-0728\(93\)02949-I](https://doi.org/10.1016/0022-0728(93)02949-I).
- [32] Tamás Pajkossy and D. M. Kolb. “Anion-Adsorption Related Frequency-Dependent Double Layer Capacitance of the Platinum Group Metals in the Double Layer Region”. In: *Electrochimica Acta* 53.25 (2008), pp. 7403–7409. DOI: <https://doi.org/10.1016/j.electacta.2007.11.068>.

- [33] Tamás Pajkossy, L.A.Kibler, and D. M. Kolb. “Voltammetry and Impedance Measurements of Ir(100) Electrodes in Aqueous Solutions”. In: *Journal of Electroanalytical Chemistry* 600.1 (2007), pp. 113–118. DOI: <https://doi.org/10.1016/j.jelechem.2006.04.016>.
- [34] Zsolt Kerner and Tamás Pajkossy. “On the origin of capacitance dispersion of rough electrodes”. In: *The Journal of Physical Chemistry C* 43.2-3 (2000), pp. 207–211. DOI: [https://doi.org/10.1016/S0013-4686\(00\)00574-0](https://doi.org/10.1016/S0013-4686(00)00574-0).
- [35] Mouhamad IBRAHIM. “MESURE DE BIOIMPEDANCE ELECTRIQUE PAR CAPTEURS INTERDIGITES”. PhD thesis. Université de Lorraine, 2012.
- [36] Tien Anh Nguyen, Tsung-I Yin, Diego Reyes, and Gerald A. Urban. “Microfluidic Chip with Integrated Electrical Cell-Impedance Sensing for Monitoring Single Cancer Cell Migration in Three-Dimensional Matrixes”. In: *Analytical chemistry* 85.22 (2013), pp. 11068–11076. DOI: <https://doi.org/10.1021/ac402761s>.
- [37] E. Freire, F. C. Gomes, R. Linden, V. M. Neto, and T. Coelho-Sampaio. “Structure of laminin substrate modulates cellular signaling for neuritogenesis”. In: *Journal of Cell Science* 115.24 (2002), pp. 4867–4876. DOI: <https://doi.org/10.1242/jcs.00173>.
- [38] Yiling Qiu and Ronglih Liao and Xin Zhang. “Real-Time Monitoring Primary Cardiomyocyte Adhesion Based on Electrochemical Impedance Spectroscopy and Electrical Cell-Substrate Impedance Sensing”. In: *Analytical Chemistry* 80.4 (2008), pp. 990–996. DOI: <https://doi.org/10.1021/ac701745c>.
- [39] Rangadhar Pradhan, Analava Mitra, and Soumen Das. “Characterization of Electrode/Electrolyte Interface of ECIS Devices”. In: *Electroanalysis* 24.12 (2012), pp. 2405–2414. DOI: <https://doi.org/10.1002/elan.201200455>.
- [40] Hugo Sanabria and John H Miller Jr. “Relaxation processes due to the electrode-electrolyte interface in ionic solutions”. In: *Physical Review E* 74.(5 Pt 1):051505 (2006), pp. 1–9. DOI: <https://doi.org/10.1103/PhysRevE.74.051505>.

Au and ITO behaviors during ECIS and cytotoxicity experiments

In this chapter we used equivalent circuit modeling for comparing and extracting the electrical parameters of our Au and ITO IDEs with breast cancer cells proliferating on the surface. In addition, we gave an example of a possible application of ECIS in drug screening. We monitored the effect of the chemotherapeutic agent 5-fluorouracil (5-FU) on the non metastatic MCF-7 cell line and the metastatic MDA-MB-231 cell line. We decided to start our study with impedance measurements carried out on MCF-7 cells with different concentrations of 5-FU using Au and ITO IDEs. We then used equivalent circuit modeling to extract and compare the electrical parameters for the MCF-7 cells and for MDA-MB-231 cells treated with 5-FU.

4.1 IDEs in contact with biological cells

In this section, we monitored cell proliferation on Au and ITO IDEs using AC impedance measurements. First, we characterize the two cell lines used in this work in terms of morphology on these two materials. Then, we carried out ECIS impedance assays combined to phase contrast microscopy in order to compare Au and ITO IDE sensitivities.

4.1.1 MCF-7 and MDA-MB-231 morphology comparison on different materials

In this section, we evaluated the behavior of both MCF-7 and MDA-MB-231 cell lines proliferating on glass and ITO substrates functionalized with CN/BSA coatings and on Petri dishes. Petri dishes are cell culture dishes manufactured in polystyrene, which provide optical transparency, they are easy to mold and can be sterilized by irradiation[1]. However, the major drawback is that polystyrene is very hydrophobic leading to poor cell attachment. Therefore, its surface must be modified. For example, some cell researchers began coating culture vessel surfaces to improve both cell attachment and performance. They used a variety of biological materials including extracellular matrix, attachment and adhesion proteins, such as collagen[2], laminin[3], fibronectin[2] and mucopolysaccharides such as heparin sulfate[4]. Moreover, commercial dishes such as the ones we used (Thermo Scientific cell culture dishes) have a Nunclon™ Delta surface. This is a fully synthetic, energy-treated surface which makes the hydrophobic polystyrene surface more hydrophilic, thus facilitating cell attachment and growth[5].

4.1. IDEs in contact with biological cells

In fig.4.1, we observe that MCF-7 cells proliferating on Petri dishes exhibit a "cobblestone" form while MDA-MB-231 cells appeared elongated and with a "stellate" structure. As for the glass slide, it can be seen that MCF-7 cells attached showing a similar morphology as in the Petri dish images. However, MDA-MB-231 appeared less elongated than in the Petri dish. This could be explained by the fact that the number of cells increased and there was less free surface for cell spreading. Regarding the ITO substrate, we observe that MCF-7 show their "cobblestone" shape and MDA-MB-231 appear elongated and with lamellipodia (cytoskeletal protein actin projections on the leading edge of the cells) as in the Petri dish. These images revealed that due to its transparency, ITO clearly enables us to obtain images comparable to those of cells grown on glass or on Petri dishes. Despite this, few studies have chosen ITO electrodes as sensors in applications combining impedance with optical measurements[6, 7, 8].

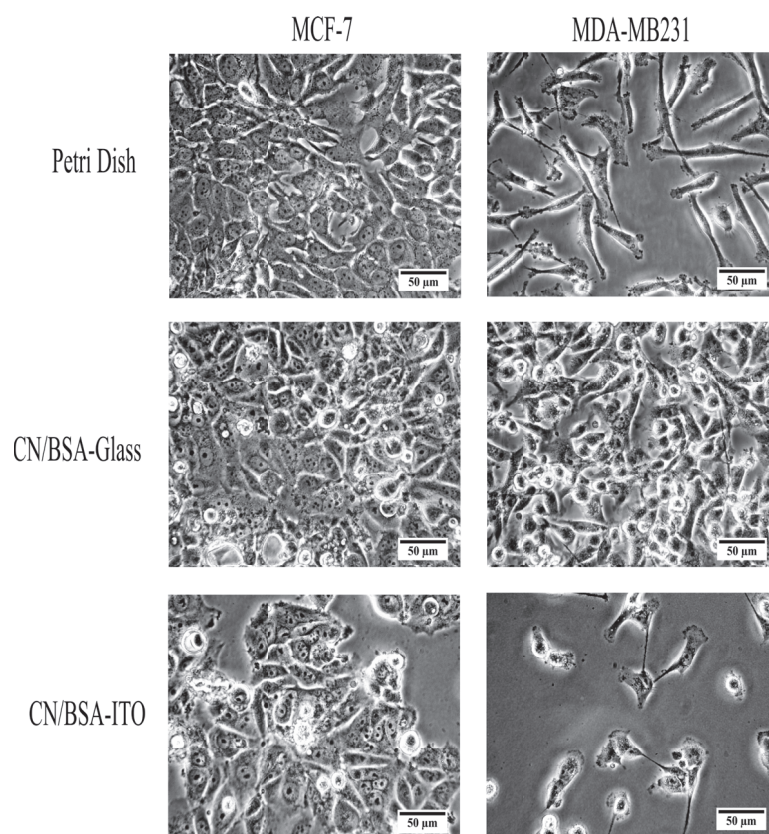


Figure 4.1 – Phase contrast micrographs of **MCF-7** and **MDA-MB-231** cells after 46 h of cell culture on different substrates covered with CN/BSA at 40X magnification (Leica D2000).

4.1. IDEs in contact with biological cells

Furthermore, we tried to determine if the two cell lines had different spreading behavior depending on the type of substrate: Petri dish, ITO-CN/BSA or Glass-CN/BSA. Using ImageJ, we manually contoured cells to find $S_{average}$, the surface occupied by a single cell spreading on each of the substrates. We also characterized the spreading behavior by the ratio of the large axis L_a and the small axis L_b (extracted with ImageJ), as depicted in Fig.4.2.

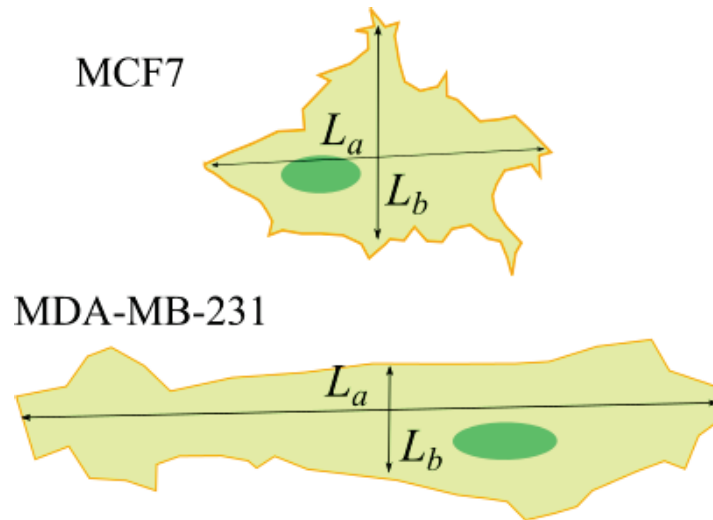


Figure 4.2 – Axes used in ImageJ for each cell line. L_a : big axis, L_b : small axis.

The values of the extracted parameters using ImageJ are shown in Table 4.1. For cells proliferating on Petri dish, we found no significant difference between $S_{average}$ for each cell line. However, we observed that the value L_a of MCF-7 is lower than that of MDA-MB-231 whereas its parameter L_b is higher. This leads to a higher ratio L_a/L_b for MDA-MB-231, showing quantitatively that these cells tend to elongate more along one axis during cell spreading while MCF-7 with their "cobblestone" shape tend to stay more "round" and show a ratio L_a/L_b close to the unity.

4.1. IDEs in contact with biological cells

Substrate	Cell line	$S_{average}$ (nm ²)	L_a (nm)	L_b (nm)	L_a/L_b
Petri dish	MCF-7	859 ± 295	30 ± 5	35 ± 10	0.9 ± 0.07
	MDA-MB-231	823 ± 275	103 ± 38	10 ± 3	10.3 ± 1.3
ITO-CN/BSA	MCF-7	855 ± 271	49 ± 11	21 ± 6	2.3 ± 0.2
	MDA-MB-231	1687 ± 725	92 ± 39	33 ± 17	2.8 ± 0.5
Glass-CN/BSA	MCF-7	997 ± 507	50 ± 14	27 ± 10	1.9 ± 0.2
	MDA-MB-231	631 ± 203	60 ± 14	14 ± 5	4.3 ± 0.5

Table 4.1 – Parameters extracted with ImageJ for each cell line proliferating on **Petri dish**, **ITO-CN/BSA** and **Glass-CN/BSA** (Mean ± SD) with n = 14 for each cell line.

In the case of ITO-CN/BSA, MDA-MB-231 occupied a larger surface than MCF-7 cells. Visually MDA-MB-231 appears globally less elongated than on Petri dish and more similar to MCF-7 cells. This can be confirmed with the ratio L_a/L_b which was found very close for both cell lines on ITO/CN-BSA surfaces. As for the spreading behavior on Glass-CN/BSA, in contrast to the previous substrate, MCF-7 cells show larger $S_{average}$ values. Regarding the axes, MCF-7 cells have lower L_a but higher L_b compared to MDA-MB-231 cells. Once more, the ratio L_a/L_b is higher for MDA-MB-231, which reinforces the idea that MDA-MB-231 cells tend to elongate along one of the cell axis during cell spreading. For example, Hermans et al.[9] studied the motility efficiency of MDA-MB-231 cells and MCF-7 cells on glass bottomed dishes coated with laminin and they found that MDA-MB-231 cells are able to spatiotemporally coordinate significant parts of the cell boundary to perform synchronized large protrusions and retractions, leading to large centroid displacements. As for MCF-7 cells, they have similar temporal protrusion-retraction activities but they do not have the ability to spatially localize/synchronize their protrusions and retractions, resulting in small net centroid displacements[9].

4.1. IDEs in contact with biological cells

It is important to realize that giving a precise estimation of the parameters shown in Table 4.1 based on the microscopy images and using ImageJ is complicated. Particularly, when manually contouring cells and the axes can introduce error in the measurement and prevent seeing real differences between the cancer cell lines. In addition, we have to bear in mind that cells were not synchronized, i.e, cells are not at the same phase in the cell cycle and they probably exhibit different morphologies during spreading. For instance, cells in mitosis become rounded and lose most of their attachment to the substratum[10]. Despite this difficulties, we can conclude that between $S_{average}$ and the ratio L_a/L_b , the latter could be more suitable in describing the spreading behavior. Basically, it revealed that on the three substrates, MDA-MB-231 cells tend to elongate more along one axis (even slightly on ITO) while MCF-7 cells tend to spread uniformly while staying more "compact". Based on this, we can hypothesize that in the same way as we found different behaviors on ITO and Petri dish, we could find different behaviors on Au as well. It would be interesting to make these measurement on Au surfaces in order to be able to discuss if these morphological changes could also explain differences in impedance measurements between Au and ITO.

4.1.2 Monitoring cell proliferation with impedance

In this section, ECIS assays were carried out using the following protocol:

First, impedance measurement of the system in absence of cells was carried out in order to obtain the impedance parameters ($|Z_0|$, ϕ_0 , $\text{Re}(Z_0)$, $\text{Im}(Z_0)$) used to normalize the data and to follow the impedance variation in the presence of cells. Then, cells were injected into the PDMS reservoir and the system was stored in an incubator. Finally, impedance measurements were performed and microscopic images were taken periodically, with a period depending on the measurement configuration. The time, t , reported on the pictures and plots is the time after cell seeding. We usually tried to inject $\sim 18,000$ cells in the 5 mm diameter reservoir. However, we observed after cell sedimentation some inhomogeneity inside the reservoir with areas more densely covered than others. In addition, we found variations between reservoirs. This resulted in poor cell density reproductibility at the start of the assay. We therefore tried to vary the injection protocol in order to improve it. Unfortunately, we were not able to fully optimize it. That is why in some experiments, due to enable meaningful comparisons, we presented our results as a function of a normalized time, T , which was computed as $T = t/t_{monolayer}$, where t , corresponds to the time after cell seeding and $t_{monolayer}$ is the time that was necessary to reach a cell monolayer during the experiment.

4.1.2.1 Preliminary experiments:

At first, we were interested in following the cell activity inside of the incubator from the moment of cell seeding to the formation of the cell monolayer on top of the electrodes. In order to achieve this, we connected the Potentiostat to our electrodes using shielded cables to prevent parasitic interferences in our measurements. However, before carrying out the measurements inside of the incubator, we verified that indeed the shielded cables did not affect our impedance data by comparing the measurements with the shielded cables, performed outside and inside of the incubator at 37 °C. Then, just before conducting an experiment with cells, we followed the impedance of the system in contact with only cell culture medium inside of the incubator. We found that every time the culture medium was refreshed, the impedance increased, leading to fluctuations in the signal. This could be due to evaporation which effectively increases the ion concentration in the medium and further decreases the resistance of the solution. Thus, when we refreshed the medium, this addition had a lower ion concentration, which increased the impedance. In the future, in order to circumvent this evaporation issue, we need to find a way to continuously refresh the medium. A possible solution to this problem, could be to work in a microfluidic environment that will also, as it was mentioned in chapter 1, reduce the sample volumes. Ideally, this microfluidic device has to enable both recirculation and refreshing of the cell culture medium during the experiment. Nevertheless, although this seems to be a promising strategy,

as previous works have outlined, there are important practical considerations related to operating microfluidic perfusion culture systems that arise, such as cell seeding, management of physicochemical properties, mass transport, shear stress, and bubble formation [11, 12]. For instance, the introduction of air bubbles inside the system can apply stress to cells and even lead to cellular death[13]. Moreover, precise control of the flow is required in order to prevent detachment of the cells by shear stress[14] and to reduce cell clogging to improve uniformity of cell distribution[15]. Taking all these considerations into account means that the fabrication process of our system and experimental set-up will have higher complexity. Therefore, in order to not waste too much time solving technical issues and optimizing the set-up, for this PhD thesis we decided culture the cells inside of the incubator but to carry out the measurements outside of the incubator where the cell culture medium could be refreshed before each impedance measurement.

4.1.2.2 Cell proliferation on Au and ITO

We used phase contrast microscopy and impedance measurement to monitor the formation of a cell monolayer of MCF-7 on the interdigitated electrodes. Microscopy images of MCF-7 cells proliferating on top of Au IDEs surface are shown in Fig.4.3. We can see that one hour following cell seeding, the majority of the cells are round shaped and they have not adhered onto the surface with a cell coverage ratio $\eta = 47\%$. At $t = 19$ h, cells have begun to adhere with a cell coverage ratio $\eta = 60\%$. It is important to note that giving a precise estimation of the cell coverage ratio η for Au IDEs was more difficult compared to ITO due to its lack of transparency. As time went by, MCF-7 cells proliferated increasing the cell coverage ratio η from 47% to 99%, corresponding to a culture time of $t = 70$ h.

As for ITO, microscopy images of cell proliferation on the electrode surface are shown in Fig.4.4. We observe that at $t = 6$ h, most of the cells are still round and have not completely adhered to the surface, which has a cell coverage ratio $\eta = 16\%$. It is only at $t = 22$ h that cells have started to adhere covering 34% of the electrode surface. Similar to the images of Au IDEs, as time went by, the cell coverage ratio η increased from 16% to 96%, corresponding to a culture time of $t = 175$ h.

For both materials, what we observed in the microscopy images is coherent with the cell adhesion process depicted in Fig.4.5 where 3 stages can be identified: (I) attachment of the cell body to its substrate after injection, (II) flattening and spreading of the cell body and (III) the organization of the actin filaments with the formation of focal adhesion between the cell body and its substrate[16]. This process takes a certain time so that the cells can attach to the surface and start growing. In ECIS experiments, the initial cell density is subjected to variations due to pipetting error and differences in the number of cells that actually survive and attach after seeding[17]. That is why, prior to any molecule or drug addition, it seems necessary to wait ~ 24 h in order to have adhesion of cells, which is consistent with what other authors have reported in the literature[18, 19, 20, 21]. For example, according to Egger et al.[22] in their study on cellular uptake of metal compounds in adherent tumor cells, preincubation in culture medium prior to drug addition varies from 8 h to 48 h or the time is adapted to fulfill the requirement of a certain degree of confluence depending on the cell line. The manufacturer of the xCELLigence system (Roche Diagnostics), it recommends that before cells are exposed to any compounds during an experiment, cells should be incubated for approximately 16 h to 24 h[18].

4.1. IDEs in contact with biological cells

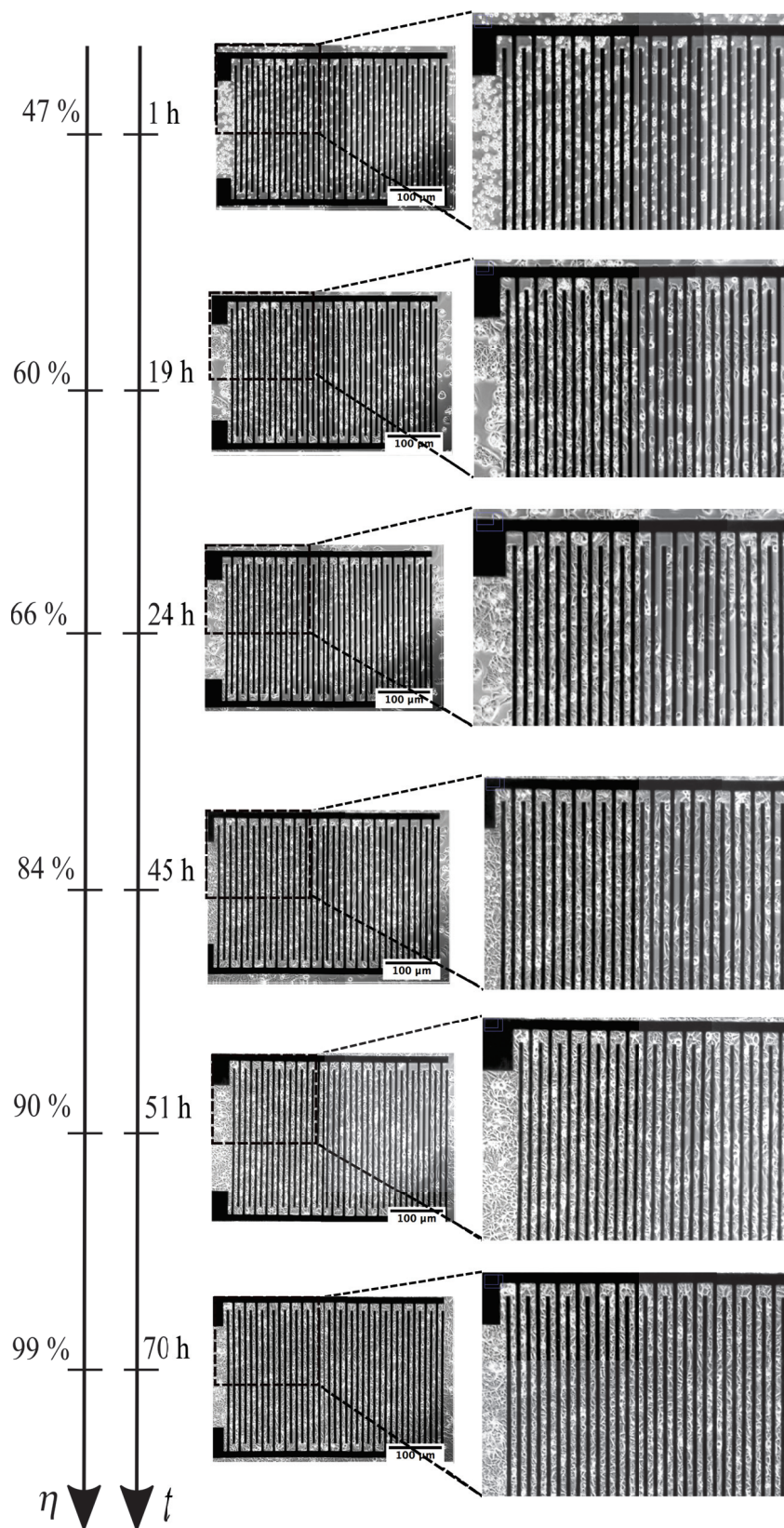


Figure 4.3 – Phase contrast micrographs of MCF-7 cells on the surface of the Au IDEs at 10X magnification (Leica D2000).

4.1. IDEs in contact with biological cells

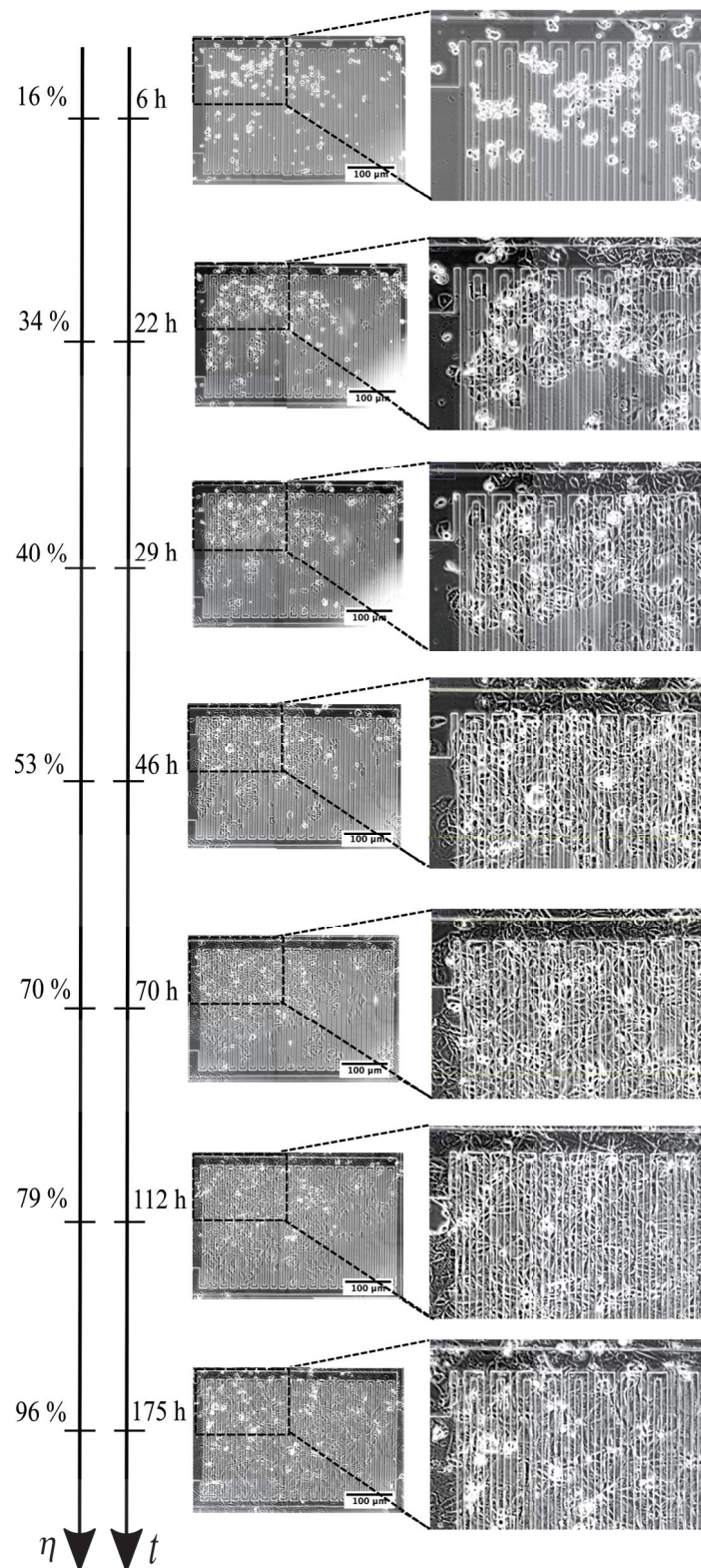


Figure 4.4 – Phase contrast micrographs of **MCF-7** cells on the surface of the **ITO** IDEs at 10X magnification (Leica D2000).

4.1. IDEs in contact with biological cells

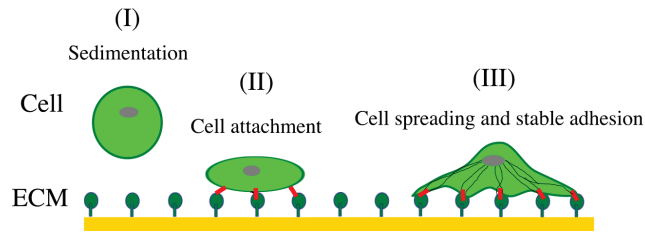


Figure 4.5 – Stages of the cell adhesion process: (I) Sedimentation, (II) Cell attachment and (III) Cell spreading and stable adhesion. Figure modified from Table 1 in[16].

In parallel, we carried out impedance measurements over the frequency range 1 MHz to 100 mHz for both materials in the presence of MCF-7 cells. Fig.4.6 shows the magnitude and phase of the impedance spectra for Au IDEs. We observe that the proliferation with time of MCF-7 affects $|Z|$ in the whole frequency range. However, the most noticeable change occurred between 10 kHz to 100 kHz, in the crossover frequency range. This latter zone is clearly more affected by the MCF-7 cells attaching to the surface, which is consistent with the literature that shows that the presence of cells on Au electrodes can be best identified in the kHz range[23, 24]. As time and surface coverage η incremented, impedance, between $1 \text{ kHz} < f < 1 \text{ MHz}$, also incremented. In addition, we found that at low frequencies ($< 10 \text{ Hz}$) the phase angle decreased and then it remained relatively rather constant ($\phi \rightarrow -85^\circ$) for a while. Soon after, it increased in the frequency range from 10 Hz to 30 kHz and then we see a "kink" appearing with a phase value around -45° . Finally, it decreased at higher frequencies ($> 30 \text{ kHz}$).

4.1. IDEs in contact with biological cells

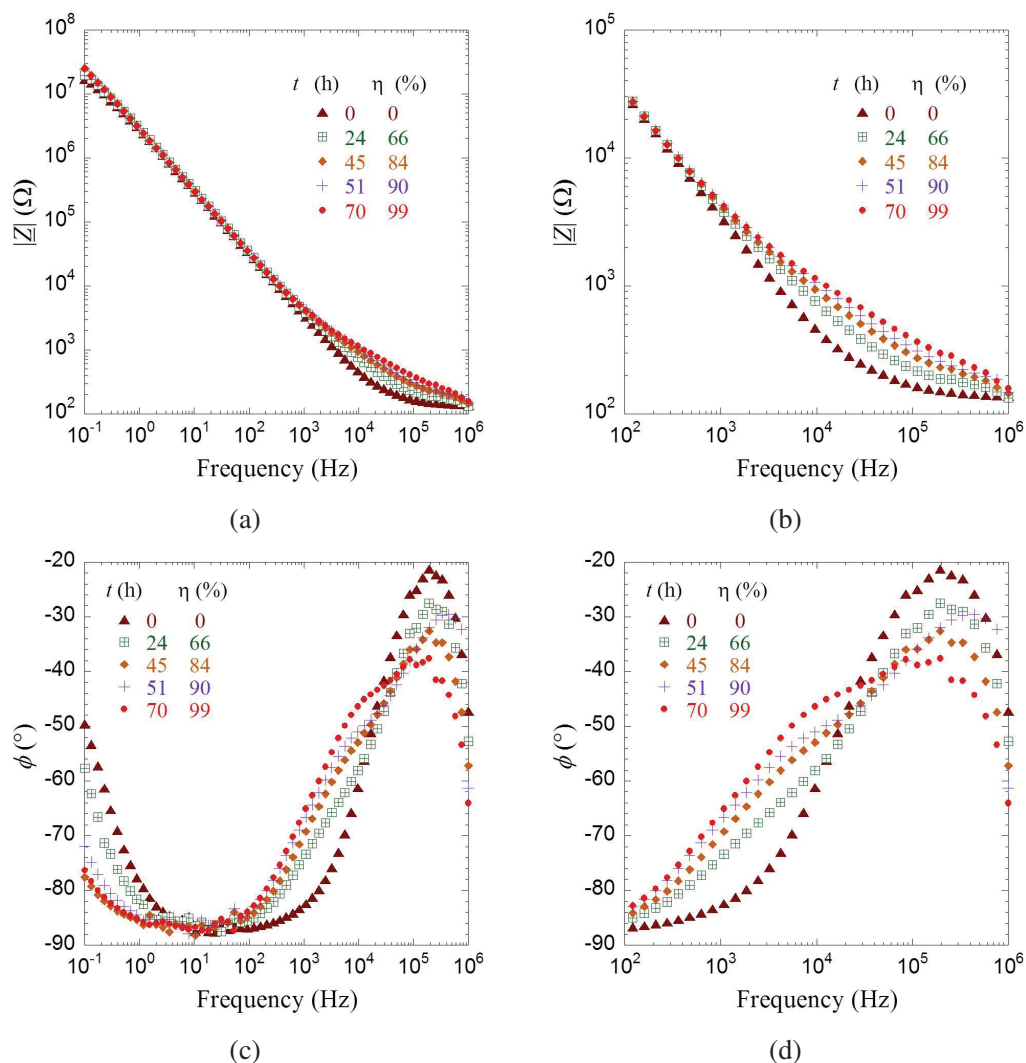


Figure 4.6 – Magnitude and Phase of the impedance spectra of **MCF-7** cells on **Au** IDEs during cell growth in the frequency range (a, c) from 1 MHz to 100 mHz and (b, d) from 1 MHz to 100 Hz.

The ITO IDEs, results are found in Fig.4.7 where, at low frequencies (<1 kHz), we observe that the impedance did not seem to be affected by cell proliferation. Nevertheless, there was a slight increase in the magnitude of $|Z|$ within a frequency range from 1 kHz to 10 kHz. Then, at higher frequencies (>10 kHz), the impedance did not appear to be influenced by cell growth. Concerning the phase angle, it remained relatively constant ($\phi \rightarrow -86^\circ$) at low frequencies (<70 Hz), associated with the electrode-solution interface (CPE_{int}). Then, almost imperceptibly, it increased over the range from 70 Hz to 3 kHz and finally slightly decreased at higher frequencies (> 3 kHz). Phase angles obtained at 194 kHz are much closer to 0° compared to those at lower frequencies, revealing more resistive characteristics at high frequencies due to the resistance of the electrode.

4.1. IDEs in contact with biological cells

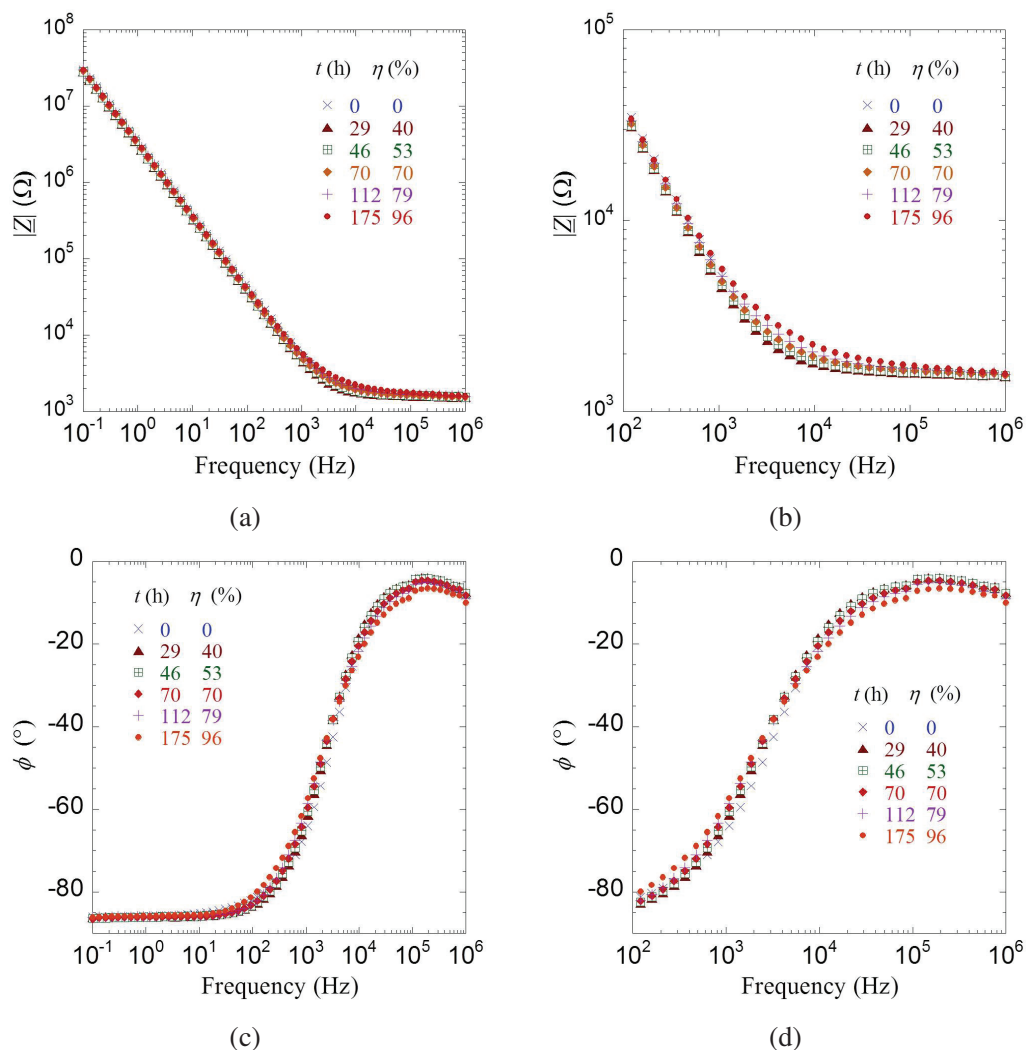


Figure 4.7 – Magnitude and Phase of the impedance spectra of **MCF-7** cells on **ITO** IDEs during cell growth in the frequency range (a, c) from 1 MHz to 100 mHz and (b, d) from 1 MHz to 100 Hz.

When we compared the Bode plots of these electrode materials we found certain significant differences. First, the range of frequencies where the impedance is influenced by the cell growth was narrower for ITO IDEs (1 kHz to 10 kHz) compared to Au IDEs (1 kHz to 1 MHz). Moreover, we noticed that for similar values of surface coverage $\eta=99\%$ (Au IDEs) and $\eta=96\%$ (ITO IDEs), the impedance variation ($\Delta|Z|$) due to cell proliferation was slightly higher for Au IDEs ($\Delta|Z|=773 \Omega$) compared to that of ITO IDEs ($\Delta|Z|=619 \Omega$). Although, we used the same cell line, MCF-7, it seems that the Au IDEs are more sensitive to cell growth than ITO IDEs. Perhaps, this means MCF-7 cells do not attach in the same way onto Au and ITO surfaces, therefore the impedance of the systems is not affected in the same way. According to Asphahani et al.[25], cell adhesion and spreading directly affect the impedance properties of cell-based sensors, and a tight cell binding to the electrode and a high surface coverage of the electrode by the cell may increase the sensitivity. Therefore, secondary studies would be needed in order to investigate the focal adhesions¹ of MCF-7 on both materials. Focal adhesions provide contacts between the cells and the surface where they are

¹Focal adhesions are complex plasma membrane-associated macromolecular assemblies that are linked with the surrounding extracellular matrix

4.1. IDEs in contact with biological cells

going to proliferate. For example, focal adhesion quantification of MCF-7 cells on Au and ITO IDEs could be achieved by identifying a focal adhesion complex and then labelling any protein within it[26] in order to understand the distribution and formation of focal adhesions by MCF-7 cells on both materials. Another possibility would be to carry out cell detachment experiments in a microfluidic environment. For example, Rupprecht et al.[27] designed and tested a simple 4-channel tapered microfluidic device for cell adhesion strength measurements based on the analysis of cellular response to varying hydrodynamic shear stresses.

The experimental data for cell growth on both materials ITO and Au were also presented using the Nyquist representation-in Fig.4.8 for Au IDEs and in Fig.4.9 for ITO IDEs. In the case of Au IDEs, at low frequencies ($f < 1$ Hz), the cell proliferation straightens up the curve. In fact, this is possibly due to the adsorption of proteins or products released during cell growth, affecting the low frequency interfacial impedance which is sensitive to surface effects. We do not know if more studies have found this behavior for Au IDEs at low frequencies because most of the time authors show impedance results using only the Bode representation and the Nyquist plot is omitted. As for mid-frequencies from 110 kHz to 5.5 kHz on the other hand, the slope of the impedance spectrum decreased from 2.8 ($\eta=66\%$) to 1.1 ($\eta=99\%$) as the electrode surface was covered by the cells.

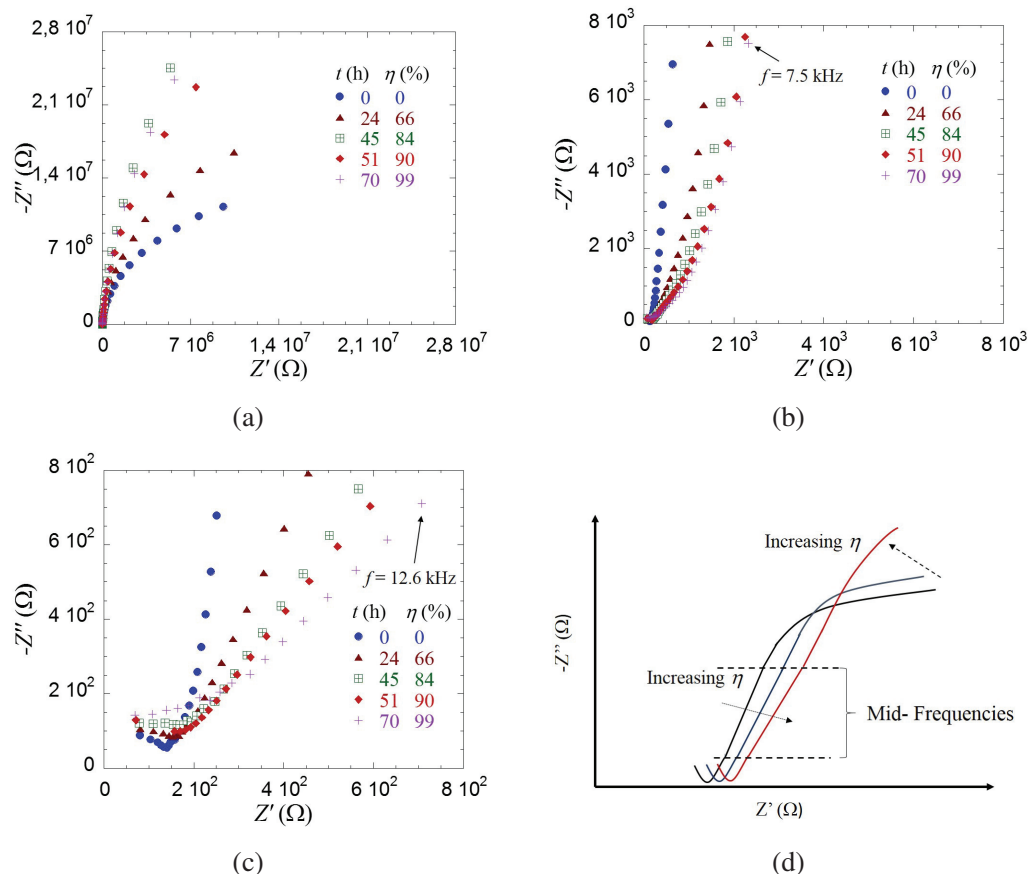


Figure 4.8 – Imaginary part vs Real part of the impedance spectra of **MCF-7** cells on **Au** IDEs in the frequency range from (a) 1 MHz to 100 mHz, (b) 476 Hz to 100 mHz, (c) 1 MHz to 12.6 kHz and (d) Diagram of the evolution of the Nyquist curves during cell growth on Au IDEs.

In contrast, the Nyquist plots for ITO in Fig. 4.9 reveal that at low frequencies, the curve is not affected by cell proliferation. However, at higher frequencies, we found that as η increased with cell growth, the

4.1. IDEs in contact with biological cells

intercept with the Z' axis slightly shifted towards higher values. Moreover, the slope of the curves at mid-frequencies (~ 3 kHz to 100 kHz) decreased from 5.7 ($\eta=40\%$) to 2.4 ($\eta=96\%$). For both materials we saw that when the MCF-7 cells attached and spread on the surface, the slopes at mid-frequencies of the Nyquist curves decreased.

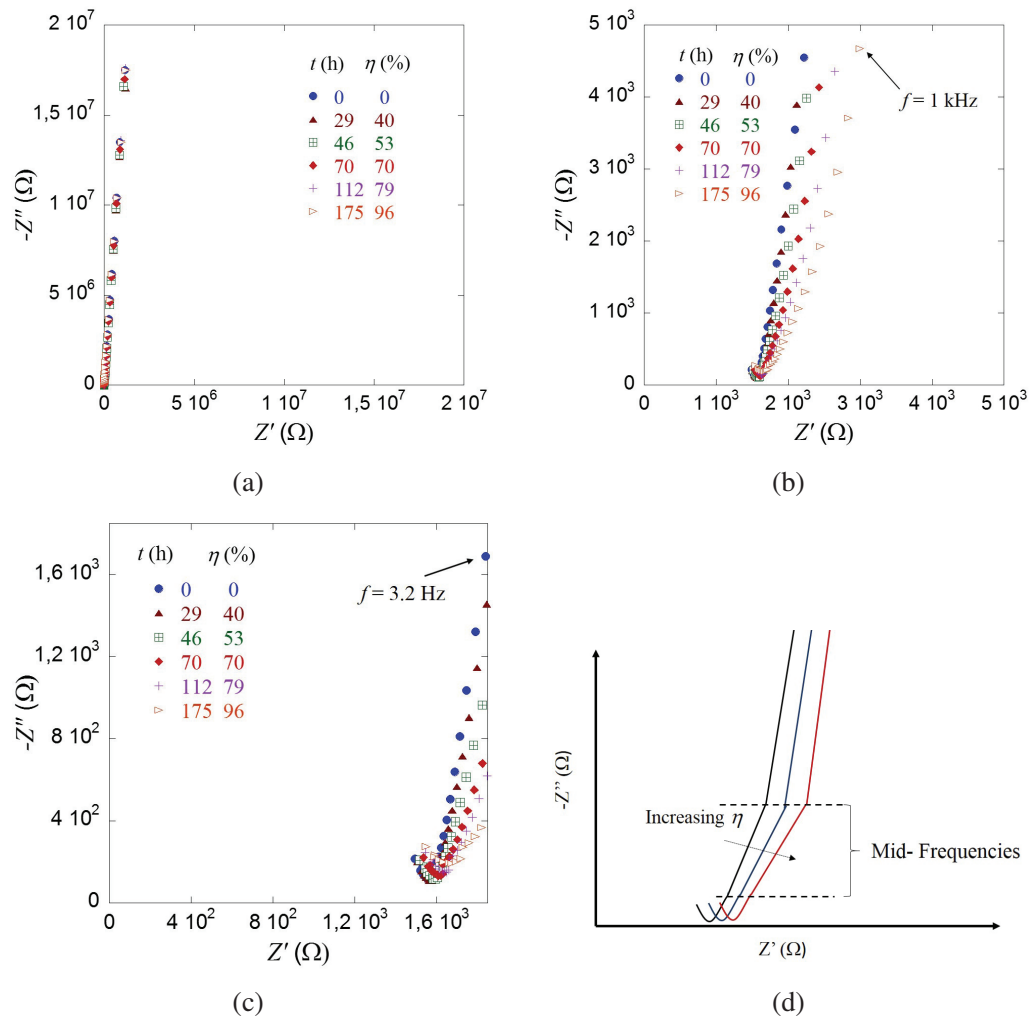


Figure 4.9 – Imaginary part vs Real part of the impedance spectra of MCF-7 cells on ITO IDEs in the frequency range from (a) 1 MHz to 100 MHz, (b) from 1 MHz to 1 kHz, (c) from 1 MHz to 3.2 kHz and (d) Diagram of the evolution of the Nyquist curves during cell growth on ITO IDEs.

4.1. IDEs in contact with biological cells

In the vast majority of ECIS assays[28, 29, 30], results are usually collected at a single frequency and represented as a normalized impedance magnitude, also termed cell index, which is defined by equation (3.12):

$$Z_{norm} = \frac{|\underline{Z}(t)_{cells}| - |\underline{Z}_0|}{|\underline{Z}_0|} \quad (4.1)$$

where $|\underline{Z}(t)_{cells}|$ is the impedance value of a cell-covered electrode at time t and $|\underline{Z}_0|$ corresponds to the impedance value of the same electrode without cells.

When cells grow and attach to the electrodes, an increase in Z_{norm} is expected. Conversely, cells detaching from the electrode leads to a decrease in Z_{norm} [31]. Various authors[32, 33, 34] have concluded that in order to follow cell proliferation, this parameter is sufficient and that the phase information is not needed. In this section, we decided to compare different strategies to analyze cell proliferation impedance assays: (i) using a normalized impedance magnitude representation and (ii) using an equivalent circuit model approach.

4.1.3 Normalized impedance Z_{norm}

Fig.4.10 presents the normalized impedance of MCF-7 proliferating on Au IDEs as a function of frequency. As expected, we observe an increase in the normalized impedance over time due to adhesion and proliferation of the cells on the electrode surface. During mammalian cell growth, the number of adherent cells attached to the interdigitated electrodes increases and they restrict the passage of electrical current giving an increase in the measured impedance. The normalized impedance plot has a "bell shape" with a maximum value that increases with time and it occurs at a specific frequency, which is in agreement with similar curves in the literature[7, 35]. The frequency at which we find the maximum value of Z_{norm} (proportional to the change in impedance) indicates the optimal frequency, f_{peak} , to provide the highest sensitivity to changes in the cell layer under study in ECIS experiments[36]. We observed that when the cell monolayer was formed, Au IDEs showed $(Z_{norm})_{peak} = 1.7$ and $f_{peak} = 21.8$ kHz. Moreover at very low frequency ($0.1 \text{ Hz} < f < 1 \text{ Hz}$), we can see that Z_{norm} decreases until it remains relatively constant around 0.

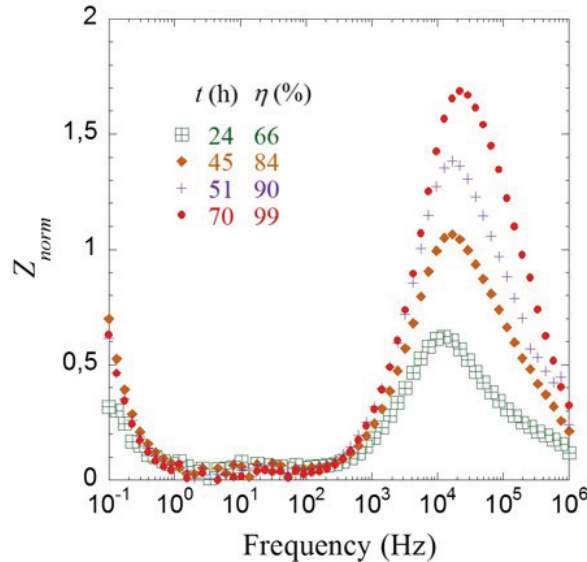


Figure 4.10 – Normalized impedance of MCF-7 cells grown on Au IDEs and measured over a frequency range from 1 MHz to 100 mHz.

4.1. IDEs in contact with biological cells

Z_{norm} for ITO IDEs is plotted in Fig.4.11, and we note a similar behavior to that of Au IDEs as time increases. Nevertheless, the values of f_{peak} and $(Z_{norm})_{peak}$ indicative of cell proliferation are different. For instance, when the cell monolayer was reached, the ITO IDEs had a maximum $(Z_{norm})_{peak}$ value of 0.27 at $f_{peak} = 5.5$ kHz. Moreover, at around 1 kHz, we observe a negative peak that disappears when η increments. We conducted various ECIS experiments with MCF-7 cells proliferating on both materials and the mean values of $(Z_{norm})_{peak}$ and f_{peak} for Au and ITO IDEs are shown in Table 4.2. In spite of using the same cell line with the same electrode geometry, we found that Au IDEs exhibit a $(Z_{norm})_{peak}$ approximately 4 times larger than that of ITO IDEs. Regarding f_{peak} , we also found differences between ITO IDEs and Au IDEs. Scientists have observed that the shape of the curve, as well as the maximum Z_{norm} obtained, is cell-type specific[32, 37]. Since Au IDEs have higher Z_{norm} values, once the monolayer is formed, we can say that these exhibit a higher sensitivity to proliferative activity of MCF-7 cells compared to ITO IDEs. This is coherent with the work of Choi et al.[38], where they found that circular 250 μm ITO electrodes showed similar but somewhat reduced sensitivity to endothelial cell attachment compared to 250 μm Au electrodes. The low sensitivity of ITO IDEs might be due to differences observed in previous sections of this thesis regarding the adhesion behaviors of cells on different materials, which appears to play an important role in the overall impedance of the system. In addition, in the previous sections we found that Au-CN/BSA IDEs showed $Q_{int} = 133 \pm 33 \times 10^{-9} \text{ s}^\alpha/\Omega$, $\alpha_{int} = 0.960 \pm 0.003$ and $R_t = 126 \pm 4 \Omega$. While ITO-CN/BSA IDEs exhibited $Q_{int} = 84 \pm 8 \times 10^{-9} \text{ s}^\alpha/\Omega$, $\alpha_{int} = 0.936 \pm 0.009$ and $R_t = 1840 \pm 71 \Omega$. Based on these results, we concluded that Au IDEs have lower interfacial impedance and lower resistive behavior compared to ITO IDEs. If we look at the schematic representation of an ECIS system depicted in Fig.3.1, a large interfacial impedance contribution and a high resistive contribution from the electrodes could mask the information pertaining to cell growth during an ECIS experiment, thus adversely affecting the measurement sensitivity. Hence, when comparing these two materials, Au IDEs with their low $Z_{CPE_{int}}$ and R_t values will experience a greater impedance variation due to cell proliferation. This means if we would like to use transparent electrodes for ECIS experiments, we would need to find a strategy that lower the interfacial and resistive contributions of ITO, as will be shown in chapter 6.

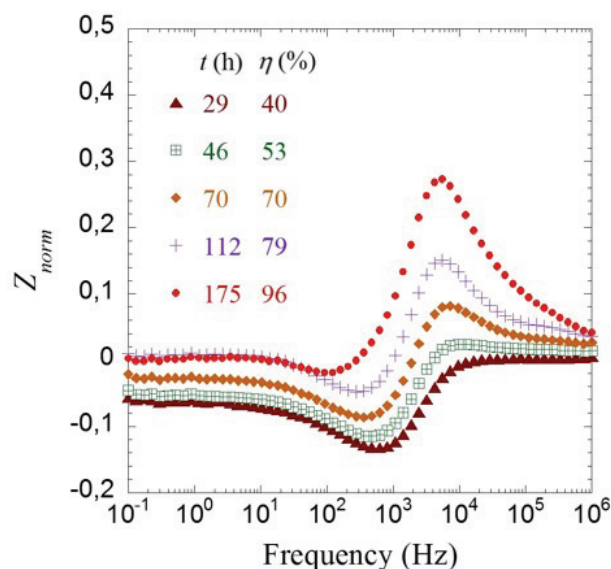


Figure 4.11 – Normalized impedance of MCF-7 cells grown on ITO IDEs and measured over a frequency range from 1 MHz to 100 mHz.

4.1. IDEs in contact with biological cells

Material	$(Z_{norm})_{peak}$	f_{peak} (kHz)
Au	1.06 ± 0.48	51 ± 43
ITO	0.24 ± 0.02	7.4 ± 1.6

Table 4.2 – $(Z_{norm})_{peak}$ and f_{peak} values when $\eta = 99\%$ for Au IDEs and $\eta = 96\%$ for ITO IDEs. (Mean \pm SD with n=6 for Au and n=4 for ITO).

4.1.4 Normalized impedance at low frequency (f_{LF}), high frequency (f_{HF} and peak frequency (f_{peak}))

Normalized impedance, also known as "cell index" is the most popular representation in ECIS to show the temporal evolution of cellular induced changes at the specific frequency, f_{peak} , where the contribution of cells to the measurement is the highest. Nevertheless, as we presented in chapter 2, in ECIS, depending on the working frequency, the current will follow different pathways. Therefore, some authors[39, 40] have proposed to distinguish cellular events by measuring the impedance spectra at distinct frequencies: low frequency (f_{LF}) and high frequency f_{HF} . f_{LF} is taken as the frequency before the current starts going through the cell membrane, which, due to its capacitive behavior acts as an insulator at low frequencies[39]. Working with f_{LF} could therefore give information concerning extracellular events occurring in the system, since the current at $f < f_{LF}$ cannot penetrate the cell membrane and must go through the spaces between cell-electrode and cell-to-cell junctions. f_{HF} , on the other hand, is taken as the frequency at which the cell membrane is short-circuited and the current can go through the cells, providing information concerning the intracellular space[39].

Contrary to f_{peak} , the determination of these two frequencies involves phase information. f_{LF} is defined as the frequency where the normalized phase angle ϕ_{norm} is maximal. ϕ_{norm} is given by the expression:

$$\phi_{norm} = \max\left(\frac{\phi_t - \phi_0}{\phi_0}\right) \quad (4.2)$$

where ϕ_t is the impedance phase angle of the cell-covered electrode at time t and ϕ_0 is the impedance phase angle of the cell-free electrode.

Eker et al.[39] found that the impedance magnitude at this maximum phase difference frequency, f_{LF} , is the most sensitive to the extracellular resistive contribution. Regarding f_{HF} , this one needs to be chosen high enough to circumvent the capacitive behavior of the cell membrane that blocks the current. Hence, f_{HF} is chosen as the frequency where the phase angle is closest to 0° .

We determined as shown in Fig.4.12, the three key frequencies for both materials. Au IDEs have the following values $f_{peak} = 21.8$ kHz, $f_{LF} = 4.2$ kHz and $f_{HF} = 194$ kHz while ITO IDEs have $f_{peak} = 5.5$ kHz, $f_{LF} = 1.8$ kHz and $f_{HF} = 194$ kHz.

4.1. IDEs in contact with biological cells

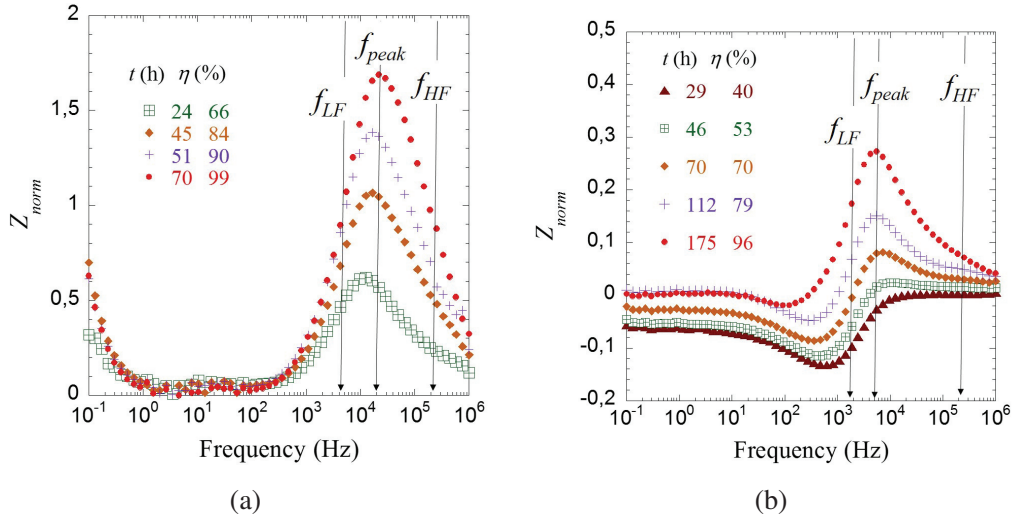


Figure 4.12 – Z_{norm} versus frequency with f_{peak} , f_{LF} and f_{HF} indicated during cell proliferation on (a) Au IDEs and (b) ITO IDEs.

The normalized impedances Z_{norm} at these specific frequencies as a function of time are presented in Fig.4.13 for Au IDEs and in Fig.4.14 for ITO IDEs. For Au IDEs, we notice that when the number of adherent cells covering the electrodes rises, the 3 signals increased. Z_{norm} at f_{LF} varied by 0.43 (from 0.46 to 0.89), Z_{norm} at f_{HF} increased by 0.72 (from 0.25 to 0.97), Z_{norm} at f_{peak} incremented, 1.11 (from 0.57 to 1.68) during cell proliferation. Surprisingly, Z_{norm} at f_{LF} has similar behavior to Z_{norm} at f_{HF} rather than to f_{peak} . We expected f_{LF} and f_{peak} to be more sensitive to cell proliferation. For instance, when measuring with f_{LF} , we are studying extracellular events such as the formation of cell-to-cell junctions during cell proliferation. Normally, cells adhere to one another through junctional structures formed by transmembrane adhesive proteins that are responsible for cell-to-cell adhesion. The transmembrane proteins interact with the cytoskeleton and stabilize the junctions between cells such as adherens junctions, tight junctions and desmosomes[41]. The formation of new junctions blocks the current, which increases Z_{norm} . While with f_{HF} , we are studying intracellular events such as cytoskeleton reorganization, which might block less the current than the formation of new cell junctions. In fact, we could say that the f_{HF} curve increases due to cell spreading. As cells spread and flatten on the electrode surface, they lead to an increase in the resistance of the cytoplasm, which is determined by cell morphology[42]. As for the ITO electrodes, we observe similar behaviors as for Au IDEs. However, in this case Z_{norm} at f_{LF} and at f_{peak} appears to increase more rapidly than Z_{norm} at f_{HF} .

4.1. IDEs in contact with biological cells

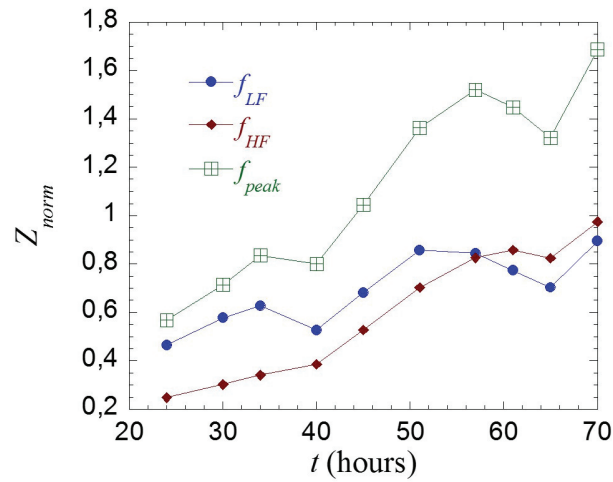


Figure 4.13 – Z_{norm} at f_{peak} (21.8 kHz), f_{LF} (4.2 kHz) and f_{HF} (194 kHz) versus time during **MCF-7** proliferation on **Au** IDEs.

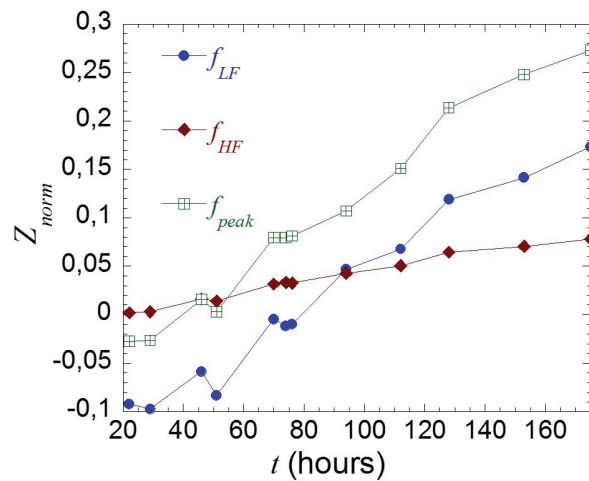


Figure 4.14 – Z_{norm} at f_{peak} (5.5 kHz), f_{LF} (1.8 kHz) and at f_{HF} (194 kHz) versus time during **MCF-7** proliferation on **ITO** IDEs.

So far, with the normalized impedance representation, we have identified 3 frequencies (f_{peak} , f_{LF} and f_{HF}) that can be used to analyze cell proliferation data. For both materials, we observed that f_{peak} increased as the cell covered electrode surface incremented whereas the f_{HF} curve seemed to be less sensitive to the presence of cells. Regarding f_{LF} , we observed that although this frequency provides information on extracellular properties, it did not show the same behavior as the f_{peak} curve for both materials. For instance, for Au IDEs, Z_{norm} at f_{LF} was not similar to Z_{norm} at f_{peak} whereas for ITO IDEs both curves were resembling. Based on this, we might conclude that, of the 3 frequencies, f_{peak} seems to be most suitable to monitor the formation of the cell monolayer, in terms of extracellular information.

4.1.5 Evolution of f_{peak} as a function of time

In the previous sections we saw that we can present the same data either as the evolution of Z_{norm} as a function of frequency or Z_{norm} at 3 different frequencies as a function of time. From these plots we can confirm that for both materials, Z_{norm} increases over time as the number of cells covering the electrodes increments, as depicted in Fig.4.4 and Fig.4.3. However, some studies suggest that monitoring the value of f_{peak} could give us supplementary information regarding cell adhesion on the electrodes.

Finite element simulations of impedance changes due to cell growth carried out by Xiaqiu et al.[43] and Greve et al.[44] have shown that f_{peak} provides information on cell attachment to the substrate and cell-surface gaps. According to them, f_{peak} depends on the cell size, the growth medium resistivity and the cell-sensing electrode gap, which may furnish more information regarding the interaction between the cells under study and the electrodes. We therefore carried out a simulation using the data of MCF-7 cells proliferating on ITO IDEs and the electrical model of the system in the presence of cells, described in the next section. Basically, we only varied the parameter R_{extra} associated with the cell-electrode gap using the values: 3.4 k Ω , 8.4 k Ω and 28.4 k Ω . Results are shown in Fig.4.15, where we observe that as R_{extra} increased, the f_{peak} shifted towards lower frequency values from 5.5 kHz to 2.4 kHz, which is in agreement with Xiaqiu's and Greve's results.

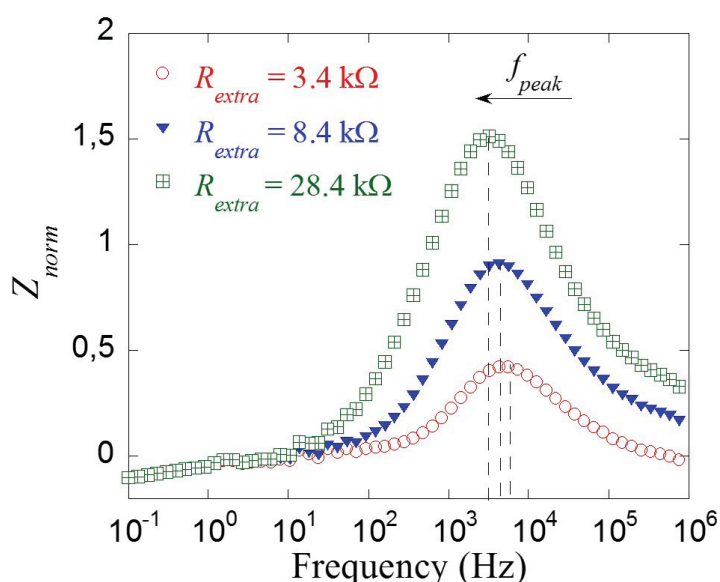


Figure 4.15 – Simulation results of Z_{norm} versus frequency for MCF-7 cells proliferating on ITO IDEs, the resistance R_{extra} was varied as described in the text. $f_{peak} = 5.5$ kHz ($R_{extra} = 3.4$ k Ω), $f_{peak} = 4.2$ kHz ($R_{extra} = 8.4$ k Ω) and $f_{peak} = 2.4$ kHz ($R_{extra} = 28.4$ k Ω).

Fig.4.16 presents the temporal evolution of f_{peak} of MCF-7 cells proliferating on Au IDEs and fig.4.17 on ITO IDEs. In the case of Au IDEs, f_{peak} decreased from 28.6 kHz to 12.6 kHz and from $t = 34$ h it increased again up to 21.8 kHz; whereas for ITO IDEs, f_{peak} decreased from 85.5 kHz to 5.5 kHz and remained relatively constant. Our experimental results are consistent with the visual observations as cells appeared rounded at the beginning of the assay and more flat during proliferation. We can hypothesize that at longer time, the cells adhere more on the surface.

During the first few hours, corresponding to the sedimentation stage, the cells have a spherical shape, which could be associated with high f_{peak} values. Once they start interacting with the substrate, they undergo morphological changes during cell attachment and finally cell spreading. When cells are allowed to settle

4.1. IDEs in contact with biological cells

on a solid surface they tend to flatten on it. Thus, we can infer that as time went on, the cells spread more on the surface of the IDEs, reducing the distance between the cell and the electrode surface, leading to lower values of f_{peak} . It appears that f_{peak} could potentially be a useful parameter reflecting the complex processes of focal adhesion formation and cellular skeleton reorganization and providing additional information to the Z_{norm} representation. Although we observed that f_{peak} for ITO and Au decreased during cell growth, Au IDEs showed higher values when the cell monolayer was formed, as shown in Table 4.2. Based on this change in f_{peak} , one can conclude that the cell attachment is not the same for each material and that probably MCF-7 spread more on the ITO IDEs than on the Au IDEs. In fact, cell attachment is a complex process, where several aspects play an important role, such as cell behavior, material surface properties and environmental factors. For instance, material surface properties include hydrophobicity, charge, roughness, softness and chemical composition of the surface.[45].

In order to validate this hypothesis, supplementary experiments that are beyond the scope of this thesis, such as cell attachment studies would need to be carried out to furnish more insight on the cytoskeleton reorganization of MCF-7 and the focal adhesions formed when they adhere to ITO and Au IDEs. These experiments cover the analysis from the formation of a molecular bond between the cell's surface receptors and the complementary ligands on the substrate to the observation of a population of cells' responses through the cells' behavior and changes in morphology during attachment events[16].

Several techniques have been developed to study cells. For instance, wash assays provide basic qualitative adhesion data by determining the fraction of cells which remain adhered after one or more washings[46, 47]. One can also use the quartz crystal microbalance that is based on changes in resonant frequency when interactions between the cell membrane and the substrate take place[48, 49]. Adhesion events can also be studied using microfluidics. In this latter technique, it is possible to observe cell spreading, tracking and migration inside a channel under the influence of fluid flow, this providing information on cell adhesion[50, 51].

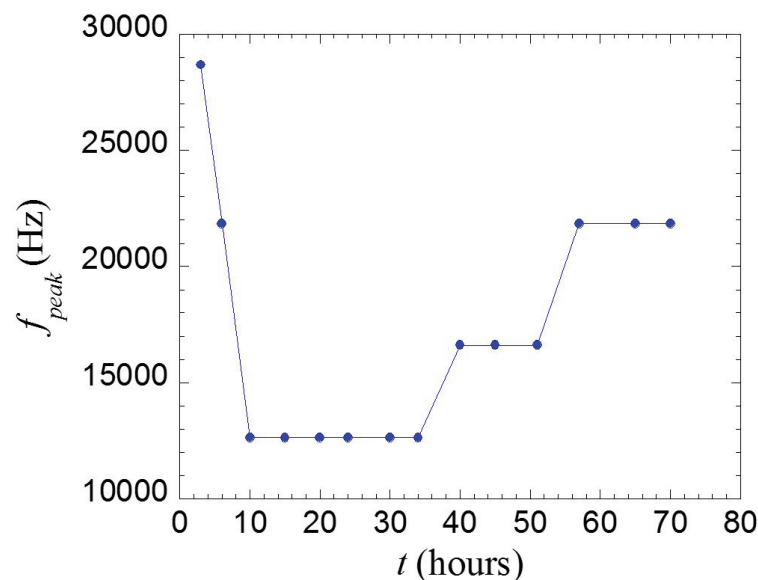


Figure 4.16 – Temporal evolution of f_{peak} of MCF-7 cells on Au IDEs

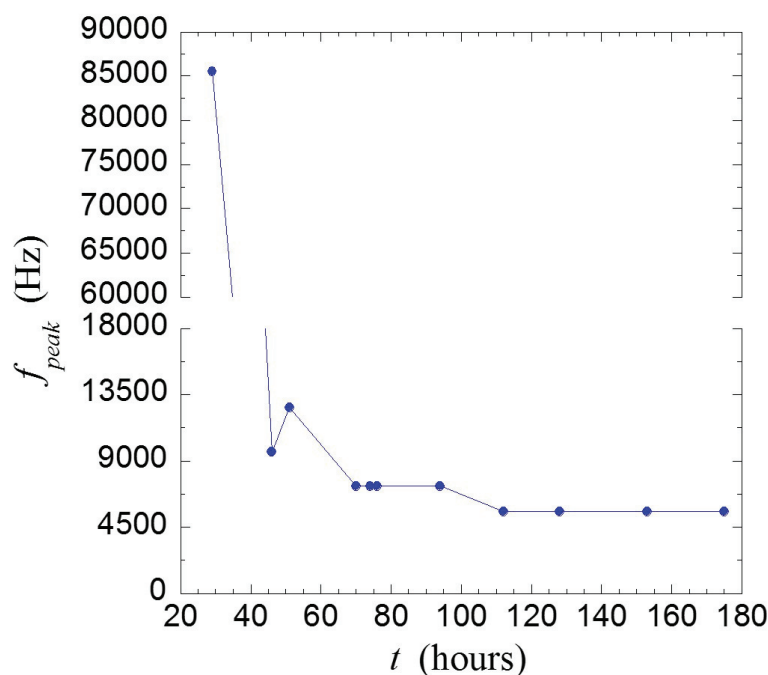


Figure 4.17 – Temporal evolution of f_{peak} of MCF-7 cells on ITO IDEs.

4.1.6 Equivalent circuit model of cells adhered on Au and ITO IDEs

We decided to fit the experimental data of IDEs using model 3 in Fig.4.18. In the previous section, we found that the semi circular arc due to $R_2 // CPE_2$ shrank for high conductivity solutions. When we fit our data with model 2 we obtained χ^2 values around 0.05. However, as mentioned earlier, $R_2 // CPE_2$ could be associated to surface roughness and this would not provide information about the cell monolayer on the surface of the electrodes. We therefore hypothesized that, since the cell culture medium is a high concentration electrolyte, adding cells to the system could mask the contribution of the semi circular arc due to $R_2 // CPE_2$. That is why we ignored these parameters in model 3 which includes the electrical parameters of the cells CPE_{cells} , R_{extra} and R_{intra} , as shown in Fig. 4.18. We used this equivalent circuit model to obtain the electrical parameters describing MCF-7 cells proliferating on top of Au and ITO IDEs and we obtained χ^2 values around 0.05, as shown in Fig. 4.19.

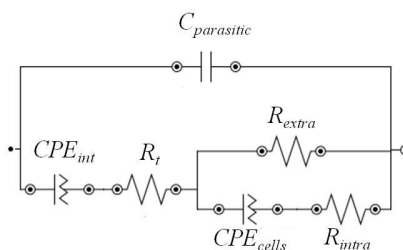
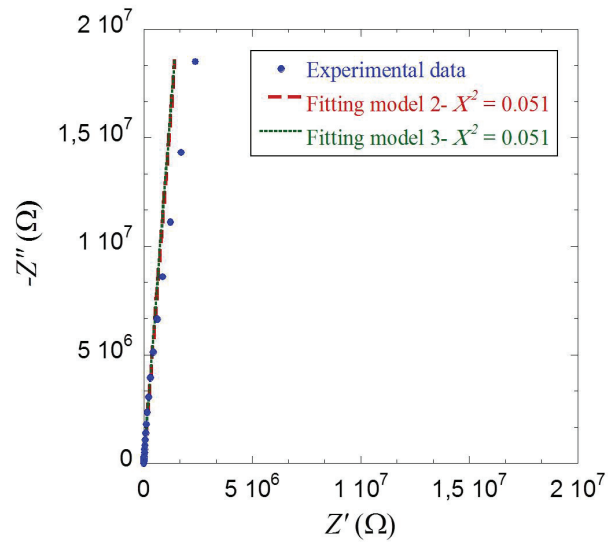
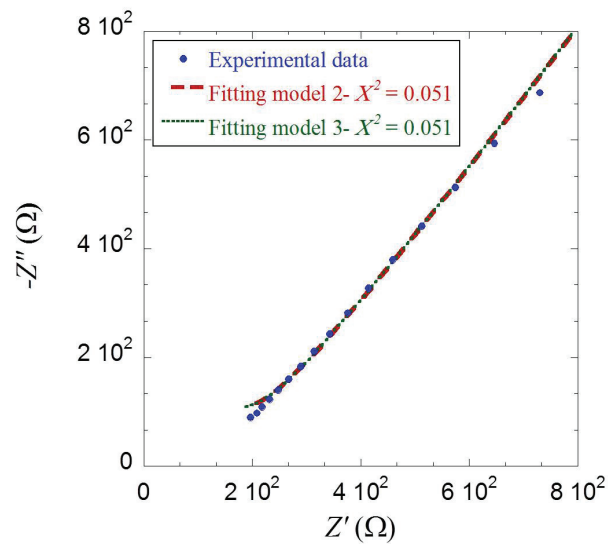


Figure 4.18 – Model 3 with R_{extra} , R_{intra} and CPE_{cells} .



(a)



(b)

Figure 4.19 – Comparing equivalent circuit models for **Au** IDEs covered with MCF-7 cell monolayer. (a) Nyquist plot in the frequency range from 1 MHz to 100 mHz and (b) from 1 MHz to 16.6 kHz.

First, we used the results in Table 3.7 of the impedance spectra of the supplemented medium without cells in order to deduce $C_{parasitic} = 185$ pF and $C_{parasitic} = 14$ pF for Au and ITO IDEs, respectively. Then, the impedance spectra of MCF-7 cells proliferating on Au and ITO IDEs were fitted with $C_{parasitic}$ as fixed value. In figures 4.20 and 4.22 we observed the temporal evolution of each parameter for Au and ITO IDEs, respectively.

4.1. IDEs in contact with biological cells

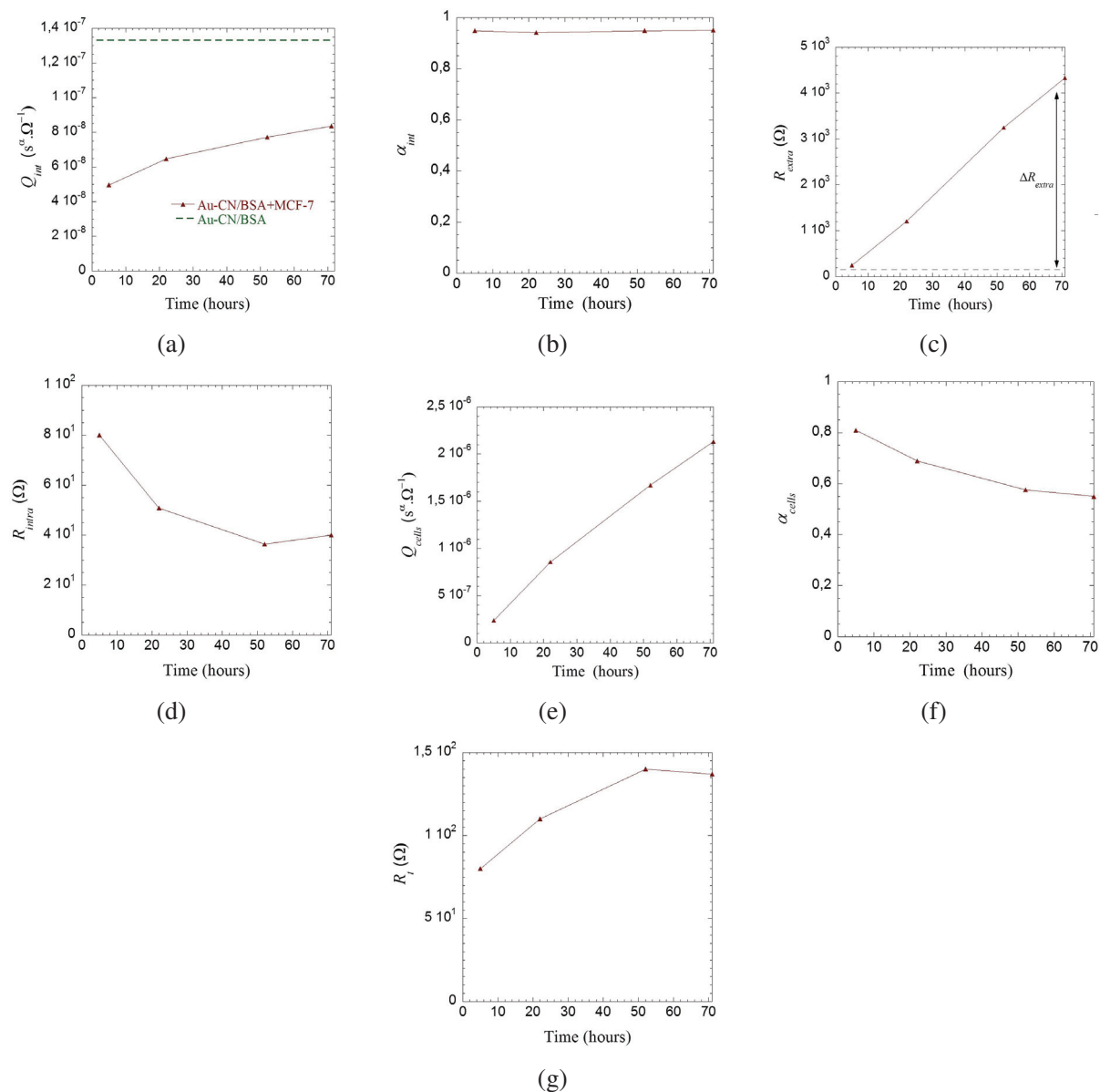


Figure 4.20 – Temporal evolution of the extracted parameters of **MCF-7** cells on top of **Au** IDEs: (a) Q_{int} , (b) α_{int} , (c) R_{extra} , (d) R_{intra} , (e) Q_{cells} , (f) α_{cells} and (g) R_t .

In the case of Au IDEs, we observed that Q_{int} slightly increased from $5 \times 10^{-8} s^\alpha \cdot \Omega^{-1}$ to $8 \times 10^{-8} s^\alpha \cdot \Omega^{-1}$ whereas α_{int} remained practically constant during cell growth. Interestingly, Q_{int} for Au IDEs with cells on the surface is lower than that of Au IDEs without the presence of cells. This could be due to the fact that when cells proliferate on the surface, they reduce the electrode area in contact with the culture medium, leading to an increase of the interfacial impedance with lower values of Q_{int} . Additionally, R_{extra} increased from 249 Ω to 4330 Ω giving a $\Delta R_{extra} \sim 4$ k Ω , once the monolayer is formed. This increment could be explained by the formation of new cell-to-cell junctions, cell spreading and new focal adhesions.

4.1. IDEs in contact with biological cells

Conversely, during the growth of the cell monolayer, R_{intra} decreased from 80Ω to 40Ω . According to Liu et al.[42], we can model the cell during the adhesion process as shown in Fig. 4.21 and the impedance of the cytoplasm $R_{cytoplasm}$ is given by the expression:

$$R_{cytoplasm} = \rho_c \frac{d}{\pi r^2} \quad (4.3)$$

where ρ_c is the resistivity of the cytoplasm, d and r correspond to the cell height and the cell radius, respectively. During proliferation, the cells' radius increases and the height decreases, leading to a decrease in the resistance of the cytoplasm $R_{cytoplasm}$. This could explain why R_{intra} decreased during cell monolayer formation.

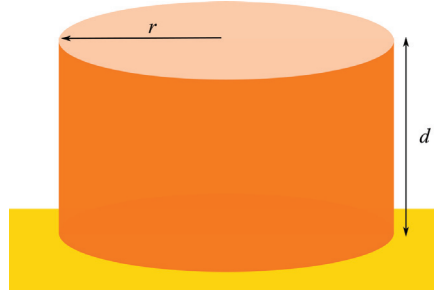


Figure 4.21 – Equivalent cylindrical shape of the cell. Figure adapted from Fig. 2 in[42]. Copyright 2014 by Taylor Francis. Adapted with permission.

As for Q_{cells} , this parameter increased during cell proliferation from $2.4 \times 10^{-7} \text{ s}^\alpha \cdot \Omega^{-1}$ to $2.1 \times 10^{-6} \text{ s}^\alpha \cdot \Omega^{-1}$ whereas α_{cells} slightly decreased. Since the number of cells adhered on the electrode surface is increasing and they start to connect to each other through tight junctions, we can consider the cell monolayer as a group of capacitances in parallel, whose equivalent value will increase as the monolayer is formed. R_t slightly increased from 80Ω to 137Ω probably due to some metabolites which are released during cell culture, affecting the conductivity of the cell culture medium.

Regarding the ITO IDEs, in Fig.4.22 we found the behaviors of the parameters similar to those of Au IDEs. For instance, parameters of the interface Q_{int} and α_{int} remained practically constant during cell growth. Moreover, R_{extra} increased from $1,420 \Omega$ to $3,500 \Omega$ giving a $\Delta R_{extra} \sim 2 \text{ k}\Omega$, once the monolayer was formed. On the other hand, R_{intra} decreased from 716Ω to 366Ω , which can be explained by equation (3.14). As for the parameter Q_{cells} , it slightly increased the first 46 h and then decreased. After that, it remained relatively constant during 38 h and then rapidly increased from $1.5 \times 10^{-7} \text{ s}^\alpha \cdot \Omega^{-1}$ to $5.8 \times 10^{-6} \text{ s}^\alpha \cdot \Omega^{-1}$ while α_{cells} took values between 0.4 and 0.6 during cell proliferation. In contrast to Au IDEs, R_t remained relatively constant during cell proliferation. This could be due to the high resistive behavior of ITO, shown earlier, which appears to mask variations for R_t .

Despite working with the same cell line, we found that a monolayer of MCF-7 cells on Au IDEs have higher R_{extra} and lower R_{intra} than MCF-7 cells on ITO IDEs. Probably, in order to find out the reason behind these differences, we would need to study MCF-7 cellular tight junctions, adhesive junctions and cytoskeleton structure by occludin staining, E-cadherin staining and actin labeling, respectively. This could help us identify structural changes due to cell monolayer formation on both materials. For example, Eker et al.[39] use these labeling techniques to investigate an increase of R_{extra} on doxorubicin resistant MCF-7 cells due to significant changes in the cell morphology and structure upon drug resistance. Regarding the parameters values, it is difficult to compare it with values found in the literature because as we mentioned before, few groups have extracted the electrical parameters associated with cell proliferation on electrodes[7, 52].

4.1. IDEs in contact with biological cells

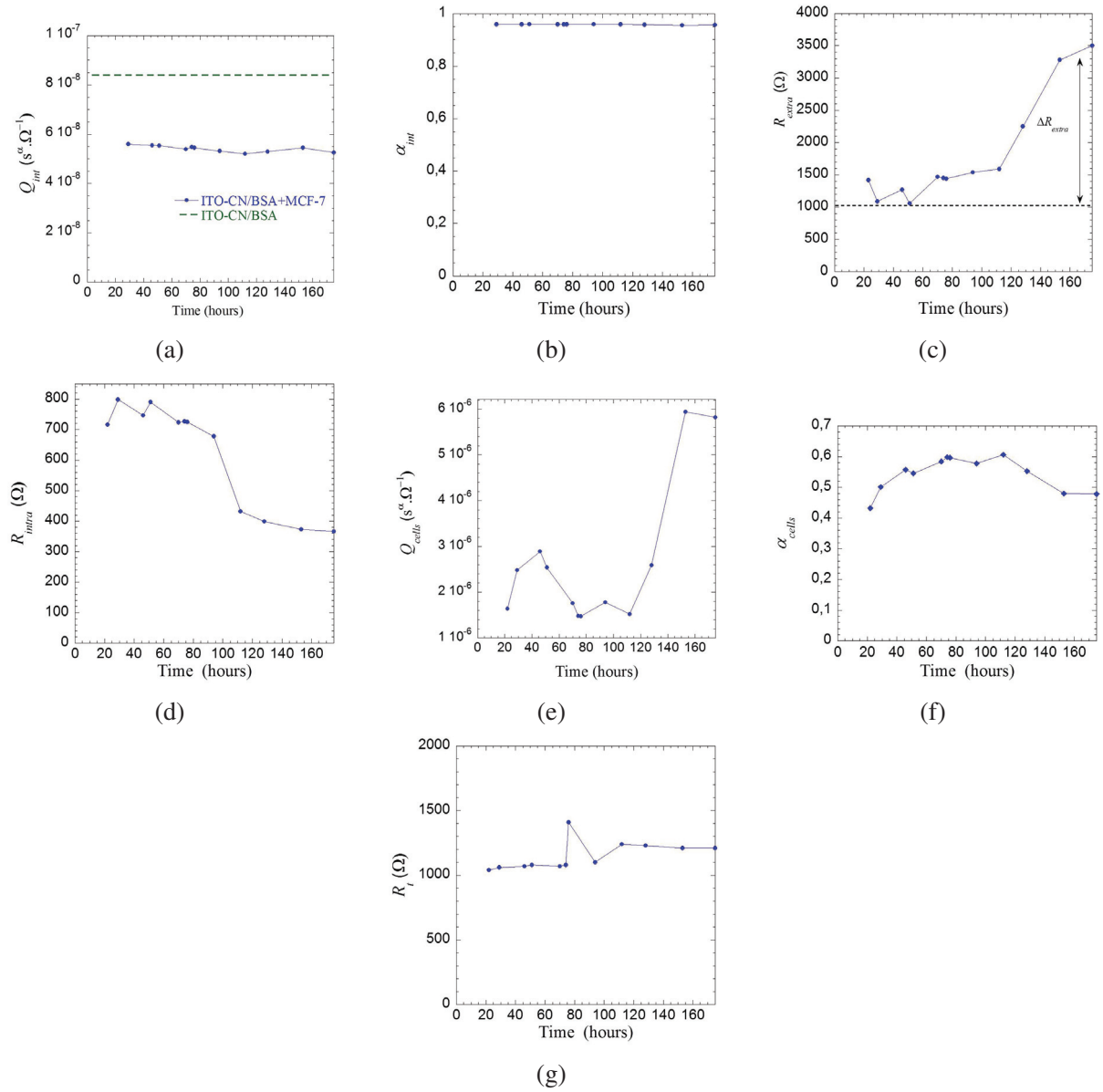


Figure 4.22 – Temporal evolution of the extracted parameters of **MCF-7** cells on top of **ITO** IDEs: (a) Q_{int} , (b) α_{int} , (c) R_{extra} , (d) R_{intra} , (e) Q_{cells} , (f) α_{cells} and (g) R_t . Monolayer reached at $\eta = 96\%$.

4.1. IDEs in contact with biological cells

In Fig. 4.23 we present how the different parts of model 3 affects impedance locus. At high frequencies, the semicircular arc is due to the contribution of $R_t // C_{parasitic}$, which were not significantly influenced by the formation of the cell monolayer. At mid-frequencies, the variation of R_{extra} clearly affects the impedance locus. In fact, for both materials, we observed that R_{extra} was the electrical parameter that varied the most with cell proliferation. When the cell monolayer is forming, neighboring cells are sticking together through cell-to-cell junctions and focal adhesions, leading to an increase of the semicircular arc associated with R_{extra} . At low frequencies, CPE_{int} , which was not affected by cell proliferation, is the electrical component that dominates the electrical impedance of the system. Based on this information, one could explain the bell shape of the graphs in Fig. 4.2 where the highest contribution due to cell proliferation occurs at mid-frequencies mostly due to variation of R_{extra} . Nevertheless, model 3 can not explain the fact that in Fig. 4.8, at low frequencies, the impedance spectrum straightens up with cell proliferation for Au IDEs. One could think that this is due to an additional contribution coming from a parallel resistance, which increases with cell proliferation. In contrast, ITO IDEs do not show this behavior at low frequencies. Supplementary experiments need to be carried out in order to confirm if this additional resistance could be associate with adsorption of proteins on the surface of Au IDEs. As mentioned earlier, it is difficult to compare our fit results with other studies because in the literature, it is very rare that authors present their results using Nyquist plots.

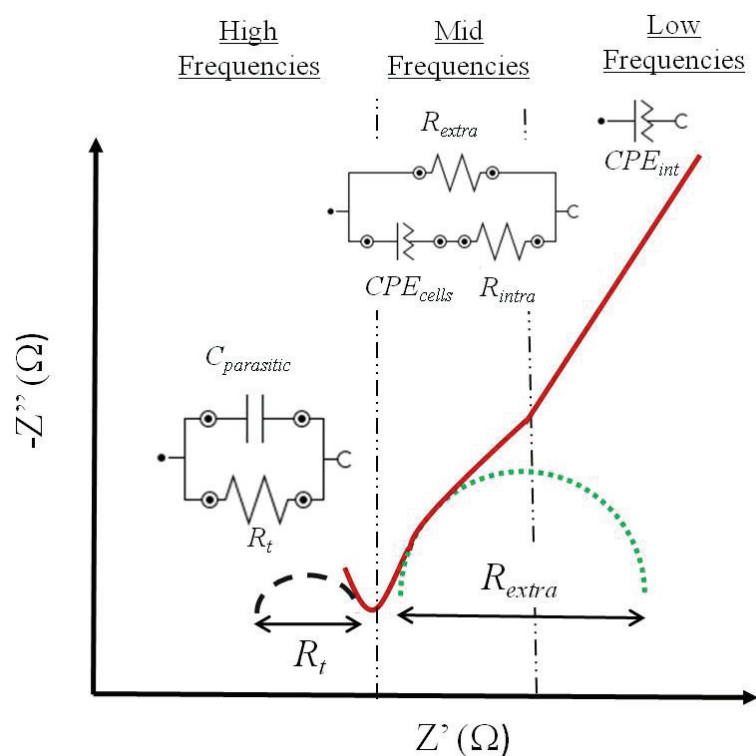


Figure 4.23 – Schematics of the different contributions of model 3 to the impedance locus for IDEs in the presence of biological cells. Drawing not to scale.

4.1. IDEs in contact with biological cells

Furthermore, in Fig. 4.24 we showed that from the three frequencies presented earlier, f_{peak} directly reflects key components of cell proliferation whereas f_{LF} and f_{HF} are indirectly influenced by several components of the system. Since f_{HF} is the frequency at which the phase angle ϕ is closest to 0° , in the impedance locus it corresponds to the "valley" point influenced by the value of R_t instead of the cell monolayer. As for f_{LF} , its position in the impedance locus depends on various parameters such as, the resistance R_t and the proliferating cells with R_{extra} , R_{intra} and CPE_{cells} . This could explain the differences observed in Figures 4.13 and 4.14, where Z_{norm} at f_{LF} for Au IDEs did not show a similar behavior as Z_{norm} at f_{peak} whereas for ITO IDEs both signals were resemblant. As mentioned earlier, f_{LF} depends on several parameters and we observed that the impedance locus for Au IDEs appeared to be affected by an additional parallel resistance which is not included in model 3. Hence, this resistance could affect the signal of f_{LF} in the case of Au IDEs but not in the case of ITO IDEs. Based on this, one could conclude that f_{peak} is the most suitable frequency to monitor cell activity using ECIS.

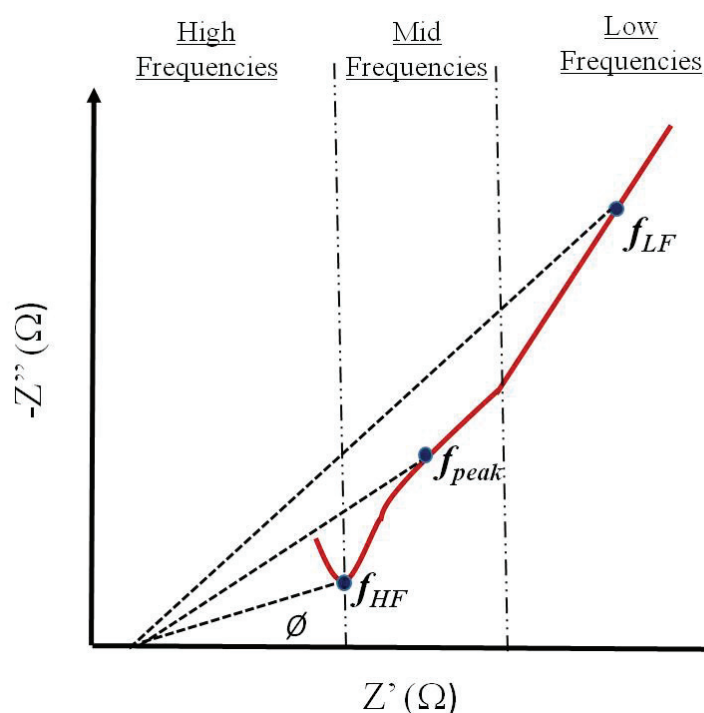


Figure 4.24 – Schematics of the dependency of the phase angle to the impedance locus for IDEs in the presence of biological cells. Drawing not to scale.

To summarize this section, we have presented 2 approaches to analyze cell proliferation impedance data: The first one is about representing the normalized impedance at a certain frequency, such as f_{peak} , which does not require phase angle information to be determined whereas f_{LF} and f_{HF} are extracted from phase angle data. Depending on the chosen frequencies, either extracellular or intracellular events can be studied. However, we observed that depending on the material Z_{norm} at f_{peak} and Z_{norm} at f_{LF} have different behaviors. The second approach consists in using an equivalent circuit model to extract the electrical parameters of the system, where the cell monolayer is covering the IDEs. Compared to the normalized impedance approach, this method enables the analysis of the temporal evolution of each part of the system in more detail. In addition, the equivalent circuit model allowed us to demonstrate why the Z_{norm} representation shows a bell-shape with cell contribution at mid-frequencies. Furthermore, we demonstrated that f_{LF} and f_{HF} are not suitable for cell monitoring because due to the fact that they are extracted using phase angle information, they are both influenced by several parameters in the model whereas f_{peak} clearly reflects the variation of impedance due to the cells.

4.2 Real-time monitoring of cellular response to 5-FU exposure

In this section, we were interested in monitoring the cytotoxic effects of the anticancer drug, 5-FU, on breast cancer cells using impedance measurements. Cytotoxicity involves inhibition of enzyme activity and of cellular respiration, resulting in an acute and immediate cell death[53]. In cancer treatment, chemotherapy relies on cytotoxic compounds administered to the patient with the aim of selectively eradicating the tumor cell population in an attempt to improve the length and quality of life of the cancer patient. Nevertheless, as mentioned in Chapter 1, this type of treatment very often comes with side effects. Classic chemotherapy agents are not tumor cell-specific and they destroy all cells actively undergoing cell division. These agents interfere with the function of intracellular signaling molecules, membrane receptors and kinases that are responsible for the proliferation of cells, inhibiting cell growth and division before inducing cell death[54]. Besides malignant cells, all normal cells found in the gastrointestinal tract, bone marrow and hair follicles and in other tissues are affected[55]. Hence, within the personalized medicine approach, it is extremely important to perform cytotoxicity assays in order to study the toxic effects of the active substances on the cancer cells of a given patient. The aim is to assess the potential of anticancer compounds, choose the most appropriate, search for the lowest cytotoxic concentration[54] and understand the action mechanism of these compounds.

4.2.1 Impedance response of cancer cells to 5-FU

We used our interdigitated electrodes to study the response of MCF-7 cell monolayers to 5-fluorouracil (5-FU) using phase contrast microscopy and electrical impedance. Treatment with 5-FU is known to improve patient survival in various cancers. The largest impact of the drug has been reported in colorectal cancer[56]. As described in chapter 2, active metabolites of 5-FU disrupt both DNA and RNA synthesis, leading to cell death. In the literature, 5-FU 10 μM to 500 μM treatment is considered to be appropriate for induction of apoptosis of cancer cells *in vitro*, but it highly depends on the cell context and medium component[57, 58, 59]. Microscopy images of the cell monolayers on Au IDEs following addition of 200 μM 5-FU are shown in Fig. 4.25. We can see that at the beginning of the experiment, 42 h after cell seeding, the cell monolayers is completely formed, covering the entire surface of the Au IDEs. Then, 2 h after drug addition, we observe that certain holes started to appear and η decreased to 97 % (44 h after cell seeding). As time went by, 24 h after drug exposure, the cell monolayer was disrupted and the number of holes increased, leading to rupture of the cell monolayer with a $\eta = 91$ % (46 h after cell seeding). At this point of the experiment, cells shrunk and started to form loosely attached cell clusters, indicating that MCF-7 cells had entered apoptosis. Apoptosis is characterized by a series of typical morphological events, such as shrinkage of the

4.2. Real-time monitoring of cellular response to 5-FU exposure

cell, fragmentation into membrane-bound apoptotic bodies and rapid phagocytosis of neighboring cells[60]. Finally, 47 h after drug addition, most of the cells had rounded shapes and had detached from the surface, leading to $\eta = 74\%$. Our microscopy images are coherent with those of other studies where MCF-7 cells were treated with 5-FU. For example, Chen et al.[61] found that MCF-7 cells treated with $960\ \mu\text{M}$ 5-FU for 48 h became round and spindle. Shah et al.[62] observed that, 48 h after exposure to $1\ \mu\text{M}$ 5-FU, MCF-7 cells appeared to have shrunk and had detached from the flask surface.

In parallel, we monitored the cellular response of MCF-7 cells to $200\ \mu\text{M}$ 5-FU using electrical impedance over the frequency range from 1 MHz to 100 mHz on Au IDEs. Fig. 4.26 shows the magnitude and phase of the impedance spectra of MCF-7 cells exposed to this chemotherapeutic drug. We observed that, as in Chapter 3, the presence of MCF-7 cells on top of Au IDEs affects the impedance spectra at low frequencies $f < 1\ \text{kHz}$ and at high frequencies $f > 1\ \text{kHz}$. However, it is only over the frequency range from $1\ \text{kHz} < f < 1\ \text{MHz}$ that the effect of 5-FU is clearly seen. As time of drug exposure incremented, η decreased due to cell death and detachment from the surface. In this case, the current is not blocked anymore by the cell monolayer and the impedance diminishes with time. In the phase plot, we found that at low frequencies ($f < 10\ \text{Hz}$) the phase angle was relatively constant ($\phi \rightarrow -85^\circ$). It increased in the frequency range from 100 Hz to 6 kHz and then we observed a "kink" appearing with a phase value around -50° . Finally, it increased at higher frequencies ($f > 20\ \text{kHz}$).

4.2. Real-time monitoring of cellular response to 5-FU exposure

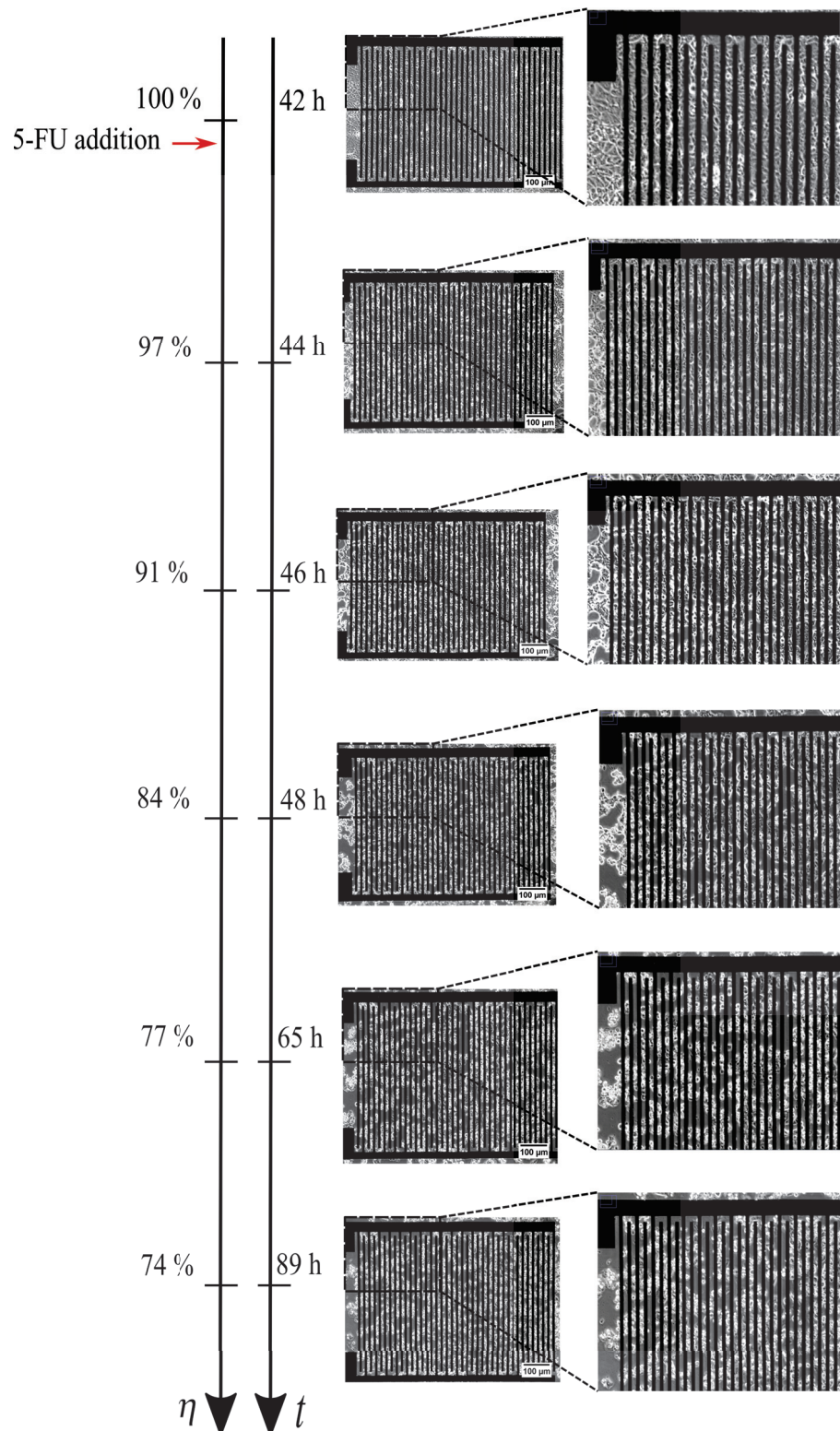


Figure 4.25 – Phase contrast images of MCF-7 after 200 μM 5-FU addition on the surface of the Au IDEs at 10 X magnification (Leica D2000). 19,800 cells were injected for this experiment.

4.2. Real-time monitoring of cellular response to 5-FU exposure

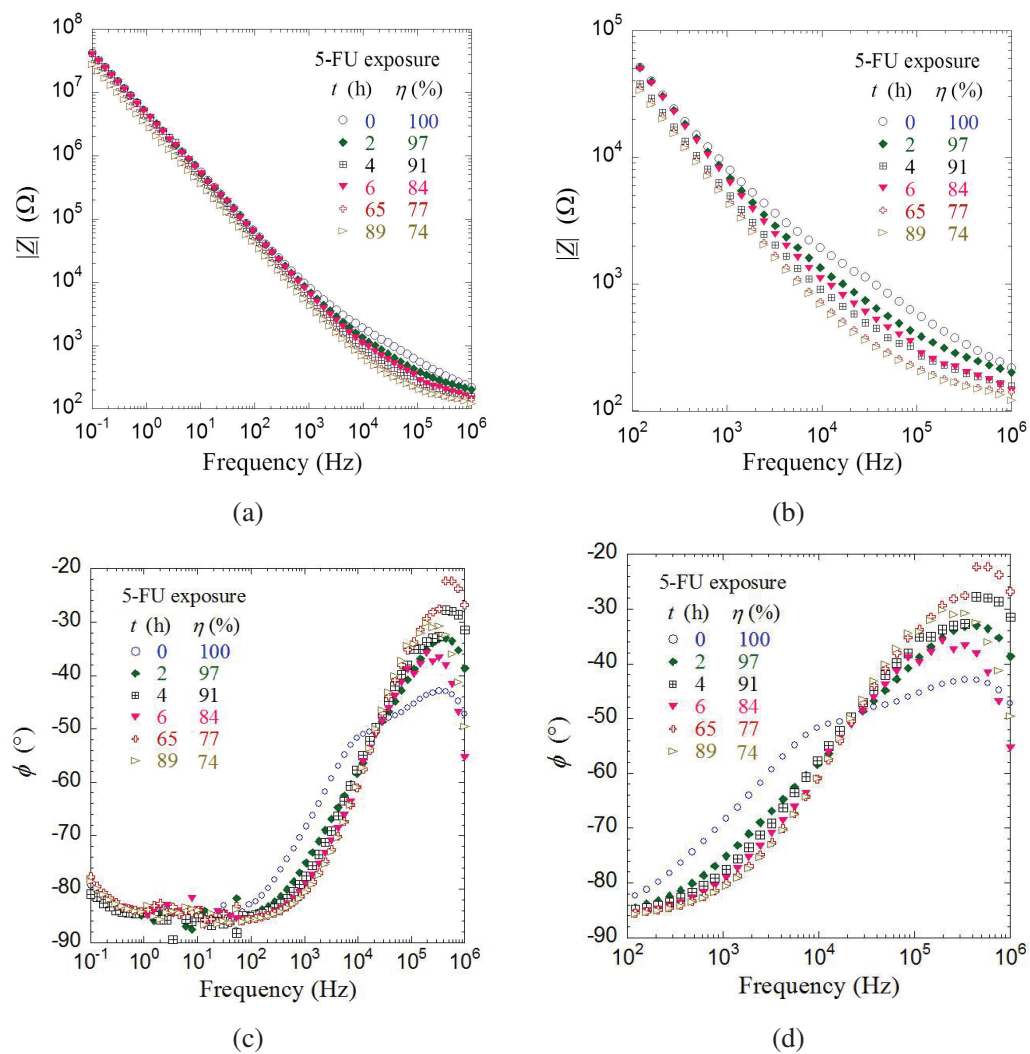


Figure 4.26 – Magnitude and Phase of the impedance spectra for **MCF-7** cells on **Au** IDEs in the frequency range (a, c) from 1 MHz to 100 mHz and (b, d) from 1 MHz to 100 Hz during 200 μM **5-FU** exposure.

4.2. Real-time monitoring of cellular response to 5-FU exposure

Additionally, we present the experimental data for MCF-7 cells exposed to 200 μM using the Nyquist representation in Fig. 4.27. In Fig.4.27a, we observe that at low frequencies ($f < 12.6$ kHz), cell activity did not affect the slopes of the spectra. In Fig.4.27b, at mid-frequencies from 255 kHz to 12.6 kHz, on the other hand, the slope of the impedance spectrum increased from 1.3 ($\eta = 100\%$) to 2.9 ($\eta = 74\%$) as the electrode surface covered by the cells decreased due to cell death. This behavior agrees with the behavior observed in Fig. 4.8 of this chapter concerning, in contrast, cell proliferating on Au IDEs, where we noticed the opposite tendencies, at mid-frequencies the slope of the spectrum decreased as cells covered the surface.

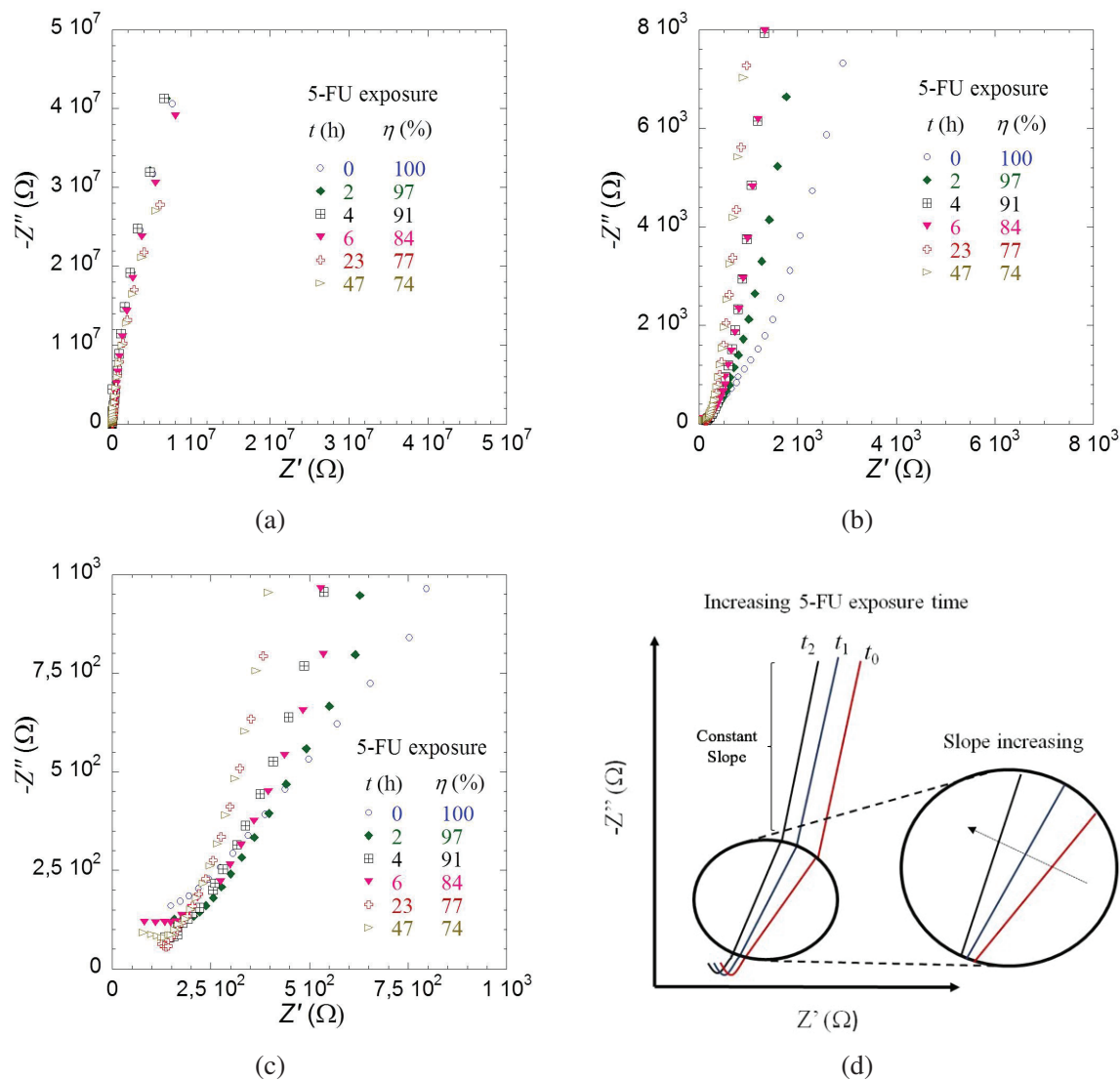


Figure 4.27 – Imaginary part vs Real part of the impedance spectra for **MCF-7** cells on **Au** IDEs over the frequency range (a) 1 MHz to 100 mHz, (b) 1 MHz to 1 kHz, (c) 1 MHz to 21.8 kHz and (d) Diagram of the evolution of the Nyquist curves during cytotoxicity experiments with 200 μM **5-FU**.

4.2. Real-time monitoring of cellular response to 5-FU exposure

We present in Fig.4.28 the evolution of the normalized Z_{norm} at f_{peak} versus T , where T is $t/t_{monolayer}$, for MCF-7 cells on Au IDEs and treated with 200 μM 5-FU. In order to compare both impedance spectra, *i.e.* the one of the negative control (treated only with cell culture medium) and the one with drug exposure, we had to normalize the Z_{norm} at f_{peak} data and the time t for each experiment. Normalized Z_{norm} at f_{peak} is $(Z(t)_{norm} \text{ at } f_{peak})/(Z(monolayer)_{norm} \text{ at } f_{peak})$, where $Z(t)_{norm}$ at f_{peak} corresponds to the normalized impedance at f_{peak} at time t after cell seeding and $Z(monolayer)_{norm}$ at f_{peak} corresponds to the normalized impedance at f_{peak} when the cell monolayer is reached before 5-FU addition. We observed that before adding 200 μM 5-FU, both signals increased, corresponding to the cell proliferation phase and to the formation of cell monolayer, as shown in this chapter. After adding 200 μM 5-FU (42 h after cell seeding), we found that the signal (dotted line) increased abruptly from 0.6 to 1 and then decreased to 0.07 within 47 h of exposure to 200 μM , indicating that the cell monolayer was destroyed. This is coherent with the images in Fig. 4.25 where cells detached after 5-FU exposure. However, for the experiment with 200 μM 5-FU, we observed that before 5-FU addition, $Z_{norm} = 1.3$ at 49 kHz and immediately after addition of 5-FU, $Z_{norm} = 2.1$. This abrupt increase in impedance after drug addition, which was observed for every experiment carried out with 5-FU, can not be associated with drug-induced cellular changes because, as mentioned earlier, 5-FU affects DNA and it would require a few hours before, it affects the genetic material of the cells in culture. In another experiment, we measured the spectra of the cell culture medium with and without 10 μM 5-FU. We did not find differences between the spectra that could explain the abrupt increase after injection of 5-FU. In fact, we observed this peak in impedance for every experiment carried out with 5-FU. Perhaps it is due to an initial reaction of cells to the chemotherapeutic drug and it would therefore need to be studied in more detail with supplementary experiments, such as fluorescent staining of cell-to-cell junctions in order determine if they are responsible for this abrupt variation.

Regarding the control signal (solid line), we saw that during the period of drug exposure, it started to decrease. This may suggest that although MCF-7 cells were not treated with 200 μM , the cell culture medium was not enough and long periods of cell culture started to affect the cell monolayer. For instance, Jacobs et al.[63] in their study involving higher density culture of human embryonic stem cells determined that medium acidification is the main causal factor of DNA damage in high-density cultures and that, by increasing the frequency of the medium refreshments, the levels of DNA damage and genetic instability can be restored[63]. According to them, the high density cultures result in a nutrient deficit and/or detrimental concentration of waste products. These can then interfere with the metabolism of the cells[64], cause replication stress, and increase the risk of DNA breakage and chromosomal abnormalities[65]. As mentioned earlier, we did not work in a microfluidic environment with a refreshing system of the cell culture medium. Moreover, more than one ECIS assay can not be carried out at the same time, making it impossible to monitor the MCF-7 cells of the control and the cells treated with 5-FU, simultaneously. Thus, in order to simplify the cytotoxicity assays and avoid long periods of cell culture, we decided to end experiments 24 h after 5-FU addition.

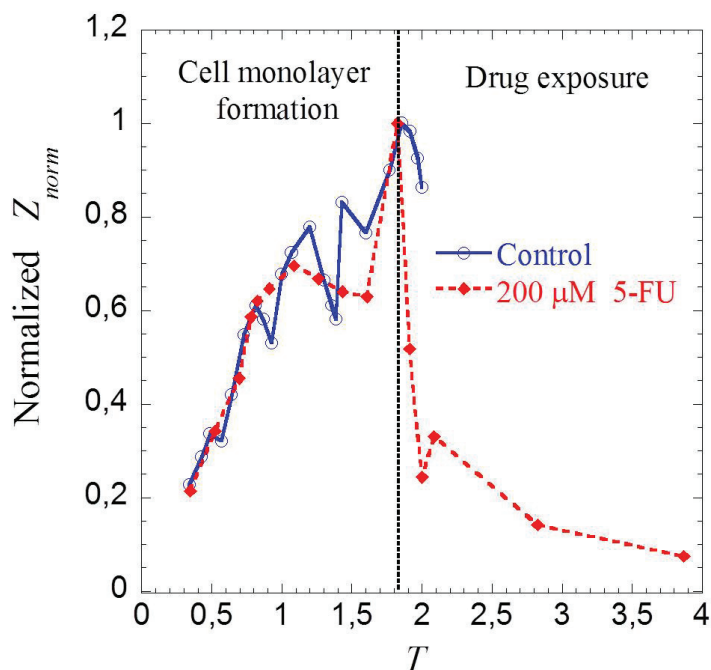


Figure 4.28 – Normalized Z_{norm} versus T for **MCF-7** cells exposed to $200\ \mu\text{M}$ **5FU** on the surface of **Au** IDEs. Measurements were carried out outside of the incubator.

4.2.2 Concentration effect of 5-FU

The MCF-7 cells were exposed to 5-FU at three different concentrations: $10\ \mu\text{M}$, $200\ \mu\text{M}$ and $50\ \text{mM}$ to study dose dependent cell responses 24 h after 5-FU injection. The microscopy images in Fig.4.29 show the cell monolayer of MCF-7 cells formed on ITO IDEs and Au IDEs before and 24 h after 5-FU exposure to $10\ \mu\text{M}$ and $50\ \text{mM}$ and $200\ \mu\text{M}$, respectively. We observed that 24 h after injection of $10\ \mu\text{M}$ 5-FU, there were no visible holes as in the images of $200\ \mu\text{M}$ 5-FU on Au IDEs. On the other hand, 24 h after exposure to $50\ \text{mM}$ 5-FU, most of the MCF-7 cells were detached and the remaining cells were loosely attached cell clusters, indicating that the speed of onset and the effectiveness of the cytotoxic effects increased with the 5-FU concentration.

4.2. Real-time monitoring of cellular response to 5-FU exposure

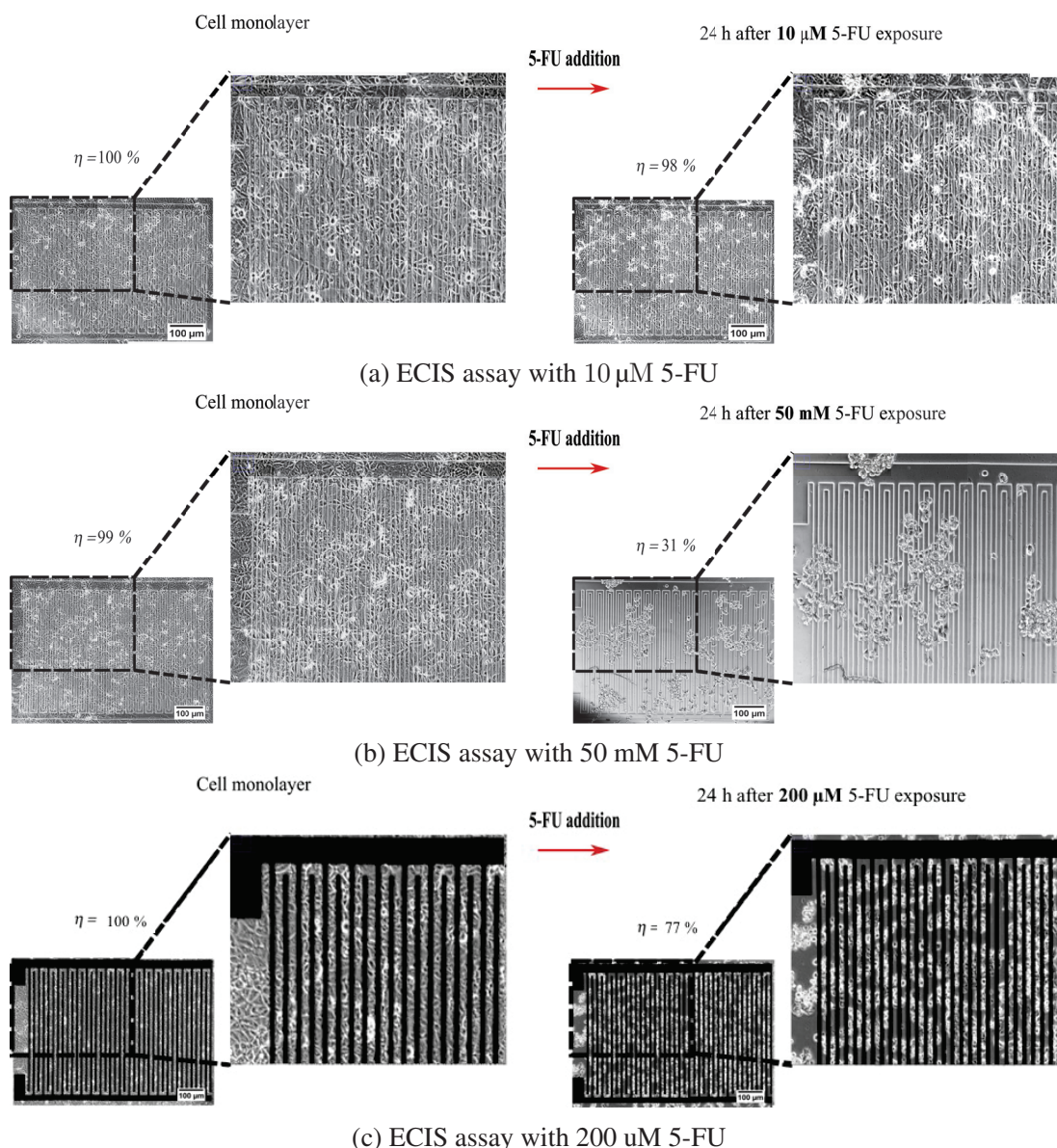


Figure 4.29 – Microscopy images of the cell monolayer before and after 24 h of exposure to (a) 10 μM 5-FU and (b) 50 mM 5-FU on ITO IDEs. (c) The cell monolayer before and after 24 h of exposure to 200 μM 5-FU on Au IDEs. Images were taken at 10 X magnification (Leica D2000).

We also took the impedance results of the cells exposed to these three concentrations and we compared it with a control experiment, where cells were not treated with 5-FU. We presented the normalized Z_{norm} values, 24 h after the 5-FU was added, in Fig. 4.30 and 48 h after the 5-FU was added, in Fig. 4.31. Similar to the microscopy results in Fig. 4.29, we found that compared to the control with a normalized Z_{norm} value of 0.85, MCF-7 cells treated with 10 μM had a slightly lower normalized Z_{norm} value of 0.83 whereas cells treated with 200 μM and 50 mM showed a greatly reduced normalized Z_{norm} values of 0.05 and -0.17, respectively. In the case of 48 h after 5-FU exposure in Fig. 4.31, we observe a similar trend. The control with a normalized Z_{norm} value of 0.84, MCF-7 cells treated with 10 μM had a slightly lower normalized Z_{norm} value of 0.82 whereas cells treated with 200 μM and 50 mM showed a greatly reduced normalized Z_{norm} values of 0.02 and -0.17, respectively. This could be explained by the fact that 5-FU is an

4.2. Real-time monitoring of cellular response to 5-FU exposure

antimetabolite drug. This type of drugs are cell-cycle specific, which affects cells only when they are in the S-phase or getting divided[66]. In fact, it is well-established that treatment of cells with 5-FU causes DNA damage, specifically double-strand and single-strand breaks, during the S-phase²[62]. Moreover, in the case of DNA damaging agents, such as 5-FU, the onset of cell death is easy to adjust. When DNA damage occurs, cells initially perceive the damage, activate cell cycle checkpoints, arrest cell cycle progression, and attempt to repair the damage[67]. Thus, at low levels of damage, such as in the case of cells treated with 10 μM 5-FU, cells may recover and continue proliferation. However, when the level of damage is too high, such as with 50 mM, the damage is beyond repair and cells can not maintain genomic stability. The damaged cells appear to undergo a mitotic "catastrophe" and then apoptosis[67, 66]. In the case of the normalized Z_{norm} values for 48 h after 5-FU exposure, shown in Fig. X, we observe a similar behavior. When the 5-FU concentration increases, the normalized Z_{norm} decreases: 0.84 for the control, 0.82 for 10 μM 5-FU, 0.02 for 200 μM 5-FU and -0.17 for 50 mM 5-FU.

It is important to realize in this section that we were expecting a higher cytotoxicity effect for a concentration of 10 μM . For example, Akbari et al.[68] determined that the half maximal inhibitory concentration (IC_{50}) for the MCF-7 cell line after 24 h of treatment was 10 μM . In cytotoxicity assays, IC_{50} is a measure of the effectiveness of a compound in inhibiting biological or biochemical functions. It indicates how much of a particular drug is needed to inhibit a given biological process[68]. In their study, 24 h after treatment with 10 μM 5-FU, 50 % of the MCF-7 were dead. In the literature, however, we can find different values of IC_{50} of 5-FU for MCF-7 cells. For instance, Hernandez-Vargas et al.[57], in their study on transcriptional profiling of MCF-7 cells in response to 5-FU, showed that 10 μM was the IC_{50} after 48 h of exposure. In contrast to Hernandez-Vargas, Jeong et al.[69], in their study on low level light therapy on cancer cells determined that IC_{50} after 48 h of exposure to 5-FU for MCF-7 cells was 70 μM . In fact, the use of IC_{50} data appears to be problematic, as they are assay specific and comparable only under certain conditions[70]. According to Aykul et al.[71] results using whole cell systems can depend on the experimental cell line used and may not differentiate a compound's ability to inhibit specific interactions[71].

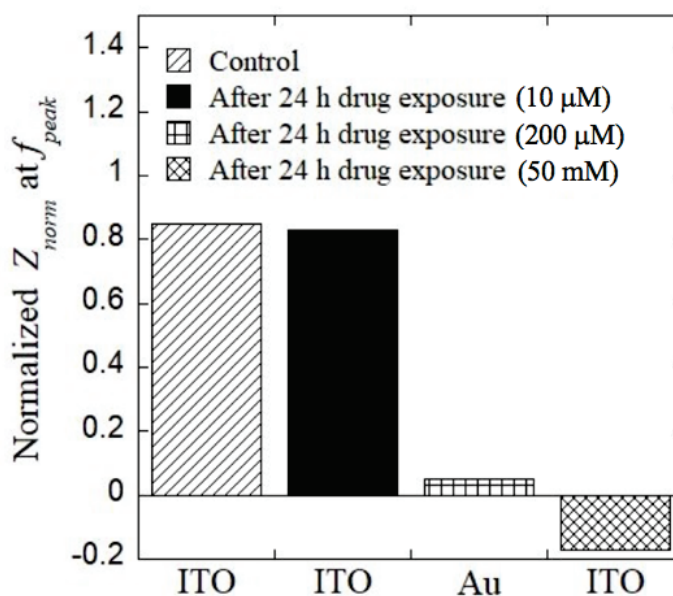


Figure 4.30 – Comparison of normalized Z_{norm} for 10 μM and 50 mM 5-FU after 24 h drug exposure to MCF-7 cells.

²S phase is the period during which DNA replication occurs

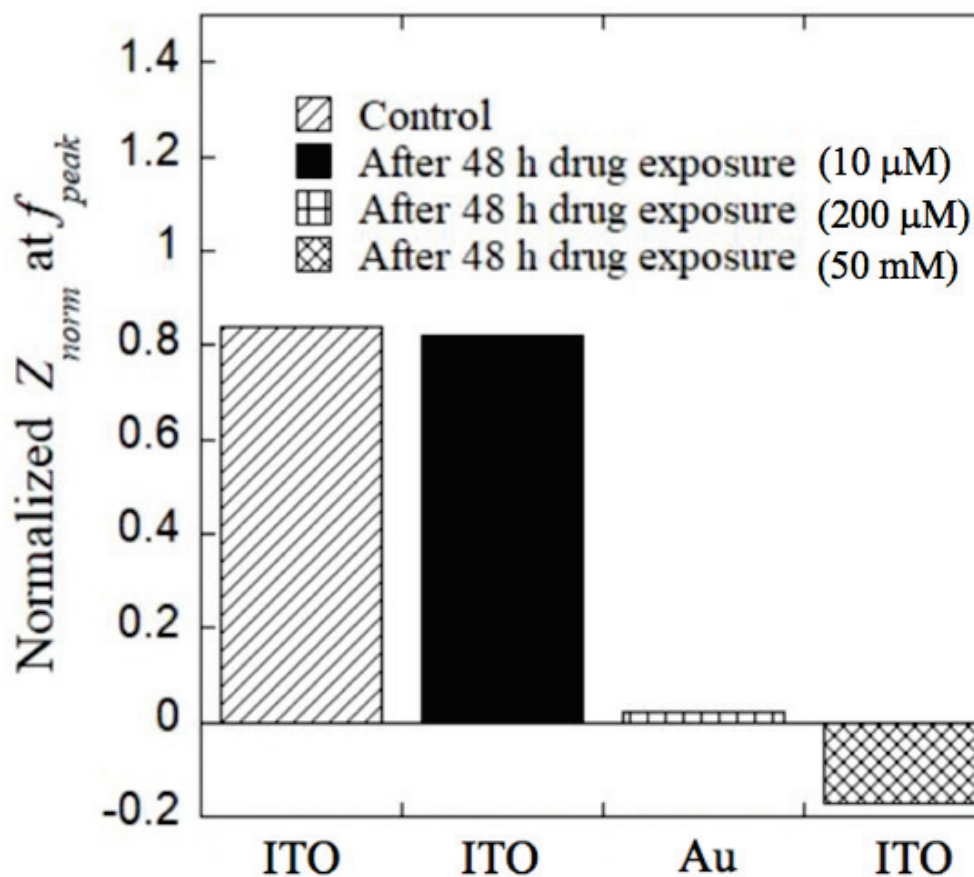


Figure 4.31 – Comparison of normalized Z_{norm} for 10 μ M and 50 mM 5-FU after 48 h drug exposure to MCF-7 cells.

So far we have seen that the magnitude of the impedance spectra in Fig. 4.26 do not provide more detailed information on cellular response after the 5-FU compound is added. We can only observe that there is a decrease in the signal due to cell detachment. Hence, we used equivalent circuit modeling as a more meaningful method to obtain information on the cytotoxic effects of 5-FU. As shown in Chapter 3, by modeling the cell monolayer-electrode system, it is possible to break down and study every component of the system.

4.3 Equivalent circuit modeling of breast cancer cells exposed to 5-FU

4.3.1 Cytotoxicity effects on MDA-MB-231 cell line

In this section, we treated the metastatic MDA-MB-231 cells, which form loosely cohesive stellate structures consistent with a highly invasive phenotype, on ITO IDEs with 100 μM 5-FU. We present the temporal evolution of each parameter in Fig. 4.32. As was done in previous sections, we fitted our data with a fixed value of $C_{parasitic} = 14$ pF. We observe that Q_{int} and α_{int} appears to be relatively constant before and after addition of the 5-FU. The parameter R_{extra} , during the first 45 h, reached 634 Ω and is associated with the cell monolayer covering the ITO surface. Then, after addition of 100 μM 5-FU, R_{extra} decreased to a value = 294 Ω . This indicates that the cell-to-cell junctions that block the current once the monolayer is formed, may be affected as cells start to die due to an accumulation of the drug. As mentioned earlier, during apoptosis cells undergo several morphological and biochemical changes. For example, it has been pointed out that in early stages, cytoplasmic Ca^{2+} levels change and the cell volume decreases and contact with neighboring cells and the extracellular matrix is lost[72].

We found that R_{intra} was not affected in the same way as R_{extra} . During the first 45 h, R_{intra} decreased from 205 Ω to 192 Ω , which can be associated with cell spreading and flattening of cells. After addition of 5-FU, it increased reaching 319 Ω , which possibly corresponds to cells having a round shape due to cell death. Regarding Q_{cells} , we observed that it increased during formation of the cell monolayer (first 45 h), from $5.7 \times 10^{-8} \text{ s}^\alpha \cdot \Omega^{-1}$ to $6.9 \times 10^{-8} \text{ s}^\alpha \cdot \Omega^{-1}$. Then, after 5-FU injection, it decreased down to $9.2 \times 10^{-9} \text{ s}^\alpha \cdot \Omega^{-1}$. This behavior can be explained in terms of cell membrane deterioration due to cell death, as described by Zhang et al.[73]. According to them, dying cells undergo some characteristic morphological changes. For example, the plasma membrane will first undergo formation of circular bulges, a transient stage which rapidly evolves toward bleb separation and generation of apoptotic bodies[73]. Finally, the parameter α_{cells} , started decreasing from 0.82 to 0.78 during the formation of the cell monolayer 27 h after 5-FU exposure, it increased and reached the value 0.98 and remained relatively constant, thereafter. One could say that this behavior is related to the morphological changes of the cell membrane when cells are under stress due to the low concentration 5-FU, but supplementary tests of the cell membrane would be needed in order to confirm this hypothesis. R_t showed relatively constant values around 1,600 Ω during the cytotoxicity assay. Based on these results, one could say that in this case our lumped equivalent circuit model is valid and provides "clear" trends, with few fluctuations, for each parameters for the interdigitated electrodes covered with MDA-MB-231 cells.

4.3. Equivalent circuit modeling of breast cancer cells exposed to 5-FU

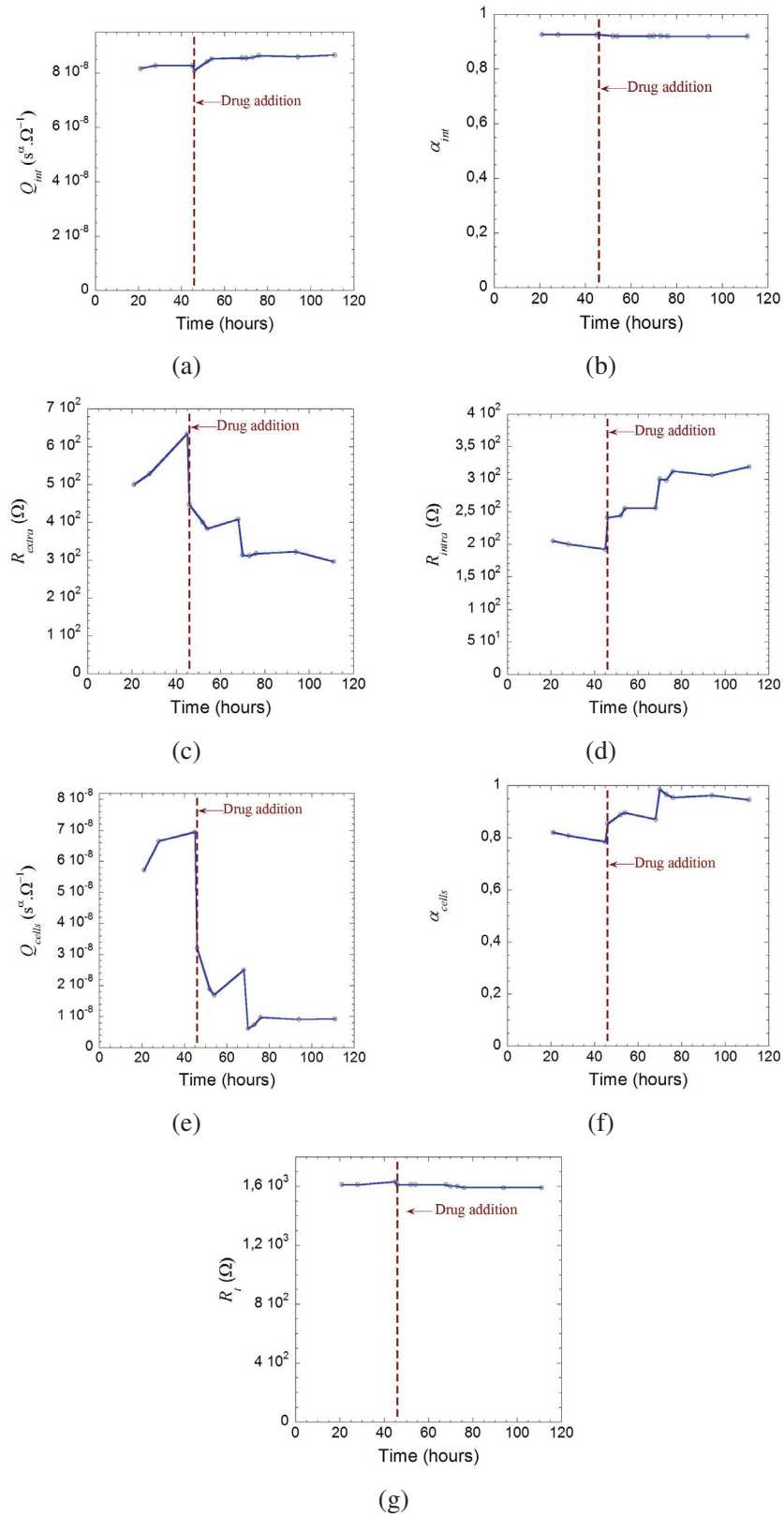


Figure 4.32 – Temporal evolution of the extracted parameters of 100 μ M 5-FU treated MDA-MB-231 cells on ITO IDEs: (a) Q_{int} , (b) α_{int} , (c) R_{extra} , (d) R_{intra} , (e) Q_{cells} , (f) α_{cells} and (g) R_t .

4.3.2 Cytotoxicity effects on MCF-7 cell line

We extracted the equivalent circuit parameters for MCF-7 cells, exposed to 10 μM 5-FU on ITO IDEs, using circuit model 3 shown in Fig. 4.18. The temporal evolution of each parameter is presented in Fig. 4.33 and the images corresponding to each arrow are shown in Fig. 4.34. Similar to the MDA-MB-231 cells, we extracted the equivalent electrical parameters of cells exposed to 5-FU, using a fixed value of $C_{parasitic} = 14$ pF. We observe that Q_{int} and α_{int} remain relatively constant before and after addition of the 5-FU. R_{extra} during the first 69 h reached 4,120 Ω , which can be associated with the formation of the cell monolayer due to new cell-to-cell junctions that block the current. Afterwards, 93 h after addition of 10 μM 5-FU, R_{extra} continue to increase from 2,840 Ω (cell monolayer) to 30,200 Ω and then it decreases until $R_{extra} = 2,090$ Ω . This type of behavior after drug addition might be explained by the fact that cells can go through morphological changes when they try to avoid induced apoptosis by cytotoxic compounds. For instance, Caviglia et al.[74] in their study on cytotoxic assays with 2.5 μM of doxorubicin on HeLa cells found an initial increase in impedance after drug addition, which was also observed by others[39, 75]. According to Caviglia, this increase in impedance could reflect intensified metabolic activity, increased adhesion properties and/or changes in cell morphology in response to the stress when cells are trying to overcome the apoptosis induced by the accumulation of the drug[74]. Imam et al.[76] treated the colon cancer cell line HCT116 with 10 μM 5-FU and they also found a dual real time monitoring profile. It started with an increase in the normalized impedance during the first 24 h of treatment and then it decreased. The increase in normalized impedance was higher than for the one involving non-treated cells, indicating that the 10 μM 5-FU treated cells established more contacts with the surface than the non-treated cells. In fact, in their study, using an MTS assay, they found that 10 μM 5-FU treated cells exhibited a constant cell viability, suggesting that the increase in normalized impedance corresponded to a change in morphological state rather than in a proliferative state[76].

Regarding R_{intra} , in contrast to the MCF-7 cells, we observe much more fluctuations over time. Despite these fluctuations, we can see that during the first 69 h, R_{intra} decreased from 385 Ω to 85 Ω due to cell spreading, as explained in Chapter 3. After addition of 5-FU, R_{intra} increased up to 200 Ω and then it decreased, staying relatively constant for 95 h. After that, it increased once again reaching 210 Ω which at this stage can be associated with the round shape that cells adopt when they die, as shown in Fig. 4.34.

Similar to R_{intra} , the parameter Q_{cells} also shows significant fluctuations. These fluctuations could be due to the inherent limitations of using a simple lumped equivalent circuit model to represent a complex system, such as the interdigitated electrodes covered with MCF-7 cells. However, a key "variation" tends to occur at the same time at which R_{extra} reaches its highest value, 30,200 Ω . 93 h after addition of 5-FU, Q_{cells} decreased from $7.7 \times 10^{-6} \text{ s}^\alpha \cdot \Omega^{-1}$ to $2 \times 10^{-6} \text{ s}^\alpha \cdot \Omega^{-1}$ and subsequently increased to $1.2 \times 10^{-5} \text{ s}^\alpha \cdot \Omega^{-1}$. This variation of Q_{cells} could be correlated with the effect of changes in the cell membrane in response to stress when cells are trying to overcome the cytotoxic effects of 5-FU, as it was observed in the case of R_{extra} . Finally, 167 h after exposure to 5-FU, Q_{cells} decreased once more reaching a value of $2.9 \times 10^{-6} \text{ s}^\alpha \cdot \Omega^{-1}$. This may be associated with the final deterioration of the cell membrane when cells enter into an apoptotic state, as described by Zhang et al.[73].

The parameter α_{cells} , started decreasing during the formation of the cell monolayer and 93 h after 5-FU exposure, it reached 0.58. Later, it decreased to 0.39 before increasing again with $\alpha_{cells} = 0.54$. Similar to the observations made concerning the MDA-MB-231 cells, supplementary tests on the cell membrane would be needed to understand the evolution of α_{cells} during cytotoxicity tests. Regarding R_t , this parameter tend to show values around 1,400 Ω but compared to the results of MDA-MB-231, some fluctuations can be observed.

4.3. Equivalent circuit modeling of breast cancer cells exposed to 5-FU

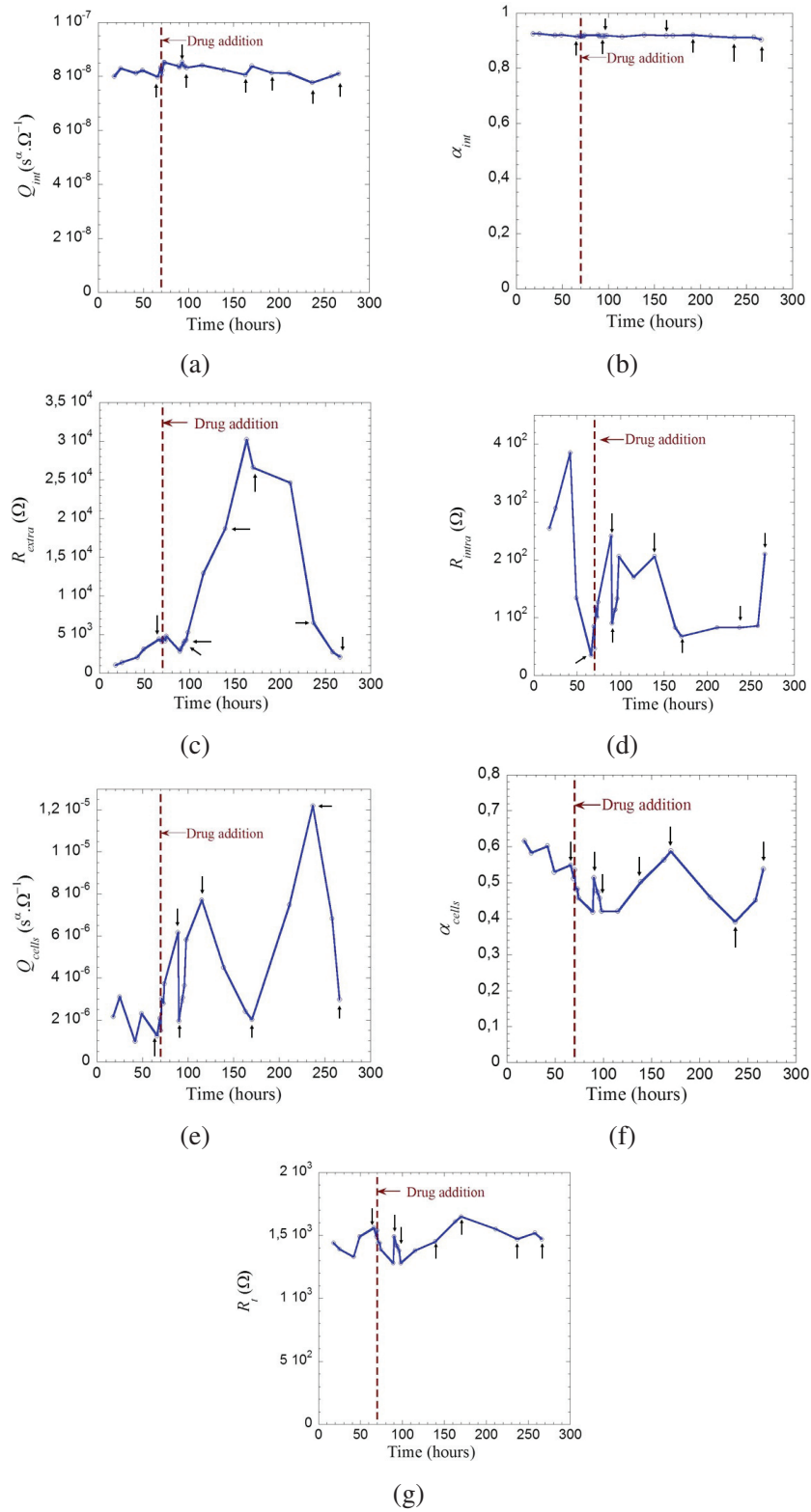


Figure 4.33 – Temporal evolution of the extracted parameters of $10\ \mu\text{M}$ 5-FU treated MCF-7 cells on ITO IDEs: (a) Q_{int} , (b) α_{int} , (c) R_{extra} , (d) R_{intra} , (e) Q_{cells} , (f) α_{cells} and (g) R_t .

4.3. Equivalent circuit modeling of breast cancer cells exposed to 5-FU

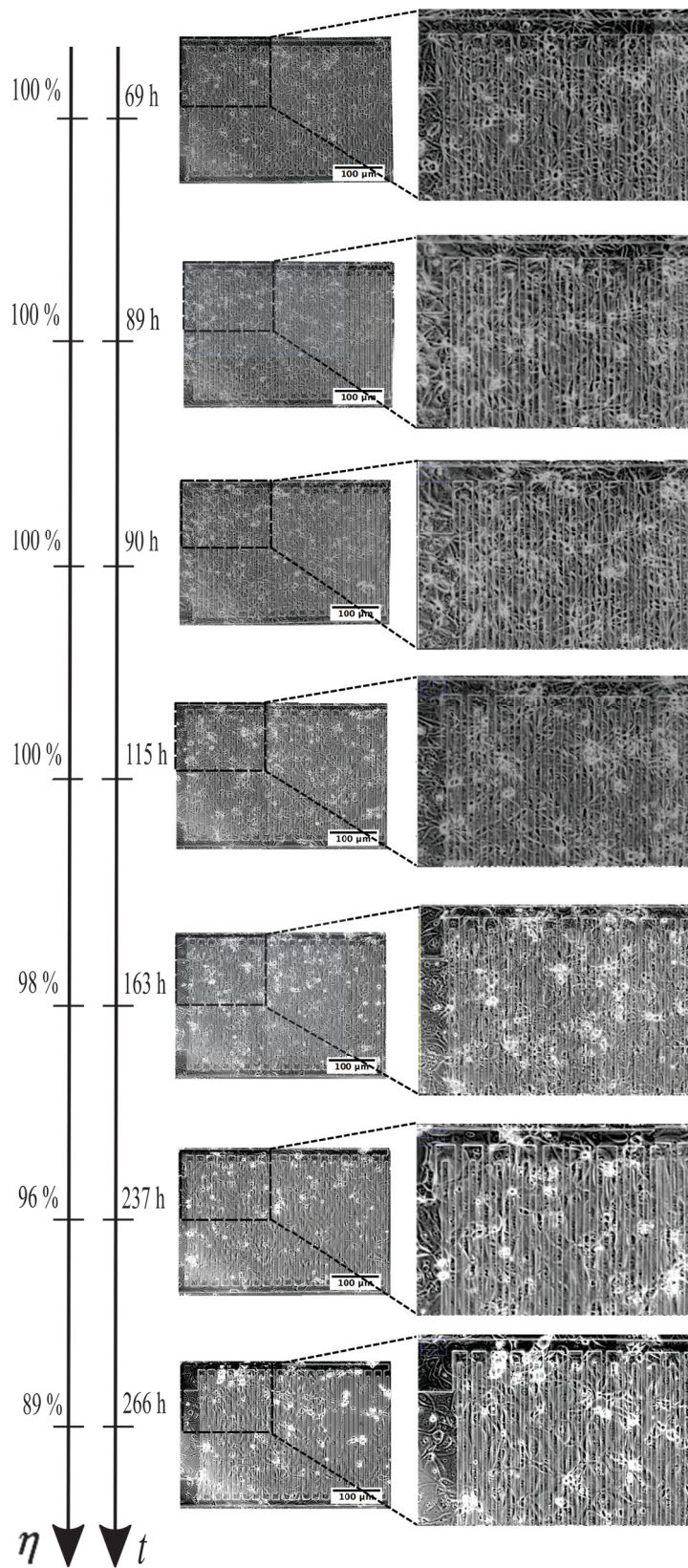


Figure 4.34 – Phase contrast micrographs of 10 μ M 5-FU treated MCF-7 cells on the surface of the ITO IDEs at 10X magnification (Leica D2000).

4.3. Equivalent circuit modeling of breast cancer cells exposed to 5-FU

In these cytotoxic assays, we observed that between the MCF-7 (at $\eta = 100\%$) and MDA-MB-231 (at $\eta > 100\%$) cell lines, there were significant differences in the order of magnitude of the parameters R_{extra} , R_{intra} and Q_{cells} . For example, MCF-7 cells presented $R_{extra} \sim 10^3 \Omega$ whereas for MDA-MB-231 cells, R_{extra} was one order of magnitude lower $\sim 10^2 \Omega$. This could be explained by the fact that MCF-7 cells tend to form tight cell-to-cell junctions[77] whereas MDA-MB-231 cells tend to form loosely structures[78]. We also found that MCF-7 showed lower values of R_{intra} ($\sim 10^3 \Omega$) compared to those of MDA-MB-231 cells ($\sim 10^4 \Omega$). This is in agreement with equation 4.14 and the results found in Chapter 3, where we observed that MDA-MB-231 cells tend to elongate more along one axis whereas MCF-7 cells tend to spread uniformly and stay more "compact". Regarding, the parameter Q_{cells} , MCF-7 cells showed higher values ($\sim 10^{-6}$) compared to those of MDA-MB-231 cells ($\sim 10^{-9}$). This difference could be associated with differences in the cell membrane properties between these cell lines. In fact, lipid alterations on the cell membrane are found in cancer cells with variations between stage and cancer types[79]. We have to bear in mind that MDA-MB-231 are more "aggressively" metastatic than MCF-7 cells. It has been demonstrated that metastatic cancer cells for many cancers are known to have altered cytoskeletal properties, in particular to be more deformable and contractile[80]. In addition, a number of changes in the biochemical characteristics of malignant cells' surfaces have been observed. These include the appearance of new surface antigens, proteoglycans, glycolipids, and mucins[81], which could differ in these breast cancer cell lines.

4.4 Conclusion

In this chapter, we first presented the impedance results for Au and ITO interdigitated electrodes in contact with breast cancer cells. We showed that ITO presents a reduced sensitivity compared to that of Au to MCF-7 cell proliferation. The same behavior was observed for endothelial cells[38]. In addition, we showed that there are different adhesion/spreading behaviors depending on the electrode material, which could also affect the sensitivity in the same way as the interfacial impedances and the resistive behaviors for Au and ITO IDEs. Furthermore, we showed 2 approaches to analyze the experimental data of cell proliferation: In the first one we represented the normalized impedance at a single frequency, such as f_{peak} , which does not require phase angle information to be determined whereas f_{LF} and f_{HF} , suggested by Eker and Meissner[39, 40], needed phase angle information. The second approach consists in using an equivalent circuit model to extract the electrical parameters of the IDEs covered with the cell monolayer. This approach in a cytotoxicity assay in which a drug effect on the cells is studied, could be helpful to analyze individually the electrical parameters and understand how the drug affects them. In contrast to the normalized impedance where we only see variation of the impedance without knowing which electrical parameters are being affected. This second approach demonstrated that the increase in $|Z|$ is mainly due to R_{extra} . In addition, the equivalent circuit model allowed us to demonstrate the bell shape of Z_{norm} versus frequency revealing cell contribution at mid-frequencies. Furthermore, we showed that in contrast to the studies of Eker and Meissner[39, 40], f_{LF} and f_{HF} are not reliable frequencies for cell monitoring due to the fact that they are extracted using phase angle information, which is influenced by various components in the impedance locus. f_{peak} appears to provide direct information on the new cell-to-cell junctions and focal adhesions formed during cell proliferation.

The second major part of this chapter was on the cytotoxicity experiments using the chemotherapeutic agent, 5-FU. We found that equivalent circuit modeling is a more fruitful method of analyzing impedance data from cytotoxicity assays compared to representing the real time variation of the magnitude of the impedance or the normalized impedance versus time. Equivalent circuit modeling provides information on each, parameter of the model and it shows how the components of the cells under study are being affected by the drug. For instance, the use, of only, graphs of real time variations of the impedance cannot determine if a decrease in overall impedance is due to the cell membrane or cell-to-cell junctions.

We observed that impedance changes due to 5-FU are time and concentration dependent. Moreover, at low concentration, 10 μ M 5-FU, MCF-7 cells showed a dual time response that may reflect the morphological changes in response to the stress when cells are trying to overcome the apoptosis induced by the accumulation of the drug. This appears to be of potential interest in drug resistance assays, where scientists seek to understand why certain cell lines do not react as expected to a certain drug concentration. In addition, we demonstrated that ECIS appears to be more sensitive to cytotoxic induced changes in the cell monolayer compared to microscopy visualization. For instance, in the experiment using 10 μ M 5-FU, even though during the first hours of drug exposure the microscopy images did not show significant morphological changes in the cell monolayer, impedance data revealed variations that can be associated with the cytotoxic effect of 5-FU. Hence, combining transparent ECIS electrodes with an optical system appears to be a promising strategy in drug screening applications. Furthermore, we demonstrated that the orders of magnitude for R_{extra} and R_{intra} are in agreement with the characteristics of MCF-7 cell line and MDA-MB-231 cell line. These results lead us to conclude that ECIS experiments combined with equivalent circuit modeling provides a promising approach for drug discovery and screening. This is particularly the case when studying the morphological changes that cells undergo before cell death, which is vital in developing new chemotherapeutic compounds for cancer treatment.

4.4. Conclusion

We found that our equivalent circuit model appears to offer a reasonable fit for the impedance data collected during the cytotoxicity assays. This is encouraging because it means that a simple lumped equivalent circuit model can provide meaningful information about the cell activity when cancer cells are exposed to a chemotherapeutic agent. However, in the case of MCF-7 cells we found much less marked trends for R_{intra} , Q_{cells} , α_{cells} and R_t due to clear fluctuations. These fluctuations could reflect the overall impedance contributions in a complex system, such as cells covering the interdigitated electrodes. A possible explanation for these fluctuations, only seen for the MCF-7 cells, could be the 10 μM 5-FU concentration. A cytotoxicity experiment using a lower concentration of 5-FU, may reflect the morphological changes in response to the stress when cells are trying to overcome the apoptosis induced by the accumulation of the drug. This will increase the complexity of the system and therefore our simple lumped equivalent circuit model will be limited by the marked fluctuations. In contrast to the experiment using 100 μM for which the MDA-MB-231 started to die without having time to overcome the induced apoptosis by the 5-FU and "clear" trends were observed for each parameter of the model.

This chapter has also opened interesting perspectives on the influence of the cell adhesion on the sensitivity of the impedance measurements. Differences on cell adhesion between Au and ITO IDEs could be a key factor in the explanation of the reduced sensitivity of ITO IDEs. Supplementary experiments need to be carried out either to study adhesion attachment or detachment events on different electrode materials. For example, microfluidic systems due to fluid manipulation and control, low fluid intake and miniaturization have become an useful tool in dynamic culturing for cell adhesion studies[16]. This technique can be used to study the ability of cells to adhere and to monitor cell spreading, tracking, and migration inside a channel under the influence of fluid flow[27, 50, 82]. Moreover, cell detachment can be assessed using applied shear stress to cell monolayers[83, 84].

Bibliography

- [1] John A. Ryan. “Evolution of Cell Culture Surfaces”. In: *Biofiles* 3.8.21 (2008), pp. 1–7.
- [2] Michelle S. Liberio, Martin C. Sadowski, Carolina Soekmadji, Rohan A. Davis, Colleen C. Nelson, and Lucia R. Languino. “Differential Effects of Tissue Culture Coating Substrates on Prostate Cancer Cell Adherence, Morphology and Behavior”. In: *PLoS One* 9.11 (2014), pp. 1–13. DOI: <https://doi.org/10.1371/journal.pone.0112122>.
- [3] DK Olivero and LT Furcht. “Type IV collagen, laminin, and fibronectin promote the adhesion and migration of rabbit lens epithelial cells in vitro”. In: *Invest Ophthalmol Vis Sci*. 34.10 (1993), pp. 2825–2834.
- [4] C.R.C. Franco, H.A.O. Rocha, E.S. Trindade, I.A.N. Santos, E.L. Leite, S.S. Veiga, H.B. Nader, and C.P. Dietrich. “Heparan sulfate and control of cell division: adhesion and proliferation of mutant CHO-745 cells lacking xylosyl transferase”. In: *Brazilian Journal of Medical and Biological Research* 34.8 (2001), pp. 971–975. DOI: <https://doi.org/10.1590/S0100-879X2001000800001>.
- [5] Thermo Scientific. *Solutions for cell culture growth and analysis*. URL: <https://tools.thermofisher.com/content/sfs/brochures/D10944.pdf>.
- [6] Eric Moore, Orla Rawley, Terri Wood, and Paul Galvin. “Monitoring of cell growth *in vitro* using biochips packaged with indium tin oxide sensors”. In: *Sensors and Actuators B: Chemical* 139.1 (2009), pp. 187–193. DOI: <https://doi.org/10.1016/j.snb.2008.11.025>.
- [7] Ilhwan Park, Tra Nguyen, Jinsoo Park, Ah Young Yoo, Jae Kweon Park, and Sungbo Cho. “Impedance Characterization of Chitosan Cytotoxicity to MCF-7 Breast Cancer Cells Using a Multidisc Indium Tin Oxide Microelectrode Array”. In: *Journal of The Electrochemical Society* 165.2 (2018), pp. 55–59. DOI: <https://doi.org/10.1149/2.1201802jes>.
- [8] Chang K. Choi, Chuck H. Margraves, Seung I. Jun, Anthony E. English, Philip D. Rack, and Kenneth D. Kihm. “Opto-Electric Cellular Biosensor Using Optically Transparent Indium Tin Oxide (ITO) Electrodes”. In: *Sensors (Basel)* 8.5 (2008), pp. 3257–3270. DOI: <https://doi.org/10.3390/s8053257>.

BIBLIOGRAPHY

- [9] Thomas M. Hermans, Didzis Pilans, Sabil Huda, Patrick Fuller, Kristiana Kandere-Grzybowska, and Bartosz A. Grzybowski. “Motility efficiency and spatiotemporal synchronization in non-metastatic vs. metastatic breast cancer cells”. In: *Integrative Biology (Camb)* 5.12 (2013), pp. 1464–1473. DOI: <https://doi.org/10.1039/c3ib40144h>.
- [10] Christoph Schorl and John M. Sedivy. “Analysis of Cell Cycle Phases and Progression in Cultured Mammalian Cells”. In: *Methods* 41.2 (2007), pp. 143–150. DOI: <https://doi.org/10.1016/j.ymeth.2006.07.022>.
- [11] L. Kim, Y. C. Toh, J. Voldman, and H. Yu. “A practical guide to microfluidic perfusion culture of adherent mammalian cells”. In: *Lab on a Chip* 7.6 (2007), pp. 681–694. DOI: <https://doi.org/10.1039/b704602b>.
- [12] Edmond W. K. Young and David J. Beebe. “Fundamentals of microfluidic cell culture in controlled microenvironments”. In: *Chemical Society Reviews* 39.3 (2010), pp. 1036–1048. DOI: <https://doi.org/10.1039/b909900j>.
- [13] ELVEFLOW. *AIR BUBBLES AND MICROFLUIDICS: TIPS AND TRICKS TO REMOVE THEM*. URL: <https://www.elveflow.com/microfluidic-tutorials/microfluidic-reviews-and-tutorials/air-bubbles-and-microfluidics/>.
- [14] Melanie E. M. Stamp, Anna M. Jötten, Patrick W. Kudella, Dominik Breyer, Florian G. Strobl, Thomas M. Geislinger, Achim Wixforth, and Christoph Westerhausen. “Exploring the Limits of Cell Adhesion under Shear Stress within Physiological Conditions and beyond on a Chip”. In: *Diagnostics (Basel)* 6.4 (2016), pp. 1–15. DOI: <https://doi.org/10.3390/diagnostics6040038>.
- [15] Jonathan W. Song, Stephen P. Cavnar, Ann C. Walker, Kathryn E. Luker, Mudit Gupta, Yi-Chung Tung, Gary D. Luker, and Shuichi Takayama. “Microfluidic Endothelium for Studying the Intravascular Adhesion of Metastatic Breast Cancer Cells”. In: *PLoS One* 4.6 (2009), pp. 1–10. DOI: <https://doi.org/10.1371/journal.pone.0005756>.
- [16] Amelia Ahmad Khalili and Mohd Ridzuan Ahmad. “A Review of Cell Adhesion Studies for Biomedical and Biological Applications”. In: *Int. J. Mol. Sci.* 16.8 (2015), pp. 18149–18184. DOI: <https://doi.org/10.3390/ijms160818149>.
- [17] Franziska Witzel, Raphaela Fritsche-Guenther, Nadine Lehmann, Anja Sieber, and Nils Blüthgen. “Analysis of impedance-based cellular growth assays”. In: *Bioinformatics* 31.16 (2015), pp. 2705–2712. DOI: <https://doi.org/10.1093/bioinformatics/btv216>.
- [18] Franck A. Atienzar, Karen Tilmant, Helga H. Gerets, Gaelle Toussaint, Sebastien Speck-aert, Etienne Hanon, Olympe Depelchina, and Stephane Dhalluin. “The Use of Real-Time Cell Analyzer Technology in Drug Discovery: Defining Optimal Cell Culture Conditions and Assay Reproducibility with Different Adherent Cellular Models”. In: *Journal of Biomolecular Screening* 16.6 (2011), pp. 575–587. DOI: <https://doi.org/10.1177/1087057111402825>.

BIBLIOGRAPHY

- [19] Jason S. Damiano, Anne E. Cress, Lori A. Hazlehurst, Alexander A. Shtil, and William S. Dalton. “Cell Adhesion Mediated Drug Resistance (CAM-DR): Role of Integrins and Resistance to Apoptosis in Human Myeloma Cell Lines”. In: *Blood* 93.5 (1999), pp. 1658–1667.
- [20] Im-Sook Song, Niramol Savaraj, Zahid H. Siddik, Peiman Liu, Yingjie Wei, Chun Jing Wu, and Macus Tien Kuo. “Role of human copper transporter Ctr1 in the transport of platinum-based antitumor agents in cisplatin-sensitive and cisplatin-resistant cells”. In: *Molecular Cancer Therapeutics* 3.12 (2004), pp. 1543–1549.
- [21] AnnaRita Ghezzi, Maurizio Aceto, Claudio Cassino, Elisabetta Gabano, and Domenico Osella. “Uptake of antitumor platinum(II)-complexes by cancer cells, assayed by inductively coupled plasma mass spectrometry (ICP-MS)”. In: *Journal of Inorganic Biochemistry* 98.1 (2004), pp. 73–78. DOI: <https://doi.org/10.1016/j.jinorgbio.2003.08.014>.
- [22] Alexander E. Egger, Christina Rappel, Michael A. Jakupec, Christian G. Hartinger, Petra Heffeter, and Bernhard K. Keppler. “Development of an experimental protocol for uptake studies of metal compounds in adherent tumor cells”. In: 24.1 (2009), pp. 51–61. DOI: <https://doi.org/10.1039/B810481F>.
- [23] Stefanie Michaelis, Rudolf Robelek, and Joachim Wegener. “Studying Cell–Surface Interactions In Vitro: A Survey of Experimental Approaches and Techniques”. In: *Advances in biochemical engineering/biotechnology* 126 (2012), pp. 33–66. DOI: https://doi.org/10.1007/10_2011_112.
- [24] Laverne D. Robilliard, Dan T. Kho, Rebecca H. Johnson, Akshata Anchan, Simon J. O’Carroll, and Euan Scott Graham. “The Importance of Multifrequency Impedance Sensing of Endothelial Barrier Formation Using ECIS Technology for the Generation of a Strong and Durable Paracellular Barrier”. In: *Biosensors* 8.64 (2018), pp. 1–16. DOI: <https://doi.org/10.3390/bios8030064>.
- [25] Fareid Asphahani, Myo Thein, Omid Veisheh, Dennis Edmondson, Ryan Kosai, Mandana Veisheh, Jian Xu, and Miqin Zhanga. “Influence of cell adhesion and spreading on impedance characteristics of cell-based sensors”. In: *Biosensors & bioelectronics* 23.8 (2008), pp. 1307–1313. DOI: <https://doi.org/10.1016/j.bios.2007.11.021>.
- [26] Owen GR, Meredith DO, ap Gwynn I, and Richards RG. “Focal adhesion quantification - A new assay of material biocompatibility? : Review”. In: *European cells & Materials* 9 (2005), pp. 85–96. DOI: <https://doi.org/10.22203/eCM.v009a10>.
- [27] Peter Rupperecht, Laurent Golé, Jean-Paul Rieu, Cyrille Vézy, Rosaria Ferrigno, Hichem C. Mertani, and Charlotte Rivière). “A tapered channel microfluidic device for comprehensive cell adhesion analysis, using measurements of detachment kinetics and shear stress-dependent motion”. In: *Biomicrofluidics* 6.1 (2012), pp. 1–12. DOI: <https://doi.org/10.1063/1.3673802>.
- [28] Weng G. Jiang. *Electric Cell-Substrate Impedance Sensing and Cancer Metastasis*. Dordrecht: Springer, 2012.

- [29] Joachim Wegener. *Measuring Biological Impacts of Nanomaterials*. Switzerland: Springer, 2016.
- [30] Paolo Armando Gagliardi, Alberto Puliafito, Laura di Blasio, Federica Chianale, Desiana Somale, Giorgio Seano, Federico Bussolino, and Luca Primo. “Real-time monitoring of cell protrusion dynamics by impedance responses”. In: *Scientific Reports* 5.10206 (2015), pp. 1–12. DOI: <https://doi.org/10.1038/srep10206>.
- [31] Maximilian Oberleitner. “Label-free and Multi-parametric Monitoring of Cell-based Assays with Substrate-embedded Sensors”. PhD thesis. University of Regensburg, 2015.
- [32] Said Rahim and Aykut Üren. “A Real-time Electrical Impedance Based Technique to Measure Invasion of Endothelial Cell Monolayer by Cancer Cells”. In: *Journal of visualized experiments* 50.2792 (2011), pp. 1–4. DOI: <https://doi.org/10.3791/2792>.
- [33] M. Ducote, B.T. Vinson, S.Hogquist, B. Riggs, J. Saksena, and D.B. Chrisey. “Electrochemical Impedance Spectroscopy (EIS) as a Tool for Pathogen Detection”. In: *Journal of Biosensors and Bioelectronics* 7.4 (2016), pp. 1–7. DOI: <https://doi.org/10.4172/2155-6210.1000224>.
- [34] Xudong Zhang, Fang Li, Anis Nurashikin Nordin, John Tarbell, and Ioana Voiculescu. “Toxicity studies using mammalian cells and impedance spectroscopy method”. In: *Sensing and Bio-Sensing Research* 3 (2015), pp. 112–121. DOI: <https://doi.org/10.1016/j.sbsr.2015.01.002>.
- [35] Fengbo Xie, Youchun Xu, Lei Wang, Keith Mitchelson, Wanli Xing, and Jing Cheng. “Use of cellular electrical impedance sensing to assess *in vitro* cytotoxicity of anticancer drugs in human kidney cell nephrotoxicity model”. In: *Analyst* 137.6 (2012), pp. 1343–1350. DOI: <https://doi.org/10.1039/c2an16141a>.
- [36] Weng G. Jiang. *Electric Cell-Substrate Impedance Sensing and Cancer Metastasis*. Dordrecht Heidelberg New York London: Springer, 1997.
- [37] Dan Kho, Christa MacDonald, Rebecca Johnson, Charles P. Unsworth, Simon J. O’Carroll, Elyce du Mez, Catherine E. Angel, and E. Scott Graham. “Application of xCELLigence RTCA Biosensor Technology for Revealing the Profile and Window of Drug”. In: *Biosensors* 5.2 (2015), pp. 199–222. DOI: <https://doi.org/10.3390/bios5020199>.
- [38] Chang K.Choi, Anthony E.English, Seung-Ik Jun, Kenneth D.Kihm, and Philip D.Rack. “An endothelial cell compatible biosensor fabricated using optically thin indium tin oxide silicon nitride electrodes”. In: *Biosensors and Bioelectronics* 22.11 (2007), pp. 2585–2590. DOI: <https://doi.org/10.1016/j.bios.2006.10.0006>.
- [39] Bilge Eker, Robert Meissner, Arnaud Bertsch, Kapil Mehta, and Philippe Renaud. “Label-Free Recognition of Drug Resistance via Impedimetric Screening of Breast Cancer Cells”. In: *PLoS One* 8.3 (2013), pp. 1–12. DOI: <https://doi.org/10.1371/journal.pone.0057423>.
- [40] Robert Meissner, Bilge Eker, Harsha Kasi, Arnaud Bertsch, and Philippe Renaud. “Distinguishing drug-induced minor morphological changes from major cellular damage via label-free impedimetric toxicity screening”. In: *Lab Chip* 11.14 (2011), pp. 2352–2361. DOI: <https://doi.org/10.1039/c1lc20212j>.

- [41] G. Bazzoni and E. Dejana. “Endothelial cell-to-cell junctions: molecular organization and role in vascular homeostasis”. In: *Physiological reviews* 84.3 (2004), pp. 869–901. DOI: <https://doi.org/10.1152/physrev.00035.2003>.
- [42] Qingjun Liu, Yanli Lu, Hua Wang, Jie Zhou, Yongsheng Zhang, Qunwei Chen, Senbiao Luo, Rong Li, and Ping Wang. “Impedance Detection and Modeling of Chemotherapeutic Agents by a Cancer Cell-Based Biosensor”. In: *Analytical Letters* 47.8 (2014), pp. 1348–1360. DOI: <https://doi.org/10.1080/00032719.2013.867498>.
- [43] Xiaoqiu Huang, Duc Nguyen, D.W. Greve, and M.M. Domach. “Simulation of micro-electrode impedance changes due to cell growth”. In: *IEEE Sensors Journal* 4.5 (2004), pp. 576–583. DOI: <https://doi.org/10.1109/JSEN.2004.831302>.
- [44] D.W. Greve, X. Huang, D. Nguyen, and M.M. Domach. “Modeling of impedance of cell-covered electrodes”. In: *IEEE SENSORS*. Vol. 2. 5. IEEE, Oct. 2003, pp. 1358–1363.
- [45] Daniel Eberli. *Regenerative Medicine and Tissue Engineering: Cells and Biomaterials*. London: IntechOpen, 2011.
- [46] Kevin V. Christ and Kevin T. Turner. “Methods to Measure the Strength of Cell Adhesion to Substrates”. In: *Journal of Adhesion Science and Technology* 24.13-14 (2010), pp. 2027–2058. DOI: <https://doi.org/10.1163/016942410X507911>.
- [47] M. Mianabadi and R. Yazdanparast. “Inhibition of substrate-tumor cell adhesion under the effect of gnidilatimonoein purified from daphne mucronata”. In: *Am. J. Chin. Med* 32.369 (2004), pp. 369–376. DOI: <https://doi.org/10.1142/S0192415X04002028>.
- [48] Joachim Wegener, Andreas Janshoff, and H.J. Galla. “Cell adhesion monitoring using a quartz crystal microbalance: comparative analysis of different mammalian cell lines”. In: *European Biophysics Journal* 28.1 (1998), pp. 26–37. DOI: <https://doi.org/10.1007/s002490050180>.
- [49] Vanessa Heitmann and Joachim Wegener. “Monitoring Cell Adhesion by Piezoresonators: Impact of Increasing Oscillation Amplitudes”. In: *Anal. Chem.* 79.9 (2007), pp. 3392–3400. DOI: <https://doi.org/10.1021/ac062433b>.
- [50] Antoine Confavreux. “Optimisation des conditions de migration et de détachement de lignées cancéreuses du cancer du sein en vue de leur tri fonctionnel”. PhD thesis. Université Claude Bernard Lyon 1, 2014.
- [51] Yi Fu, Robert Kunz, Jianhua Wu, and Cheng Dong. “Study of Local Hydrodynamic Environment in Cell-Substrate Adhesion Using Side-View μ PIV Technology”. In: *PLoS One* 7.2 (2012), pp. 1–13. DOI: <https://doi.org/10.1371/journal.pone.0030721>.
- [52] Guo Xiaoliang, Zhu Rong, and Zong Xianli. “A microchip integrating cell array positioning with *in situ* single-cell impedance measurement”. In: *Analyst* 140.19 (2015), pp. 1–16. DOI: <https://doi.org/10.1039/c5an01193k>.
- [53] Victor R. Preedy and Vinood Patel. *Biosensors and Environmental Health*. Boca raton, FL: CRC Press, 2012.

- [54] Leyla Turker Sener, Gurcan Albeniz, Bircan Dinç, and Isil Albeniz. “iCELLigence real-time cell analysis system for examining the cytotoxicity of drugs to cancer cell lines”. In: *Experimental and Therapeutic Medicine* 14.3 (2017), pp. 1866–1870. DOI: <https://doi.org/10.3892/etm.2017.4781>.
- [55] John A. Yagiela, Frank J. Dowd, Bart Johnson, Angelo Mariotti, and Enid A. Neidle. *Pharmacology and Therapeutics for Dentistry*. MOSBY Elsevier,
- [56] Daniel B. Longley, D. Paul Harkin, and Patrick G. Johnston. “5-Fluorouracil: mechanisms of action and clinical strategies”. In: *Nature Reviews Cancer* 3.5 (2003), pp. 330–338. DOI: <https://doi.org/10.1038/nrc1074>.
- [57] Hector Hernandez-Vargas, Esteban Ballestar, Pedro Carmona-Saez, Cayetano von Kobbe, Inmaculada Banon-Rodriguez, Manel Esteller, Gema Moreno-Bueno, and Jose Palacios. “Transcriptional profiling of MCF7 breast cancer cells in response to 5-Fluorouracil: Relationship with cell cycle changes and apoptosis, and identification of novel targets of p53”. In: *International Journal of Cancer* 119.5 (2006), pp. 1164–1175. DOI: <https://doi.org/10.1002/ijc.21938>.
- [58] Michael A. Koldobskiy, Anutosh Chakraborty, J. Kent Werner, Jr. Adele M. Snowman, Krishna R. Juluri, M. Scott Vandiver, Seyun Kima, Shira Heletz, and Solomon H. Snyder. “p53-mediated apoptosis requires inositol hexakisphosphate kinase-2”. In: *Proceedings of the National Academy of Sciences* 107.49 (2010), pp. 20947–20951. DOI: <https://doi.org/10.1073/pnas.1015671107>.
- [59] M Olsson, H Vakifahmetoglu, P. M. Abruzzo, K. Högstrand, A. Grandien, and B. Zhivotovskiy. “DISC-mediated activation of caspase-2 in DNA damage-induced apoptosis”. In: *Oncogene* 28.18 (2009), pp. 1949–1959. DOI: <https://doi.org/10.1038/onc.2009.36>.
- [60] Antti Saraste and Kari Pulkki. “Morphologic and biochemical hallmarks of apoptosis”. In: *Cardiovascular Research* 45.3 (2000), pp. 528–537.
- [61] Xuesong Chen, Yu Li, Qiushi Lin, Yan Wang, Hong Sun, Jian Wang, Guoquan Cui, Li Cai, and Xiaoqun Dong. “Tea polyphenols induced apoptosis of breast cancer cells by suppressing the expression of Survivin”. In: *Scientific Reports* 4.4416 (2014), pp. 1–5. DOI: <https://doi.org/10.1038/srep04416>.
- [62] Maitri Yogen Shah. “Effects of 5-fluorouracil Drug Treatment on the Expression Profile of MicroRNAs in MCF7 Breast Cancer Cells”. PhD thesis. East Carolina University, 2010.
- [63] Kurt Jacobs, Filippo Zambelli, Afroditi Mertzaniidou, Ilse Smolders, Mieke Geens, Ha Thi Nguyen, Lise Barbe, Karen Sermon, and Claudia Spits. “Higher-Density Culture in Human Embryonic Stem Cells Results in DNA Damage and Genome Instability”. In: *Stem Cell Reports* 6.3 (2016), pp. 330–341. DOI: <https://doi.org/10.1016/j.stemcr.2016.01.015>.
- [64] Xiaoli Chen, Allen Chen, Tsung Liang Woo, Andre B.H. Choo, Shaul Reuveny, and Steve K.W. Oh. “Investigations into the metabolism of two-dimensional colony and suspended microcarrier cultures of human embryonic stem cells in serum-free media.” In: *Stem Cells and Development* 19.11 (2010), pp. 1781–1792. DOI: <https://doi.org/10.1089/scd.2010.0077>.

- [65] Rebecca A. Burrell, Sarah E. McClelland, David Endesfelder, Petra Groth, Marie-Christine Weller, Nadeem Shaikh, Enric Domingo, Nnennaya Kanu, Sally M. Dewhurst, Eva Gronroos, Su Kit Chew, Andrew J. Rowan, Arne Schenk, Michal Sheffer, Michael Howell, Maik Kschischo, Axel Behrens, Thomas Helleday, Jiri Bartek, Ian P. Tomlinson, and Charles Swanton. “Replication stress links structural and numerical cancer chromosomal instability”. In: *Nature* 494.7438 (2013), pp. 492–496. DOI: <https://doi.org/10.1038/nature11935>.
- [66] Paula M De Angelis, Debbie H Svendsrud, Katherine L Kravik, and Trond Stokke. “Cellular response to 5-fluorouracil (5-FU) in 5-FU-resistant colon cancer cell lines during treatment and recovery”. In: *Molecular Cancer* 5.20 (2006), pp. 1–25. DOI: <https://doi.org/10.1186/1476-4598-5-20>.
- [67] Alan Eastman. “Improving anticancer drug development begins with cell culture: misinformation perpetrated by the misuse of cytotoxicity assays”. In: *Oncotarget* 8.5 (2017), pp. 8854–8866. DOI: <https://doi.org/10.18632/oncotarget.12673>.
- [68] Reyhaneh Akbari and Hamid Akbari Javar. “Efficacy of Capecitabine and 5-Fluorouracil (5-FU) on the human breast cancer cell line (MCF7)-effect of concentration”. In: *American Journal of Research Communication* 1.6 (2013), pp. 75–91.
- [69] Andrew S. Jeong. “Safety evaluation of low level light therapy on cancer cells”. PhD thesis. Boston University, 2016.
- [70] Tuomo Kalliokoski, Christian Kramer, Anna Vulpetti, and Peter Gedeck. “Comparability of Mixed IC₅₀ Data – A Statistical Analysis”. In: *PLoS One* 8.4 (2013), pp. 1–12. DOI: <https://doi.org/10.1371/journal.pone.0061007>.
- [71] Senem Aykul and Erik Martinez-Hackert. “Determination of half-maximal inhibitory concentration using biosensor-based protein interaction analysis”. In: *Analytical Biochemistry* 508 (2016), pp. 97–103. DOI: <https://doi.org/10.1016/j.ab.2016.06.025>.
- [72] Manon van Engeland, Helma J.H. Kuijpers, Frans C.S. Ramaekers, Chris P.M. Reutelingsperger, and Bert Schutte. “Plasma Membrane Alterations and Cytoskeletal Changes in Apoptosis”. In: *Experimental Cell Research* 235.2 (1997), pp. 421–430. DOI: <https://doi.org/10.1006/excr.1997.3738>.
- [73] Yingying Zhang, Xin Chen, Cyril Gueydan, and Jiahuai Han. “Plasma membrane changes during programmed cell deaths”. In: *Cell Research* 28.1 (2018), pp. 9–21. DOI: <https://doi.org/10.1038/cr.2017.133>.
- [74] C. Caviglia, K. Zór, S. Canepa, M. Carminati, L. B. Larsen, R. Raiteri, T. L. Andresen, A. Heiskanena, and J. Emnéus. “Interdependence of initial cell density, drug concentration and exposure time revealed by real-time impedance spectroscopic cytotoxicity assay”. In: *Analyst* 140.10 (2015), pp. 3623–3629. DOI: <https://doi.org/10.1039/C5AN00097A>.
- [75] Claudia Caviglia, Kinga Zór, Lucia Montini, Valeria Tilli, Silvia Canepa, Fredrik Melander, Haseena B. Muhammad, Marco Carminati, Giorgio Ferrari, Roberto Raiteria, Arto Heiskanen, Thomas L. Andresen, and Jenny Emnéus. “Impedimetric Toxicity Assay in Microfluidics Using Free and Liposome-Encapsulated Anticancer Drugs”. In: *Analytical Chemistry* 87.4 (2015), pp. 2204–2212. DOI: <https://doi.org/10.1021/ac503621d>.

BIBLIOGRAPHY

- [76] Zeina Bash Imam. “Effect of 5-Fluorouracil on translational regulation in colorectal cancer cells”. PhD thesis. Université Claude Bernard Lyon 1, 2015.
- [77] Xiaofeng Dai, Hongye Cheng, Zhonghu Bai, and Jia Li. “Breast Cancer Cell Line Classification and Its Relevance with Breast Tumor Subtyping”. In: *Journal of Cancer* 8.16 (2017), pp. 3131–3141. DOI: <https://doi.org/10.7150/jca.18457>.
- [78] Deborah L Holliday and Valerie Speirs. “Choosing the right cell line for breast cancer research”. In: *Breast Cancer Research* 13.4 (2011), pp. 1–7. DOI: <https://doi.org/10.1016/j.molonc.2010.11.003>.
- [79] Sara Zalba and Timo L.M.ten Hagen. “Cell membrane modulation as adjuvant in cancer therapy”. In: *Cancer Treatment Reviews* 52 (2017), pp. 48–57. DOI: <https://doi.org/10.1016/j.ctrv.2016.10.008>.
- [80] Samanthe M. Lyons, Elaheh Alizadeh, Joshua Mannheimer, Katherine Schuamberg, Jordan Castle, Bryce Schroder, Philip Turk, Douglas Thamm, and Ashok Prasad. “Changes in cell shape are correlated with metastatic potential in murine and human osteosarcomas”. In: *Biology Open* 5.3 (2016), pp. 289–299. DOI: <https://doi.org/10.1242/bio.013409>.
- [81] Donald W. Kufe, Raphael E Pollock, Ralph R. Weichselbaum, Robert C. Bast, Ted S. Gansler, James F. Holland, and Emil Frei. *Holland-Frei Cancer Medicine Volume Two*. Hamilton, ON: BC Decker, 2004.
- [82] K. C. Chaw, M. Manimaran, E. H. Tayad, and S. Swaminathane. “Multi-step microfluidic device for studying cancer metastasis”. In: *Lab on Chip* 7.8 (2007), pp. 1041–1047. DOI: <https://doi.org/10.1039/B707399M>.
- [83] Keon Woo Kwon, Sung Sik Choi, Sang Ho Lee, Byungkyu Kim, Se Na Leea, Min Cheol Park, Pilnam Kim, Se Yon Hwang, and Kahp Y. Suh. “Label-free, microfluidic separation and enrichment of human breast cancer cells by adhesion difference”. In: *Lab on Chip* 7.11 (2007), pp. 1461–1468. DOI: <https://doi.org/10.1039/B710054J>.
- [84] Zhonglan Tang and Yoshikatsu Akiyama, Kazuyoshi, Itoga Jun Kobayashi, Masayuki Yamato, and Teruo Okano. “Shear stress-dependent cell detachment from temperature-responsive cell culture surfaces in a microfluidic device”. In: *Biomaterials* 33.30 (2012), pp. 7405–7411. DOI: <https://doi.org/10.1016/j.biomaterials.2012.06.077>.

Strategy to enhance sensitivity of ITO IDEs

In chapter 3, we demonstrated that ITO IDEs have lower sensitivity during ECIS experiments than Au IDEs. We attributed this result to the lower global impedance of Au electrodes, corresponding to both a lower interfacial impedance and a lower resistive contribution for Au IDEs compared to those of ITO. This explains why Au remains the standard electrode material in ECIS experiments. Nevertheless, as already reported by various authors[1, 2, 3], the possibility of combining impedance and optical measurements is advantageous in order to be able to monitor cellular morphology and cytoskeletal organization. Microscopy techniques such as Differential Interference Contrast Microscopy (DCIM)[4] or Interference Reflection Contrast Microscopy(IRCM)[5] enable visual confirmation of cell-to-cell and cell-to-substrate adhesions, which complement impedance readings. These could be helpful in understanding and unraveling drug action on cancerous cells. This is why, authors are interested in the transparency of ITO for the observation of cells during an ECIS experiment. During this thesis, we therefore sought a strategy to enhance the sensitivity of the ITO IDEs without affecting their transparency. This strategy consisted of modifying the electrode surface using IrO_x electrodeposition in order to decrease the interfacial impedance of the IDEs. In chapter 3, we also presented the simple model of De Levie[6]. This model successfully explains qualitatively many aspects of interface impedance[7]. According to De Levie, apart from the effective area of the electrode, the pores on the electrode surface play an important role in the interfacial impedance and they can be represented by transmission lines. De Levie postulates that for "rough" electrodes, the interfacial impedance is proportional to the square root of the "smooth surface" impedance, particularly at high frequency and that the phase angle decreases when the surface roughness increases[6].

In the literature more complex transmission line models have since been suggested. For instance, Keiser et al[8] showed that the pore shape has an important impact on the impedance locus. Pores have been represented by non-uniform ladder networks whose elements vary with pore depth[9] in an attempt to describe the observed form of the interface impedance. Polydimensional[10] and hierarchical branching ladder networks[11] have also been proposed. Several distributions of pore location, depth and width have been tried[12] in order to improve the fit with experimental data. Although the aforementioned models have been found to more accurately reproduce measured impedances, many of them include arbitrary and questionable assumptions and the increased number of variables involved make the drawing of meaningful conclusions difficult[7]. An alternative approach is to use fractal geometry, which is a mathematical concept that describes objects of irregular shape, in order to describe the expected physics of the system under study. For instance, Ball et al.[13] presented a fractal model for a rough interface between an electrode and an electrolyte.

In this chapter we first studied the effect of the IrO_x coating on the electrode impedance, more precisely on the interfacial impedance of Au IDEs by electrical equivalent circuit modeling. Afterwards, we determined the number of cycles that we would need to use during the electrodeposition using cyclic voltammetry of the ITO IDEs. After that, we studied the electrical responses of the ITO IDEs before and after the electrodeposition of the iridium oxide in KCl solution. We then focused on IrO_x modified ITO IDEs covered with CN/BSA and in contact with the supplemented DMEM. We measured the interfacial impedance after surface modification. Finally, we used the "enhanced" electrodes to monitor the proliferation of MCF-7 cells.

5.1 Surface modification of electrodes used in ECIS

We mentioned earlier that biological *in-vitro* assays, in the context of personalized medicine, need to be carried out in a miniaturized environment in order to optimally adapt to the small volume samples. This means that for ECIS, the size of the electrodes has to be reduced in order to be compatible with the miniaturized environment. However, reducing the size of the electrodes results in higher impedance[14] and the large electrode-electrolyte interfacial impedance becomes one of the critical issues. Here, we present a strategy (IrO_x electrodeposition), commonly used to reduce the impedance of the electrodes in neural and electrostimulation applications by means of nanostructuring of the surface. Nevertheless, even if nanostructuring is a widely used strategy in the improvement of biosensor performances, this strategy has been only applied to ECIS recently. For instance, V. Srinivasaraghavan et al.[15] compared the influence of a nanoscale coating made either of gold nanoparticles (AuNP) or carbon nanotubes (CNT) on gold electrodes. Using the MDA-MB-231 human breast cancer line in ECIS assay, they showed that the impedance change in response to metastatic breast cancer cells was maximal on the CNT coated electrodes followed by the AuNP electrodes. The authors also detected a shift in the frequency corresponding to the normalized peak impedance due to the coating of the electrodes. They observed a decrease in this frequency for CNT and Au coatings. M. Abdolahad et al.[16] used nanograss Si electrodes obtained by Reactive Ion Etching to detect by impedance variation, the presence of a few human, colon invasive, cancer cells (SW48) in a mixed cell culture of primary cancerous colon cells (HT29).

Basically, in order to reduce the interfacial impedance, one approach consists in artificially increasing the active surface area of the electrodes. This can be achieved by two strategies: (i) bulk and (ii) surface processes[17]. In bulk processes, direct modification of the metallic surface can be achieved by laser roughening[18] or metal etching[19]. Although these can modify the roughness without significantly changing the electrode chemistry, the benefits are limited because the material properties and compatibility with biological molecules remains unchanged[20]. In contrast, surface processes, on which we will elaborate more in this section, rely on modifying the electrode surface through a variety of methods including electrochemical, physical or vapor deposition, spin coating and dip coating[20, 21]. Here, some of the widely used high surface area (HSA) coatings, such as platinum black, titanium nitride, carbon nanotubes, conducting polymers, gold nanostructures and iridium oxide[14] are presented. These coatings provide different surface modifications leading to different forms of roughness, which as shown before go beyond the concept of surface "irregularities".

- **Platinum black:** (Pt-black) is a conductive material which has a rough surface structure and it is widely used for high surface area low-impedance applications[22]. Pt-black can be electrochemically deposited over conductive and semiconductive materials such as aluminium, platinum, silver, gold, tin-copper alloy, indium-tin-oxide, stainless steel, and copper by reaction of platinum chloride (PtCl_4) with lead acetate ($\text{Pb}(\text{CH}_3\text{COO})_2$) [23]. The name of Pt-black comes from the deep black color and dull surface of the deposit. The dark black color appears when lead is used as an additive[24]. This coating material has a highly "chondritic" fractal surface as shown in Fig.5.1a that strongly increases the active surface area of an electrode[25]. This material has been used to lower the electrode impedance in various applications. For example, Desai et al.[26] in *in vivo* durability, stimulation and recording assays in the frequency range from 10 to 10 kHz, reduced approximately twelve fold the impedance of tungsten electrodes with Pt-black, which were implanted into the brain of rats. Similarly, Kisban et al.[27] implanted into the cortex of Macaque monkeys, sharp tips made of Pt-black/Pt for recording action potential of neurons, in the frequency range from 100 Hz to 10 kHz. After deposition of Pt-black, the impedance decreased by up to two orders of magnitude without any cytotoxic effect. Jun et al.[28] decreased the impedance of Ti electrodes only one order of magnitude for electrical stimulation with 5 Hz, 20 Hz and 100 Hz pulses on primary hippocampal neurons. Maoz et al.[29] in their study on measuring field potentials of cardiomyocytes and TEER measurements in the frequency range from 10 Hz to 100 kHz, demonstrated that Pt-black decreased the impedance values three orders of magnitude in comparison to regular Pt electrodes. However, despite its use in several applications, Pt-black's major drawback is the lack of mechanical stability. It tends to flake-off from the metal substrate surface during the application of stress[22]

5.1. Surface modification of electrodes used in ECIS

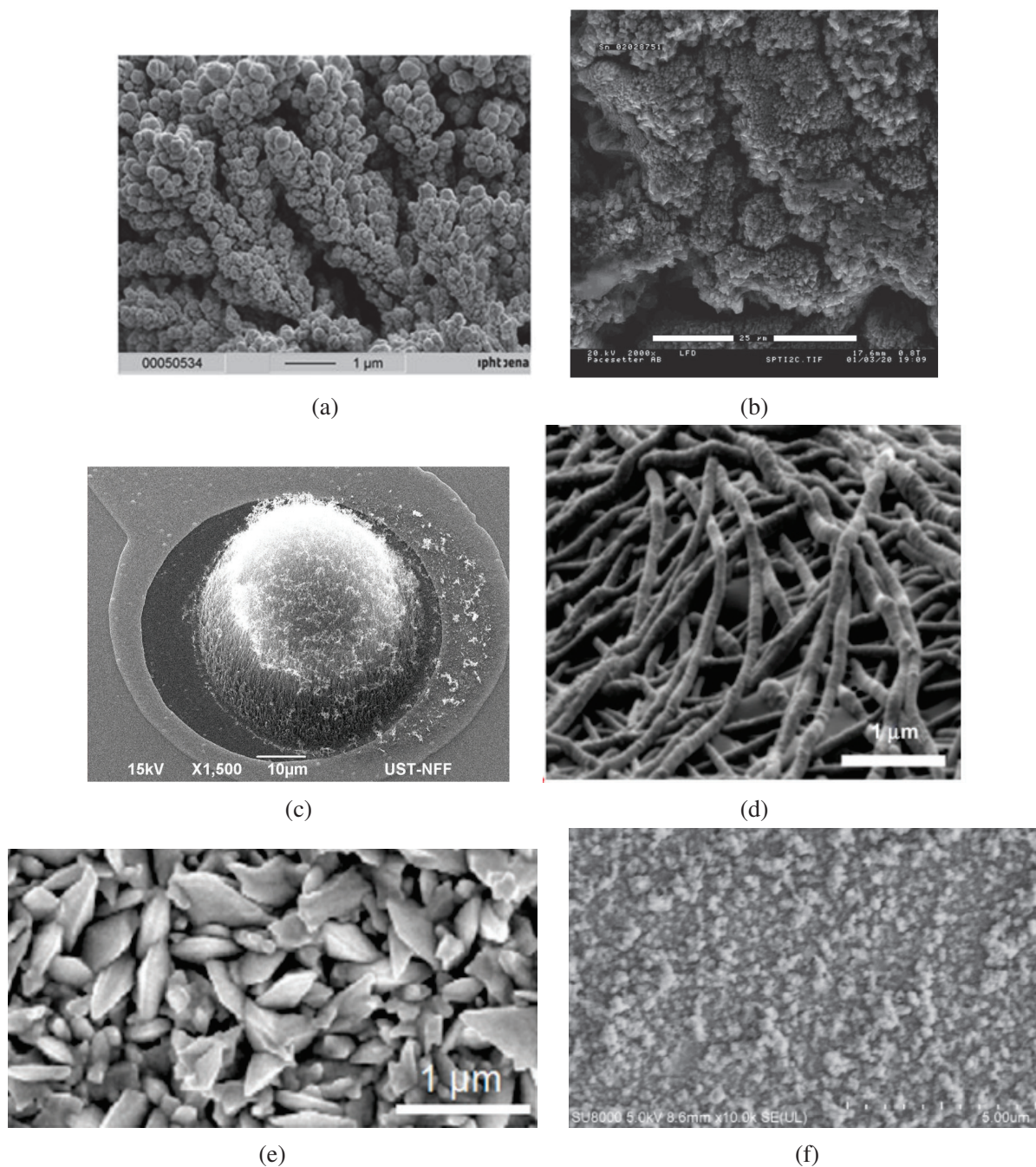


Figure 5.1 – SEM images of (a) platinum black electrochemically synthesized on platinum substrate (Figure adapted from figure 1 in [23]), (b) titanium nitride deposited by physical vapor deposition on titanium substrate (Figure adapted with permission from figure 1 in [30]. Copyright 2002 by Elsevier.), (c) CNTs grown by CVD on a Ti-barrier layer (Figure adapted with permission from figure 1 in [31]. Copyright 2015 by Elsevier.), (d) PEDOT electrodeposited on Au neural microelectrode. (Figure adapted with permission from figure 4 in [32]. Copyright 2008 by Elsevier.), (e) Gold nanoflakes on gold electrodes. (Figure adapted with permission from figure 3 in [14]. Copyright 1990 by IOP Publishing.) and (f) electrodeposited IrO_x by cyclic voltammetry on Pt electrodes. (Figure adapted with permission from figure 2 in [33]. Copyright 2018 by Elsevier).

- **Titanium nitride:** (TiN) has a metal-like conductivity, excellent mechanical and chemical properties and it is known as a high surface area coating capable of reducing electrode impedance[30]. This type of nitride provides a highly porous coating, as shown in Fig. 5.1b, which can be deposited by physical vapor deposition (CVD) using a titanium metal target[34]. TiN films have been used in cardiac pacemakers[35, 36] and neural stimulation applications where high charge injection capacity is needed[37, 38]. For example, XiaoQian et al.[39] investigated flexible gold electrodes modified by TiN, Pt-black and IrO_x for functional electrical stimulation. They found that the impedance of the gold electrodes decreased 4 fold from its initial value before surface modification with TiN. They concluded that TiN, which is compatible with integrated circuit processes should be first considered consideration if the impedance does not need to greatly decrease. Otherwise, other coatings must be considered. This is coherent with the results of the study of Weiland et al.[40], in which iridium oxide and titanium nitride stimulating electrodes were compared. They found that although TiN has the advantage of being more compatible with the microfabrication methods used to make silicon probes, iridium oxide remains the most effective material for injecting charge while minimizing power consumption in stimulating electrodes.
- **Carbon nanotubes:** Some studies have focused on using carbon nanotubes (CNTs), as shown in Fig.5.1c, to increase the active electrode area. These organic structures have high surface to volume ratios, which make them good candidates for fabricating electrodes with lower impedances[41]. Surface modification with CNTs can be carried out using two different techniques:
 1. CVD involves direct growth of CNT films by means of a thin catalyst layer coated onto the electrode[25]. Depending on the growth conditions, vertically aligned or randomly deposited CNTs can be obtained[42, 43, 31].
 2. The other method of modifying the surface with CNTs involves electrochemical co-deposition, a technique that does not require high temperatures. It consists in dissolving the monomer of a conducting polymer in a suspension of CNTs, and then co-depositing the polymer with the CNTs into a composite coating on an electrode[44, 45, 46].

Regarding possible applications, coatings of CNTs have been shown to improve sensitivity of electrochemical sensors. For instance, Gaio et al.[43] demonstrated the biocompatibility of cobalt grown CNTs by seeding human pluripotent stem cell-derived cardiomyocytes on the surface and reported a reduction in the overall impedance of 95 % in comparison to TiN electrodes. Abdolahad et al.[16] developed a vertically aligned CNT-based electrical cell impedance sensing biosensor, in which CNTs arrays act as both adhesive and conductive agents for the study of SW48 colon cancer cells. According to these authors, impedance changes with the CNTs were achieved in as little as 30 s. Similarly, Srinivasaraghavan et al.[15] demonstrated that changes in the impedance due to the adherence of MDA-MB-231 breast cancer cells were most significant on CNT's coated Au electrodes. Although it seems a promising strategy to enhance the sensitivity, the biocompatibility of CNTs remains a controversial issue in the literature[25].

- **Conducting polymers:** Coatings of conducting polymers such as polypyrrole (PPy) or Poly(3,4-ethylenedioxythiophene) (PEDOT) have also been used to decrease the electrode impedance due to their rough surfaces, as shown in Fig.5.1d, after being electrodeposited on the electrode[25, 47, 48]. Most of these researchers have electrodeposited the polymer layer onto inert electrodes: Pt, Au or glassy carbon as substrate using either aqueous solutions or organic solvents[49]. Charkhkar et al.[47] modified gold electrodes with the conductive polymer PEDOT and added a smaller counter ion tetrafluoroborate (TfB) during electrodeposition in order to increase the stability of the PEDOT coating *in vitro*. The PEDOT-TfB coating decreased seventh fold the impedance of the electrodes, which were implanted into the primary motor cortex of rats for neural recordings. In a similar manner, Karimullah et al.[50] demonstrated that PEDOT doped with poly(styrene sulfonate) PEDOT:PSS,

decreased seventh fold the impedance of gold electrodes. In their MDCK kidney cell proliferation experiments, an enhancement in sensitivity of PEDOT:PSS electrodes was observed due to the significantly lower interfacial impedance compared to that of gold electrodes. Furthermore, in another study, Ateh et al.[51] found that cell-induced impedance changes for lower cell densities of SVK14 keratinocytes were easily detected by PPy modified gold electrodes when compared with bare gold electrodes.

- **Gold nanostructures:** Recently, gold due to its high conductivity, chemical stability and biocompatibility[52] has been widely used to fabricate nanoparticles and nanostructures in order to increase the effective surface area of electrodes, as shown in Fig. 5.1e. For example, Xiaoliang et al.[53] enlarged the effective surface areas of their measuring gold electrodes using gold nanostructures, leading to a decrease of the initial electrode impedance down to 85 % and 95 %. In a similar way, Koklu et al.[54] developed two kinds of gold nanostructured electrodes that had increased effective surfaces compared to flat gold electrodes. They investigated gold nanostructured electrodes by varying the duration and electric potential involved while fabricating gold granulated electrodes using tannic acid and citrate and a temperature treatment. In contrast to most of the studies concerning HSA coatings, they went further and, by using equivalent circuit modeling, they determined the effect of surface modification on the interfacial impedance of the electrodes. They found that gold nanostructured electrodes increased by almost 400 the Q_{int} value whereas gold granulated electrodes only increased the initial value of Q_{int} by around 50. This demonstrated that gold nanostructured electrodes are an attractive strategy to increase the sensitivity of biosensors. Kim et al.[14] explored another type of structure termed "nanoflakes" (flake-like gold nanostructures deposited on gold electrodes). They obtained a reduction in the impedance of ~ 43 . They also demonstrated good biocompatibility by maintaining healthy hippocampal neurons for a month on the modified electrodes, showing that these electrode structures could be advantageous for neural applications.

- **Iridium oxide IrO_x :**

Another type of coating capable of modifying the electrode surface is iridium oxide (IrO_x), as shown in Fig. 5.1f. This is a commonly used material in a range of applications, such as measurement of extracellular acidification[55, 56]; detection of neurotransmitters[57, 58], hydrogen peroxide[59, 60] and insulin[61]. It is also used for pH sensing[62, 63], in neural stimulation and in recording electrodes[64, 65]. This material can store extremely high amounts of charges and deliver it without damaging biological tissues by minimizing electrochemically irreversible processes at the electrode tissue interface. An additional technological advantage is the ability to deposit IrO_x layers using different chemical and physical techniques, which can match a range of application-specific requirements in chemistry, biology and medicine. In the literature, four different processes have been observed to form iridium oxide films[66, 67]:

- From metallic iridium (Ir) using an electrochemical activation process (**AIROFs**)[68]: Marzouk et al.[56] demonstrated that AIROF has excellent pH response characteristics, such as working lifetime of at least 1 month with an accuracy of about 0.02 pH unit and a fast response time. They tested the electrodes in extracellular myocardial acidosis during a brief regional ischemia in a swine heart and during no-flow ischemia in an isolated rabbit papillary muscle. Blau et al.[69] studied the electrodeposition of IrO_x on Pt electrodes for *in vivo* nerve signal recording and stimulation. They found that AIROF decreased the electrode impedance by three orders of magnitude and increased the charge delivery capacity. Additionally, in the fabrication process, large amounts of water were incorporated into the structure during prolonged potential cycling, leading to highly porous and low density AIROFs. Nevertheless, although the resulting highly porous structure appeared to be attractive for achieving high charge storage capacities, it was reported to lead to flaking and delamination of AIROFs from the substrate during long term use[25].

5.1. Surface modification of electrodes used in ECIS

- Reactive sputtering of Ir in the presence of oxidizing plasma (**SIROFs**)[64]: Iridium oxide films can also be formed from an iridium metal target by reactive sputtering in an oxidizing plasma. For example, Cogan et al.[70] confirmed that the SIROF can be easily deposited and patterned using conventional sputtering and photolithographic techniques. They observed that the impedance of SIROF in the frequency range from 50 mHz to 100 kHz, compared to that of the uncoated electrode site is reduced by more than a factor of 10, making it suitable as a low impedance recording or a stimulation coating for flexible and rigid planar multielectrode arrays in neural stimulation applications. However, it was found that high amounts of oxygen during the sputtering process could lead to lower mechanical stability and a decrease in charge storage capacities[25].
- Thermal decomposition of iridium salts to form thermal iridium oxide films (**TIROFs**)[71]: This type of films have similar electrochemical behaviors and charge injection properties to AIROF[65]. For example, Robblee et al.[72] found that Ti and Pt electrodes modified with TIROF films had charge injection capabilities similar to AIROFs. In addition, the TIROF coatings remained firmly attached to the substrate metal during long term pulsing and abrasion tests. This means that thermally-prepared Ir oxide films may have wide applicability in neural prosthesis development, in which improving the charge transfer properties of the electrode material is important. However, TIROF is not used extensively due to the high decomposition temperature (> 300 °C) necessary to form the oxide, which may not be suitable for several electrode fabrication protocols[65].
- Electrodeposition of iridium oxide onto metals (**EIROFs**)[73]: In this technique, the iridium oxide is deposited from an iridium salt solution in a process that involves direct growth of the oxide rather than deposition and subsequent activation of the metal as in AIROFs. There are two types of deposition solution described in the literature: those that do and those that do not involve oxalate anions as ligands complexing Ir(IV)[74]. The first group corresponds to oxalate-based deposition solutions, which are the most commonly used and were introduced by Yamanaka[75] and later modified by Petit et al[76]. Whereas in the second group we find two principal examples of deposition solutions made without oxalate ligands. One type, introduced by Yoshino et al.[77], uses a mixture of sulfanatoiridate complexes, predominantly anhydrous iridium III sulfate, which is dissolved in deionized DI water to saturation and left to stir for a week. A second type, introduced by Baur et al.[78], involves deposition with either iridium III hexachloride or iridium IV hexachloride, which is then reduced to iridium III under ethanol flux. Meyer et al.[65] deposited EIROF on gold electrodes using a solution similar to that of Yamanaka and they decreased the electrode impedance by two orders of magnitude. These are promising results for retinal stimulation electrodes that have exposed gold electrode sites. According to Meyer, the primary usefulness of EIROF compared to AIROF is its suitability for deposition on a variety of metal electrodes, such as Au, Pt, PrIr and stainless steel alloy 316LVM without the need of a metallic iridium surface for activation[65]. Furthermore, biocompatibility of IrO_x has also been explored. For instance, Cruz et al.[73] demonstrated that electrodeposited IrO_x allowed neuronal adhesion and survival with elongation of axons and dendrites, which contrast with the work of Thanawala et al.[79], where they reported poor adhesion and growth of rat cerebral cortex neurons on sputtered IrO_x films. According to Cruz, as long as the oxide surface is well functionalized for cell adhesion and does not dissolve or delaminate from the electrode, toxic or growth inhibitory response should not be expected.

From all the above strategies to enhance electrode performance, we decided to modify the electrodes with EIROFs as it does not involve high temperatures, it is compatible with different metallic substrates and it was already studied at our laboratory in a previous work on pH sensing, where it showed promising results in terms of sensitivity and mechanical stability.[80].

5.2 Surface-modified electrodes with IrO_x

5.2.1 Electrodeposition of IrO_x on Au and ITO IDEs

IrO_x has been electrodeposited on various substrates, such as Au, Pt, Ir, PtIr and stainless steel[68, 81, 82, 83, 84]. However, very few studies have explored using ITO as a substrate. For instance, Young-Jin et al.[85] deposited iridium oxide on ITO to develop a novel pH microsensor with a built-in reference electrode while Yamanaka [75] investigated iridium oxide films on ITO for electrochromic display devices.

In the literature, multiple electrodeposition procedures for iridium oxide have been reported:

- **Galvanostatic deposition:** This procedure uses fixed anodic current densities to grow IrO_x films. For example, Yamanaka and Petit both used current densities ranging from 35 μA/cm² to 0.3 mA/cm² and deposition times ranging from 60 to 10,000 s[75, 76]. Elsen et al.[74] found that increasing the film thickness progressively results in less uniform and more fragile films.
- **Potentiostatic deposition:** In this method, a constant potential between 0.6 and 0.7 V/AgAgCl is applied to a static or turning electrode. It is the most suitable procedure for preparing thick layers and it is possible to roughly determine the time at which a complete iridium oxide layer is formed[74].
- **Pulsed Potential:** In this procedure, IrO_x is deposited by repeated application of short oxidizing potentials, with the layer thickness determined by the length of time for which the potential pulsing is allowed to continue. For example, Carroll et al.[82], by pulsing the potential between 0 V and 0.55 V/AgAgCl for 40 min, obtained thick, visually uniform, and reproducible IrO_x deposits that were chemically and mechanically stable in buffer solutions for months. In addition, this protocol yields films with more constricted and narrow pore structures[74].
- **Cyclic voltammetry:** Similar to pulsed depositions, exists potential sweep methods also known as cyclic growth deposition procedures, in which some parameters, such as the potential, sweep rate and number of cycles can be varied. For instance, in Elsen et al.[74]'s work, the potential was cycled between 0.7 and -0.5 V vs SCE at a sweep rate of 5 V/s to 10 V/s for microelectrodes and 1V/s to 2.5 V/s for macroelectrodes over 100 to several thousand cycles.

Feriel AIT-ALI[80] in her PhD thesis research on pH microsensors, determined that of all the IrO_x deposition procedures, cyclic voltammetry was the most suitable in terms of sensitivity and mechanical stability for pH measurements. We therefore decided to explore the same deposition protocol developed in the laboratory but for ECIS measurements.

The cyclic voltammogram of the electrodeposition of IrO_x on Au and ITO IDEs after 25 cycles is presented in Fig. 5.2. For Au IDEs, we observe that during the first cycle, the current remained relatively constant and then, at around 0.6 V/AgAgCl, it rapidly increased. According to Elsen et al. [74], this sudden rise is due to the fact that iridium oxide is being deposited. During the electrodeposition, the chemical reaction that takes place involves the oxalate complex in the Ir(IV) solution[80]:

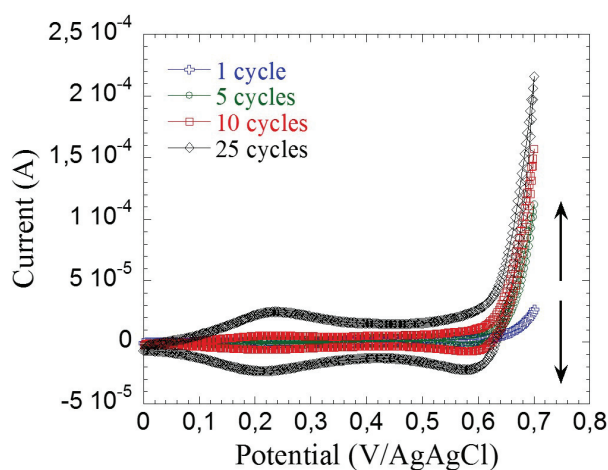


The oxalate-containing solutions are supposed to function via the oxidation of the carbon-to-carbon bond in the oxalate complex $[(\text{Ir}(\text{OH})_4(\text{C}_2\text{O}_4))]^{2-}$, resulting in carbon dioxide CO₂ and in the insoluble oxide IrO₂ that then precipitates onto the electrode. When the number of cycles increased, two redox peaks appeared within the potential range of 0.2 to 0.3 V/AgAgCl, suggesting that the deposition of IrO_x was

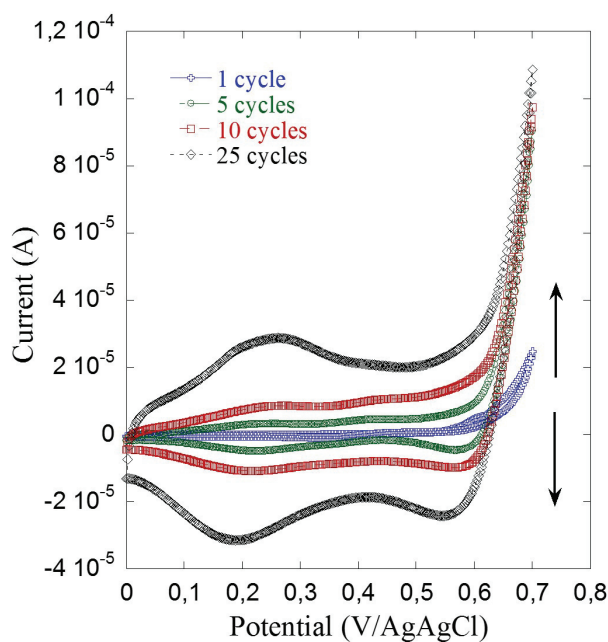
5.2. Surface-modified electrodes with IrO_x

occurring at the surface of the gold electrodes. Those peaks correspond to the reduction-oxidation of the couple Ir(IV)/Ir(V) at pH 10.5[80] and an increase in their values means that the IrO_x film is growing. For 25 cycles, Au IDEs have a peak of $-23.2 \mu\text{A}$ at 0.21 V/AgAgCl and another peak of $24.8 \mu\text{A}$ at 0.27 V/AgAgCl .

Regarding the electrodeposition on ITO IDEs, we can see a similar behavior in their voltammograms. As the number of cycles incremented, the values of the redox peaks increased. For 25 cycles, ITO IDEs have one peak of $28.7 \mu\text{A}$ at 0.26 V/AgAgCl and another peak of $-3.14 \mu\text{A}$ at 0.19 V/AgAgCl . Although, the redox peaks of ITO IDEs are slightly higher than those of Au IDEs, we found that they are visible within the same potential range, suggesting that the electrodeposition protocol can be used to modify ITO IDEs with IrO_x.



(a)



(b)

Figure 5.2 – (a) Cyclic voltammogram of IrO_x growth at pH 10.5 with 20 mV/s scan rate and cycling potential between 0 and 0.7 V Ag-AgCl on (a) Au IDEs and (b) ITO IDEs.

5.2. Surface-modified electrodes with IrO_x

Since we aim at modifying the ITO IDEs without affecting their transparency, we first had to determine the number of cycles that we were going to use for the electrodeposition by cyclic voltammetry. As shown in Fig.5.3, when the number of cycles of the CV is incremented, the total impedance at 10 Hz decreased from 4.15 k Ω to 3 k Ω , 1.9 k Ω and 1.6 k Ω for 5, 10 and 25 cycles, respectively. This could be explained by the fact, that as can be seen in Fig. 5.3b, the number of IrO_x particles covering the electrode surface increased.

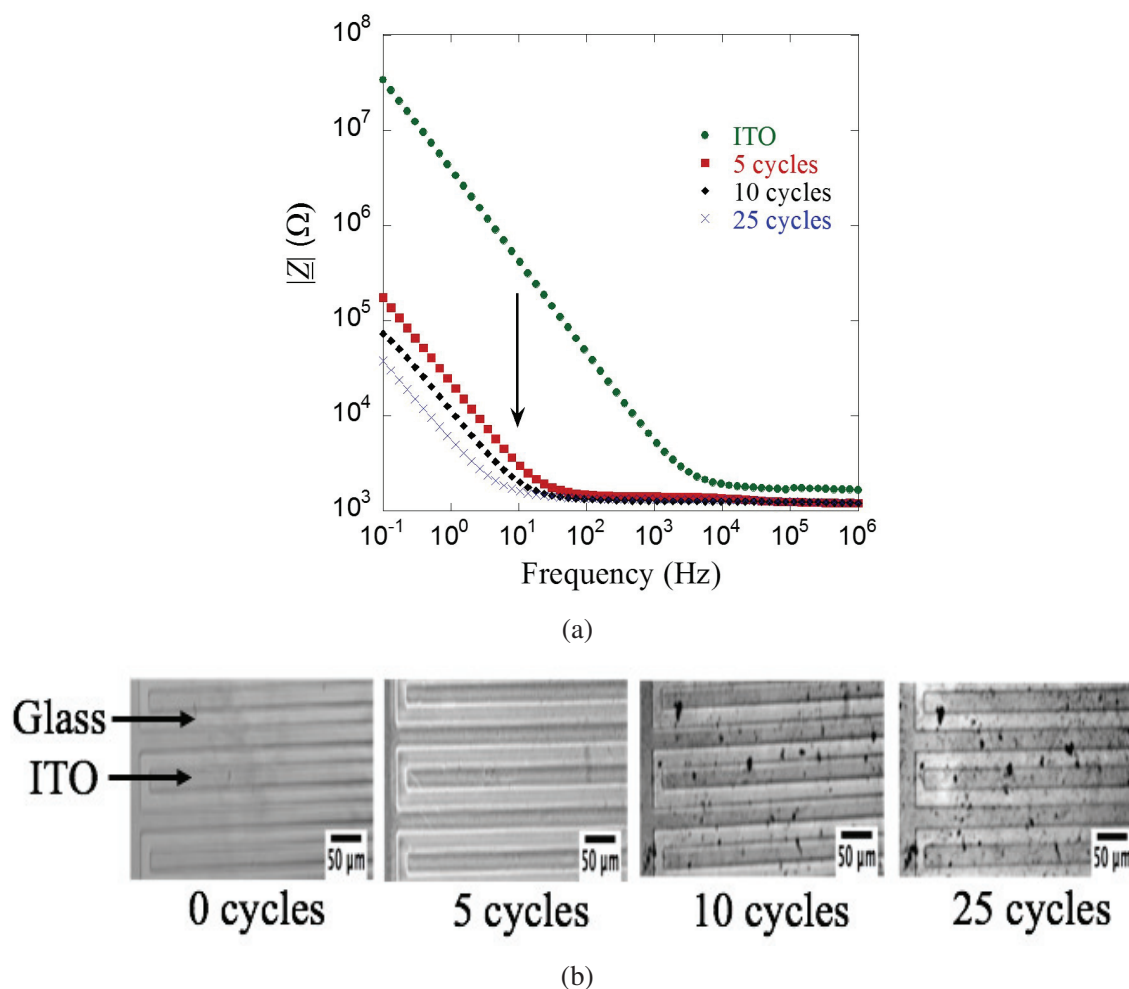


Figure 5.3 – (a) Magnitude of impedance versus frequency of ITO IDEs after different number of cycles in contact with 1 M KCl. (b) Microscopic images of ITO IDEs after electrodeposition. Magnification 10X.

5.2. Surface-modified electrodes with IrO_x

In contrast, in fig.5.4, the impedance of the ITO IDEs, which did not undergo electrodeposition but was in contact with the Ir(IV) solution, was not significantly affected by the contact time.

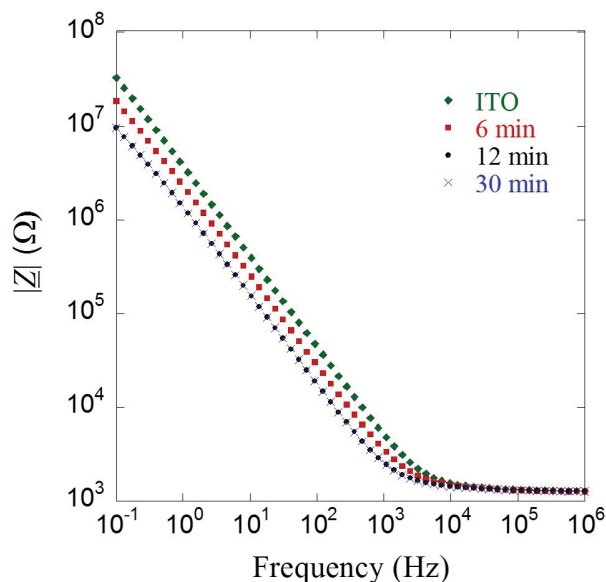


Figure 5.4 – Magnitude of impedance versus frequency of **ITO** IDEs in contact with **Ir(IV)** solution for different time intervals.

Regarding the effect of the number of cycles on the phase of the impedance in Fig.5.5, we observe that the spectrum shifted towards low frequencies as the number of cycles increased. This shift is not as significant in the spectra of the ITO IDEs that were not electrochemically modified, confirming that only being in contact with the Ir(IV) solution is not enough to modify the impedance of the ITO IDEs.

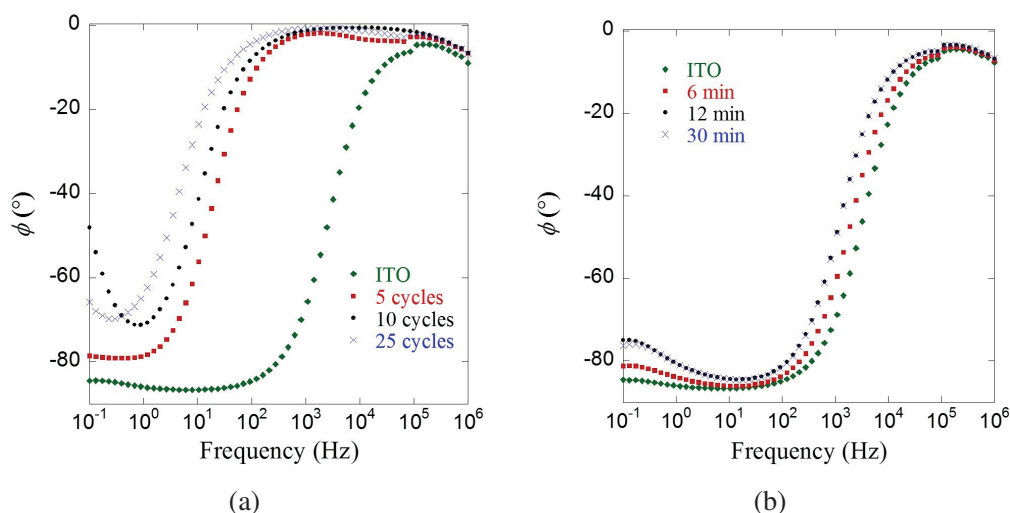


Figure 5.5 – Phase impedance spectra of **ITO** IDEs (a) after IrO_x electrodeposition and (b) after being in contact with the Ir(IV) solution without cycling potential.

5.2. Surface-modified electrodes with IrO_x

In addition, the Nyquist plot in fig.5.6 also showed the reduction of the impedance as the number of cycles increased, leading to lower values of $-Z''$ and Z' . Moreover, we found that at low frequencies $f < 3$ Hz, as the number of cycles incremented, the spectra tilted over and curved towards the Z' axis. This effect could be associated with the surface modification by the IrO_x coating, which affects the interfacial impedance. In addition, at high frequencies from 65 kHz to 4.2 Hz we saw that Z' shifted towards lower values and, particularly at 5 cycles, formed a high frequency Nyquist semi-arc, which could be associated with a coating response[86]. Nevertheless, this semi-arc disappeared from the diagram for 10 and 25 cycles. We could hypothesize that this semi-arc represents a transitional state of the coating only visible after 5 cycles before more particles are deposited as the number of cycles increases. This could be confirmed with further studies about surface composition, such as X-ray photoelectron spectroscopy (XPS), in which differences in composition of the coating using 5 cycles could explain the transitional state visible in the Nyquist plot at high frequencies.

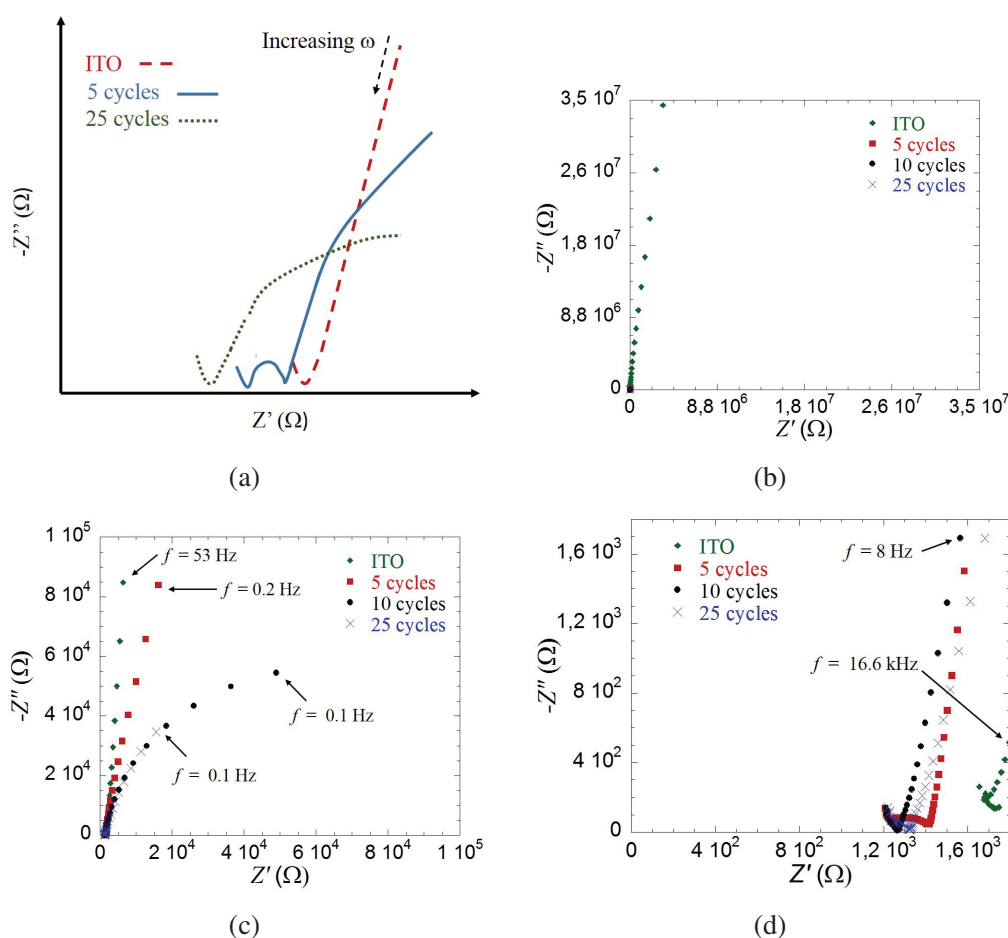


Figure 5.6 – (a) Sketch of the Nyquist plot of ITO IDEs after different IrO_x coating cycles. Nyquist representation of the ITO IDEs after different IrO_x coating cycles and in contact with **100 mM KCl** in the frequency range from (b) 1 MHz to 100 mHz, (c) from 1 MHz to 53 Hz and (d) from 1 MHz to 18 Hz.

5.2. Surface-modified electrodes with IrO_x

Additionally, using equivalent circuit modeling we determined the electrical parameters for the ITO IDEs in contact with 100 mM KCl solution for the different cycles and the results are listed in table 5.1. We found that as the number of cycles increased, $C_{parasitic}$ remained nearly constant, R_t slightly decreased after 5 cycles but then it stayed relatively constant. Even though it is accepted that roughness decreases high frequency impedance[6, 87], the decrease of R_t could be explained by the fact that due to the band structure of iridium oxide, one should expect the oxide to switch its conductivity from low to high upon oxidation[88]. Therefore, this change in the conductivity of the electrode material could decrease the resistive behavior. In contrast, Q_{int} clearly increased from $51.6 \times 10^{-9} \text{ s}^\alpha \cdot \Omega^{-1}$ to $4.7 \times 10^{-5} \text{ s}^\alpha \cdot \Omega^{-1}$ whereas α_{int} decreased from 1 to 0.847. This is coherent with what we observed in Fig. 5.7, in which the topology of the electrodes changed after EIROF deposition. These AFM measurements on $2\mu\text{m} \times 2\mu\text{m}$ areas confirmed that IrO_x actually increased the electrode roughness from RMS = 6 nm (ITO IDEs) to RMS = 19.4 nm (IrO_x/ITO IDEs).

Cycles	$C_{parasitic}$ (pF)	R_t (Ω)	CPE_{int}	
			Q_{int} ($\text{ns}^\alpha \cdot \Omega^{-1}$)	α_{int}
0	17.2	1720	51.6	1
5	16.2	1220	8490	0.915
10	15.4	1210	20400	0.836
25	16.1	1230	40700	0.847

Table 5.1 – Impedance fitting results of the ITO IDEs in contact with 100 mM KCl for different electrodeposition cycles.

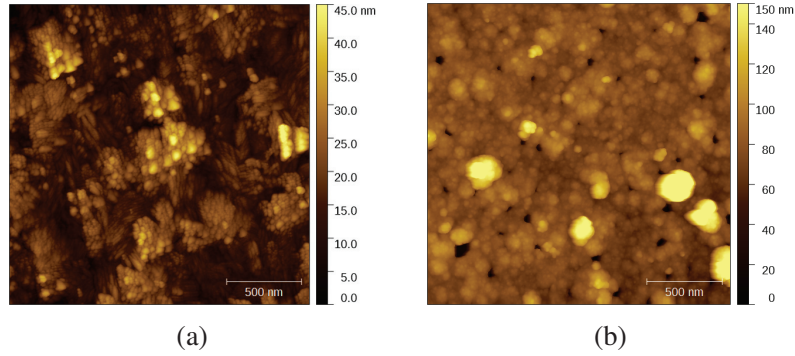


Figure 5.7 – AFM images of the ITO IDEs surface (a) before and (d) after IrO_x on $2\mu\text{m} \times 2\mu\text{m}$ areas.

We then focused on the parameters of CPE_{int} and the equation 4.11 to compute the interfacial impedance Z_{int} at 10 Hz for each cycle, as shown in Fig. 5.8 (~ 10 Hz corresponds to f_{peak} of IrO_x/ITO IDEs in contact with cells detailed later in this chapter). We observed that Z_{int} decreased from 2.9 M Ω to 22 k Ω , 10.5 k Ω and 5.1 k Ω for 5, 10 and 25 cycles, respectively. This is coherent with the literature where modifying the electrode surface helped reduce the interfacial impedance of small electrodes[67, 17]. Although we found the lowest interfacial impedance with 25 cycles, we chose 10 cycles because we believed there is a trade-off between a low interfacial impedance and the transparency of the material. As can be seen in Fig.5.3 after 10 cycles, the transparency of ITO seemed to be adversely affected by the coating.

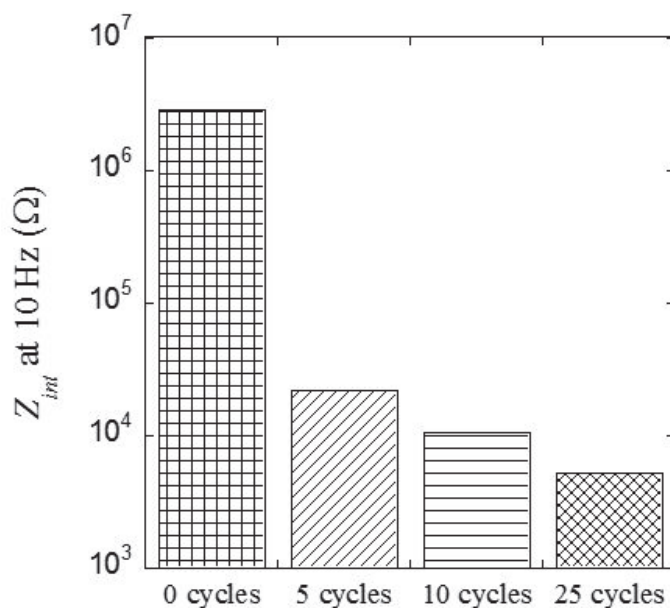
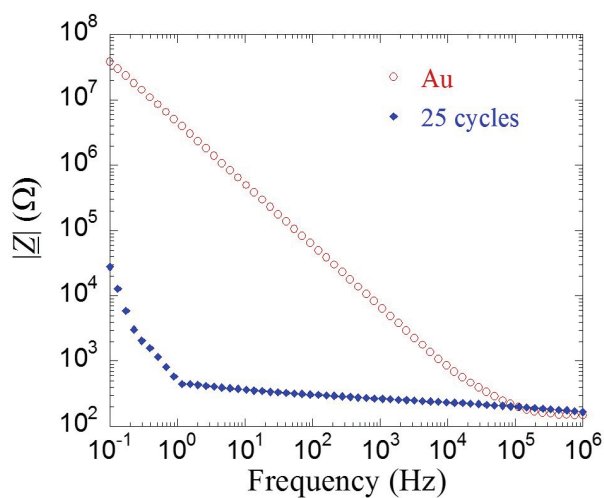


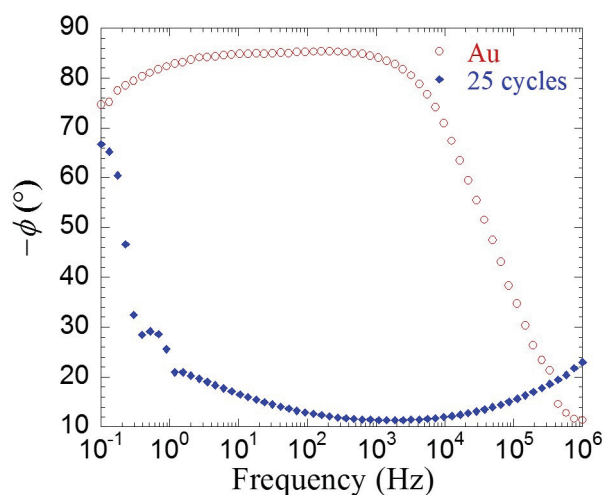
Figure 5.8 – Z_{int} at 10 Hz for the ITO IDEs before and after 5, 10 and 25 cycles of coating. Measurements carried out in 100 mM KCl solution.

5.2.2 Modified electrodes in cell culture medium

In this section, we explored the response of Au and ITO IDEs coated with CN/BSA and modified with IrO_x in contact with the supplemented DMEM, which is the solution used to keep the cells alive during the ECIS experiments. For IrO_x/Au IDEs, the magnitude and the phase of the impedance versus frequency are shown in Fig. 5.9. We can see that $|Z|$ at 10 Hz decreased from 496 k Ω to 365 Ω and the cut-off frequency f_{low} was significantly reduced from ~ 112 kHz to ~ 2 Hz. This is coherent with the literature where previous studies[68, 81, 82, 83, 84] have reported that the benefit of IrO_x is in decreasing the electrode impedance. Moreover, as mentioned in Chapter 3, according to Ibrahim et al.[89], by shifting f_{low} towards lower frequencies we are minimizing the influence of the interfacial double layer on the total impedance, leading to an enhanced electrode sensitivity. Regarding the phase spectrum, after 25 cycles, the capacitive plateau ($\rightarrow 85^\circ$) of Au IDEs without IrO_x disappears from our experimental frequency range due to the f_{low} shift and most of the spectrum reveals an almost resistive behavior with $\phi \sim -10^\circ$.



(a)



(b)

Figure 5.9 – (a) Magnitude and (b) Phase impedance spectra of **Au** IDEs before and after IrO_x electrodeposition in contact with **the supplemented DMEM**.

We present the Nyquist plots in Fig. 5.10. We observe that the coating drastically reduced the $-Z''$ and Z' values and slightly shifted the spectrum to the right. In the Au IDEs spectrum we identified three regions with different slopes. First region (i) with a slope of 3.7 from 1 MHz to 21.8 kHz. Then, a second segment (ii) with a slope of 12.8 from 21.8 kHz to 92 Hz and one third zone (iii) at low frequencies ($f < 92$ Hz) with 10.6 as slope value. After 25 cycles, the spectrum tilted towards the Z' axis and we identified two parts in the spectrum with lower slopes. The first part corresponds to the frequency range over 200 Hz to 0.2 Hz with a slope of 0.6 and a second region with a slope of 2.6 at low frequencies ($f < 0.4$ Hz).

5.2. Surface-modified electrodes with IrO_x

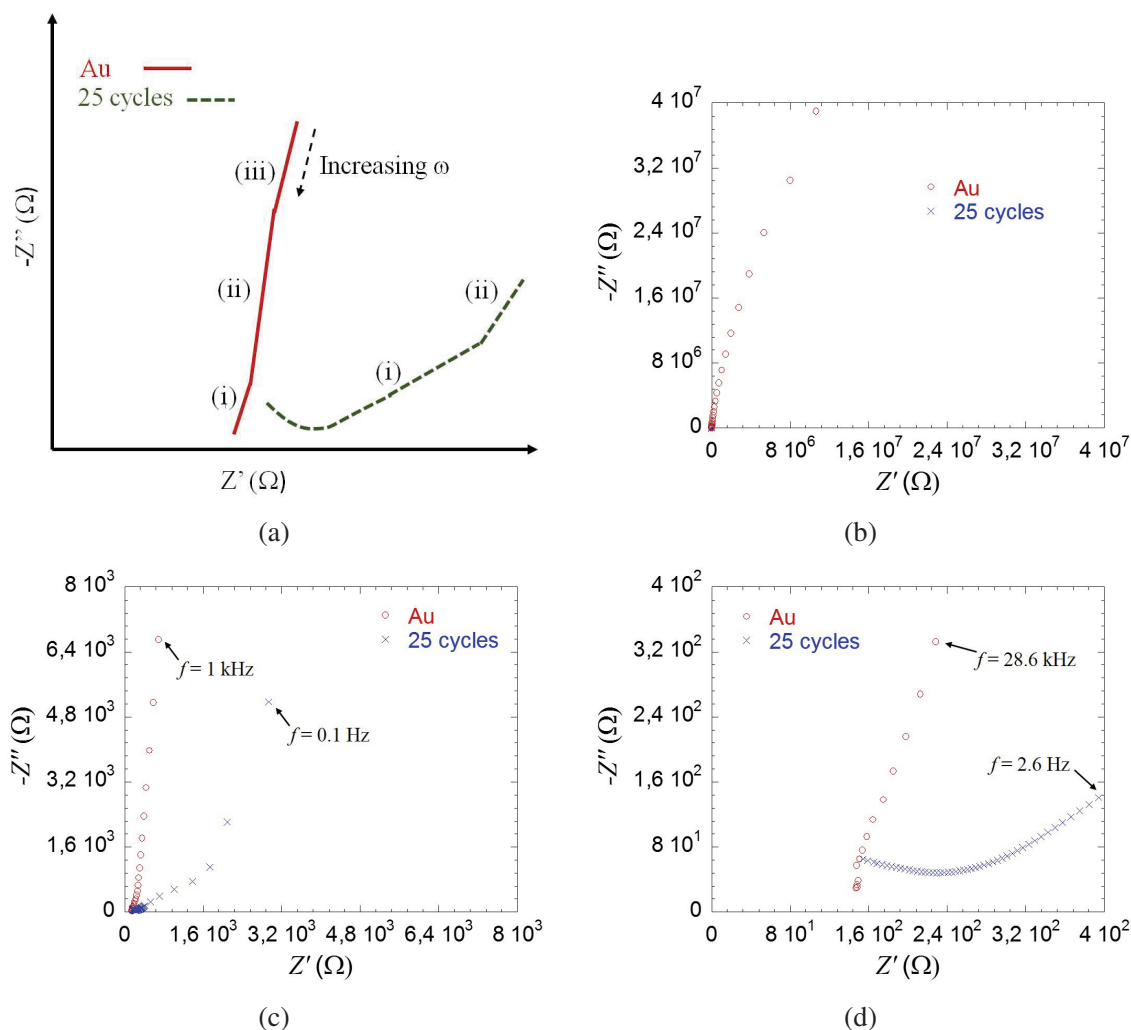


Figure 5.10 – (a) Sketch of the Nyquist plot of **Au** IDEs before and after 25 cycles of cyclic voltammetry. Nyquist representation of the **Au** IDEs before and after 25 cycles of IrO_x coating and in contact with **the supplemented DMEM** in the frequency range from (b) 1 MHz to 100 mHz, (c) from 1 MHz to 1 kHz and (d) from 1 MHz to 28.6 kHz.

In the case of IrO_x modified ITO IDEs, the Bode representations are shown in Fig.5.11. We can see that similar to Au IDEs, after the IrO_x coating, the magnitude of the impedance $|Z|$ at 10 Hz decreased from 241 k Ω to 4.3 k Ω and the cut-off frequency f_{low} was reduced from ~ 1.4 kHz to ~ 20 Hz. As for the phase plot, the spectrum shifted towards lower frequencies and the capacitive plateau ($\rightarrow 80^\circ$) became invisible in our frequency range due to f_{low} shifting.

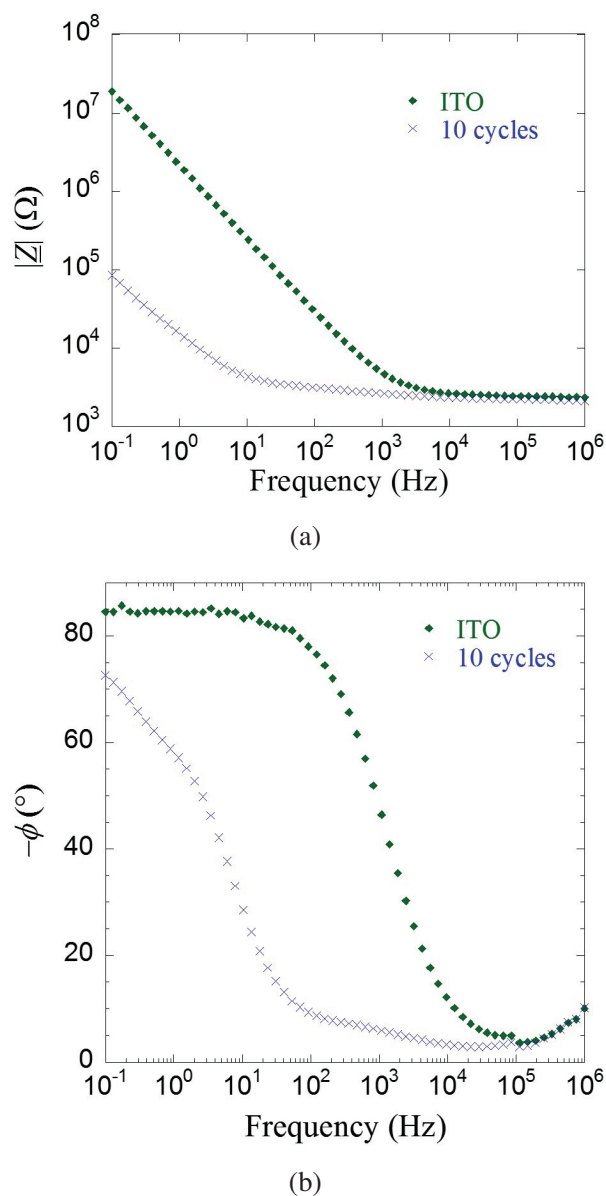


Figure 5.11 – (a) Magnitude and (b) Phase impedance spectra of **ITO IDEs** before and after IrO_x electrodeposition in contact with **the supplemented DMEM**.

Additionally, we presented the Nyquist plots of the same IDEs in Fig. 5.12 where we found that the coating significantly reduced the $-Z''$ and Z' values, and that it affected the slopes of the spectrum. Before 10 cycles, we identified two regions in the spectrum of the ITO IDEs : (i) at mid-frequencies from 21.8 kHz to 1 kHz with a slope of 4.4 and (ii) at low frequencies (< 1 kHz) with a slope of 10.7. Then, after depositing the IrO_x, we identified three regions in the spectrum: (i) from 12.7 kHz to 31 Hz with a slope of 0.4. Another zone (ii) from 31 Hz to 230 mHz with a slope of 2.7 and a third region at really low frequencies (< 230 mHz) with a slope of 4.6.

5.2. Surface-modified electrodes with IrO_x

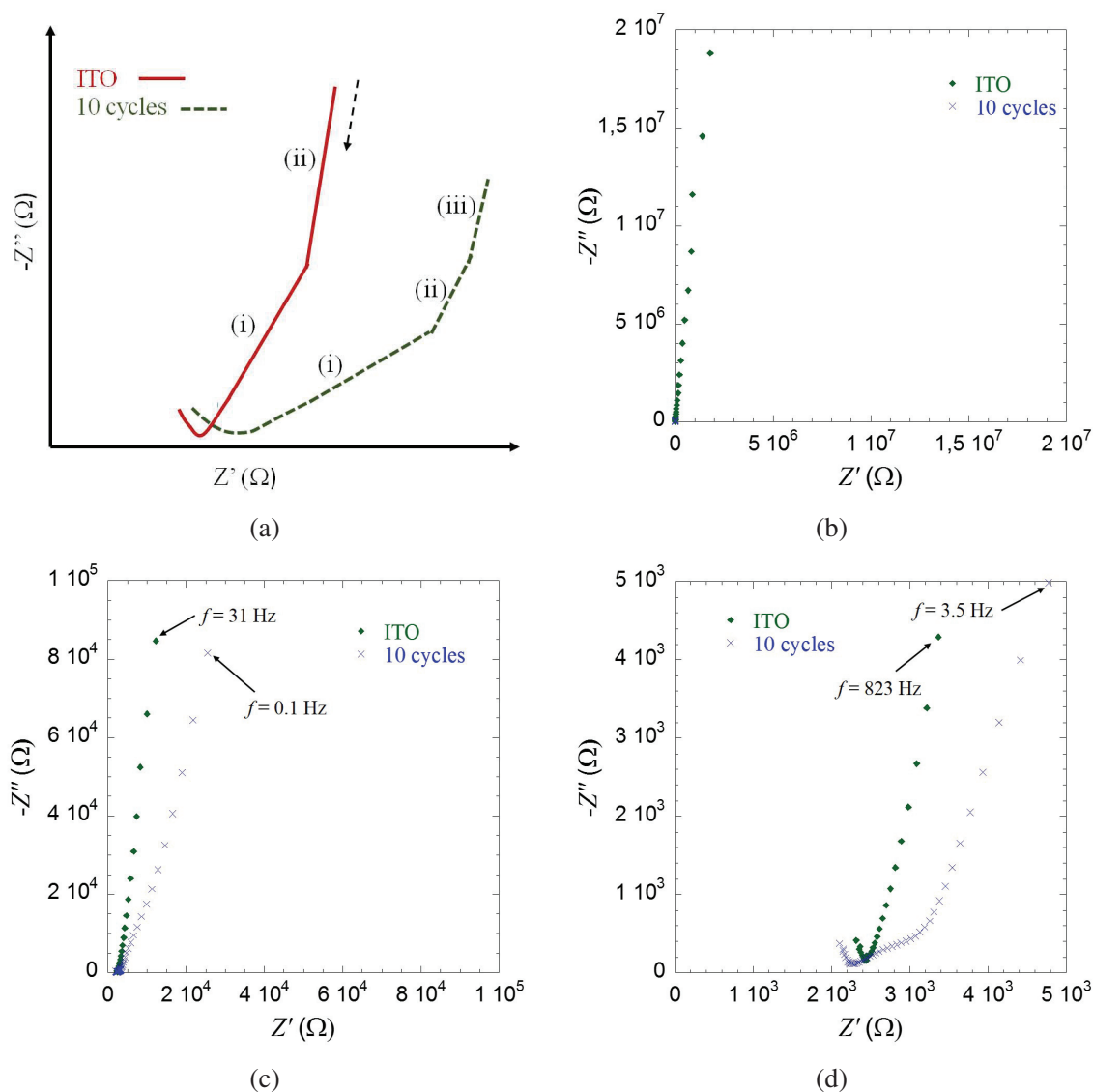


Figure 5.12 – (a) Diagram of the Nyquist plot of **ITO** IDEs before and after 10 cycles of cyclic voltammetry. Nyquist representation of the **ITO** IDEs before and after 10 cycles of IrO_x coating and in contact with **the supplemented DMEM** in the frequency range from (b) 1 MHz to 100 mHz, (c) from 1 MHz to 31 Hz and (d) from 1 MHz to 823 Hz.

In this section we have seen that electrodeposition of IrO_x had similar effects on both materials Au and ITO. We found in Bode plots that the coating helps to decrease the electrode impedance and that by shifting f_{low} , the interfacial contribution is reduced. Although the spectra in the Nyquist plots are quite similar, the reduction of the impedance is not the same for both materials due to the difference in electrodeposition cycles. IrO_x/Au IDEs impedance decreased almost 1,300 times the initial impedance while IrO_x/ITO decreased 56 times the initial impedance before coating.

5.2.3 Electrical parameters in cell culture medium

We focused on the effect of IrO_x on the electrical properties of the ECIS system using equivalent circuit modeling. Table 5.2 shows the electrical parameters of the system, extracted using the fitting model 2, before and after the surface modification with IrO_x. In order to compare each parameter, we did a *t-test* to find statistically significant differences between each parameter for both materials. Fig. 5.13 shows the comparison of each parameter before and after coating on Au IDEs and Fig. 5.14 on ITO IDEs. Although it is commonly accepted that roughness decreases high frequency impedance[6, 87], we observe that R_t for Au IDEs increased whereas R_t for ITO IDEs did not change. This increment might be due to protein adsorption on the surface of the electrode. It has been found that IrO_x electrodeposited material has a large affinity for proteins and other organic molecules in the cell culture medium than for water or for purely ionic media such as sodium chloride solutions[73]. This might explained why we did not see this effect in impedance measurements with 100 mM KCl which do not contain proteins. Regarding the ITO IDEs, we suggest that its high resistive behavior could mask this variation of R_t after IrO_x coating. Furthermore, as expected, the parameters of CPE_{int} for both materials were affected by the iridium oxide. Q_{int} for Au IDEs increased approximately 371 times after the coating whereas α_{int} decreased. Similarly, Q_{int} for ITO IDEs also incremented 255 times after coating and α_{int} decreased. This confirms that the electrodeposition clearly affects the interfacial contribution to the overall impedance of the ECIS system. We then computed the interfacial impedance at 10 Hz using the parameters of CPE_{int} and equation 3.8, as shown in Fig. 5.15. We found the same effect as in the case of Au and ITO IDEs in contact with 100 mM KCl solution, where the IrO_x coating decreased the interfacial impedance. In this case, the Z_{int} of IrO_x/Au IDEs was almost 128 times lower than that of Au IDEs without coating while the Z_{int} of IrO_x/ITO IDEs was 124 times lower than that of Au IDEs without coating.

Material	$C_{parasitic}$ (pF)	R_t (Ω)	CPE_{int}	
			Q_{int} ($ns^\alpha \cdot \Omega^{-1}$)	α_{int}
Au	185 ± 18	126 ± 4	133 ± 23	0.960 ± 0.003
IrO _x /Au 25 cycles	195 ± 23	185 ± 11	49400 ± 10500	0.745 ± 0.040
ITO	14 ± 1	1840 ± 71	84 ± 8	0.936 ± 0.009
IrO _x /ITO 10 cycles	16.6 ± 2.5	1840 ± 154	21400 ± 4200	0.795 ± 0.065

Table 5.2 – Impedance fitting results of the **Au** and **ITO** IDEs in contact with **the supplemented DMEM** before and after IrO_x electrodeposition. n=5 for IrO_x/Au, n=5 for Au, n=4 for IrO_x/ITO and n=8 for ITO (Mean ± SD).

5.2. Surface-modified electrodes with IrO_x

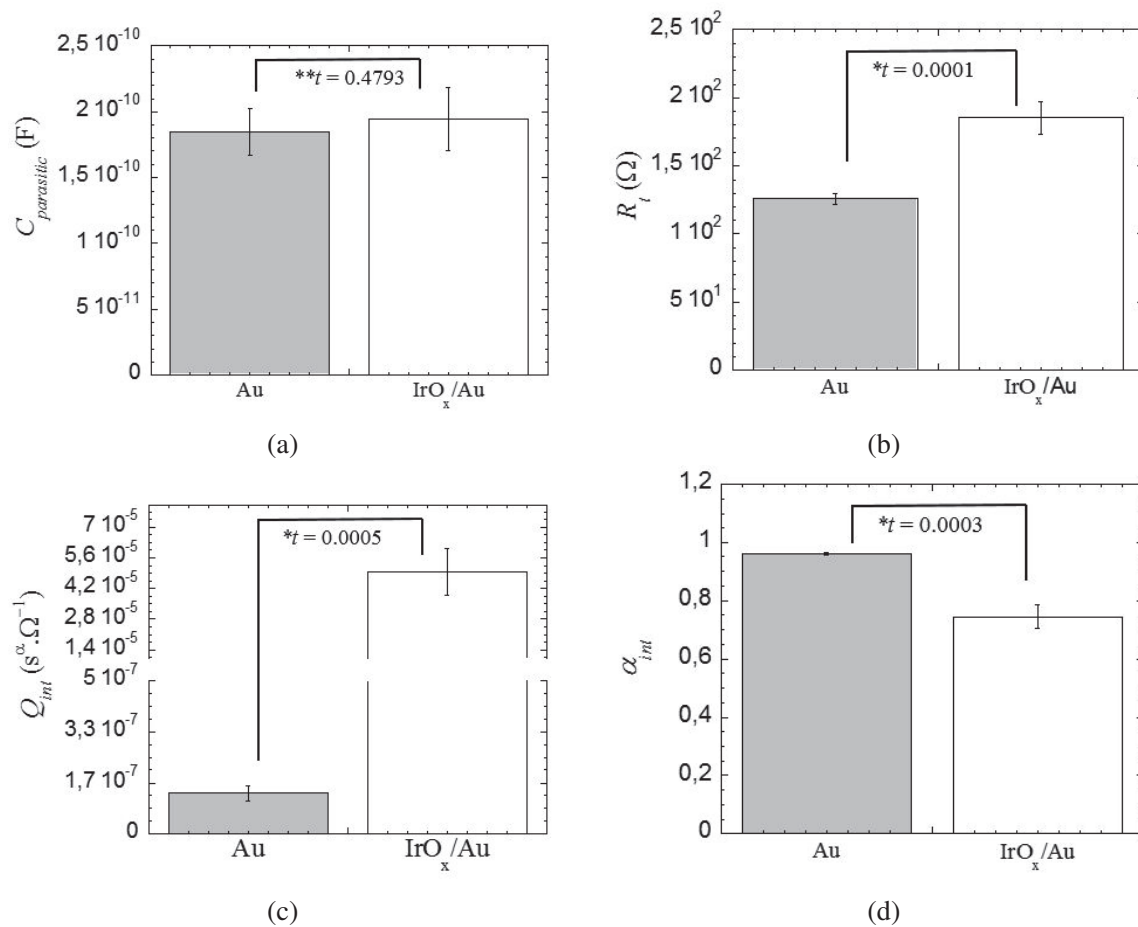


Figure 5.13 – Comparison of the electrical parameters of the **Au** IDEs coated with CN/BSA and in contact with **the supplemented DMEM** before and after 25 cycles of IrO_x: (a) $C_{parasitic}$ (b) R_t (c) Q_{int} and (d) α_{int} . Error bars are the standard deviation with n=5 for IrO_x/Au and n=5 for Au. * : Significantly different and ** : Not significantly different.

5.2. Surface-modified electrodes with IrO_x

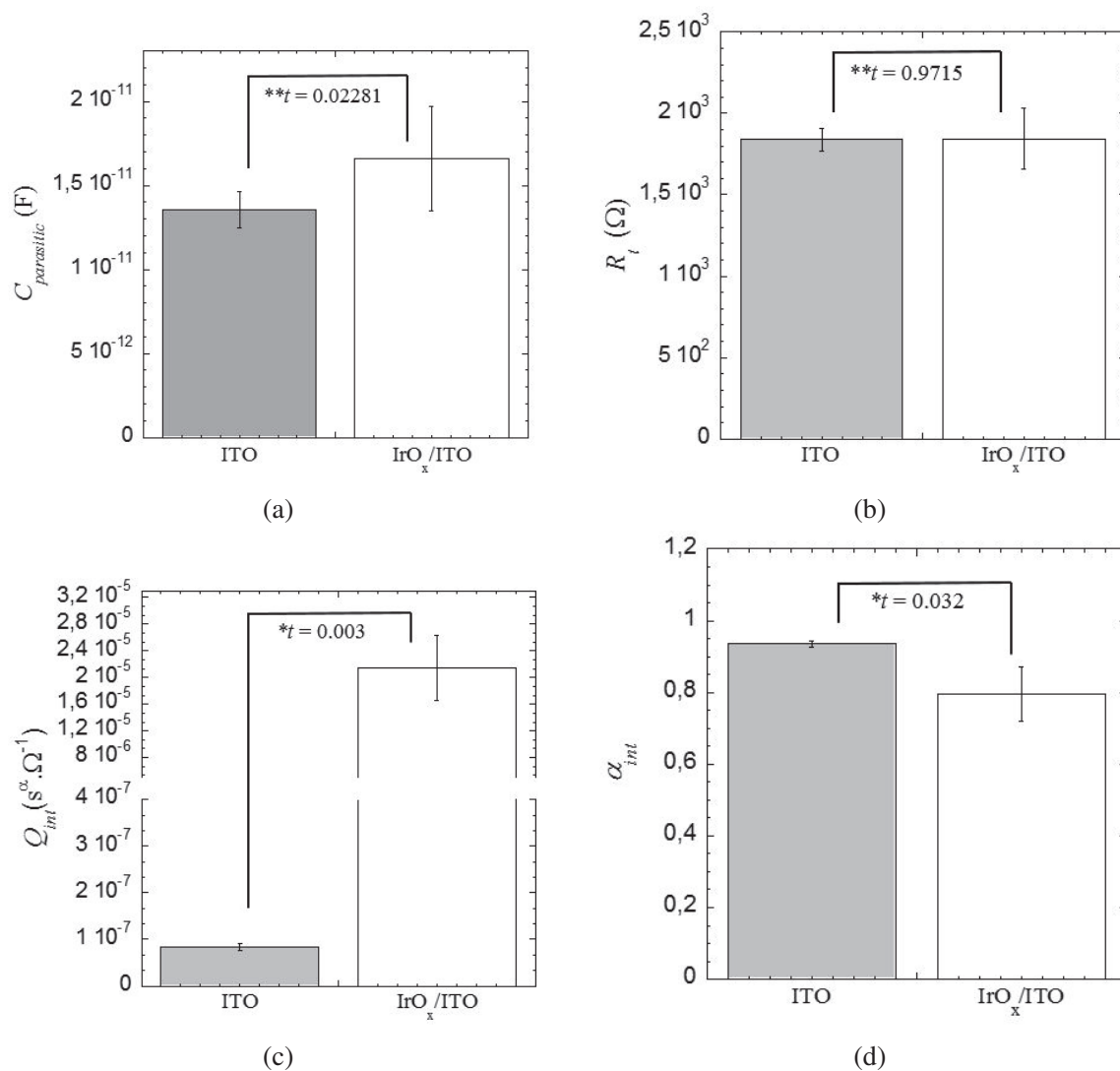
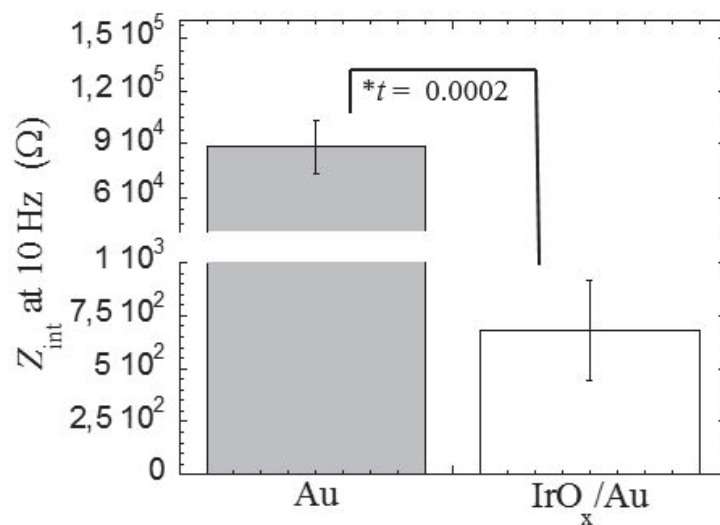
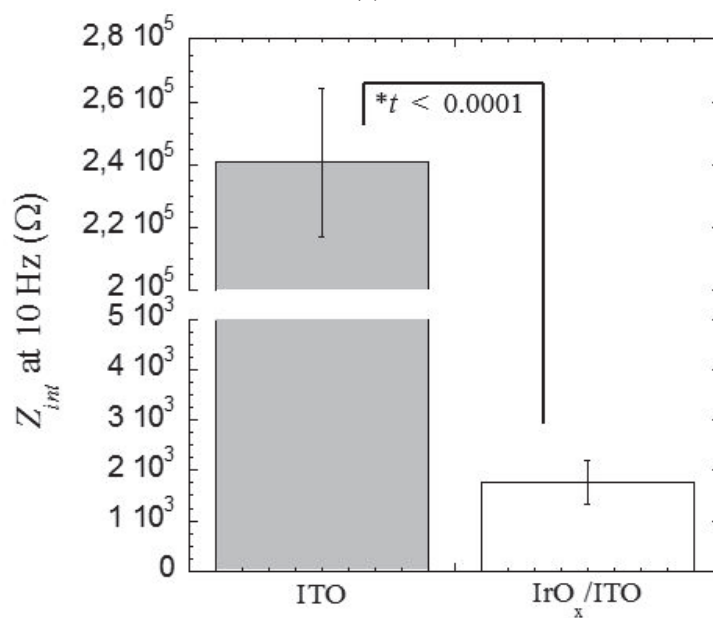


Figure 5.14 – Comparison of the electrical parameters of the **ITO** IDEs coated with CN/BSA and in contact with **the supplemented DMEM** before and after 10 cycles of IrO_x: (a) $C_{parasitic}$ (b) R_t (c) Q_{int} and (d) α_{int} . Error bars are the standard deviation with n=4 for IrO_x/ITO and n=8 for ITO. * : Significantly different and ** : Not significantly different.



(a)



(b)

Figure 5.15 – Z_{int} at 10 Hz for (a) the **Au** IDEs before and after 25 cycles and (b) the **ITO** IDEs before and after 10 cycles. Both electrodes in contact with **the supplemented DMEM**. Error bars correspond to the standard deviations with $n = 5$ for IrO_x/Au and Au; $n = 4$ for IrO_x/ITO and $n = 8$ for ITO. * : Significantly different and ** : Not significantly different.

5.3 Monitoring cell growth with IrO_x modified ITO IDEs

In the previous sections, we confirmed that we could significantly decrease the interfacial impedance of the ITO IDEs using 10 deposition cycles of IrO_x without affecting the transparency of the electrodes for monitoring cells. In this section, we show the impedance results of these IrO_x modified ITO electrodes in contact with MCF-7 cells proliferating on the surface.

5.3.1 Impedance response of IrO_x/ITO in contact with cells

In this case, we followed the proliferation of MCF-7 cells on top of IrO_x/ITO IDEs using phase contrast microscopy, as shown in Fig. 5.16. At $t = 6$ h, most of the cells had a round shape and had not completely adhered to the surface, which was covered 65 %. It was only at $t = 21$ h that MCF-7 cells began to spread covering 72 % of the electrode surface. As time went on, MCF-7 cells continued to proliferate increasing the cell coverage ratio η from 72 % to 94 %, corresponding to a culture time of $t = 52$ h. Visually, we found no differences in the proliferation process compared to the images shown in Chapter 3 for the experiments carried out with Au IDEs and ITO IDEs. This is coherent with previous studies, where it was demonstrated that IrO_x enabled neuronal adhesion and survival with elongation of axons and dendrites[73, 90].

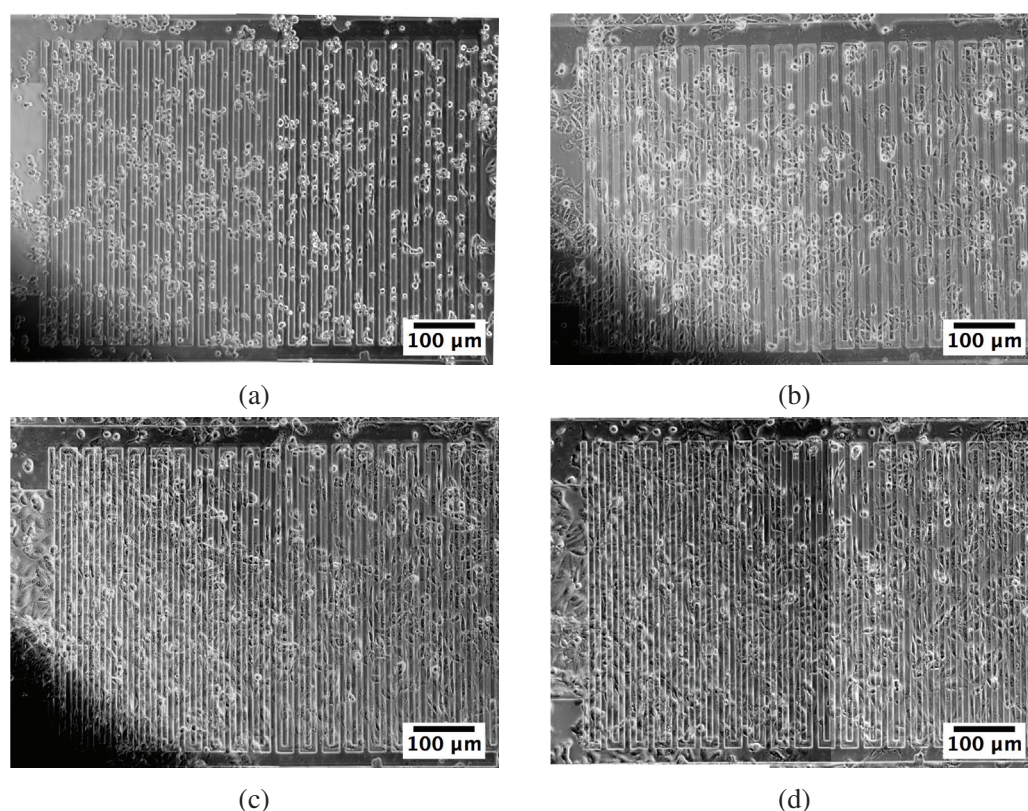


Figure 5.16 – Phase contrast micrographs of MCF-7 cells on the surface of IrO_x/ITO IDEs at 10X magnification (Leica D2000): (a) $t = 6$ h, $\eta = 65$ %; (b) $t = 21$ h, $\eta = 72$ %; (c) $t = 30$ h, $\eta = 80$ %; (d) $t = 52$ h, $\eta = 94$ % (20 600 cells were injected).

5.3. Monitoring cell growth with IrO_x modified ITO IDEs

Additionally, in Fig. 5.17 we showed the Bode representation of the growth of a cell monolayer on top of the IrO_x/ITO IDEs. We observed that the impedance increased over the frequency range 335 kHz to 100 mHz. Then, at higher frequencies (> 335 kHz), the impedance did not appear to be influenced by the cell monolayer. For the phase angle, it increased over the range 100 mHz to 8 Hz and finally decreased at higher frequencies (> 8 Hz). Similar to the graph of MCF-7 growing on ITO IDEs, the phase angles obtained at high frequencies were closer to 0° compared to those at lower frequencies, revealing a more resistive behavior at high frequencies due the cells covering the electrodes. Regarding the Nyquist plots in fig.5.18, we identified 4 zones in the spectra, as depicted in Fig.5.18a: (I) A first part consisting of a semicircular arc from 1 MHz to ~ 9.6 kHz associated with $C_{parasitic}$ and the conductivity of the supplemented DMEM. Half of the semicircular arc is not completely visible within the frequency range of measurement. (II) A second zone from 9.6 kHz to 53 Hz for the electrodes before cell injection, but as the cells proliferated on the surface, we observed that this zone got wider and the slope slightly increased from 0.91 (without cells) to 1.2 ($\eta=94\%$). (III) A third part of the spectrum with decreasing slopes from 3.1 (without cells) to 2.1 ($\eta=94\%$) as cells grew on the surface. Finally, we found a fourth zone (IV) that it was only visible in the spectra of the IDEs without cells and in the curve of $\eta=65\%$ sharing similar slopes of approximately 6.6. It appeared to be that as cell proliferation continued, the third zone increased so that the fourth zone was out of the frequency range (< 100 mHz).

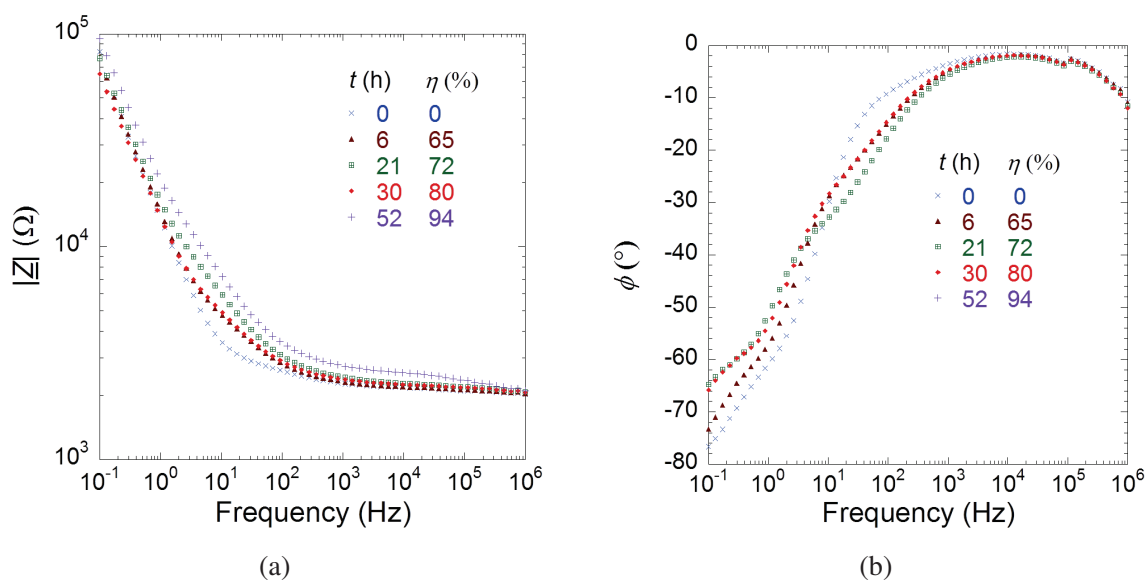


Figure 5.17 – (a) Magnitude and (b) Phase of impedance of IrO_x/ITO IDEs in contact with MCF-7 cells.

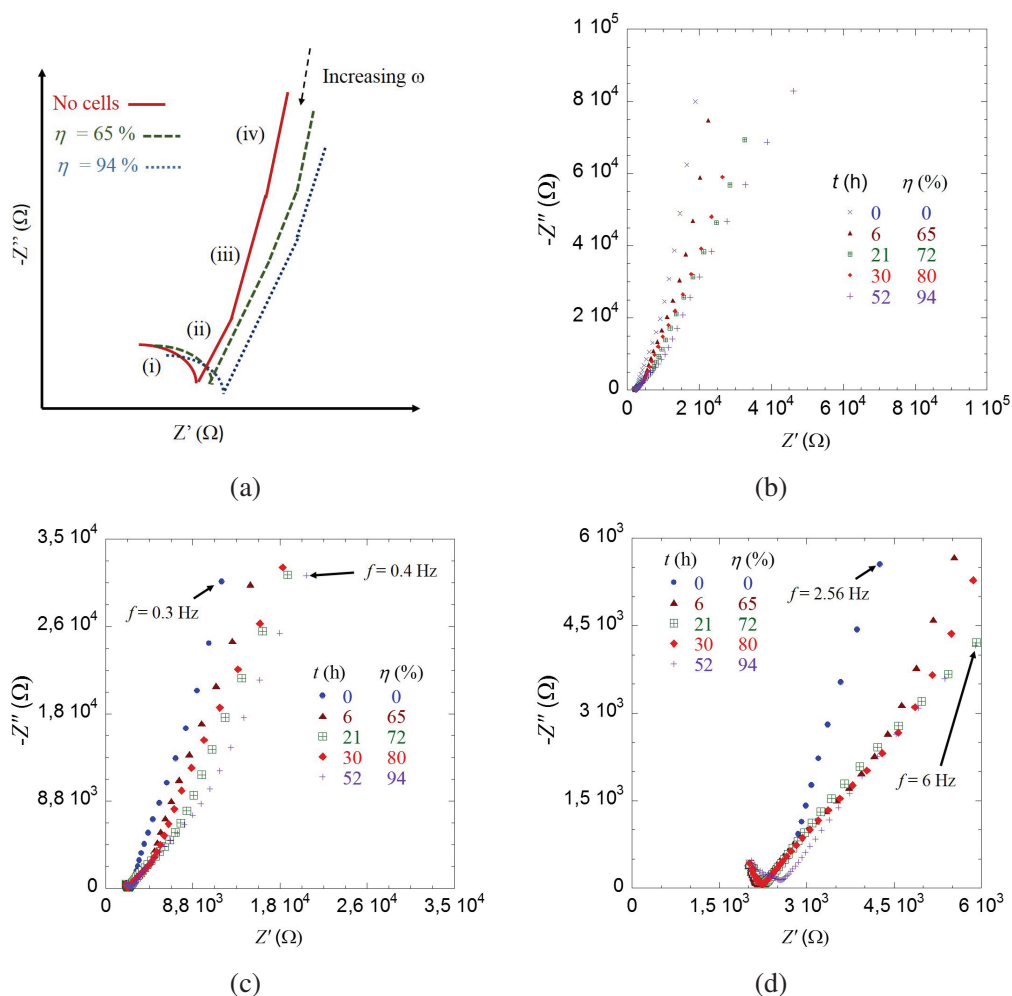


Figure 5.18 – (a) Sketch of the Nyquist plots for MCF-7 cells proliferating on IrO_x/ITO IDEs. Nyquist representation of the IrO_x/ITO IDEs covered with MCF-7 cells in the frequency range from (b) 1 MHz to 100 mHz, (c) from 1 MHz to 0.4 Hz and (d) from 1 MHz to 6 Hz.

5.3.2 Normalized impedance

In Fig. 5.19 we compared the normalized impedance of the modified electrodes with those of Au and ITO electrodes covered by a cell monolayer of MCF-7. We found that coating the ITO IDEs with IrO_x increased and shifted the peak of Z_{norm} from 0.27 at 5.5 kHz to 1.7 at 8 Hz. This increase of almost 6 times the Z_{norm} value without IrO_x could be explained by the fact that the coating reduced the interfacial impedance of the ITO IDEs, leading to an enhancement of the sensitivity of the ECIS measurement. In addition, we found that using IrO_x we could obtain a Z_{norm} maximum value that is closer to that of Au IDEs as shown in Chapter 3 ($Z_{norm} = 1.22$ at 65 kHz). Based on this, one could conclude that using IrO_x modified ITO IDEs for ECIS experiments is a promising strategy because these electrodes not only provide transparency but they also have a sensitivity similar to that of gold, which is the standard electrode material in ECIS.

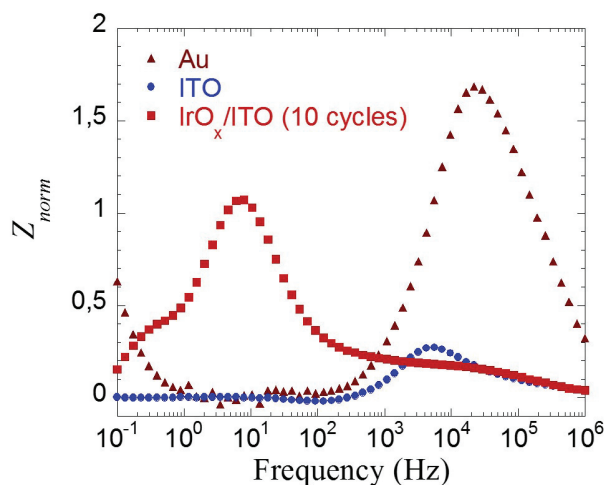


Figure 5.19 – Normalized impedance of MCF-7 cells grown on ITO IDEs, IrO_x/ITO IDEs and Au IDEs. ($\eta = 99\%$ for Au, $\eta = 96\%$ for ITO and $\eta = 94\%$ for IrO_x/ITO).

5.3.3 Equivalent circuit model of MCF-7 cells adhered on IrO_x/ITO IDEs

Similarly to Chapter 3, we used model 3 to extract the electrical parameters of the IrO_x/ITO IDEs covered with MCF-7 cells, as shown in Fig. 5.20. Here, we observe clear trends for each of the parameters. During cell proliferation, Q_{int} and α_{int} remained relatively constant. Regarding the element CPE_{cells} , we observe that Q_{cells} increased from $2.8 \times 10^{-5} \text{ s}^\alpha/\Omega$ to $4 \times 10^{-5} \text{ s}^\alpha/\Omega$ which is associated with the increasing number of cells covering the interdigitated electrodes. α_{cells} slightly decreased from 0.55 to 0.45 during cell proliferation. The parameter R_{extra} clearly increased from 2.5 k Ω to 15 k Ω suggesting that new cell-to-cell junctions and cell adhesions were formed during cell culture. On the other hand, R_{intra} increased from 48 Ω to 158 Ω , which is the opposite trend that we observed for ITO IDEs covered with MCF-7 cells. This is probably due to a different cytoskeleton reorganization of the MCF-7 cells in contact with IrO_x which we could not observe before for the ITO IDEs due to their high interfacial impedance. However, supplementary experiments with cytoskeleton staining need to be carried out to confirm the cause of this trend. Regarding R_t , during the cell proliferation its value remained around 2 k Ω .

5.3. Monitoring cell growth with IrO_x modified ITO IDEs

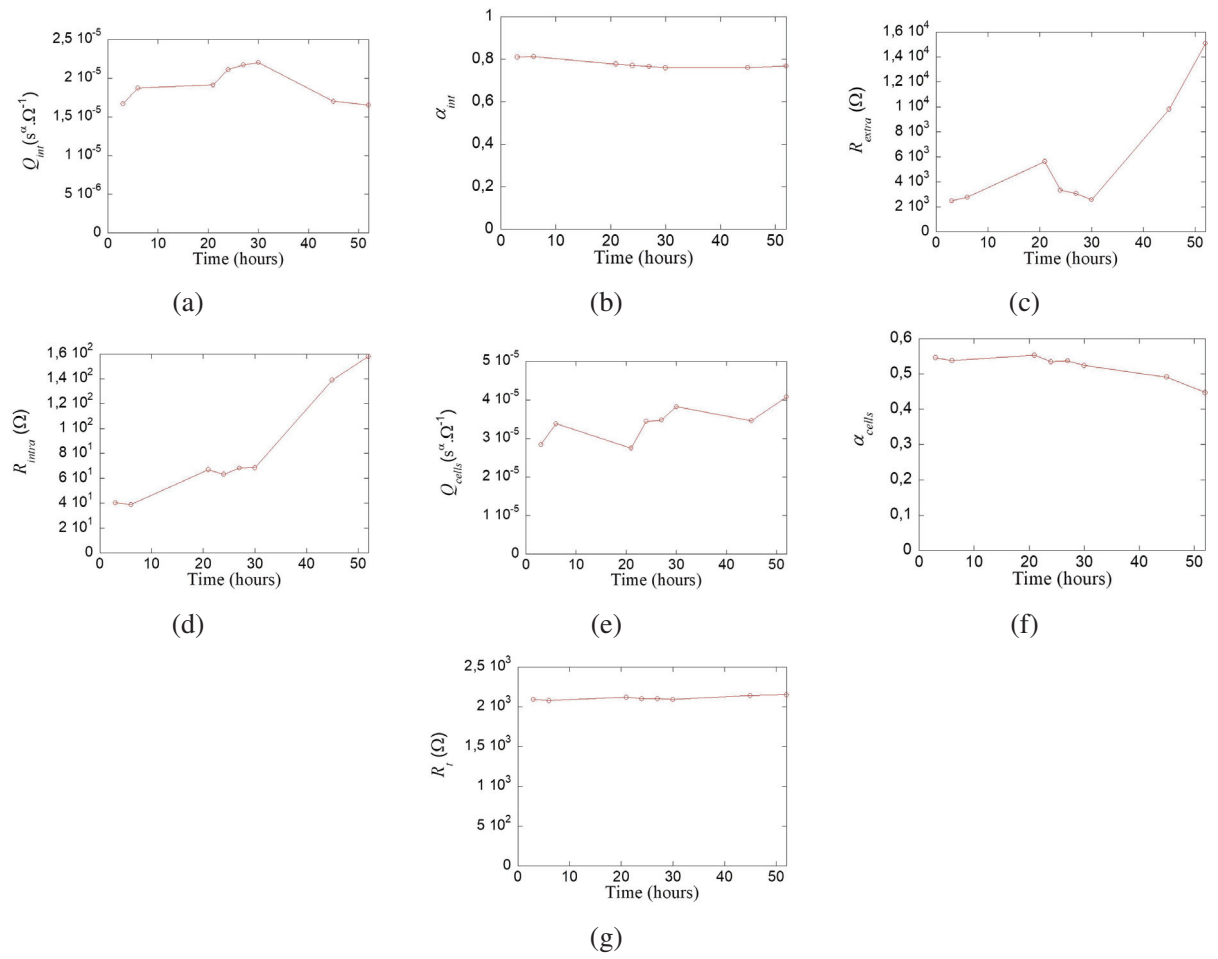


Figure 5.20 – Temporal evolution of the extracted parameters of MCF-7 cells on IrO_x /ITO IDEs: (a) Q_{int} , (b) α_{int} , (c) R_{extra} , (d) R_{intra} , (e) Q_{cells} , (f) α_{cells} and (g) R_t .

5.4 Conclusion

In this chapter we showed a range of possible high surface area coatings capable of modifying the impedance of the small electrodes used specifically for neural and stimulation applications, where the high impedance of the microelectrodes is a critical issue. From the several coatings reported in the literature, we decided to deposit IrO_x on the surface of our ITO IDEs. As we wanted to keep the transparency of the electrodes for a better visualization of the cells during the ECIS experiments, we therefore tested several deposition cycles and we found a good trade-off between transparency and impedance reduction using 10 cycles.

We characterized the electrical response of the ITO IDEs in contact with KCl solution and in contact with the supplemented DMEM before and after 10 cycles. In both cases, we found that the main effect of the coating was to significantly reduce the interfacial impedance, Z_{int} for the ITO electrodes. In contrast, it did not appear to affect the resistive behavior of the electrodes represented by R_t (~ 1 k Ω) as shown in Chapter 3. In addition, we carried out impedance measurements with MCF-7 cells and we observed that the coating enhanced the sensitivity of the electrodes to cell proliferation. In fact, we obtained a Z_{norm} value similar to that of Au IDEs. The main advantage of this strategy is the fact that we greatly reduced the interfacial impedance of the ITO IDEs without compromising the transparency of the material. As far as we know, there are no reported studies of ITO IDEs modified with IrO_x and here we confirmed that combining ITO with IrO_x could be used as an electrode material to monitor the cell proliferation of cancer cells with a sensitivity closer to that of Au IDEs. However, coating stability experiments for IrO_x/ITO IDEs in contact with only the cell culture medium need to be carried out in order to confirm that the iridium oxide coating do not change through time affecting the enhanced sensitivity of the impedance measurement when cells proliferate on the surface of the interdigitated electrodes.

In the context of personalized medicine, where working in a microfluidic environment appears to be highly useful, the fabrication process of the IrO_x/ITO needs to be changed. This is because of the complexity of carrying out an electrodeposition of IrO_x in a microfluidic environment with our 3 electrode configuration set-up. Therefore, new strategies need to be explored. An alternative solution for this fabrication challenge is chemical bath deposition, in which the iridium precursors undergo oxidation reactions initiated by selectively incorporated oxidizers. This approach does not require externally imposed current/voltage and allows semiconducting materials to be used as the substrates for film growth[91]. The idea is to simply submerge the electrodes into an aqueous solution of IrO_x, allowing for targeted deposition without the necessity for masking, patterning or use of external voltage to drive deposition. Chen et al.[91] developed a formulation to deposit IrO₂ films on an ITO substrate and observed that these films show moderate surface roughness. This could be an interesting fabrication process to modify the ITO IDEs in a microfluidic channel, leading to carry out additional experiments in order to assess the sensitivity and transparency of the electrodes after coating.

Bibliography

- [1] Ilhwan Park, Tra Nguyen, Jinsoo Park, Ah Young Yoo, Jae Kweon Park, and Sungbo Cho. “Impedance Characterization of Chitosan Cytotoxicity to MCF-7 Breast Cancer Cells Using a Multidisc Indium Tin Oxide Microelectrode Array”. In: *Journal of The Electrochemical Society* 165.2 (2018), pp. 55–59. DOI: <https://doi.org/10.1149/2.1201802jes>.
- [2] Chang K.Choi, Anthony E.English, Seung-Ik Jun, Kenneth D.Kihm, and Philip D.Rack. “An endothelial cell compatible biosensor fabricated using optically thin indium tin oxide silicon nitride electrodes”. In: *Biosensors and Bioelectronics* 22.11 (2007), pp. 2585–2590. DOI: <https://doi.org/10.1016/j.bios.2006.10.0006>.
- [3] Tibor Izák, Katarína Novotná, Ivana Kopová, Lucie Bacáková, Bohuslav Rezek, and Alexander Kromka. “H-terminated diamond as optically transparent impedance sensor for real-time monitoring of cell growth”. In: *Physica Status Solidi B* 250.12 (2013), pp. 2741–2746. DOI: <https://doi.org/10.1002/pssb.201300098>.
- [4] Benjamin D. Matthews, Darryl R. Overby, Francis J. Alenghat, John Karavitis, Yasuchi Numaguchi, Philip G. Allen, and Donald E. Ingber. “Mechanical properties of individual focal adhesions probed with a magnetic microneedle”. In: *Biochemical and Biophysical Research Communications* 313.3 (2004), pp. 758–764. DOI: <https://doi.org/10.1016/j.bbrc.2003.12.005>.
- [5] Chang Kyoung Choi, Mugdha Sukhthankar, Chul-Ho Kim, Seong-Ho Lee, Anthony English, Kenneth D. Kihm, and Seung Joon Baek. “Cell adhesion property affected by cyclooxygenase and lipoxygenase: Opto-electric approach”. In: *Biochemical and Biophysical Research Communications* 391.3 (2010), pp. 1385–1389. DOI: <https://doi.org/10.1016/j.bbrc.2009.12.069>.
- [6] R. De Levie. “The influence of surface roughness of solid electrodes on electrochemical measurements”. In: *Electrochimica Acta* 10.2 (1965), pp. 113–130. DOI: [https://doi.org/10.1016/0013-4686\(65\)87012-8](https://doi.org/10.1016/0013-4686(65)87012-8).

- [7] E. T. McAdams and J. Jossinet. “Electrode-Electrolyte interface impedance and polarization”. In: *Medical Bioelectric and Thermal Surface Sensors*. Innovation, Technology in biology, and Medicine, June 1990, pp. 12–20.
- [8] H. Keiser, K. D. Beccu, and M. A. Gutjahr. “Abschätzung der Porenstruktur poroser Elektroden aus Impedanzmessungen”. In: *Electrochimica Acta* 21.8 (1976), pp. 539–543. DOI: [https://doi.org/10.1016/0013-4686\(76\)85147-X](https://doi.org/10.1016/0013-4686(76)85147-X).
- [9] J. C. Wang and J. B. Bates. “Model for the interfacial impedance between a solid electrolyte and a blocking metal electrode”. In: *Solid State Ionics* 18-19.1 (1986), pp. 224–228. DOI: [https://doi.org/10.1016/0167-2738\(86\)90116-5](https://doi.org/10.1016/0167-2738(86)90116-5).
- [10] Walter Scheider. “Theory of the frequency dispersion of electrode polarization. Topology of networks with fractional power frequency dependence”. In: *Journal of Physical Chemistry* 79.2 (1975), pp. 127–136. DOI: <https://doi.org/10.1021/j100569a008>.
- [11] S. H. Liu. “Fractal model for the ac response of a rough interface”. In: *Physical Review Letters* 55.5 (1985), pp. 529–532. DOI: <https://doi.org/10.1103/PhysRevLett.55.529>.
- [12] Michael Kramer and Micha Tomkiewicz. “Porous Electrodes I. Numerical Simulation Using Random Network and Single-Pore Models”. In: *Journal of the Electrochemical Society* 131.6 (1984), pp. 1283–1288. DOI: <https://doi.org/10.1149/1.2115807>.
- [13] Robin Ball and Martin Blunt. “A fractal model for the impedance of a rough surface”. In: *Journal of Physics A: Mathematical and General* 21.1 (1988), pp. 197–204. DOI: <https://doi.org/10.1088/0305-4470/21/1/024>.
- [14] Ju-Hyun Kim, Gyumin Kang, Yoonkey Nam, and Yang-Kyu Choi. “Surface-modified microelectrode array with flake nanostructure for neural recording and stimulation”. In: *Nanotechnology* 21.8 (2010), pp. 1–8. DOI: <https://doi.org/10.1088/0957-4484/21/8/085303>.
- [15] V. Srinivasaraghavan, J. Strobl, D. Wang, J. R. Heflin, and M. Agah. “A comparative study of nano-scale coatings on gold electrodes for bioimpedance studies of breast cancer cells”. In: *Biomedical microdevices* 16.5 (2014), pp. 689–696. DOI: <https://doi.org/10.1007/s10544-014-9873-1>.
- [16] Mohammad Abdolahad, Mohammad Taghinejad, Hossein Taghinejad, Mohsen Janmalekib, and Shams Mohajerzadeh. “A vertically aligned carbon nanotube-based impedance sensing biosensor for rapid and high sensitive detection of cancer cells”. In: *Lab on a Chip* 12.6 (2012), pp. 1183–1190. DOI: <https://doi.org/10.1039/c2lc21028b>.
- [17] C. Boehler, T. Stieglitz, and M. Asplund. “Nanostructured platinum grass enables superior impedance reduction for neural microelectrodes”. In: *Biomaterials* 67 (2015), pp. 346–353. DOI: <https://doi.org/10.1016/j.biomaterials.2015.07.036>.
- [18] Rui Vilar. *Laser Surface Modification of Biomaterials Techniques and Applications*. Cambridge, USA: Woodhead Publishing, 2016.

BIBLIOGRAPHY

- [19] Pietro Mandracci, Federico Mussano, Paola Rivolo, and Stefano Carossa. “Surface Treatments and Functional Coatings for Biocompatibility Improvement and Bacterial Adhesion Reduction in Dental Implantology”. In: *Coatings* 6.1 (2016), pp. 1–22. DOI: <https://doi.org/10.3390/coatings6010007>.
- [20] Ulises A. Aregueta-Robles, Andrew J. Woolley, Laura A. Poole-Warren, Nigel H. Lovell, and Rylie A. Green. “Organic electrode coatings for next-generation neural interfaces”. In: *Frontiers in Neuroengineering* 7.15 (2014), pp. 1–18. DOI: <https://doi.org/10.3389/fneng.2014.00015>.
- [21] Elisa Castagnola, Alberto Ansaldo, Emma Maggiolini, Tamara Ius, Miran Skrap, Davide Ricci, and Luciano Fadiga. “Smaller, softer, lower-impedance electrodes for human neuroprosthesis: a pragmatic approach”. In: *Frontiers in Neuroengineering* 7.8 (2014), pp. 1–17. DOI: <https://doi.org/10.3389/fneng.2014.00008>.
- [22] Sanjay Mathur and Mrityunjay Singh. *Nanostructured Materials and Nanotechnology*. Hoboken, New Jersey: John Wiley & Sons, 2008.
- [23] S. E. Stanca, F. Hänschke, A. Ihring, G. Zieger, J. Dellith, E. Kessler, and H.-G. Meyer. “Chemical and Electrochemical Synthesis of Platinum Black”. In: *Scientific Reports* 7.1074 (2017), pp. 1–8. DOI: <https://doi.org/10.1038/s41598-017-01040-8>.
- [24] Allen J. Bard, György Inzelt, and Fritz Scholz. *Electrochemical Dictionary*. Verlag Berlin Heidelberg: Springer, 2012.
- [25] Matthias Heim, Blaise Yvert, and Alexander Kuhn. “Nanostructuring strategies to enhance microelectrode array (MEA) performance for neuronal recording and stimulation”. In: *Journal of Physiology-Paris* 106.3-4 (2011), pp. 1–9. DOI: <https://doi.org/10.1016/j.jphysparis.2011.10.001>.
- [26] Sharanya Arcot Desai, John D. Rolston, Liang Guo, and Steve M. Potter. “Improving Impedance of Implantable Microwire Multi-Electrode Arrays by Ultrasonic Electroplating of Durable Platinum Black”. In: *Frontiers in Neuroengineering* 3.5 (2010), pp. 1–11. DOI: <https://doi.org/10.3389/fneng.2010.00005>.
- [27] S. Kisban, S. Herwik, K. Seidl, B. Rubehn, O. Paul, P. Ruther, T. Stieglitz, and A. Jezzini. “Microprobe Array with Low Impedance Electrodes and Highly Flexible Polyimide Cables for Acute Neural Recording”. In: *EMBS 2007. 29th Annual International Conference of the IEEE*. IEEE, Aug. 2007, pp. 175–178.
- [28] Sang Beom Jun, Matthew R. Hynd, Karen L. Smith, Jong Keun Song, James N. Turner, William Shain, and Sung June Kim. “Electrical stimulation-induced cell clustering in cultured neural networks”. In: *Medical & Biological Engineering & Computing* 45.11 (2007), pp. 1015–1021. DOI: <https://doi.org/10.1007/s11517-007-0218-6>.
- [29] Ben M. Maoz, Anna Herland, Olivier Y. F. Henry, William D. Leineweber, Moran Yavid, John Doyle, Robert Mannix, Ville J. Kujala, Edward A. FitzGerald, Kevin Kit Parker, and Donald E. Ingber. “Organs-on-Chips with combined multi-electrode array and transepithelial electrical resistance measurement capabilities”. In: *Lab on a Chip* 17.13 (2017), pp. 2294–2302. DOI: <https://doi.org/10.1039/c7lc00412e>.

- [30] A. Norlin, J. Pan, and C. Leygraf. “Investigation of interfacial capacitance of Pt, Ti and TiN coated electrodes by electrochemical impedance spectroscopy”. In: *Biomolecular Engineering* 19.2-6 (2002), pp. 67–71. DOI: [https://doi.org/10.1016/S1389-0344\(02\)00013-8](https://doi.org/10.1016/S1389-0344(02)00013-8).
- [31] Adam Khalifa, Zhaoli Gao, Amine Bermak, Yi Wang, Leanne Lai, and Hang Chan. “A novel method for the fabrication of a high-density carbon nanotube microelectrode array”. In: *Sensing and Bio-Sensing Research* 5 (2015), pp. 1–7. DOI: <https://doi.org/10.1016/j.sbsr.2015.04.001>.
- [32] M. R. Abidian and D. C. Martin. “Experimental and theoretical characterization of implantable neural microelectrodes modified with conducting polymer nanotubes”. In: *Biomaterials* 29.9 (2008), pp. 1273–1283. DOI: <https://doi.org/10.1016/j.biomaterials.2007.11.022>.
- [33] Zejie Zhu, Xiaoyan Liu, Zhenni Ye, Jianqing Zhang, Fahe Cao, and Junxi Zhang. “A fabrication of iridium oxide film pH micro-sensor on Pt ultramicroelectrode and its application on in-situ pH distribution of 316L stainless steel corrosion at open circuit potential”. In: *Sensors and Actuators B: Chemical* 255.2 (2017), pp. 1974–1982. DOI: <https://doi.org/10.1016/j.snb.2017.08.219>.
- [34] Bin He. *Neural Engineering*. New York: Kluwer Academic Publishers, 2005.
- [35] O. I. Obrezkov, V. P. Vinogradov, V. I. Krauz, D. V. Mozgrin, I. A. Guseva, E. S. Andreev, A. A. Zverev, and A. L. Starostin. “Study of electrochemical properties of thin film materials obtained using plasma technologies for production of electrodes for pacemakers”. In: *Journal of Physics: Conference Series* 748.012018 (2016), pp. 1–4. DOI: <https://doi.org/10.1088/1742-6596/748/1/012018>.
- [36] A. Norlin, J. Pan, and C. Leygraf. “Investigation of Electrochemical Behavior of Stimulation/Sensing Materials for Pacemaker Electrode Applications I. Pt, Ti, and TiN Coated Electrodes”. In: *Journal of the Electrochemical Society* 152.2 (2005), pp. 7–15. DOI: <https://doi.org/10.1149/1.1842092>.
- [37] Stuart F. Cogan. “Neural Stimulation and Recording Electrodes”. In: *Annual Review of Biomedical Engineering* 10 (2008), pp. 275–309. DOI: <https://doi.org/10.1146/annurev.bioeng.10.061807.160518>.
- [38] Suzan Meijs, Morten Fjorback, Carina Jensen, Søren Sørensen, Kristian Rechendorff, and Nico J. M. Rijkhoff. “Electrochemical properties of titanium nitride nerve stimulation electrodes: an in vitro and in vivo study”. In: *Frontiers in Neuroengineering* 9.268 (2015), pp. 1–11. DOI: <https://doi.org/10.3389/fnins.2015.00268>.
- [39] Li XiaoQian, Pei WeiHua, Tang RongYu, Gui Qiang, Guo Kai, Wang Yu, and Chen HongDa. “Investigation of flexible electrodes modified by TiN, Pt black and IrO_x”. In: *Science China Technological Sciences* 54.9 (2011), pp. 2305–2309. DOI: <https://doi.org/10.1007/s11431-011-4436-7>.
- [40] James D. Weiland, David J. Anderson, and Mark S. Humayun. “In Vitro Electrical Properties for Iridium Oxide Versus Titanium Nitride Stimulating Electrodes”. In: *IEEE TRANSACTIONS ON BIOMEDICAL ENGINEERING* 49.12 (2002), pp. 1574–1579. DOI: <https://doi.org/10.1109/TBME.2002.805487>.

- [41] Jung Hwal Shin, Guk Bae Kim, Eun Joo Lee, Taechang An, Kumjae Shin, Seung Eun Lee, WooSeok Choi, Sukchan Lee, Charles Latchoumane, Hee-Sup Shin, and Geunbae Lim. “Carbon-Nanotube-Modified Electrodes for Highly Efficient Acute Neural Recording”. In: *Advanced Healthcare Materials* 3.2 (2014), pp. 245–252. DOI: <https://doi.org/10.1002/adhm.201300183>.
- [42] Andrew O. Fung, Christos Tsiokos, Omeed Paydar, Li Han Chen, Sungho Jin, Yibin Wang, and Jack W. Judy. “Electrochemical Properties and Myocyte Interaction of Carbon Nanotube Microelectrodes”. In: *Nano Letters* 10.11 (2010), pp. 4321–4327. DOI: <https://doi.org/10.1021/nl1013986>.
- [43] N. Gaio, B. van Meer, C. Silvestri, S. Pakazad, S. Vollebregt, C. L. Mummery, and R. Dekker. “Upside-down Carbon nanotube (CNT) micro-electrode array (MEA)”. In: *2015 IEEE SENSORS*. IEEE, Apr. 2015.
- [44] Chuang Peng, Jun Jin, and George Z.Chen. “A comparative study on electrochemical co-deposition and capacitance of composite films of conducting polymers and carbon nanotubes”. In: *Electrochimica Acta* 53.2 (2007), pp. 525–537. DOI: <https://doi.org/10.1016/j.electacta.2007.07.004>.
- [45] Mark Hughes, George Z. Chen, Milo S. P. Shaffer, Derek J. Fray, and Alan H. Windle. “Electrochemical Capacitance of a Nanoporous Composite of Carbon Nanotubes and Polypyrrole”. In: *Chemistry of Materials* 14.4 (2002), pp. 1610–1613. DOI: <https://doi.org/10.1021/cm010744r>.
- [46] Mark Hughes, Milo S. P. Shaffer, Annette C. Renouf, Charanjeet Singh, George Z. Chen, Derek J. Fray, and Alan H. Windle. “Electrochemical Capacitance of Nanocomposite Films Formed by Coating Aligned Arrays of Carbon Nanotubes with Polypyrrole”. In: *Advanced Materials* 14.5 (2002), pp. 382–385. DOI: [https://doi.org/10.1002/1521-4095\(20020304\)14:5<382::AID-ADMA382>3.0.CO;2-Y](https://doi.org/10.1002/1521-4095(20020304)14:5<382::AID-ADMA382>3.0.CO;2-Y).
- [47] Hamid Charkhkar, Gretchen L. Knaack, Daniel G. McHail, Himadri S. Mandal, Nathalia Peixoto, Judith F. Rubinson, Theodore C. Dumas, and Joseph J. Pancrazio. “Chronic intracortical neural recordings using microelectrode arrays coated with PEDOT-TFB”. In: *Acta Biomaterialia* 32 (2016), pp. 57–67. DOI: <https://doi.org/10.1016/j.actbio.2015.12.022>.
- [48] Alexander R. Harris, Simeon J. Morgan, Jun Chen, Robert M. I. Kapsa, Gordon G. Wallace, and Antonio G. Paolini. “Conducting polymer coated neural recording electrodes”. In: *Journal of Neural Engineering* 10.1 (2013), pp. 1–16. DOI: <https://doi.org/10.1088/1741-2560/10/1/016004>.
- [49] S. Biallozor and A. Kupniewska. “Conducting polymers electrodeposited on active metals”. In: *Synthetic Metals* 155.3 (2005), pp. 443–449. DOI: <https://doi.org/10.1016/j.synthmet.2005.09.002>.
- [50] Affar S. Karimullah, David R.S. Cumming, Mathis Riehlec, and Nikolaj Gadegaard. “Development of a conducting polymer cell impedance sensor”. In: *Sensors and Actuators B: Chemical* 176 (2013), pp. 667–674. DOI: <https://doi.org/10.1016/j.snb.2012.09.075>.

- [51] D. D. Ateh, A. Waterworth, D. Walker, B.H. Brown, H. Navsaria, and P. Vadgama. “Impedimetric sensing of cells on polypyrrole-based conducting polymers”. In: *Journal of Biomedical Materials Research Part A* 83.2 (2007), pp. 391–400. DOI: <https://doi.org/10.1002/jbm.a.31308>.
- [52] Y. Nam, J. C. Chang, B. C. Wheeler, and G. J. Brewer. “Gold-coated microelectrode array with thiol linked self-assembled monolayers for engineering neuronal cultures”. In: *IEEE Transactions on Biomedical Engineering* 51.1 (2004), pp. 158–165. DOI: <https://doi.org/10.1109/TBME.2003.820336>.
- [53] Guo Xiaoliang, Zhu Rong, and Zong Xianli. “A microchip integrating cell array positioning with *in situ* single-cell impedance measurement”. In: *Analyst* 140.19 (2015), pp. 1–16. DOI: <https://doi.org/10.1039/c5an01193k>.
- [54] Anil Koklu, Ahmet C. Sabuncu, and Ali Beskok. “Rough Gold Electrodes for Decreasing Impedance at the Electrolyte/Electrode Interface”. In: *Electrochimica Acta* 205 (2016), pp. 215–225. DOI: <https://doi.org/10.1016/j.electacta.2016.04.048>.
- [55] Ching-Chou Wu, Wei-Cheng Lin, and Shih-YuFu. “The open container-used microfluidic chip using IrOx ultramicroelectrodes for the *in situ* measurement of extracellular acidification”. In: *Biosensors and Bioelectronics* 26.10 (2011), pp. 4191–4197. DOI: <https://doi.org/10.1016/j.bios.2011.04.034>.
- [56] Sayed A.M. Marzouk, Richard P. Buck, Larry A. Dunlap, Timothy A. Johnson, and Wayne E. Cascio. “Measurement of extracellular pH, K⁺, and lactate in ischemic heart”. In: *Analytical Biochemistry* 308.1 (2002), pp. 52–60. DOI: [https://doi.org/10.1016/S0003-2697\(02\)00220-8](https://doi.org/10.1016/S0003-2697(02)00220-8).
- [57] Salimi Abdollah, Vali Alizadeh, and Richard G. Compton. “Disposable amperometric sensor for neurotransmitters based on screen-printed electrodes modified with a thin iridium oxide film”. In: *Analytical Sciences: the international journal of the Japan Society for Analytical Chemistry* 21.11 (2005), pp. 1275–1280.
- [58] Cuong M. Nguyen, Smitas Rao, J.-C. Chiao, Hung Cao, Ailing Li, and Yuan Bo Peng. “Miniature neurotransmitter sensors featured with iridium oxide nanorods”. In: *SENSORS, 2014 IEEE*. IEEE, Nov. 2014, pp. 1869–1872.
- [59] Chiaki Terashima, Tata N. Rao, Bulusu V. Sarada, Nicolae Spataru, and Akira Fujishima. “Electrodeposition of hydrous iridium oxide on conductive diamond electrodes for catalytic sensor applications”. In: *Journal of Electroanalytical chemistry* 544 (2003), pp. 65–74. DOI: [https://doi.org/10.1016/S0022-0728\(03\)00066-4](https://doi.org/10.1016/S0022-0728(03)00066-4).
- [60] Hanna Elzanowska, Erfan Abu-Irhayem, Beata Skrzynecka, and Viola I. Birss. “Hydrogen Peroxide Detection at Electrochemically and Sol-Gel Derived Ir Oxide Films”. In: *ELECTROANALYSIS* 16.6 (2004), pp. 478–490. DOI: <https://doi.org/10.1002/elan.200402837>.
- [61] Michael Pikulski and Waldemar Gorski. “Iridium-Based Electrocatalytic Systems for the Determination of Insulin”. In: *Analytical Chemistry* 72.13 (2000), pp. 2696–2702. DOI: <https://doi.org/10.1021/ac000343f>.

BIBLIOGRAPHY

- [62] Prats-Alfonso, Abad L, Casañ-Pastor N, Gonzalo-Ruiz J, and Baldrich E. “Iridium oxide pH sensor for biomedical applications. Case urea-urease in real urine samples”. In: *Biosensors Bioelectronics* 39.1 (2013), pp. 163–169. DOI: <https://doi.org/10.1016/j.bios.2012.07.022>.
- [63] Wen-Ding Huang, Hung Cao, Sanchali Deb, Mu Chiao, and J. C. Chiao. “A flexible pH sensor based on the iridium oxide sensing film”. In: *Sensors and Actuators A: Physical* 169.1 (2011), pp. 1–11. DOI: <https://doi.org/10.1016/j.sna.2011.05.016>.
- [64] S Negi, R Bhandari, L Rieth, and F Solzbacher. “In vitro comparison of sputtered iridium oxide and platinum-coated neural implantable microelectrode arrays”. In: *Biomedical Materials* 5.1 (2010), pp. 1–9. DOI: <https://doi.org/10.1088/1748-6041/5/1/015007>.
- [65] RD Meyer, SF Cogan, TH Nguyen, and RD Rauh. “Electrodeposited iridium oxide for neural stimulation and recording electrodes”. In: *IEEE Transactions on Neural Systems and Rehabilitation Engineering* 9.1 (2001), pp. 2–11. DOI: <https://doi.org/10.1109/7333.918271>.
- [66] EIC Laboratories. *Electroplated Iridium Oxide EIROF*. URL: <http://www.eiclabs.com/IrOxideEIROF.pdf>.
- [67] Matthias Heim, Blaise Yvert and Alexander Kuhn. “Nanostructuring strategies to enhance microelectrode array (MEA) performance for neuronal recording and stimulation”. In: *Journal of Physiology* (2011), pp. 1–9. DOI: <https://doi.org/10.1016/j.jphysparis.2011.10.001>.
- [68] RD Meyer, SF Cogan, TH Nguyen and RD Rauh. “Electrodeposited iridium oxide for neural stimulation and recording electrodes”. In: *IEEE Trans Neural Syst Rehabil Eng.* (2001), pp. 2–11. DOI: <https://doi.org/10.1109/7333.918271>.
- [69] A. Blau, Ch. Ziegler, M. Heyer, F. Endres, G. Schwitzgebel, T. Matthies, T. Stieglitz, J.-U. Meyer, and W. Göpel. “Characterization and optimization of microelectrode arrays for in vivo nerve signal recording and stimulation”. In: *Biosensors & Bioelectronics* 12.9-10 (1997), pp. 883–892. DOI: [https://doi.org/S0956-5663\(97\)00017-1](https://doi.org/S0956-5663(97)00017-1).
- [70] Stuart F. Cogan and Julia Ehrlich, Timothy D. Plante, Anton Smirnov, Douglas B. Shire, Marcus Gingerich, and Joseph F. Rizzo. “Sputtered iridium oxide films (SIROFs) for neural stimulation electrodes”. In: *The 26th Annual International Conference of the IEEE Engineering in Medicine and Biology Society*. IEEE, Sept. 2004, pp. 4153–4156.
- [71] L.S. Roblee, M.M. Mangaudis, E.D. Lasinsky, A.G. Kimball, and S.B. Brummer. “Charge Injection Properties of Thermally-Prepared Iridium Oxide Films”. In: *Materials Research Society Symp. Proc.* 55 (1986), pp. 303–310. DOI: <https://doi.org/10.1557/PROC-55-303>.
- [72] Lois S. Robblee, Michael J. Mangaudis, Ellen D. Lasinsky, Angela G. Kimball, and S. Barry Brummer. “Charge Injection Properties of Thermally-Prepared Iridium Oxide Films”. In: *Symposium G – Biomedical Materials*. Materials Research Society, Feb. 1985, pp. 303–310.

- [73] A.M. Cruz, Ll. Abad, N.M. Carretero, J. Moral-Vico, J. Fraxedas, P. Lozano, G. Subías, V. Padiá, M. Carballo, J.E. Collazos-Castro, and N. Casañ-Pastor. “Iridium Oxohydroxide, a Significant Member in the Family of Iridium Oxides. Stoichiometry, Characterization, and Implications in Bioelectrodes”. In: *Journal of Physical Chemistry C* 116.8 (2012), pp. 5155–5168. DOI: <https://doi.org/10.1021/jp212275q>.
- [74] Heather A. Elsen, Christopher F. Monson, and Marcin Majda. “Effects of Electrodeposition Conditions and Protocol on the Properties of Iridium Oxide pH Sensor Electrodes”. In: *Journal of The Electrochemical Society* 156.1 (2009), F1–F6. DOI: <https://doi.org/10.1149/1.3001924>.
- [75] Kazusuke Yamanaka. “Anodically Electrodeposited Iridium Oxide Films (AEIROF) from Alkaline Solutions for Electrochromic Display Devices”. In: *Japanese Journal of Applied Physics* 28.4 (1989), pp. 1–9. DOI: <https://doi.org/10.1143/jjap.28.632>.
- [76] Michel A. Petit and Vincent Plichon. “Anodic electrodeposition of iridium oxide films”. In: *Electroanalytical Chemistry* 444.2 (1998), pp. 247–252. DOI: [https://doi.org/10.1016/S0022-0728\(97\)00570-6](https://doi.org/10.1016/S0022-0728(97)00570-6).
- [77] Takako Yoshino, Nobuyoshi Baba, and Kenji Arai. “Electrochromic IrO^x Thin Films Formed in Sulfatoiridate (III, IV) Complex Solution by Periodic Reverse Current Electrolysis (PRIROF)”. In: *Japanese Journal of Applied Physics* 26.9 (1987), pp. 1547–1549. DOI: <https://doi.org/10.1143/JJAP.26.1547>.
- [78] John E. Baur and Thomas W. Spaine. “Electrochemical deposition of iridium (IV) oxide from alkaline solutions of iridium(III) oxide”. In: *Journal of Electroanalytical Chemistry* 443.2 (1998), pp. 208–216. DOI: [https://doi.org/10.1016/S0022-0728\(97\)00532-9](https://doi.org/10.1016/S0022-0728(97)00532-9).
- [79] Sachin Thanawala, Olena Palyvoda, Daniel G. Georgiev, Saida P. Khan, Ibrahim A. Al-Homoudi, Golam Newaz, and Gregory Auner. “A neural cell culture study on thin film electrode materials”. In: *Journal of Materials Science: Materials in Medicine* 18.9 (2007), pp. 1745–1752. DOI: <https://doi.org/10.1007/s10856-007-3054-1>.
- [80] Imene Feriel AIT-ALI. “Développement et intégration de microcapteurs de pH et de température dans des dispositifs microfluidiques polymères”. PhD thesis. Université Claude Bernard Lyon 1, 2014.
- [81] Sayed A. M. Marzouk. “Improved Electrodeposited Iridium Oxide pH Sensor Fabricated on Etched Titanium Substrates”. In: *Analytical Chemistry* 75.6 (2003), pp. 1258–1266. DOI: <https://doi.org/10.1021/ac0261404>.
- [82] Susan Carroll and Richard P. Baldwin. “Self-Calibrating Microfabricated Iridium Oxide pH Electrode Array for Remote Monitoring”. In: *Analytical Chemistry* 82.3 (2010), pp. 878–885. DOI: <https://doi.org/10.1021/ac9020374>.
- [83] Carmen C. Mayorga Martínez, Rossana E. Madrid, and Carmelo J. Felice. “Electrochemical and geometrical characterization of iridium oxide electrodes in stainless steel substrate”. In: *Sensors and Actuators B: Chemical* 133.2 (2008), pp. 682–686. DOI: <https://doi.org/10.1016/j.snb.2008.03.037>.

BIBLIOGRAPHY

- [84] H. Yang, S. K. Kang, C. A. Choi, H. Kim, D. H. Shin, Y. S. Kim, and Y. T. Kim. “An iridium oxide reference electrode for use in microfabricated biosensors and biochips”. In: *Lab on a Chip* 4.1 (2003), pp. 42–46. DOI: <https://doi.org/10.1039/b309899k>.
- [85] Kim Young-Jin Kim, Lee Young-Chul, Sohn Byung-Ki, and Lee Jung-Hee. “A Novel pH Microsensor with a Built-in Reference Electrode”. In: *Journal of the Korean Physical Society* 43.5 (2003), pp. 769–772.
- [86] I. Thompson and D. Campbell. “Interpreting Nyquist responses from defective coatings on steel substrates”. In: *Corrosion Science* 36.1 (1994), pp. 187–198. DOI: [https://doi.org/10.1016/0010-938X\(94\)90119-8](https://doi.org/10.1016/0010-938X(94)90119-8).
- [87] Damien W. M. Arrigan. *Electrochemical Strategies in Detection Science*. Cambridge, UK: Royal Society of Chemistry, 2016.
- [88] Liudmila Ilyukhina, Svein Sunde, and Richard G. Haverkamp. “Electronic Structure and Growth of Electrochemically Formed Iridium Oxide Films”. In: *Journal of Electrochemical Society* 164.14 (2017), F1662–F1670. DOI: <https://doi.org/10.1149/2.1351714jes>.
- [89] Mouhamad IBRAHIM. “MESURE DE BIOIMPEDANCE ELECTRIQUE PAR CAPTEURS INTERDIGITES”. PhD thesis. Université de Lorraine, 2012.
- [90] Katrin Göbbels, Thomas Kuenzel, André van Ooyen, Werner Baumgartner, Uwe Schnakenberg, and Peter Bräunig. “Neuronal cell growth on iridium oxide”. In: *Biomaterials* 31.6 (2010), pp. 1055–1067. DOI: <https://doi.org/10.1016/j.biomaterials.2009.10.029>.
- [91] Jing-Yu Chen, Yong-Min Chen, Yu Sun, Jyh-Fu Lee, San-Yuan Chen, Po-Chun Chen, and Pu-Wei Wu. “Chemical bath deposition of IrO₂ films on ITO substrate”. In: *Ceramics International* 40.9 (2014), pp. 14983–14990. DOI: <https://doi.org/10.1016/j.ceramint.2014.06.098>.

Conclusion

In this PhD thesis, we aimed at developing a transparent interdigitated electrode-based device for impedance sensing, which could be coupled with optical measurements and integrated in a microfluidic environment for anti-cancer drug screening applications. We first presented the characterization of Au and ITO IDEs in the absence and presence of breast cancer cells proliferating on the surface. We demonstrated two major differences between these two electrode materials: ITO has high interfacial impedance and resistive behavior compared to those of Au, which is considered the standard material for electrodes used in ECIS. These two differences were observed with measurements carried out using KCl solutions and cell culture medium, as the electrolyte. Moreover, we developed an equivalent circuit model that we believe includes contribution from the pores on the surface of the electrodes, which is not commonly found in studies on equivalent circuits for a metallic electrode in contact with an electrolyte. We have also demonstrated that in the characterization process by electrical impedance, the term "roughness" goes beyond the concept of some irregularities on the electrode surface. For instance, there are atomic scale irregularities that can not be monitored with microscopy techniques, such as AFM, which could provide an apparent erroneous information concerning an electrode's actual degree of surface "roughness" and its effects on the measured interface impedance.

The cytotoxicity assays using the chemotherapeutic agent 5-FU lead to conclude that ECIS experiments combined with equivalent circuit modeling provides a promising approach for drug discovery and screening. Particularly, for studying the morphological changes that cells undergo before cell death, which is vital in developing new chemotherapeutic compounds for cancer treatment. In addition, we observed that the orders of magnitude of the electrical parameters R_{extra} and R_{intra} were in agreement with the characteristics of MCF-7 cell line and MDA-MB-231 cell line. One could think to use these parameters as biomarkers to monitor the effect of different anticancer compounds or to characterize cell lines with different degrees of metastatic activity. Furthermore, bioimpedance experiments with breast cancer cells also revealed that ITO has a lower sensitivity to breast cancer cell proliferation compared to that of Au. We therefore decided to modify the surface of the ITO IDEs in order to enhance their sensitivity. From all the possible available strategies described in the literature, we showed that coating the ITO electrodes with IrO_x significantly decreased the interfacial impedance, leading to a Z_{norm} value close to that of gold in the bioimpedance experiments. It appeared to be that the coating only affected the interfacial impedance of the electrodes and the resistive behavior of ITO was not affected after the coating. As far as we know, there are no reported studies of ITO IDEs modified with IrO_x for ECIS sensing and here we confirmed that modifying ITO with IrO_x could be used as a substitute for Au to monitor the proliferation of cancer cells in a sensitive and transparent microfluidic device where ECIS and microscopy could be coupled.

This PhD research project has opened interesting perspectives on ECIS sensors for drug screening applications in cancer treatment. It presents transparent IrO_x/ITO interdigitated electrodes that allow a better observation of morphological changes of cells during cytotoxicity assays and show similar sensitivity to Au electrodes, which have always been the "standard" electrodes for ECIS experiments. Nevertheless, more studies need to be carried out to understand and characterize the morphology of the IrO_x coating on the ITO surface. Moreover, different high surface area coating materials could be tested in order to determine if the enhanced sensitivity of ITO is due to the IrO_x coating itself or due to the surface modification that could be achieved with other materials. In addition, it appears to be relevant to find a strategy to reduce the contribution of R_t for the ITO IDEs to the overall impedance. For example, one could think of including an isolation layer for the ITO traces, leaving only the interdigitated electrodes and contact pads exposed. This means, the complexity of the fabrication process will increase due to supplementary photolithography and alignment steps, necessary for making the IDEs to be only in contact with the electrolyte during the impedance measurement.

Additionally, combining ECIS and microscopy data could provide an insightful description as to how chemotherapeutic drugs affect cancer cells. This could be of interest to biologists who would like to monitor in parallel morphological changes of cells after addition of the compound or drug under study. For instance, one could think of carrying out ECIS experiments combined with fluorescent immunostaining as a strategy to study epithelial tight and adherens junctions by targeting proteins such as e-cadherin, occluding and myosin II of cancer cells in contact with commonly used chemotherapeutic agents such as Cisplatin, Doxorubicin, Paclitaxel or Capecitabine. Furthermore, equivalent circuit modeling appears to be a helpful tool during analysis of the ECIS data and it could reveal some effects of the drugs that are not observable in the microscopic images. With this approach, one could get information on the evolution of the electrical parameters of the system revealing some trends for the cancer cells under study. However, further experiments need to be carried out in order to correlate the trends observed for the electrical parameters with the morphological changes of cells in contact with the chemotherapeutic agents. In the same way, equivalent circuit modeling could be used in further studies for characterizing and differentiating metastatic and non-metastatic tumor cells or for studying resistance of cell lines to several drugs in breast, lung and pancreatic cancers.

In the context of personalized medicine, IrO_x/ITO interdigitated electrodes appear to be promising candidates for developing an impedimetric microfluidic system for cytotoxicity assays. However, working in a microfluidic environment, leads to some fabrication challenges, such as investigating on the design, size, layout of the electrodes and modifying the electrodeposition process of IrO_x with the 3 electrode configuration set-up. An alternative solution for this latter fabrication challenge is to use chemical bath deposition. This alternative approach does not require externally imposed current/voltage and it consists of simply submerging the electrodes into an aqueous solution of IrO_x, allowing for targeted deposition. This could allow the modification of the ITO IDEs in a microfluidic channel, which constitutes a baseline for the development of transparent impedimetric microfluidic systems with enhanced sensitivity for monitoring cell activity during cytotoxicity assays with chemotherapeutic agents. Another challenge that needs to be addressed is to maintain the optimal cell culture conditions in a microfluidic system. For example, strategies to refresh the medium and keep the cell monolayer under flow need to be explored before starting to work with cells coming from biopsies such as circulating tumor cells due to the importance of this type of samples.